

GEMS & GEMOLOGY

FALL 2021
VOLUME LVII

THE QUARTERLY JOURNAL OF THE GEMOLOGICAL INSTITUTE OF AMERICA



Internal Structures of Cultured Pearls from
Pinctada maxima

Sudoite in Caribbean Jewelry from the Ceramic Age

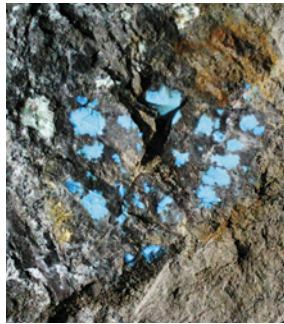
Field Report from Iran's Largest Turquoise Mine



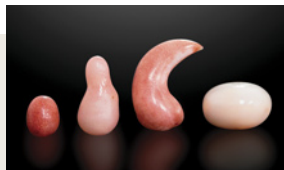
p. 187



p. 229



p. 247



p. 264



p. 268



p. 290

EDITORIAL

- 185** *Pinctada maxima* Pearls from Operated Mollusks, Sudoite in Ceramic-Age Caribbean Jewelry, Persian Turquoise Field Report, and More
Duncan Pay

FEATURE ARTICLES

- 186** Internal Structures of Known *Pinctada maxima* Pearls: Cultured Pearls from Operated Marine Mollusks

Artitaya Homkrajae, Nanthaporn Nilpetploy, Areeya Manustrong, Nicholas Sturman, Kwanreun Lawanwong, and Promlikit Kessrapong

A selection of 74 non-bead cultured and 12 bead cultured pearls grown in cultured pearl sacs and harvested directly from operated mollusks were collected and their internal structures examined using real-time microradiography and X-ray computed microtomography analyses.

- 206** First Identification of Sudoite in Caribbean Ceramic-Age Lapidary Craftmanship

Alain Queffelec, Ludovic Bellot-Gurlet, Eddy Foy, Yannick Lefrais, and Emmanuel Fritsch

Extensive analysis of early beads and pendants from archaeological sites in the French islands of the Lesser Antilles identified the objects as sudoite, which has never before been documented in any lapidary production.

- 228** Purple Gem Spinel from Vietnam and Afghanistan: Comparison of Trace Element Chemistry, Cause of Color, and Inclusions

Philippe M. Belley and Aaron C. Palke

A chemical and spectroscopic comparison of two purple gem spinel samples, one of them the first reported example of a spinel with a saturated purple color caused predominantly by chromium and cobalt.

FIELD REPORTS

- 240** Persian Turquoise: The Ancient Treasure of Neyshabur

Bahareh Shirdam, Andy H. Shen, Mingxing Yang, Zahra Mokhtari, and Hamed Fazliani

Reports on the geology, background, and current state of mining and production at Iran's largest turquoise mine.

REGULAR FEATURES

- 238** 2021 Challenge Winners

- 258** Lab Notes

HPHT-processed diamond with counterfeit GIA inscription • Double cat's-eye emerald • Fossilized shell consisting of emerald • Glass imitation of star sapphire • New laboratory-grown CVD diamond material • Laboratory-grown CVD diamond with internal laser markings • Dyed non-nacreous pearls • Zircon with unusual color-change behavior

- 268** *G&G* Micro-World

Apatite in blue sapphire • Octahedral-shaped inclusion in diamond • Hematite "rose" in aquamarine • Parasite in emerald • Iridescent akoya pearl • "Snake" and "fish" fluid inclusions in Chinese ruby • Tourmaline in Paraíba tourmaline • Willemite in topaz • Quarterly Crystal: Inclusions in pink euclase

- 276** Gem News International

Fura Gems' inaugural ruby sale • Cultured mabe pearls from Mayotte • Honey brown and light yellow hydrogrossular imitating jade • Pink aventurine quartz with alurgite inclusions • FTIR observations of sapphire treated with heat and pressure • Heat treatment effects in low-iron metamorphic sapphire • Low-temperature heated blue to violet spinel • GIA Library and Museum Facebook group • James Shigley receives Shipley Award

Editorial Staff

Editor-in-Chief

Duncan Pay

Managing Editor

Stuart D. Overlin

soverlin@gia.edu

Associate Editor

Brooke Goedert

Technical Editors

Tao Z. Hsu

tao.hsu@gia.edu

Jennifer Stone-Sundberg

jstone@gia.edu

Editors, Lab Notes

Thomas M. Moses

Shane F. McClure

Editors, Micro-World

Nathan Renfro

Elise A. Skalwold

John I. Koivula

Editors, Gem News

Emmanuel Fritsch

Gagan Choudhary

Christopher M. Breeding

Contributing Editors

James E. Shigley

Raquel Alonso-Perez

Editor-in-Chief Emeritus

Alice S. Keller

Assistant Editor

Erin Hogarth

Customer Service

Amanda Perez

(760) 603-4200

gandg@gia.edu

Production Staff

Creative Director

Faizah Bhatti

Production and Multimedia Specialist

Michael Creighton

Photo/Video Producer

Kevin Schumacher

Photographer

Robert Weldon

Illustrator

Russel Samson

Multimedia Associate

Christopher Bonine

Production Supervisor

Richard Canedo

Video Production

Albert Salvato

Editorial Review Board

Ahmadjan Abduriyim

Tokyo, Japan

Timothy Adams

San Diego, California

Edward W. Boehm

Chattanooga, Tennessee

James E. Butler

Washington, DC

Alan T. Collins

London, UK

Sally Eaton-Magaña

Carlsbad, California

John L. Emmett

Brush Prairie, Washington

Emmanuel Fritsch

Nantes, France

Eloïse Gaillou

Paris, France

Al Gilbertson

Carlsbad, California

Gaston Giuliani

Nancy, France

Lee A. Groat

Vancouver, Canada

Yunbin Guan

Pasadena, California

Peter Heaney

University Park, Pennsylvania

Richard W. Hughes

Bangkok, Thailand

Jaroslav Hryšl

Prague, Czech Republic

Dorrit Jacob

Canberra, Australia

A.J.A. (Bram) Janse

Perth, Australia

Mary L. Johnson

San Diego, California

Stefanos Karamelas

Paris, France

Lore Kiefert

Lucerne, Switzerland

Simon Lawson

Maidenhead, UK

Ren Lu

Wuhan, China

Thomas M. Moses

New York, New York

Laura Otter

Canberra, Australia

Aaron Palke

Carlsbad, California

Ilene Reinitz

Chicago, Illinois

Nathan Renfro

Carlsbad, California

Benjamin Rondeau

Nantes, France

George R. Rossman

Pasadena, California

Sudarat Saeseaw

Bangkok, Thailand

Karl Schmetzer

Petershausen, Germany

Andy Shen

Wuhan, China

Guanghai Shi

Beijing, China

James E. Shigley

Carlsbad, California

Elisabeth Strack

Hamburg, Germany

Nicholas Sturman

Bangkok, Thailand

D. Brian Thompson

Florence, Alabama

Fanus Viljoen

Johannesburg, South Africa

Wuyi Wang

New York, New York

Christopher M. Welbourn

Reading, UK

Chunhui Zhou

New York, New York

J.C. (Hanco) Zwaan

Leiden, The Netherlands

Subscriptions

Copies of the current issue may be purchased for \$29.95 plus shipping. Subscriptions are \$79.99 for one year (4 issues) in the U.S. and \$99.99 elsewhere. Canadian subscribers should add GST. Discounts are available for renewals, group subscriptions, GIA alumni, and current GIA students. To purchase print subscriptions, visit store.gia.edu or contact Customer Service. For institutional rates, contact Customer Service.

Database Coverage

Gems & Gemology's impact factor is 1.775, according to the 2020 Thomson Reuters Journal Citation Reports (issued June 2021). *G&G* is abstracted in Thomson Reuters products (Current Contents: Physical, Chemical & Earth Sciences and Science Citation Index—Expanded, including the Web of Knowledge) and other databases. For a complete list of sources abstracting *G&G*, go to gia.edu/gems-gemology, and click on "Publication Information."

Manuscript Submissions

Gems & Gemology, a peer-reviewed journal, welcomes the submission of articles on all aspects of the field. Please see the Author Guidelines at gia.edu/gems-gemology or contact the Managing Editor. Letters on articles published in *G&G* are also welcome. Please note that Field Reports, Lab Notes, Gem News International, Micro-World, Diamonds from the Deep, and Charts are not peer-reviewed sections but do undergo technical and editorial review.

Copyright and Reprint Permission

Abstracting is permitted with credit to the source. Libraries are permitted to photocopy beyond the limits of U.S. copyright law for private use of patrons. Instructors are permitted to reproduce isolated articles and photographs/images owned by *G&G* for noncommercial classroom use without fee. Use of photographs/images under copyright by external parties is prohibited without the express permission of the photographer or owner of the image, as listed in the credits. For other copying, reprint, or republication permission, please contact the Managing Editor.

Gems & Gemology is published quarterly by the Gemological Institute of America, a nonprofit educational organization for the gem and jewelry industry.

Postmaster: Return undeliverable copies of *Gems & Gemology* to GIA, The Robert Mouawad Campus, 5345 Armada Drive, Carlsbad, CA 92008.

Our Canadian goods and service registration number is 126142892RT.

Any opinions expressed in signed articles are understood to be opinions of the authors and not of the publisher.

About the Cover

The Neyshabur turquoise mine in Iran is the subject of an in-depth field report in this issue. Shown on the cover are a three-strand necklace and earrings featuring Persian turquoise beads. The necklace, designed by Suzanne Belperron (1900–1983), contains graduated beads measuring 6.3–14.68 mm and complemented by a diamond clasp. The Art Deco earrings with articulated baguette and old mine cut diamonds contain turquoise drops measuring 35 mm in length. Photo by Robert Weldon/GIA; courtesy of Sima G. Ltd., New York.

Printing is by L+L Printers, Carlsbad, CA.



Pinctada maxima Pearls from Operated Mollusks, Sudoite in Ceramic-Age Caribbean Jewelry, Persian Turquoise Field Report, and More



We invite you to cozy up with the new Fall edition of *G&G!* Travel to Western Australia as we continue the series on *Pinctada maxima* pearls, this time with a focus on cultured pearls harvested directly from operated marine mollusks. Then let two historical articles transport you back in time with the discovery of Ceramic-Age objects fashioned from sudoite in the Lesser Antilles and a look at the state of Iran's Neyshabur turquoise mine, the source of treasures dating back to the Neolithic period.

This issue opens with part two in a three-part series on *Pinctada maxima* pearls. Artitaya Homkrajae and fellow GIA researchers investigate the internal structures of 86 saltwater

“An examination of lapidary craft from five archaeological excavations in the French West Indies has revealed the use of a rare gem material: sudoite.”

cultured pearls collected directly from operated mollusks off the coast of Western Australia. Real-time microradiography and X-ray computed microtomography revealed several broad growth structural types, some of which may overlap with their natural counterparts. This study illustrates some of the challenges laboratories face, as the distinction between non-bead cultured and natural pearls is not always clear.

An examination of lapidary craft from five archaeological excavations in the French West Indies has revealed the use of a rare gem material: sudoite. In the second article of this issue, Alain Queffelec and coauthors provide a mineralogical and geological analysis of nine sudoite objects to understand the provenance of the material and the trade networks of Amerindian cultures from the Early Ceramic period.

Next, Philippe Belley and Aaron Palke compare trace element chemistry and visible light absorption spectra of two purple gem spinels from Luc Yen, Vietnam, and Badakhshan, Afghanistan. Their study presents the first reported example of a saturated purple color in spinel attributed to chromium and cobalt.

Historically, the Neyshabur mine has produced the majority of Iranian turquoise, which possesses a unique color and quality and has been prized by civilizations dating back to the Neolithic period. In this field report, Bahareh Shirdam and coauthors uncover the current state of the Neyshabur mine and document the different techniques used to extract this vivid blue to green gem turquoise.

Highlights from the *Lab Notes* section include a unique emerald cabochon with two distinct chatoyant bands, the creative use of manufactured glass to imitate star sapphire, and zircon with unusual color-change behavior when viewed under different illuminants. Explore the inner beauty of gemstones with the *Micro-World* section, featuring a stunning apatite crystal floating over a cloud of silk in a star sapphire, a diamond with an octahedral-shaped cloud inclusion resembling a six-pointed star, and hematite reminiscent of a blossoming rose in aquamarine. In *Gem News International*, you'll find a study on mabe pearl cultivation in the French territory of Mayotte, as well as a report on Fura Gems' inaugural auction for rough untreated Mozambican rubies, and much more.

We hope you enjoy this exciting Fall edition of *Gems & Gemology!*

A handwritten signature in black ink, appearing to read 'Duncan Pay'.

Duncan Pay | Editor-in-Chief | dpay@gia.edu

INTERNAL STRUCTURES OF KNOWN *PINCTADA MAXIMA* PEARLS: CULTURED PEARLS FROM OPERATED MARINE MOLLUSKS

Artitaya Homkrajae, Nanthaporn Nilpetploy, Areeya Manustrong, Nicholas Sturman, Kwanreun Lawanwong, and Promlikit Kessrapong

Saltwater non-bead cultured pearls, sometimes referred to as “keshi,” are byproducts of the bead cultured pearl cultivation process and are mainly composed of solid nacre, in keeping with natural pearls. They often form as individual pearls or may be seen as additional features on the surfaces of some bead cultured (BC) pearls, sometimes known as “Tokki pearls.” The 86 saltwater cultured samples in this study, comprising 74 non-bead cultured (NBC) pearls and 12 BC pearls with intriguing additional surface features, were collected directly from the gonads of operated *Pinctada maxima* mollusks by two of the authors during a visit to a pearl farm. They were collected in order to study the internal structures using real-time microradiography and X-ray computed microtomography analyses. Three structural types—including organic-rich concentric, void, and linear—were observed in the NBC samples, as expected for saltwater NBC pearls produced by *Pinctada* species. The structures were also observed within the associated additional features related to the bead nuclei in the BC pearl samples. The internal features of most of the NBC samples permitted them to be separated from their natural counterparts. Nevertheless, a limited number of NBC samples contained particular structural forms similar to those observed in known *P. maxima* natural pearls previously studied, or they contained complex overlapping features that do not conform to the majority of structures observed in NBC pearls in this study and previous publications. This illustrates the challenges GIA and other gemological laboratories face with some pearl identification cases. Therefore, GIA’s procedure in addressing such cases is discussed and demonstrated. Since the pearl identification stated on reports is an opinion based on a reference collection database and the gemologist’s experience, possible differences of opinion among various gemologists and organizations are hardly surprising. This study on known cultured pearls provides additional reliable data that is essential in consolidating GIA’s reference collection database on the internal structures of pearls.

Pinctada maxima (the silver- or gold-lipped pearl oyster), *Pinctada margaritifera* (the black-lipped pearl oyster), and *Pinctada fucata (martensii)* (“the akoya pearl oyster”) are the main mollusks of the *Pinctada* genus that are commercially farmed. They are routinely used to produce bead cultured (BC) pearls and, as a consequence, sometimes also produce non-bead cultured (NBC) pearls (Otter et al., 2014; Sturman et al., 2016; Nilpetploy et al., 2018a). *P. maxima* is the largest species in the genus (Scarratt et al., 2012) and generally requires a minimum two-year growth period to yield BC pearls with the thickest nacre layers of all BC pearls

(Gervis and Sims, 1992; Cartier and Krzemnicki, 2016). Cultured pearls from the *P. maxima* mollusk are often referred to as “South Sea” in the market.

Australia is the largest producer of white *P. maxima* (silver-lipped) cultured pearls, while Indonesia, Myanmar, and the Philippines are major producers of “golden” *P. maxima* (gold-lipped) cultured pearls. The farms producing these pearls are located between the Tropic of Cancer and the Tropic of Capricorn, which coincides with the native *P. maxima* mollusk’s geographic distribution. The silver-lipped shells are found mostly south of the equator, while the gold-lipped shells populate the region north of the equator (Strack, 2006). *P. maxima* mollusks used for pearl culturing production in Australia are predominantly wild-caught shells collected in accordance with the annual quota that takes the shell sizes into account (between 120 and 175 mm shell length) and allows fishing

See end of article for About the Authors and Acknowledgments.

GEMS & GEMOLOGY, Vol. 57, No. 3, pp. 186–205,

<http://dx.doi.org/10.5741/GEMS.57.3.186>

© 2021 Gemological Institute of America



Figure 1. A selection of *P. maxima* cultured pearls (pictured with a *P. maxima* shell) randomly drawn from a total of 86 pearl samples examined. These consist of NBC pearls as well as BC samples with additional features attached to the surface (“Tokki pearls”). The largest center pearl measures 22.05 × 14.07 × 13.24 mm. Photo by Nuttapol Kitdee.

within specific commercial pearl oyster fishery zones (Western Australia Department of Fisheries, 2016). Hatchery-bred shells are also used to supplement the wild stock (Gervis and Sims, 1992; Southgate and Lucas, 2008). Although BC pearls are the primary production goal, some NBC pearls are also unintentionally produced as a secondary product.

The general technique for cultivating saltwater BC pearls was originally developed for the Japanese akoya pearl culturing industry before being accepted for other culturing operations globally (Otter et al., 2017). It begins with the insertion of a bead nucleus (referred to as a seeding or nucleation process), along with a small piece of mantle tissue (*saibo* in Japanese) that is cut from a donor mollusk in a grafting process and subsequently inserted into the gonad of a living host mollusk (Al-Alawi et al., 2020; Sturman et al., 2020). Shell bead nuclei are usually fashioned from American freshwater mussels of the *Unionidae* family such as washboard (*Megaloniaias nervosa*), ebony (*Fusconaia ebena*), and three-ridge (*Amblema plicata*), which are the most widely used source material for saltwater BC pearl production (Hsu et al., 2016; Sturman et al., 2020). Other materials have been used on an experimental basis in

place of traditional shell beads, including plastic, resin, gemstones, dolomite, bironite, organic gelatinous polymer (superabsorbent polymer, or SAP), low-quality natural pearls, freshwater NBC pearls, and shell beads

In Brief

- Bead cultured (BC) pearls are primary products of pearl cultivation, and some non-bead cultured (NBC) pearls occur as a byproduct. NBC pearls are composed mainly of solid nacre, similar to natural pearls.
- 74 NBC and 12 BC pearls with intriguing additional surface features were collected directly from the gonads of operated *Pinctada maxima* mollusks, and their internal structures were analyzed using RTX and μ -CT.
- Organic-rich concentric, void, and linear structural types were observed in the NBC samples and presented as associated additional features in the BC samples.
- Most NBC samples contained characteristic internal features that differentiated them from their natural counterparts. Nevertheless, some NBC samples showed particular structural forms comparable to the *P. maxima* natural pearls previously studied.

produced from *Tridacna* shell (Snow, 1999; Hänni et al., 2010; Cartier and Krzemnicki, 2013; Cartier et al., 2013; Scarratt et al., 2017; Kessrapong and Lawanwong, 2020). However, none have matched the success of traditional freshwater mussel shell nuclei or been widely adopted for commercial use.

The grafted mantle tissue ideally consists of the outer ectoderm layer containing epithelium cells that are responsible for shell and pearl formation via the production of calcium carbonate (CaCO_3) polymorph aragonite in a brick-type arrangement, as well as organic matrix that is composed of proteins and polysaccharides (Crichton, 2019). Together these are referred to as nacre or mother-of-pearl (MOP). The epithelium cells within the gonad exist as a result of the grafted mantle tissue and are involved in the biomineralization process, while the host's gonad is the reproductive organ and cannot procreate CaCO_3 (Hänni, 2012). After insertion, the epithelium cells multiply by cell division and link together to form a pearl sac that surrounds the bead nucleus and subsequently deposits nacre to form a pearl. Since this pearl sac is a result of the cultivation process, it is sometimes referred to as a "cultured pearl sac" in this study to differentiate it from a pearl sac that is naturally formed without any human intervention. The location from which mantle cells were extracted determines the type of calcium carbonate polymorph that results (Marie et al., 2012). Genetics, as well as the suitability of the mantle tissue selected, greatly impact the properties and quality of the resulting pearl (Otter et al., 2017). Therefore, the mantle tissue is usually selected from donor mollusks that have produced superior quality MOP exhibiting high luster and desirable color. Additionally, it is important to ensure that the transplanted mantle tissue maintains good contact with the bead nucleus and that the bead's resulting encapsulation by the pearl sac is as complete as possible before the nacre is secreted in order to form a high-quality BC pearl. The pearl sac will continue to produce nacreous layers around the bead nucleus as long as conditions are suitable for the host to do so or until the pearl is harvested. If the mantle tissue is not ideal, or the initial development of the pearl sac is not optimal, the pearl sac and additional features formed during nacre deposition may result in a baroque and/or lower-quality pearl. After harvesting the first BC pearls, farmers usually re-nucleate the mollusk, as the existing pearl sac is still productive and will accept a second bead (second operation). The *P. maxima* mollusk can be operated on up to three times, although in very rare cases four

operations have occurred (Gervis and Sims, 1992). The number of operations will be determined by the mollusk's health and the quality of pearl produced.

In cases where the grafted mantle tissue separates from the bead, the mantle tissue continues to secrete nacre and the formation of a pearl sac is still possible. If the pearl sac does form, it is possible for an NBC pearl to develop (Southgate and Lucas, 2008; Hänni, 2012). It is also possible that individual epithelium cells will break away from the main mantle tissue during the first operation to form additional pearl sac(s). Such accidental pearl sacs function in the same way by secreting nacre and may form an unintentional NBC pearl, in parallel with the creation of the intended BC pearl forming in the primary pearl sac created by the original mantle tissue (Strack, 2006). This additional NBC pearl may form as a feature on the surface of a BC pearl, which may subsequently detach from the surface and appear to be a separate individual NBC pearl later. A BC pearl with an additional feature(s) attached to the surface is also known as a "Tokki pearl" (figure 1 and table 4; see also Krzemnicki et al., 2011). *Tokki* is a Japanese term referring to a surface protuberance. In yet another scenario, the bead nucleus is ejected from an already formed or partially formed pearl sac and an NBC pearl forms in its place (figure 2).

NBC pearls are mainly composed of nacreous layers similar to their natural counterparts, and they are often referred to as "keshi" in the market. However, this Japanese term (meaning "poppy seed") was originally used for natural saltwater seed pearls measuring 1–3 mm (Sturman and Al-Attawi, 2006), before being applied to byproducts found in the mantle area of Japanese akoya cultured pearls (Landman et al., 2001; Hänni, 2006). The World Jewellery Confederation (CIBJO) states that the use of "keshi" alone is misleading and inappropriate, and instead recommends using the term with a qualification such as "keshi cultured pearl" (CIBJO, 2020). The term "keshi" is not used on GIA pearl reports.

Three internal structural types—organic-rich concentric, void, and linear—have been reported in the majority of NBC pearls previously studied (Hänni, 2006; Wehrmeister et al., 2008; Sturman, 2009; Krzemnicki et al., 2010, 2011; Sturman et al., 2016, 2017; Nilpetploy et al., 2018a; Manustrong, 2018; Manustrong et al., 2019; Al-Alawi et al., 2020). Most NBC pearls show characteristic structural features belonging to these three groups that allow gemologists to differentiate them from natural pearls. However, some NBC pearls contain particular forms of these



Figure 2. One example where the authors (AH and NN) found an ejected shell bead nucleus (7.53×6.94 mm) inside a mollusk's gonad. When the shell was opened, a pea crab (*Pinnotheres villosulus*), which has a symbiotic relationship with *P. maxima* mollusks (Scarratt et al., 2012), was observed next to the ejected bead. A 6.92×4.95 mm NBC pearl (inset) was found together with the bead. Photos by Nanthaporn Nilpetploy.

structures that are comparable with those observed in natural pearls, or they contain complex overlapping structures that do not correspond with the structures typically observed in NBC pearls. Moreover, some natural pearls also possess structures that resemble those observed in NBC pearls. These can be challenging to correctly identify, especially when the pearls are submitted without any provenance (Scarratt et al., 2012; Sturman et al., 2019; Homkrajae et al., 2021). To better understand the characteristic internal features of *P. maxima* NBC pearls, as well as BC pearls with associated additional surface growths, the authors studied a selection of NBC and BC pearls grown in cultured pearl sacs and harvested directly from the gonads of operated mollusks. The various types of internal structure recorded in these samples are presented here, the second in a series of three articles that investigate the internal structures of *P. maxima* pearls produced by different growth mechanisms. The natural pearls retrieved directly from unoperated wild mollusks were covered in Homkrajae et al. (2021), and the final article will address pearls that form in the mantle area or adductor muscle, or are found attached to the shell of operated wild and hatchery mollusks.


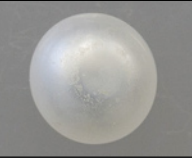
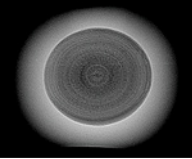
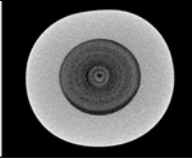
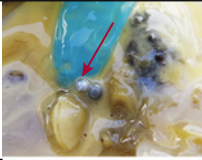

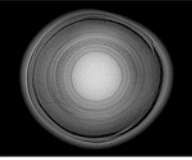
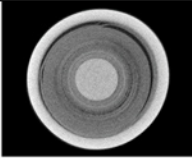


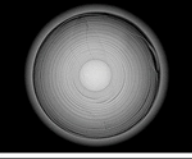
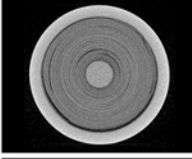


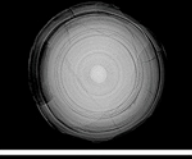
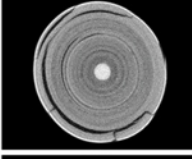


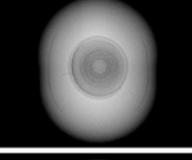
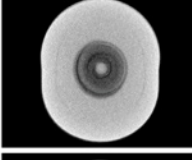


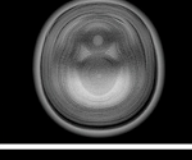
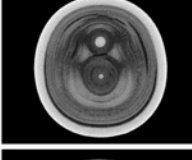

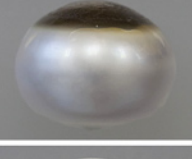
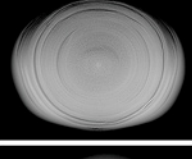
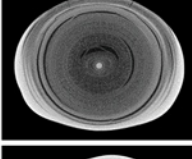
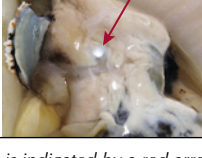

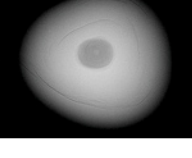
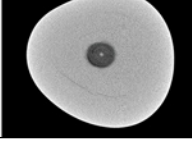
Figure 3. A map showing the location of the Paspaley Pearling Company farm near Middle Osborn Island in Western Australia, where GIA collected cultured pearls from operated *P. maxima* mollusks. Image from Google Maps.

MATERIALS AND METHODS

In October 2014, two members of GIA's pearl team (authors AH and NN) visited a farm owned and operated by the Paspaley Pearling Company located near Middle Osborn Island, off the coast of the Kimberley region in Western Australia, approximately 560 km southwest of Darwin (figure 3). The purpose of the trip was to collect known samples of South Sea cultured pearls (again, see figure 1), particularly NBC pearls, directly from cultured pearl sacs that had developed from pieces of mantle tissue inserted into the gonads of host mollusks. Throughout the seven-



TABLE 1. Examples of NBC pearls from operated mollusks with organic-rich concentric structures (type 1).

Sample details	Position where found in the mollusk	Macro image	RTX image	μ-CT image
Dark gray core				
1-1 (3rd operation wild shell) 0.35 ct 3.95 x 3.82 x 3.08 mm				
Light gray core				
1-2 (3rd operation wild shell) 0.29 ct 3.92 x 3.78 x 3.51 mm				
1-3 (3rd operation wild shell) 0.66 ct 4.80 x 4.77 mm				
1-4 (3rd operation wild shell) 0.30 ct 4.10 x 3.75 mm				
1-5 (3rd operation wild shell) 0.33 ct 4.04 x 3.35 mm				
1-6 (3rd operation wild shell) 1.05 ct 6.04 x 5.63 mm				
1-7 (2nd operation hatchery shell) 2.08 ct 7.97 x 6.39 mm				
1-8 (3rd operation wild shell) 1.80 ct 6.57 x 6.50 x 5.95 mm				



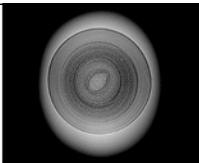
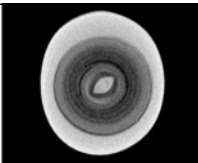
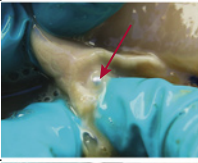
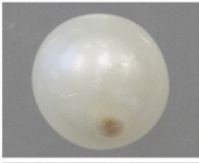
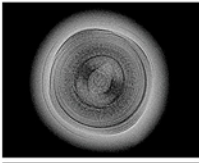
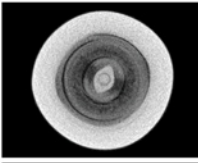


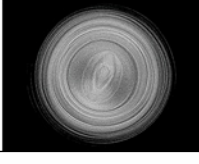
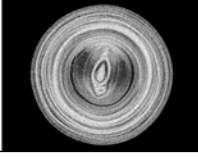

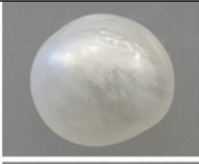
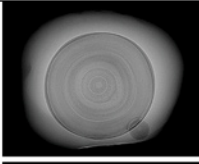
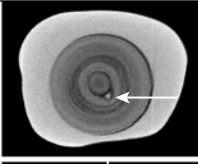


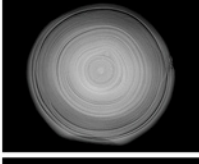
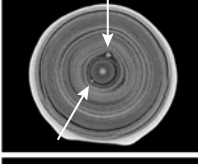
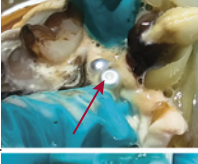
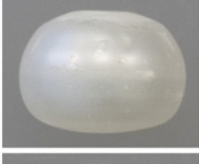
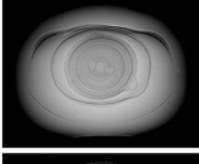
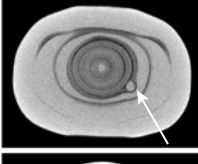

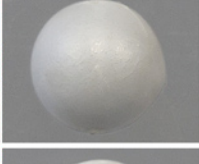
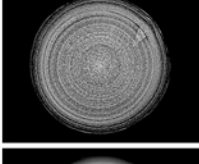
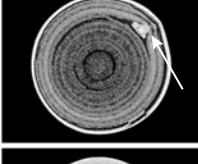


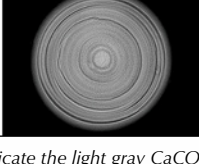
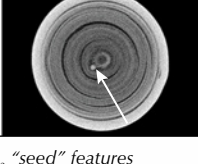
The position of the pearl in the mollusk is indicated by a red arrow.

day visit, nearly 925 mollusks from approximately 10,000 operated shells available were inspected, and a total of 86 cultured pearls (74 NBC and 12 BC) were selected for this study. Only the BC pearls with in-

triguing surface protrusions were selected from the numerous BC pearls recovered.

GIA created pearl sample classification codes to differentiate the degrees of origin dependability, as

TABLE 1. (continued).

Sample details	Position where found in the mollusk	Macro image	RTX image	μ -CT image
Off-round (spindle-shaped) core				
1-9 (3rd operation wild shell) 0.30 ct 4.13 x 3.56 x 3.42 mm				
1-10 (3rd operation wild shell) 0.09 ct 2.60 x 2.47 mm				
1-11 (1st operation wild shell) 0.18 ct 3.24 x 3.20 mm				
Light gray CaCO₃ "seed" features				
1-12 (3rd operation wild shell) 0.62 ct 5.00 x 4.11 mm				
1-13 (2nd operation hatchery shell) 1.19 ct 6.26 x 5.89 mm				
1-14 (2nd operation hatchery shell) 0.97 ct 5.66 x 4.03 mm				
1-15 (1st operation wild shell) 0.09 ct 2.81 x 2.72 mm				
1-16 (2nd operation hatchery shell) 0.30 ct 3.80 x 3.72 mm				

The position of the pearl in the mollusk is indicated by a red arrow. The white arrows indicate the light gray CaCO₃ "seed" features (more radiopaque) observed.

previously described by Homkrajae et al. (2021; see table 1 of that article). Since 86 pearl samples in this study were harvested *in situ* from the gonads of freshly opened mollusks by two of the authors and

their positions were documented by photos and videos, they are of known origin and may accordingly be classified as B1 samples (Homkrajae et al., 2021; see table 1).

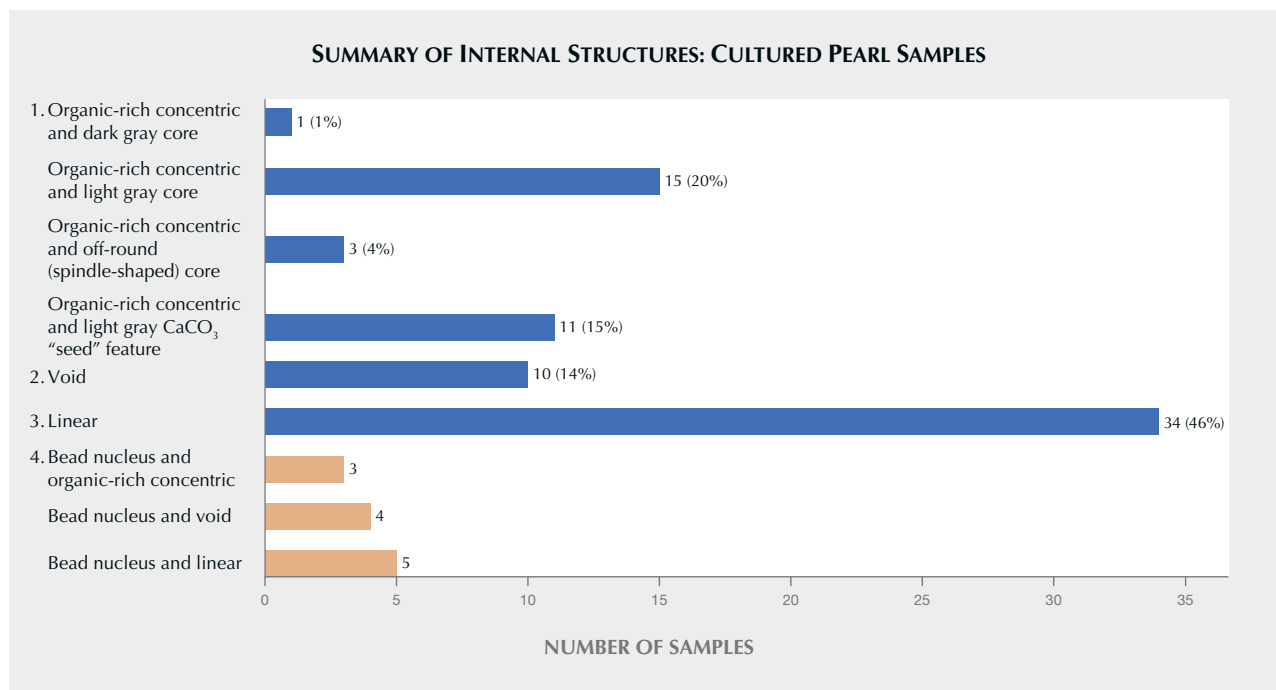


Figure 4. Summary of the four main internal structural types, including any variations found in the 86 cultured pearl samples studied (types 1–3 are observed in NBC and type 4 only in BC). The percentage of each structure recorded in the 74 NBC pearl samples is also shown.

The majority of the host mollusks (90%) were wild shells collected from the ocean floor, while the remainder (10%) were hatchery produced. The age and operation history of the host mollusks varied. Some were older and had already been operated on three times, while others were younger and had only been operated on once. The measurements and weights of the 74 NBC pearls ranged from 1.80 × 1.61 × 1.28 mm to 10.42 × 10.30 × 8.50 mm, and from 0.02 to 6.28 ct. The 12 BC pearls measured from 14.80 × 13.06 × 12.35 mm to 32.51 × 15.62 × 15.40 mm and weighed from 14.31 to 43.33 ct.

The samples were loaned to GIA, and their internal structures were recorded using real-time microradiography (RTX) and X-ray computed microtomography (μ-CT). The RTX analysis was performed using a Pacific X-ray Imaging GenX-90P X-ray system with 4-micron microfocus, 90 kV voltage, and 0.16 mA current X-ray source with an exposure time of 200–400 milliseconds per frame, combined with a PerkinElmer 1512 flat-panel detector with an average maximum of 128 frames and 74.8 micropixel pitch with 1944 × 1536 pixel resolution on all the samples. The samples that showed intriguing or indistinct structures were selected for more detailed viewing with μ-CT. The μ-CT work was carried out with a Pro-Con CT-mini X-ray system with a 5-micron microfocus, 90 kV voltage, and a 0.18 mA X-ray current

source. Two detectors with a frame grabber card were used to capture the results: a Hamamatsu C7921CA-29 flat-panel detector with 50 micropixel pitch and 1032 × 1032 pixel resolution, and a Varex 1207 flat-panel detector with 74.8 micropixel pitch and 1536 × 864 pixel resolution. RTX and μ-CT data were collected in GIA's Bangkok laboratory. Photomicrographs were obtained to show certain features in greater detail using a Nikon SMZ18 stereomicroscope with an SHR Plan Apo 1× objective lens and NIS-Elements imaging software. As with Homkrajae et al. (2021), the purpose of this work was only to investigate the samples' internal characteristics.

OBSERVATIONS AND RESULTS

The characteristic internal features observed in the 86 cultured pearl samples using RTX and μ-CT analyses can be categorized into four broad growth structural types (figure 4). Types 1–3 correspond to NBC samples, and type 4 applies to BC samples only.

1. Organic-rich concentric
2. Void
3. Linear
4. Bead nucleus and associated additional features

Thirty NBC and eight BC pearls from the samples studied were selected as representative samples to

show the variations in the internal structures of the four main structural types and to serve as a reference for future pearl identification. Information and results for each sample are shown in tables 1 to 4. The sample number, weight, measurements, and the number of times the mollusk was operated on are listed in the first column. The second column contains images showing the position of the pearl in each shell when retrieved (indicated by a red arrow). Macro, RTX, and μ -CT results, respectively, are shown in the third through fifth columns. Since RTX and μ -CT are microradiography techniques, all the relevant images in this study are shown in a grayscale intensity scheme. Thus, the internal growth patterns/features display varying intensities of gray corresponding to the differing X-ray densities or radiopacity of the materials that make up the pearls. CaCO_3 polymorphs such as aragonite (nacre or shell bead) are mineralized materials that are denser to X-rays (more radiopaque) than organic-rich material or voids (i.e., areas filled with gases and/or liquids) that are more radiolucent and allow more X-rays to pass through (Wehrmeister et al., 2008; Sturman, 2009; Otter et al., 2014). Therefore, aragonite typically appears light gray, while organic-rich material or voids have a darker gray to black intensity. [Note: In this article, the description of an internal structure as “dark gray” and “light gray” corresponds to its X-ray density, not its actual color.]

Type 1: Organic-Rich Concentric Structures. Various organic-rich concentric structures were observed in 30 of the NBC pearl samples. Sixteen were selected as representative of these structures (table 1). Organic-rich concentric structures were visible as dark gray concentric layered areas in the center and occupied a large portion of the pearl’s volume in most samples. The concentric structures in samples 1-4, 1-13, and 1-15 occupied most of the pearls’ interior, and only a thin light gray layer corresponding to nacre was present on the outermost surface.

Most of the RTX images of the samples contained a dark gray (more radiolucent) or light gray (more radiopaque) core at the center of the concentric structures, similar to some observations in natural *P. maxima* pearls (Homkrajae et al., 2021). However, the core in each of these samples differed in size and form from those observed in the natural pearls. Only sample 1-1 showed a dark gray core consistent with those often encountered in natural pearls. Yet it is worth noting that the large area covered by the concentric structure and the lack of obvious growth fea-

tures in the nacre overlying the structure are observations consistent with NBC pearls examined previously. This combination of features could lead to a wide range of opinions from different gemologists. The rest of the samples showed a light gray core composed of denser X-ray material similar in radiopacity to the outer nacreous layer. The majority of the cores appeared rounded (samples 1-2 through 1-8 and 1-12 through 1-16), and only three samples displayed off-round (spindle-shaped) forms (samples 1-9 through 1-11). The sizes of the light gray core varied from large, in sample 1-2, to a tiny spot in sample 1-8. These cores resemble ones observed in natural pearls, though the very large cores in samples 1-2 and 1-3 have not been observed in any natural pearls to our knowledge. In sample 1-6, a twin center consisting of organic-rich concentric features with two light gray cores, one larger than the other, is intriguing as a similar twin structure was reported in a 0.11 ct natural pearl from a *Pinctada maculata* mollusk (Nilpetploy et al., 2018b). Nevertheless, the concentric growth layers in the center of sample 1-6 are much larger and more evenly spaced, and the distinct round light gray cores in the center of each organic-rich feature, one larger than the other, are also absent in the natural *P. maculata* pearl (figure 5). Moreover, the acicular features shown within the organic-rich area in the natural *P. maculata* pearl are not present in sample 1-6. These differing aspects may also result in a wide range of identification calls. In the authors’ opinion, the structure corresponds more closely with NBC pearls, and thus GIA would consider this pearl to be NBC. This is confirmed by the sample’s provenance. Although an oval core has been observed in a natural pearl (Homkrajae et al., 2021), the authors believe that the spindle-shaped cores in samples 1-9 through 1-11 have only been reported in NBC pearls.

Light gray CaCO_3 “seed” features of various size, shape, and quantity were revealed in different positions within the concentric structures (samples 1-12 through 1-16, indicated by the white arrows in table 1). These “seed” features are generally rounded and contain no discernible structure within, aside from sample 1-15 where the “seed” feature is irregularly shaped and a growth ring is present inside. Such CaCO_3 “seed” features have previously been reported in South Sea and *P. margaritifera* (Tahitian) NBC pearls (Krzemnicki et al., 2010, 2011; Nilpetploy et al., 2018a), and they do not exist in any natural *P. maxima* pearls previously examined (Homkrajae et al., 2021). The presence of such CaCO_3 “seed” features in association with organic-rich concentric

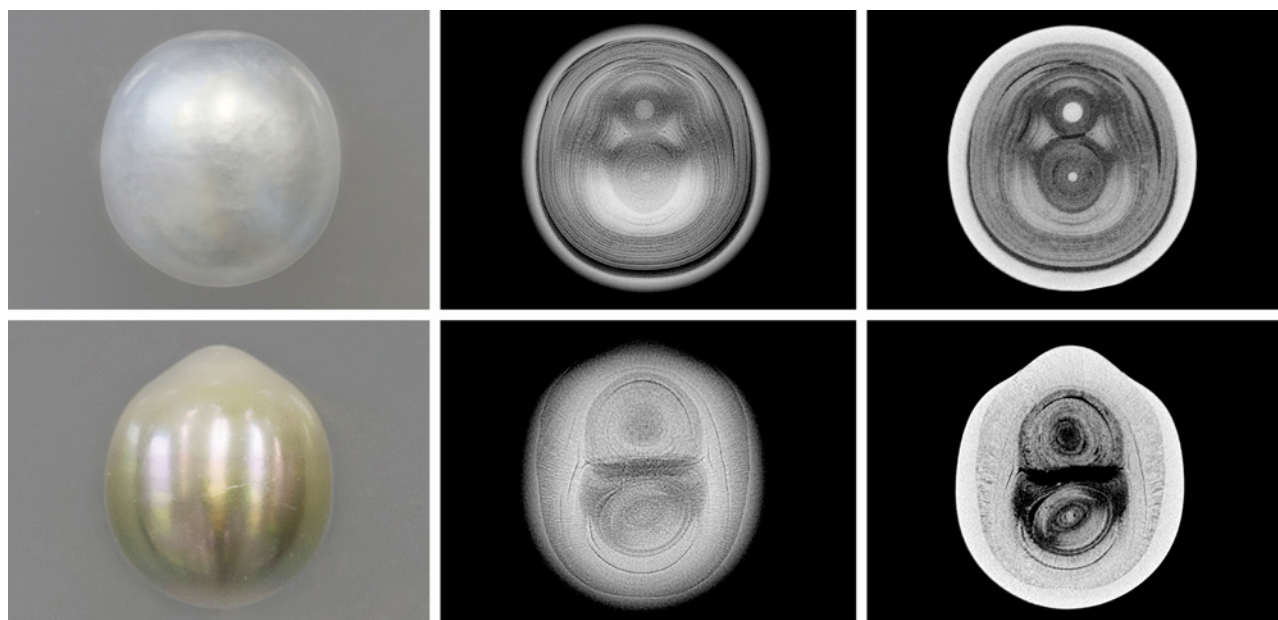


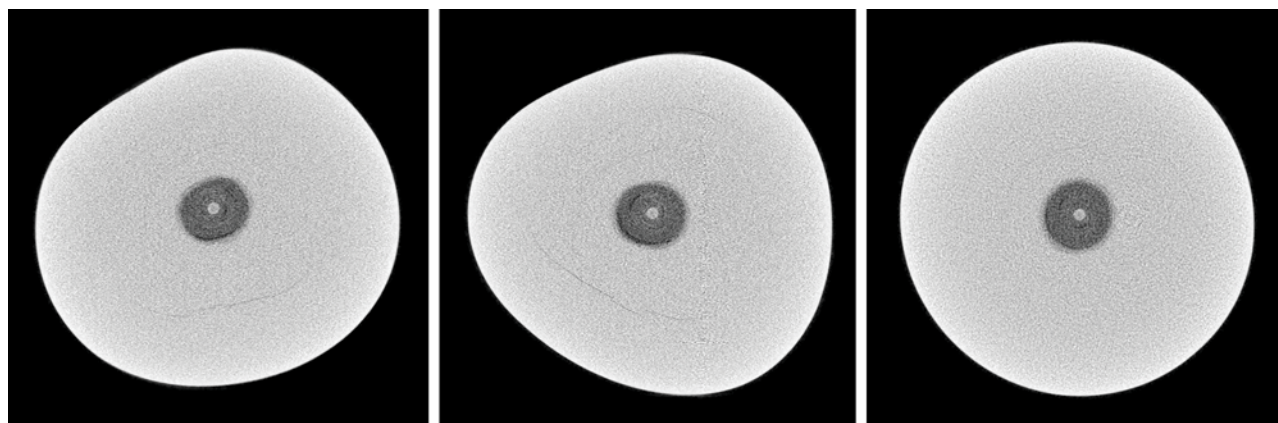
Figure 5. Macro images, RTX images, and μ -CT slices of sample 1-6 (top row), and a 0.11 ct natural *P. maculata* pearl (bottom row) previously studied by Nilpetploy et al. (2018b; see sample 1). Both pearls show similar twin organic-rich concentric features. However, sample 1-6 exhibits larger and more evenly spaced growth layers that incorporate two light gray cores at the center of each, one larger than the other, while the *P. maculata* natural pearl lacks these features and shows acicular formations within the organic-rich area. Photos by Sasithorn Engniwat.

structures is therefore a strong indicator of NBC formation. Additional details on similar CaCO_3 “seed” features found in some non-nacreous *P. maxima* NBC pearls were covered by Manustrong et al. (2019; see table 4).

Some NBC pearls showed ambiguous structures or failed to reveal enough evidence to conclusively identify their origin. Samples 1-5 and 1-8 are good examples. Both showed relatively small areas of dark gray

concentric layers, the light gray cores were small and rounded, no CaCO_3 “seed” features appeared to exist, and a few growth structures were visible in the overlying nacre. In particular, the growth pattern of sample 1-8 (magnified in figure 6) closely resembles structures often observed in natural pearls from various *Pinctada* species (Krzemnicki et al., 2010; Scarratt et al., 2012; Nilpetploy et al., 2018b; Homkrajae et al., 2021) and is comparable to a 0.30 ct known natural *P. maxima*

Figure 6. μ -CT slices in three directions of sample 1-8 reveal a small area of organic-rich concentric structure, a tiny light gray core, and a few growth structures in the surrounding nacre. No CaCO_3 “seed” features were observed within the organic structure. All these observations are consistent with natural pearls, not NBC pearls.



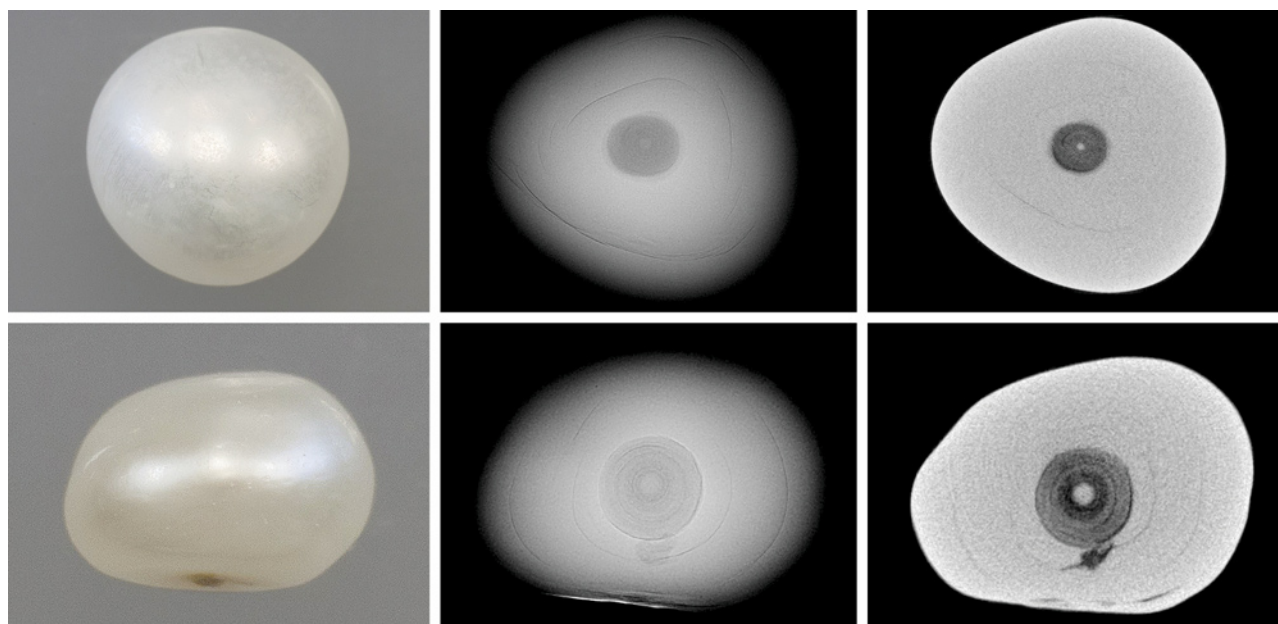


Figure 7. Macro images, RTX images, and μ -CT slices of sample 1-8 (top row) and a 0.30 ct known natural *P. maxima* pearl (bottom row) previously studied by Homkrajae et al. (2021; see sample 2-9). Both pearls show similar internal structures. The light gray cores are relatively small, as are the dark gray concentric layers, and subtle growth patterns surround the central structures. Photos by Sasithorn Engniwat.

pearl sample (figure 7) previously studied by Homkrajae et al. (2021; see sample 2-9). It would be challenging to correctly identify such a pearl as NBC according to its known provenance, and it would almost certainly be classified as natural in standard laboratory testing conditions.

It is also interesting to note that some pearl samples were found together in the same mollusk and share similar internal characteristics. For example, samples 1-9, 1-10, and 1-12 were found together, and a BC pearl was also recovered from the same mollusk. They revealed large organic-rich concentric structures and lacked any growth structures in the surrounding nacreous areas. Samples 1-9 and 1-10 contained a spindle-shaped core, while sample 1-12's core is very small and rounded but also accompanied by a couple of "seed" features. Based on the combination of these internal characteristics, all three pearls would be classified as NBC. Samples 1-13 and 1-14 were found in the gonad next to one another, as shown by the images in the second column in table 1. While their organic-rich concentric structures are quite different in pattern and size, it was intriguing to note that both pearls contained the CaCO_3 "seed" features within the concentric structure (magnified in figure 8). Another observation of note is that most of the samples in this group exhibited a nacreous sur-

face, much like the vast majority of NBC *P. maxima* pearls, yet six samples displayed a non-nacreous surface. The external and internal characteristics of these non-nacreous NBC pearls were recorded in a detailed study by Manustrong et al. (2019), and two samples from that study are also included here (samples 1-4 and 1-11). Sample 1-7 showed both nacreous and non-nacreous surfaces. The nacreous surface exhibited a platy structure, while the non-nacreous part showed transparent features that were circular and bumpy, similar to those of the six non-nacreous samples included in this study.

Type 2: Void Features. Void and linear features are internal cavities or areas filled with gas and/or liquid phases, which are more transparent to X-rays (radiolucent) and appear on RTX and μ -CT images as various tones of gray, usually dark, depending on size and volume. Because voids generally occupy a greater area than linear features (thin or slender voids) and therefore look different, they have been separated into different structural types in this article. Voids are often seen in saltwater NBC pearls, and gemologists use them to separate NBC from natural pearls. While *P. maxima* mollusks produce the majority of NBC pearls seen in the market, other *Pinctada* species also produce them (Wehrmeister et al., 2008;

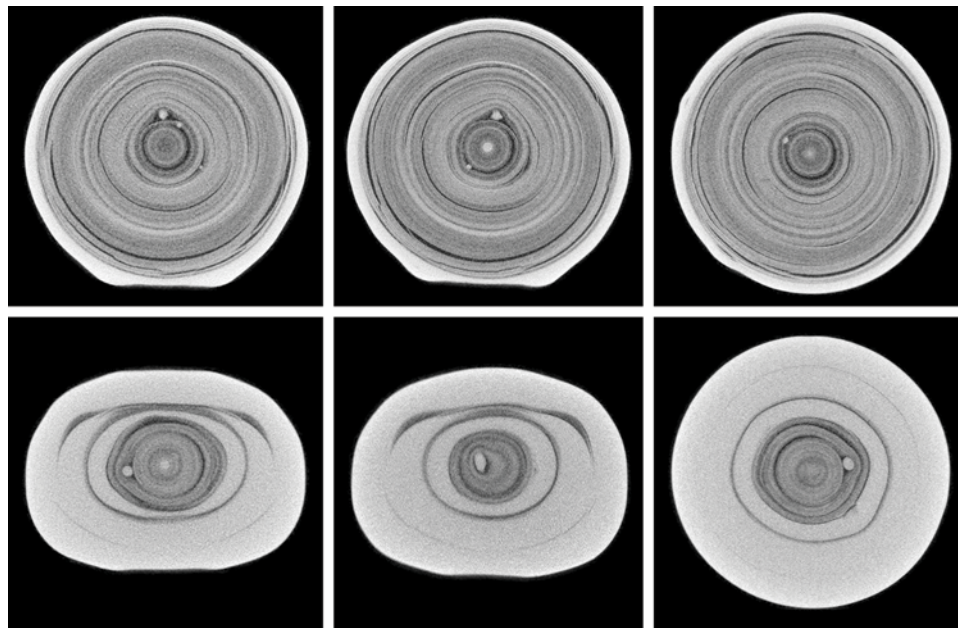


Figure 8. μ -CT slices in three directions of samples 1-13 (top row) and 1-14 (bottom row) reveal some light gray CaCO_3 “seed” features within the concentric structures of both samples. They were found next to one another in the gonad of the same mollusk.

Sturman, 2009; Krzemnicki et al., 2010; Sturman et al., 2016, 2017; Nilpetploy et al., 2018a; Manustrong, 2018; Al-Alawi et al., 2020). Thus, it was unexpected that only 10 of the 74 NBC pearls in this study dis-

played void features. Four were selected to show the various types of voids encountered (table 2). Most of the voids observed in this study were elongated (i.e., ellipse and ovoid cavities filled with gas and/or liquid

TABLE 2. Examples of NBC pearls from operated mollusks with void features (type 2).

Sample details	Position where found in the mollusk	Macro image	RTX image	μ -CT image
2-1 (1st operation wild shell) 3.35 ct 8.65 x 8.24 x 6.83 mm				
2-2 (1st operation wild shell) 2.48 ct 7.92 x 6.77 x 6.41 mm				
2-3 (1st operation wild shell) 2.70 ct 9.30 x 6.90 x 5.63 mm				
2-4 (1st operation wild shell) 1.37 ct 6.56 x 5.32 mm				

The position of the pearl in the mollusk is indicated by a red arrow.

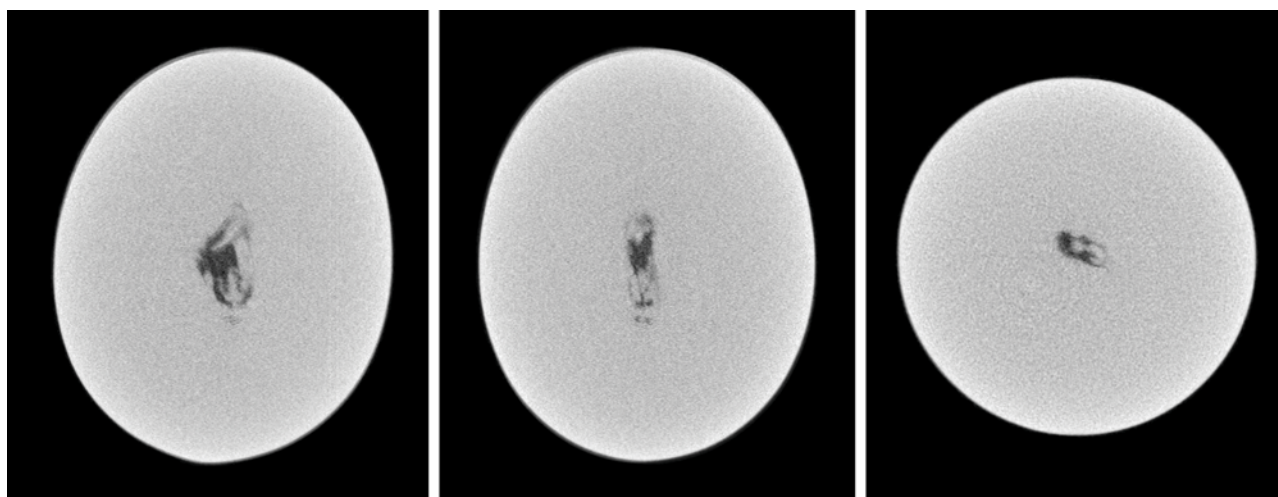


Figure 9. μ -CT slices in three directions of sample 2-4 reveal a combination of dark gray and light gray features inside the elongate void. This type of void is rarely observed in NBC pearls, and it has similarities to some previously observed in natural pearls.

phases) and oriented along the longest direction of the pearl. The light gray, representing the overlying nacre around the voids, was generally tight or only contained a few growth lines comparable with most NBC pearls in the type 1 group. Although only single voids were observed in samples from this study, double or multiple voids are sometimes observed in NBC pearls (Sturman et al., 2016).

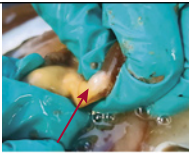

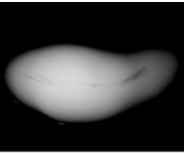
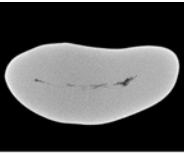
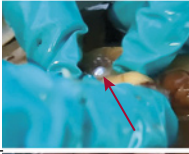


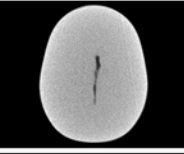


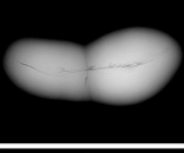
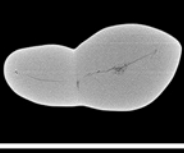






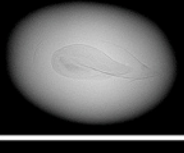
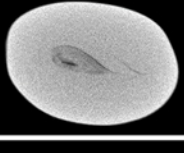


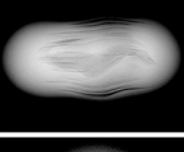
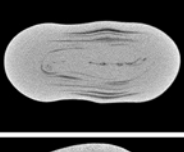


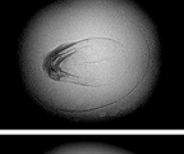
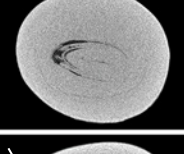


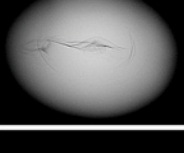
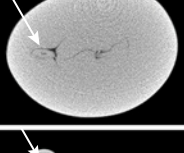


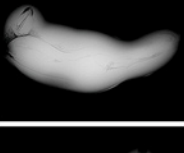
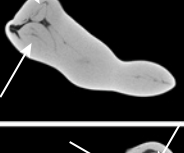


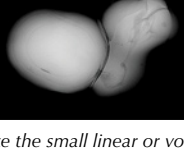
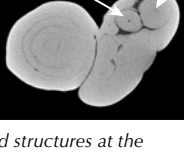
Sample 2-1 revealed a large void that took up nearly half of the pearl's volume. However, the void is not entirely empty, as a dark gray material can be seen within the virtually black center. This material could be a semi-solid organic-rich phase that is found in many voids in pearls both natural (Homkrajae et al., 2021) and cultured (Otter et al., 2014, Nilpetploy et al., 2018a). However, the organic-rich feature lacks any fine growth structure, which is uncharacteristic of natural pearls. Based on the large void's absence of any clear growth structure in the organic-rich area, the pearl would be identified as NBC. The hollow slender void present in sample 2-2 is characteristic of voids found in many saltwater NBC pearls. Sample 2-3 showed a central cavity with an inner light gray feature with a radiopacity similar to that of the nacre. This type of void feature has been reported in some NBC pearls from *P. margaritifera* (Nilpetploy et al., 2018a) and *Pinctada fucata (martensii)* (Manustrong, 2018). It has also been observed in some saltwater NBC pearls submitted for examination in GIA's global laboratory locations. Sample 2-4 displayed a combination of dark gray and light gray features inside the elongated void that is

sometimes observed in NBC pearls (magnified in figure 9). However, similar alternating dark and light gray patterns have been observed in some natural pearls (Homkrajae et al., 2021), and thus it is possible that some gemologists would identify this pearl as natural. Conversely, some gemologists could interpret the elongated shape and position of the void to be more typical of NBC pearls. This complex divergence reveals the challenges gemologists face in pearl identification, and an inconclusive opinion may well be the result.

Type 3: Linear Structures. Linear structures are the most common type encountered in NBC pearls produced by various mollusks originating from saltwater and freshwater environments (Scarratt et al., 2000; Hänni, 2006; Sturman, 2009; Krzemnicki et al., 2010; Sturman et al., 2016, 2017; Nilpetploy et al., 2018a; Manustrong, 2018; Al-Alawi et al., 2020; Kessrapong and Lawanwong, 2020). Not surprisingly, almost half of the NBC samples showed linear features, and 10 samples with various forms of these are presented in table 3. Samples 3-1 through 3-4 showed classic linear structures typically observed in NBC pearls. The extended linear feature displayed is the dominant structure seen running the length of each pearl. Even though samples 3-1 and 3-2 look different externally, they were harvested from the gonad of the same mollusk and share similar linear structures.

The linear structures visible in samples 3-5 through 3-10 are more complex, and some are seldom

TABLE 3. Examples of NBC pearls from operated mollusks with linear structures (type 3).

Sample details	Position where found in the mollusk	Macro image	RTX image	μ-CT image
3-1 (3rd operation wild shell) 5.37 ct 14.18 x 9.16 x 6.29 mm				
3-2 (3rd operation wild shell) 0.39 ct 4.36 x 3.40 mm				
3-3 (3rd operation wild shell) 3.06 ct 11.65 x 7.00 x 5.45 mm				
3-4 (1st operation wild shell) 1.21 ct 6.92 x 4.95 mm				
3-5 (3rd operation wild shell) 0.28 ct 3.96 x 3.49 x 2.76 mm				
3-6 (2nd operation hatchery shell) 0.535 ct 6.31 x 3.89 x 2.90 mm				
3-7 (3rd operation wild shell) 0.22 ct 3.37 x 3.11 mm				
3-8 (3rd operation wild shell) 0.70 ct 5.51 x 4.78 x 3.60 mm				
3-9 (3rd operation wild shell) 3.96 ct 15.30 x 6.28 x 5.65 mm				
3-10 (2nd operation hatchery shell) 2.10 ct 9.88 x 7.20 x 5.14 mm				

The position of the pearl in the mollusk is indicated by a red arrow. The white arrows indicate the small linear or void structures at the core of each defined demarcation.

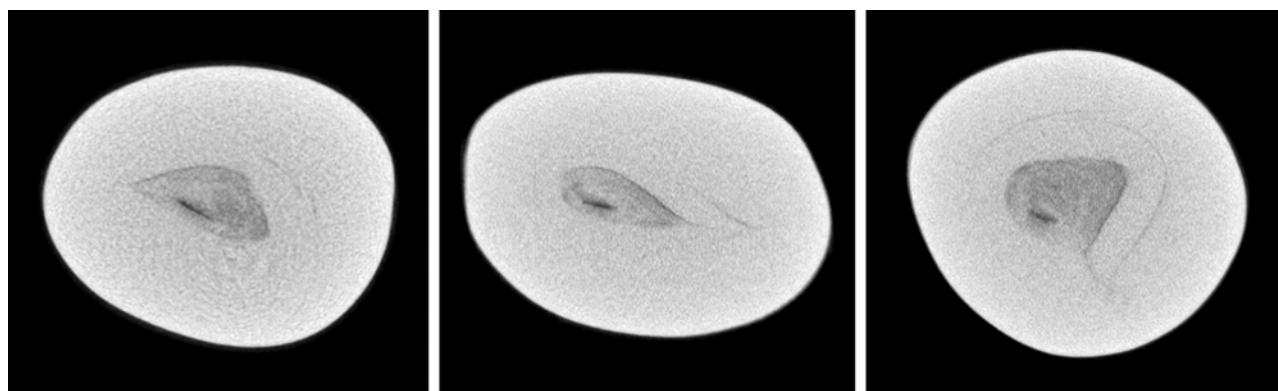


Figure 10. μ -CT slices in three directions of sample 3-5 reveal a dark gray line inside an area of organic-rich growth. Although the linear feature appears characteristic of NBC pearls, the organic-rich growth structure is more typical of natural pearls.

encountered in NBC pearls. Therefore, the identification of some NBC pearls is not straightforward. Sample 3-5 revealed a pear-shaped dark gray, organic-rich structure with an unclear associated darker feature in the RTX image that appears more likely to be a natural pearl structure. However, the dark feature shows up more clearly (magnified in figure 10) when analyzed by a high-resolution μ -CT unit, and it appears to be more linear and thus possibly more characteristic of some NBC pearls. Yet this feature does not correspond with the majority of linear associated structures observed in NBC and natural pearls, and therefore an inconclusive opinion may result. However, some gemologists may consider the linear feature sufficient evidence to identify this pearl as NBC, which would be consistent with its recorded provenance.

Distinct layered growth structures enclosing a linear feature, as shown in samples 3-6 and 3-7, are not typically encountered in NBC pearls. This is because NBC pearls generally lack any growth layers/features in the surrounding nacre, as has already been noted, although the linear features in the

center commonly correspond with those observed in other NBC pearls. Moreover, similar growth layers of alternating light and dark gray features related to the difference in organic content have been observed in some natural pearls (Homkrajae et al., 2021; see figure 15). Samples 3-8 through 3-10 showed combination structures consisting of multiple cores or segments, as well as linear features. Samples 3-8 and 3-9 revealed a long linear structure in the main body with shorter linear or void features in the center of each segment (table 3, indicated by the white arrows). On the other hand, the main body of sample 3-10 showed only growth rings and no evidence of a linear feature (magnified in figure 11). Only when the other segments were inspected were linear or void features revealed (table 3, indicated by a white arrow). The structures presented in samples 3-8 and 3-9 are more characteristic of NBC pearls (Nilpetploy et al., 2018a). While the linear features visible in the small segments point to an NBC origin, the overall structure of sample 3-10 is doubtful and this pearl may be considered inconclusive.

Figure 11. μ -CT slices in three directions of the largest segment of sample 3-10 only revealed growth rings. However, linear features and voids are present in other parts. The overall internal structure is doubtful and points to an NBC origin.

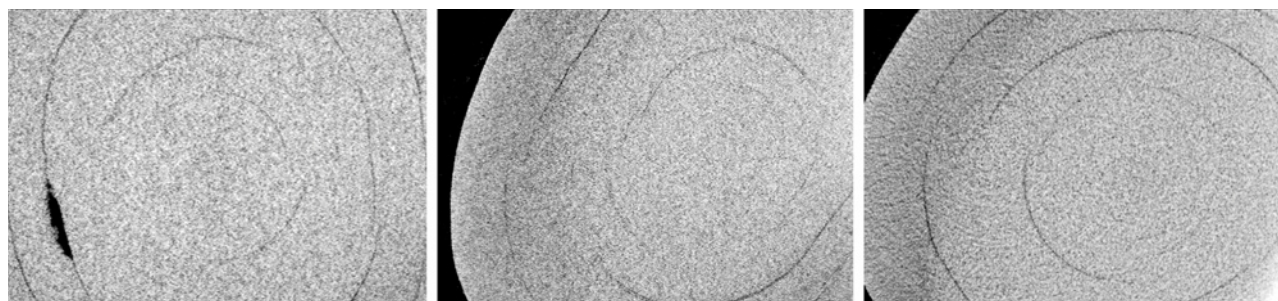
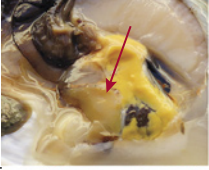

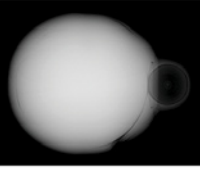
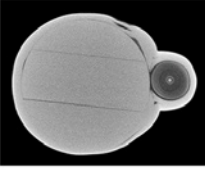


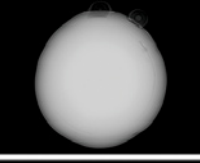
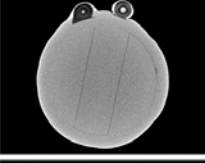


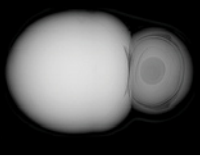
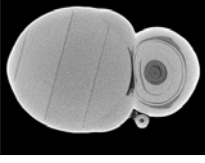


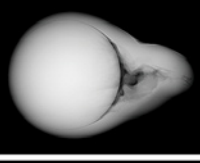
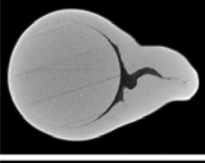


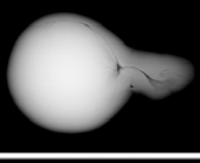
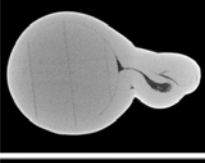



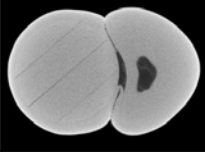


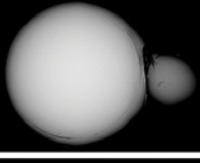
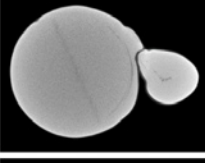


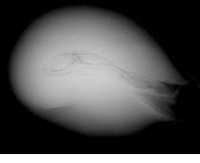
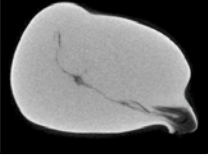


TABLE 4. Examples of BC pearls from operated mollusks with a bead nucleus and associated additional features (“Tokki”) (type 4 only in BC).

Sample details	Position where found in the mollusk	Macro image	RTX image	μ-CT image
Bead nucleus and organic-rich concentric				
4-1 (3rd operation wild shell) 14.77 ct 15.78 x 12.14 mm				
4-2 (3rd operation wild shell) 18.12 ct 15.12 x 13.47 mm				
4-3 (3rd operation wild shell) 17.22 ct 18.39 x 12.05 mm				
Bead nucleus and void				
4-4 (3rd operation wild shell) 38.51 ct 23.75 x 16.30 x 16.15 mm				
4-5 (3rd operation wild shell) 23.99 ct 21.90 x 14.28 x 14.12 mm				
4-6 (3rd operation wild shell) 26.53 ct 19.90 x 13.28 x 13.05 mm				
Bead nucleus and linear				
4-7 (3rd operation wild shell) 21.86 ct 14.53 x 14.24 x 14.13 mm				
4-8 (3rd operation wild shell) 24.78 ct total 15.44 x 15.14 x 14.68 mm and 6.10 x 5.37 x 4.19 mm				

The position of the pearl in the mollusk is indicated by a red arrow.

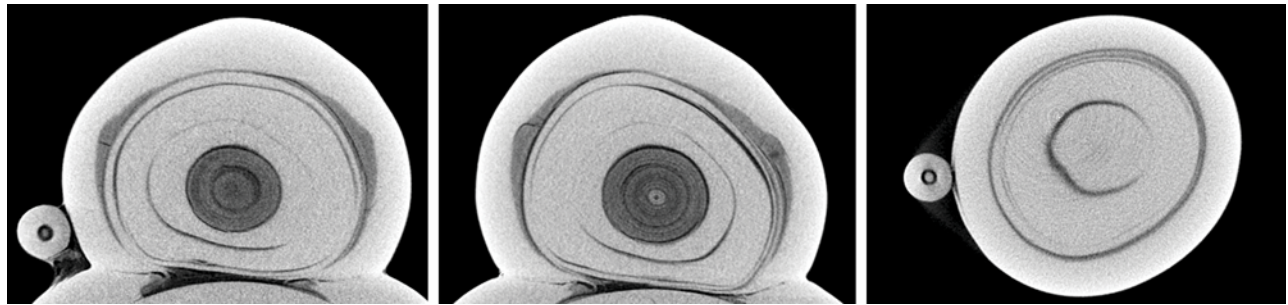


Figure 12. μ -CT slices in three directions of sample 4-3's feature revealed an organic-rich concentric structure that formed next to the bead nucleus. The small dark gray concentric area, tiny light gray core, and growth layers surrounding the dark gray area are similar to some observed in natural rather than NBC pearls.

Type 4: Bead Nucleus and Associated Additional Features. Twelve BC pearls with potentially intriguing additional features were selected from the many BC pearls recovered during the harvest. These additional features displayed organic-rich concentric, void, and linear features similar to the structures typically encountered in NBC samples; eight representative samples are shown in table 4. The additional features directly affected the pearls' external appearance, often resulting in baroque shapes. Although the pearls possessed additional features, their main body contained a bead nucleus and thus they would be classified as BC pearls. These extra features can form next to the bead nucleus (samples 4-1, 4-4, and 4-5) or independently from the bead nucleus and still be firmly attached to the outer nacreous layers (samples 4-2, 4-3, and 4-6). They may also form independently from the BC pearl and be loosely attached to the surface, where they are likely to separate later and become individual NBC pearls (samples 4-7 and 4-8).

As with all bead cultured pearls examined by RTX, the bead nuclei showed a distinct round dark gray feature at the interface between the beads themselves and the point of initial nacre contact. Some demarcation rings are more obvious than others, usually depending on the amount of organic matter deposited by the mollusk after the nucleation procedure has ended and the initial recovery period takes place. Straight parallel lines related to the banded structure of the shell bead nucleus, or boundaries delineating multiple sections of shell used to create laminated beads (Manustrong and Lawanwong, 2020), are also sometimes observed inside the main demarcation boundary.

Organic-rich concentric structures visible on samples 4-1 through 4-3 manifest themselves as rounded protrusions on the pearl surface. This type of additional feature is commonly associated with BC pearls

and has been reported in cultured pearls produced by *Pinctada* species mollusks (Krzemnicki et al., 2010, 2011; Al-Alawi et al., 2020). They may form as single, double, or multiple growths. RTX and μ -CT analyses revealed the dark gray organic-rich concentric structures constituting the majority of the features in samples 4-1 and 4-2. This is in keeping with the structures of most type 1 NBC samples, and to a lesser degree with the organic-rich concentric structures found in the natural *P. maxima* pearls previously reported by Homkrajae et al. (2021); see type 2 in that article. In contrast, sample 4-3 showed an organic-rich concentric structure similar to that of some natural pearls. The structure consisted of a small dark gray concentric area, a tiny light gray core, and growth structure surrounding the dark gray area (magnified in figure 12). If this additional feature were to become detached, resulting in a separate pearl, it would be challenging to identify the origin correctly. The additional features in samples 4-4 through 4-8 exhibited voids or linear structures. Those in samples 4-4 and 4-5 are associated directly with the bead nuclei, while the feature in sample 4-6 forms in the center and is not in contact with the bead nucleus. Sawing would be required to separate the additional features from the main bead cultured pearl in samples 4-1 through 4-6, as they are firmly attached to each other. Samples 4-7 and 4-8 showed a fine linear structure at the center of their additional features. When harvested, they were loosely attached to the main BC pearls. Later, the thin nacreous and organic-rich layer that bonded the features to the main BC pearls dried out, resulting in the separation of individual NBC pearls. Remnants of the organic-rich bond that held the two sections of sample 4-7 prior to separation, as well as the area where both segments were attached, are shown in figure 13.



Figure 13. Photomicrographs of sample 4-7, showing the area where both segments were loosely attached at the time of harvest (A and B; field of view 19.20 mm and 4.80 mm, respectively). Over time, the bonding dried out and the two parts separated into individual pearls: NBC on the left and BC on the right (C; field of view 19.20 mm). Photos by Nanthaporn Nilpetploy.

DISCUSSION

Various forms of internal structure were observed in the 74 NBC *P. maxima* pearls studied, although they can simply be classified into three broad types: organic-rich concentric structures (40%), void features (14%), and linear structures (46%). These three structural types were also noted as associated additional features in 12 BC pearls investigated. More importantly, certain forms of these structures were reported in some natural pearls, which highlights the challenges in separating some NBC from natural pearls, especially when tested in laboratory conditions and their provenance is unknown (Sturman et al., 2019).

Organic-rich concentric structures have been reported in cultured pearls produced by *Pinctada* species mollusks (Krzemnicki et al., 2010, 2011; Sturman et al., 2017; Nilpetploy et al., 2018a; Manustrong et al., 2019; Al-Alawi et al., 2020), and some natural pearls formed by various mollusk species (Krzemnicki et al., 2010; Scarratt et al., 2012; Sturman et al., 2014; Karampelas et al., 2017; Nilpetploy et al., 2018b; Homkrajae et al., 2021). Some differences noted by the authors could be useful indicators in distinguishing NBC pearls from their natural counterparts. The organic-rich concentric areas in most NBC samples are generally large and cover over half of the pearl's interior, whereas the concentric layered areas in natural samples tend to occupy a relatively small portion of the interior. The concentric rings within the organic-rich areas are more distinct and uniformly arranged in NBC samples than in natural pearls, although in some NBC samples the rings seem to cross over and merge with others. This uniformity is not observed in natural samples. An uneven or "spotty" appearance was visible in the dark concentric layered areas of some NBC samples but not apparent in the natural pearls. Dark and light gray cores were observed within the dark concentric

organic structures of both NBC and natural pearls, but only one NBC sample exhibited a dark core. In contrast, many of the natural pearls contained a dark gray core, which would seem to indicate a natural rather than NBC origin. The light gray cores usually appeared tight (radiopaque) and rounded in both kinds of pearls, yet the very large light gray cores were only observed in NBC pearls, while the majority of light gray cores seen in the natural pearls were small. The off-round (spindle-shaped) light gray cores and light gray CaCO_3 "seed" features observed in different positions within the dark gray organic-rich concentric structures were found in NBC but not natural pearl samples. When two or more of these characteristic features are combined, they provide sufficient proof to classify a pearl as NBC. Additionally, the dark gray organic-rich concentric structures within most of the NBC samples appeared uniformly symmetrical in shape with near-round, oval, and button outlines, while those in the natural pearls were of various shapes and many appeared asymmetrical.

Voids and linear structures are known to be key identification features for NBC pearls produced by *Pinctada* species mollusks (Wehrmeister et al., 2008; Sturman, 2009; Krzemnicki et al., 2010; Sturman et al., 2016, 2017; Nilpetploy et al., 2018a; Manustrong, 2018; Al-Alawi et al., 2020). However, a small percentage of natural saltwater pearls have also been shown to contain these two structural types (Scarratt, 2019; Homkrajae et al., 2021). Around 14% and 46% of all NBC pearl samples studied in this work displayed void and linear features, respectively. Both structural types, especially the linear structures encountered in NBC samples in this study and previous studies, share the common characteristic of being elongated and extending the length of the pearl. Usually, the linear features also extend over half of the pearl's length. Voids in natural pearls range in size and can be large, but in Homkrajae et al. (2021) the samples appeared to oc-

cupy relatively small portions, approximately 30% or less of the pearl's volume, and revealed organic-rich growth features within the voids when examined by μ -CT. These differences are helpful in distinguishing NBC from natural pearls. By comparison, linear structures are the most challenging to interpret in natural pearls. However, linear structures are typically observed in NBC pearls and less frequently in natural pearls, although the chances increase when extremely baroque pearls are considered. All the natural samples that were found to contain linear features tended to be baroque (Homkrajae et al., 2021), whereas linear features were observed in both baroque and symmetrically shaped NBC pearls such as the oval and drop shapes (samples 3-2 and 3-4). Therefore, any pearl with a distinct linear feature would most likely be identified as NBC.

What follows are the identification characteristics observed for the three main structural categories from the known natural and NBC *P. maxima* pearl samples (figure 14). The first category includes the structures that were only found in natural pearl samples. The structures that fall into this category are (1) tight or minimal growth that lack any clear internal growth features or only showed a few weak growth patterns; (2) an organic-rich concentric structure and patchy light and dark gray center resulting from differences in the organic content within these areas;

(3) a dense, solid light gray core not enclosed by any clear organic-rich concentric structure; and (4) a marine organism entombed by nacre deposition. Severely fractured central internal structures were found only in natural pearl samples (Homkrajae et al., 2021; see samples 6-5 and 6-6), yet they appear to be related to later stages of the pearls' formation and not their initial formation. Therefore, this type of structure may also be observed in NBC pearls and cannot be used as an indicator of a pearl's identity.

The second category involves the internal structures that are only found in NBC samples, including (1) an organic-rich concentric structure and off-round (spindle-shaped) core and (2) an organic-rich concentric structure and accompanying light gray CaCO_3 "seed" feature.

The last category includes overlapping structures that have been observed in natural and NBC pearl samples. Therefore, they are less indicative of any specific type of pearl unless certain internal characteristics previously mentioned are considered. These structures include (1) an organic-rich concentric structure and dark gray core, (2) an organic-rich concentric structure and light gray core, (3) void features, and (4) linear structures.

Lastly, NBC pearls often form after the mollusk has rejected the bead nucleus and the empty pearl sac continues to produce an accidental pearl. This can

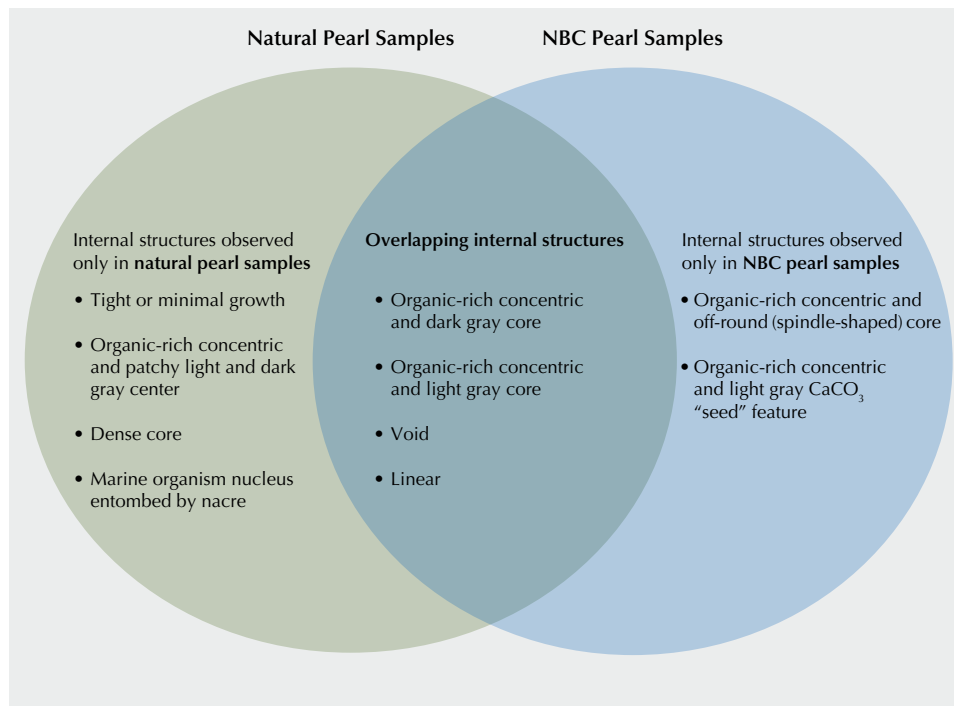


Figure 14. A diagram illustrating the three main categories of internal structures as radioimages. The two circles represent internal structures observed only in known natural *P. maxima* pearl samples in Homkrajae et al. (2021, left) and known NBC *P. maxima* pearl samples in this study (right). The area of overlap represents internal structures found in both natural and NBC pearl samples.

occur during the first operation or in any subsequent operations the mollusk endures during its life. It is worth noting that many of the NBC pearl samples with distinct linear features formed in mollusks following their second or third operation, and they often exhibit a flattened baroque shape. This observation is in agreement with studies by Hänni (2006) and Krzemnicki et al. (2010). Additionally, organic-rich concentric structures were discovered in NBC pearls from all three operations, and BC pearl samples with the additional surface features were produced by mollusks following the third operation.

CONCLUSIONS

Organic-rich concentric structures, void features, and linear structures are the three main structural types found in the NBC pearl samples studied, and within the additional features found on the BC pearls examined. The majority of the NBC samples exhibited one of two typical internal characteristics—relatively large voids or distinct linear features—helping prove their cultured origin. Other structural features help identify pearls as NBC when observed in conjunction with each other or with the two main NBC structures. These include a large light gray core, an off-round (spindle-shaped) core, and light gray CaCO_3

“seed” features found within organic-rich concentric structures. However, as discussed earlier in this study, some particular forms of these three structural types can be observed in some natural pearls, and thus greater care is needed in their interpretation. This illustrates that the distinction between NBC and natural pearls is not always straightforward, and therefore different identification opinions or inconclusive calls may result in certain cases. The results obtained from different analytical methods may also influence the identification results. Factors such as instrument quality and resolution, the operator’s experience, and even the level of care taken during analysis can combine to further hinder identification. In challenging cases, the use of μ -CT is necessary to provide the best possible data for interpreting a pearl’s structure. Lastly, only 86 *P. maxima* cultured pearl samples were examined in this study. Additional cultured pearl samples are necessary to gain an even greater understanding about the range of possible structures in cultured pearls and to benefit the identification process. The continued study of the internal structures of known cultured pearls provides dependable results that enhances GIA’s reference collection database and can provide clients with greater peace of mind.

ABOUT THE AUTHORS

Mrs. Homkrajae is a senior staff gemologist at GIA in Carlsbad, California. Ms. Nilpetpoy is a senior staff gemologist, Ms. Manutrong is a staff gemologist, Mr. Sturman is a consultant to GIA, Ms. Lawanwong is an analytics technician, and Mr. Kessrapong is a former analytics technician, all in GIA’s Bangkok laboratory.

ACKNOWLEDGMENTS

The authors wish to extend their appreciation to Paspaley Pearlring Company, Australia, for loaning the samples to GIA’s Bangkok laboratory for this study and inviting GIA staff to visit Australia to retrieve the pearls in person. We also wish to thank Tom Moses and Kenneth Scaratt for their support and for making the trips to Paspaley possible. Sasithorn Engniwat’s assistance in providing the macro images in all the tables is also greatly appreciated. Lastly, we would like to thank the peer reviewers for valuable and constructive comments that improved this article.

REFERENCES

- Al-Alawi A., Ali Z., Rajab Z., Albedal F., Karampelas S. (2020) Salt-water cultured pearls from *Pinctada radiata* in Abu Dhabi (United Arab Emirates). *Journal of Gemmology*, Vol. 37, No. 2, pp. 164–179.
- Cartier L.E., Krzemnicki M.S. (2013) New developments in cultured pearl production: Use of organic and baroque shell nuclei. *Australian Gemmologist*, Vol. 25, No. 1, pp. 6–13, <https://www.ssef.ch/wp-content/uploads/2018/06/2013-Organic-baroque-shell-nuclei-Cartier-Krzemnicki-GAA.pdf>
- (2016) Golden South Sea cultured pearls: Cultivation steps & gemmological investigations. *The Journal of the Gemmological Association of Hong Kong*, Vol. 37, pp. 16–21, <http://www.gahk.org/journal/2016/a5.pdf>
- Cartier L.E., Krzemnicki M.S., Rere J. (2013) Pearl or gemstone? Galatea pearls: A ‘new’ pearl product from French Polynesia. *33rd International Gemmological Conference*, Hanoi, Vietnam, pp. 64–66.
- CIBJO, The World Jewellery Confederation (2020) *The Pearl Book*. CIBJO Pearl Commission, 79 pp.
- Crichton R. (2019) *Biological Inorganic Chemistry: A New Introduction to Molecular Structure and Function*, 3rd ed. Université Catholique de Louvain, Belgium, <https://doi.org/10.1016/C2016-0-01804-1>
- Gervis M.H., Sims N.A. (1992) *The Biology and Culture of Pearl Oysters (Bivalvia: Pteriidae)*. ICLARM Studies and Reviews 21, Manila, Philippines, 49 pp.

- Hänni H.A. (2006) A short review of the use of 'keshi' as a term to describe pearls. *Journal of Gemmology*, Vol. 30, No. 1/2, pp. 51–58.
- (2012) Natural pearls and cultured pearls: A basic concept and its variations. *Australian Gemmologist*, Vol. 24, No. 11, pp. 258–266.
- Hänni H.A., Krzemnicki M.S., Cartier L. (2010) Appearance of new bead material in cultured pearls. *Journal of Gemmology*, Vol. 32, No. 1, pp. 31–37.
- Homkrajae A., Manustrong A., Nilpetploy N., Sturman N., Lawanwong K., Kessrapong P. (2021) Internal structures of known *Pinctada maxima* pearls: Natural pearls from wild marine mollusks. *G&G*, Vol. 57, No. 1, pp. 2–21, <http://dx.doi.org/10.5741/GEMS.57.1.2>
- Hsu T., Zhou C., Homkrajae A., Ho J.W.Y., Yazawa E., Padua P. (2016) Freshwater pearling in Tennessee. *GIA Research News*, October 7, <https://www.gia.edu/gia-news-research/freshwater-pearling-tennessee>
- Karampelas S., Al-Alawi A.T., Al-Attawi A., Scarratt K. (2017) Natural pearls found from *Pinctada radiata* in the Kingdom of Bahrain: Characteristic structures, comparison and identification. *35th International Gemmological Conference*, Windhoek, Namibia, pp. 103–104.
- Kessrapong P., Lawanwong K. (2020) Atypical bead cultured *Pinctada maxima* pearls nucleated with freshwater non-bead cultured pearls. *GIA Research News*, April 6, <https://www.gia.edu/doc/Atypical-Bead-Cultured-Nucleated-with-Freshwater-NBCP.pdf>
- Krzemnicki M., Friess D., Chalup P., Hänni H.A., Karampelas S. (2010) X-ray computed microtomography: Distinguishing natural pearls from beaded and non-beaded cultured pearls. *G&G*, Vol. 46, No. 2, pp. 128–134, <http://dx.doi.org/10.5741/GEMS.46.2.128>
- Krzemnicki M.S., Müller, Hänni H.A., Gut H.-P., Düggelein M. (2011) Tokki pearls: Additional cultured pearls formed during pearl cultivation: External and internal structures. *32nd International Gemmological Conference*, Interlaken, Switzerland, https://www.ssef.ch/wp-content/uploads/2018/01/SSEF_Tokki_pearls.pdf
- Landman N.H., Mikkelsen P.M., Bieler R., Bronson B. (2001) *Pearls: A Natural History*. Harry N. Abrams, Inc., New York, 232 pp.
- Manustrong A. (2018) Gems News International: Very small akoya cultured pearls. *G&G*, Vol. 54, No. 1, pp. 103–105, <https://www.gia.edu/gems-gemology/spring-2018-gemnews-very-small-akoya-cultured-pearls>
- Manustrong A., Lawanwong K. (2020) Lab Notes: Saltwater bead cultured pearl with laminated nucleus. *G&G*, Vol. 56, No. 1, pp. 138–139, <https://www.gia.edu/gems-gemology/spring-2020-labnotes-cultured-pearl-laminated-nucleus>
- Manustrong A., Kessrapong P., Lawanwong K., Nilpetploy N., Homkrajae A. (2019) Known non-nacreous non-bead cultured pearls and similar unknown pearls of likely cultured origin from *Pinctada maxima*. *GIA Research News*, September 4, <https://www.gia.edu/gia-news-research/known-non-nacreous-non-bead-cultured-pearls>
- Marie B., Joubert C., Tayalé A., Zanella-Cléon I., Belliard C., Piquemal D., Cochenec-Laureau N., Marin F., Gueguen Y., Montagnani C. (2012) Different secretory repertoires control the biomineralization processes of prism and nacre deposition of the pearl oyster shell. *Proceedings of the National Academy of Sciences*, Vol. 109, No. 51, pp. 20986–20991, <http://dx.doi.org/10.1073/pnas.1210552109>
- Nilpetploy N., Lawanwong K., Kessrapong P. (2018a) Non-bead cultured pearls from *Pinctada margaritifera*. *GIA Research News*, April 27, <https://www.gia.edu/ongoing-research/non-bead-cultured-pearls-from-pinctada-margaritifera>
- (2018b) The gemological characteristics of Pipi pearls reportedly from *Pinctada maculata*. *G&G*, Vol. 54, No. 4, pp. 418–427, <http://dx.doi.org/10.5741/GEMS.54.4.418>
- Otter L.M., Wehrmeister U., Enzmann F., Wolf M., Jacob D.E. (2014) A look inside a remarkably large beaded South Sea cultured pearl. *G&G*, Vol. 50, No. 1, pp. 58–62, <http://dx.doi.org/10.5741/GEMS.50.1.58>
- Otter L.M., Oluwatoosin B.A., Huong L.T., Häger T., Jacob D.E. (2017) Akoya cultured pearl farming in eastern Australia. *G&G*, Vol. 53, No. 4, pp. 423–437, <http://dx.doi.org/10.5741/GEMS.53.4.423>
- Scarratt K. (2019) A recent expedition to acquire & characterise natural pearls from Australian *Pinctada* [video presentation]. *The Pearl Symposium*, November 21, <https://www.youtube.com/watch?v=Ogu3467SaBY>
- Scarratt K., Moses T.M., Akamatsu S. (2000) Characteristics of nuclei in Chinese freshwater cultured pearls. *G&G*, Vol. 36, No. 3, pp. 98–109, <http://dx.doi.org/10.5741/GEMS.36.2.98>
- Scarratt K., Bracher P., Bracher M., Attawi A., Safar A., Saeseaw S., Homkrajae A., Sturman N. (2012) Natural pearls from Australian *Pinctada maxima*. *G&G*, Vol. 48, No. 4, pp. 236–261, <http://dx.doi.org/10.5741/GEMS.48.4.236>
- Scarratt K., Sturman N., Tawfeeq A., Bracher P., Bracher M., Homkrajae A., Manustrong A., Somsa-ard N., Zhou C. (2017) Atypical “beading” in the production of cultured pearls from Australian *Pinctada maxima*. *GIA Research News*, <https://www.gia.edu/gia-news-research/atypical-beading-production-cultured-pearls-australian-pinctada-maxima>
- Snow M. (1999) Bironite: A new source of nuclei. *Pearl Oyster Bulletin*, No. 13, pp. 19–21.
- Southgate P.C., Lucas J.S (2008) *The Pearl Oyster*. Elsevier, Oxford, 574 pp.
- Strack E. (2006) *Pearls*. Rühle-Diebener-Verlag, Stuttgart, Germany.
- Sturman N. (2009) The microradiographic structures of non-bead cultured pearls. *GIA Research News*, <https://www.gia.edu/gia-news-research-NR112009>
- Sturman N., Al-Attawi A. (2006) The “keshi” pearl issue. *G&G*, Vol. 42, No. 3, p. 142.
- Sturman N., Homkrajae A., Manustrong A., Somsa-ard N. (2014) Observations on pearls reportedly from the Pinnidae family (Pen pearls). *G&G*, Vol. 50, No. 3, pp. 202–215, <http://dx.doi.org/10.5741/GEMS.50.3.202>
- Sturman N., Bergman J., Poli J., Homkrajae A., Manustrong A., Somsa-ard N. (2016) Bead-cultured and non-bead-cultured pearls from Lombok, Indonesia. *G&G*, Vol. 52, No. 3, pp. 288–297, <http://dx.doi.org/10.5741/GEMS.52.3.288>
- Sturman N., Manustrong A., Lawanwong K., Kessrapong P., Somsa-ard N., Homkrajae A. (2017) “Golden” *Pinctada maxima* non-bead cultured pearls with an emphasis on their internal structures. *Proceedings of the 35th International Gemmological Conference*, Windhoek, Namibia, pp. 100–102.
- Sturman N., Otter L.M., Homkrajae A., Manustrong A., Nilpetploy N., Lawanwong K., Kessrapong P., Jochum K.P., Stoll B., Götz H., Jacob D.E. (2019) A pearl identification challenge. *G&G*, Vol. 55, No. 2, pp. 229–243, <http://dx.doi.org/10.5741/GEMS.55.2.229>
- Sturman N., Lawanwong K., Kitdee N., Chodhry D. (2020) Vietnam: Shell nuclei, pearl hatcheries, and pearl farming. *G&G*, Vol. 56, No. 3, pp. 402–415, <http://dx.doi.org/10.5741/GEMS.56.3.402>
- Wehrmeister U., Goetz H., Jacob D.E., Soldati A., Duschner W., Xu H., Hofmeister W. (2008) Visualization of the internal structures of cultured pearls by computerized X-ray microtomography. *Journal of Gemmology*, Vol. 31, No. 1/2, pp. 15–21.
- Western Australia Department of Fisheries (2016) Pearl Oyster Fishery: Western Australian silver-lipped pearl oyster (*Pinctada maxima*) resource harvest strategy 2016–2021, Version 1.0. Fisheries Management Paper No. 276, http://www.fish.wa.gov.au/Documents/management_papers/fmp276.pdf

FIRST IDENTIFICATION OF SUDOITE IN CARIBBEAN CERAMIC-AGE LAPIDARY CRAFTSMANSHIP

Alain Queffelec, Ludovic Bellot-Gurlet, Eddy Foy, Yannick Lefrais, and Emmanuel Fritsch

Lapidary craftsmanship was an important part of the material culture of Amerindians in the Antilles during the Early Ceramic period (400 BCE to 400 CE). Exhaustive analysis of archaeological beads and pendants from the French islands of the Lesser Antilles has revealed a green lapidary material used for the production of nine artifacts from five archaeological sites: sudoite. This di-trioctahedral member of the chlorite group has the relatively simple chemical formula of $Mg_2Al_3Si_3AlO_{10}(OH)_8$. Previously unknown in sizes suitable for carving, it has never before been identified in any lapidary production and therefore warranted a multi-analytical nondestructive approach to confirm this identification. The analysis was conducted through Raman spectroscopy, FTIR spectroscopy, and X-ray diffraction. The texture and the chemical composition were assessed through SEM-EDS. Color, UV luminescence, and other gemological parameters were studied through standard gemological methods, UV-Vis-NIR spectroscopy, and fluorimetry. Finally, the provenance of the material is considered following a geological approach. The recovery of sudoite artifacts in several archaeological Amerindian sites of the Lesser Antilles supports the already established theory of a pan-Caribbean trade network as old as the first several centuries Before the Common Era.

During the Early Ceramic age, between 400 BCE and 400 CE (Bérard, 2019), a people from northeastern South America appropriated the entire Lesser Antilles, replacing or assimilating the inhabitants of these Caribbean islands (Hofman et al., 2007; Wilson, 2007; Nägele et al., 2020). Indeed, these fishermen-cultivators arrived on the islands with a great innovation: ceramic technology. Several cultural components existed within this period, with a common background called Saladoid, named after the site of Saladero (Rouse, 1992; Bérard, 2019). The inhabitants of the West Indies at this time possessed a complex culture, some characteristics of which are common to the different islands and sub-periods. These include certain ceramic decorations, simple lithic tools, the important use of shells for tools and adornment, and distinctive funerary practices (Bérard, 2013). The lapidary craft, which will be of particular interest to us in this work, is very diversified in terms of both forms and raw materials (Cody, 1993; Murphy

et al., 2000; Queffelec et al., 2018; Falci et al., 2020; Queffelec et al., 2020). These materials and artifacts are the subject of various studies examining the supply, distribution, and trade networks of the fishermen-cultivators who inhabited the entire archipelago but whose origins can be traced back to the northeastern part of South America.

In Brief

- Analysis of beads and pendants from several archaeological sites in the Lesser Antilles has revealed the first documented use of sudoite in lapidary craftsmanship.
- A multi-analytical process was applied to confirm and describe this material in detail through non-invasive means.
- The provenance of this material is hypothesized to come from ophiolite suture zones located in the Greater Antilles or Mesoamerica.

An exhaustive study of the ornamental objects of this period recovered from archaeological sites in the French West Indies has revealed a material not mentioned in the classic list of “green rocks” used for

See end of article for About the Authors and Acknowledgments.

GEMS & GEMOLOGY, Vol. 57, No. 3, pp. 206–226,

<http://dx.doi.org/10.5741/GEMS.57.3.206>

© 2021 Gemological Institute of America



Figure 1. The nine Amerindian archaeological objects identified as sudoite. The beads on the left are, from top to bottom: SM-02-033, GD-02-028, and SM-02-086. The pendants in the center are, from left to right: GD-09-001, GD-02-003, and GD-01-017. The beads on the right are, from top to bottom: GD-01-020, GD-01-019, and MA-02-027. The central artifact is 43.5 mm high. Photos by Alain Queffelec.

the craft: sudoite. This mineral belonging to the chlorite group was named by G. Müller (Müller, 1961; v. Engelhardt et al., 1962) in honor of Toshio Sudo (1911–2000), professor of mineralogy at the University of Tokyo and a pioneer of clay science (Kohyama, 2000). It is a sheet silicate (and thus easy to carve), more precisely a magnesium-rich di-trioctahedral chlorite found mainly in hydrothermal or high-pressure/low-temperature (HP/LT) metamorphism contexts. Its relatively simple chemical makeup, $Mg_2Al_3Si_3AlO_{10}(OH)_8$, does not contain any rare or unusual elements.

Few other chlorite-group minerals have been reported as gems (Bukanov, 2006), and sudoite is not listed in any gemological compilation (e.g., Desautels, 1973; Arem, 1987; Duda and Relj, 1999; Manutchehr-Danai, 2005; O'Donoghue, 2006). It is thus necessary to confirm the mineralogical composition of these nine ornamental objects, initially carried out by Raman spectroscopy and for five artifacts by X-ray diffraction, using a multi-analytical approach that entails nondestructive methodologies applicable to archaeological objects. This mineralogical study will be sup-

plemented by a geological analysis in order to provide a better understanding of the distribution and potential provenance of this rare lithic material.

MATERIALS

Archaeological Artifacts. The nine archaeological objects studied in this work were discovered in five archaeological excavations carried out in Guadeloupe, Martinique, and Saint Martin (figure 1 and table 1). A thorough description and the archaeological context surrounding the artifacts can be found in previous publications (Bonnissent, 2008; Queffelec et al., 2018, 2020, 2021). The inventory numbers are taken from the database that records all the lapidary objects from the Lesser Antilles (Queffelec et al., 2021). The inventory codes consist of two letters identifying the island on which the object was found, two digits indicating the archaeological site on this island, and three digits indicating the number of the object in the site. Of these nine artifacts, five were the subject of extensive study in Bordeaux and Paris, while four have only been analyzed on-site using mobile instru-

TABLE 1. Description of the nine sudoite artifacts examined in this study.

Inventory no.	Island	Archaeological site	Weight (g)	Dimension (mm)	Type	Excavator (year)
GD-01-017*	Guadeloupe	Gare Maritime	0.48	13.9 × 7.2 × 4.2	Zoomorphic pendant	Romon (2006)
GD-01-019*	Guadeloupe	Gare Maritime	0.51	7.9 × 7.9 × 6.1	Subspherical bead	Romon (2006)
GD-01-020*	Guadeloupe	Gare Maritime	0.06	4.2 × 4.2 × 2.1	Discoid bead	Romon (2006)
GD-02-003	Guadeloupe	Morel	14.2	43.5 × 18.5 × 14.5	Zoomorphic pendant	Durand (1987)
GD-02-028*	Guadeloupe	Morel	0.47	8.6 × 8.6 × 4.7	Bitronconic bead	Delpuech (1995)
GD-09-001*	Guadeloupe	Cathédrale Basse-Terre	1.78	19.7 × 13.2 × 6.4	Zoomorphic pendant	Bonnissent (2004)
MA-02-027	Martinique	Vivé	0.3	6.4 × 6.8 × 3.3	Discoid bead	Giraud (1999)
SM-02-033	Saint Martin	Hope Estate	0.1	5.6 × 5.2 × 3.1	Discoid bead	Henocq (1994)
SM-02-086	Saint Martin	Hope Estate	0.3	7.2 × 7.0 × 3.2	Discoid bead	Henocq (1994)

*Artifacts studied in detail in Bordeaux and Paris.

ments during two study missions to the Antilles (table 1).

Mineralogy. Sudoite is a phyllosilicate of the chlorite group, with a stacking of sheets (figure 2) formed of T-O'-T layers (T: layer composed of tetrahedra; O': layer composed of octahedra) separated by O layers (Brigatti et al., 2011). In the T-O'-T layers, the T layers are formed of (Si,Al)O₄ aluminosilicate tetrahe-

dra. They enclose a layer of octahedra whose vertices are O²⁻ anions or (OH)⁻ hydroxyl groups, while the octahedral center is occupied by a cation.

Sudoite, within the chlorite group, is one of the minerals of the di-trioctahedral subgroup (table 2). This implies that the octahedral cationic sites of the T-O'-T sheets are two-thirds (di-) occupied by trivalent cations, here Al³⁺, creating O' sites of the formula AlO₄(OH)₂. The octahedral cationic sites of the

Figure 2. Representation of the sudoite mineralogical structure, projected down the b-axis. Modified after the cookeite structure (Wikimedia Commons).

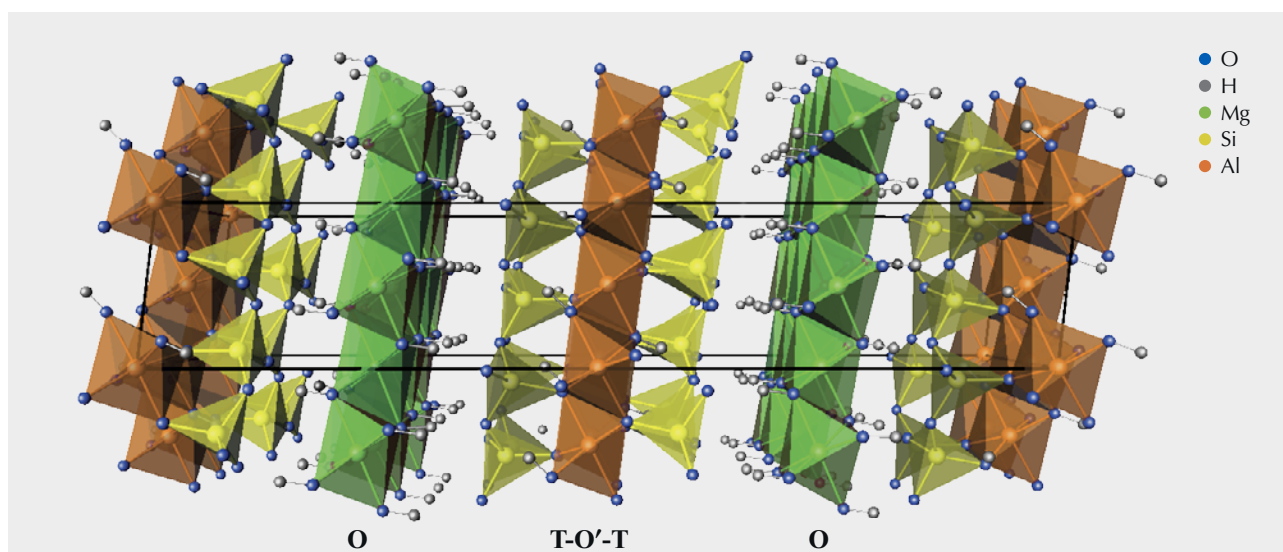


TABLE 2. Classification of the minerals from the chlorite group as a function of octahedral site composition (modified after Bailey, 1980).

Layer T-O'-T	Interlayer space O	Mineral name
Di octahedral	Di octahedral	Donbassite
Di octahedral	Tri octahedral	Cookeite, sudoite
Tri octahedral	Di octahedral	Unknown
Tri octahedral	Tri octahedral	Brunsvigite, chamosite, clinochlore, diabantite, penninite, ripidolite, sheridanite, thuringite

O sheets are occupied entirely (tri-) by bivalent cations Mg^{2+} , creating O sites of the formula $Mg_3(OH)_6$.

This structure and the cationic composition of the octahedral sites lead to a sudoite formula of $Mg_2Al_3Si_3AlO_{10}(OH)_8$. This ideal formula is somewhat different from the formulas derived experimentally, which always contain a variable but not negligible proportion of iron in substitution for aluminum at O' sites (e.g., Billault et al., 2002; Ruiz Cruz and de Galdeano, 2005).

METHODS

With the dual objective of confirming the characterization as sudoite and presenting a first series of gemological parameters for this material, several methods of gemological and mineralogical characterization were deployed on five archaeological objects (table 1), which were temporarily removed to Bordeaux, France. As for the objects that remained in their Caribbean curation site, mineralogical identification relied on portable Raman spectroscopy and basic observation.

The objects were observed with the unaided eye, using a 10× triplet loupe and a Leica Z16APO microscope, and photographed. Their dimensions were measured with an electronic caliper, and their mass and density were recorded using a hydrostatic balance (Mettler-Toledo XS104) or a conventional balance (Kern TAB 20-3) for objects that remained in the Caribbean. Whenever possible, the refractive index of the objects taken to France was measured using a spot reading method, despite the inherent difficulty of doing so on poorly polished objects. Ultraviolet (UV) luminescence was observed and photographed under short-wave (254 nm) and long-wave (365 nm) UV light (Wilber Lourmat VL-6LC, 6W per tube). We

examined the optic character of the more translucent artifacts using a GIA Gem Instruments polariscope.

Various complementary methods were applied to the objects when possible in order to confirm and refine our knowledge of this material. Raman microspectroscopy was the first method applied, being used routinely on all the archaeological objects studied in the project to characterize the lithic materials used by the Amerindians to produce ornamental objects in the Saladoid period. The five objects that could be taken to France were analyzed by a Bruker Senterra Raman microspectrometer equipped with a 532 nm laser, and a 1200-line diffraction grating resulting in a resolution of 3 to 5 cm^{-1} . The objects were analyzed repeatedly and at several locations on each sample with a 50× objective and a nominal laser power of 20 mW in order to confirm the representativeness of the measured signal. Four objects were analyzed at their place of storage in Martinique, Guadeloupe, and Saint Martin during a second phase of the project (table 1) using a portable Raman spectrometer. This Horiba Jobin-Yvon HE532 Raman microspectrometer was equipped with a fixed 920 lines/mm parabolic grating to record the signal in a fixed spectral window from 80 to 3300 cm^{-1} with a spectral resolution of about 5 cm^{-1} . The analyses were conducted using a long working distance 50× objective with a 532 nm laser whose power was modulated to about 10 mW on the sample.

Infrared spectroscopy was carried out in attenuated total reflection (ATR) mode using a Bruker Alpha spectrometer, measuring absorbance between 400 and 4000 cm^{-1} with a resolution of 4 cm^{-1} . In all, 48 scans were carried out to obtain a spectrum of sufficient quality, despite the difficulties encountered in positioning the objects and creating sufficient optical contact between the diamond crystal of the ATR and the archaeological artifact without damaging it.

The objects' mineralogical composition was confirmed by X-ray diffraction. The analyses were carried out using a Rigaku RU200BH X-ray generator, with the $K\alpha$ line of molybdenum ($\lambda = 0.709 \text{ \AA}$). Measurements were performed either in macrobeam (100 μm) in transmission (if the artifact was sufficiently thin) or in microbeam (30 μm) in low-angle ($\sim 5^\circ$) reflection configuration (figure 3). The diffraction image was recorded and stored on a photostimulated image detector. After scanning, the image was converted to a 2 θ diagram using Fit2D software (Hammersley, 2016). Using Bruker's Diffrac-EVA software, the diagram was then compared to reference databases from the International Centre for Diffraction Data (ICDD) (Gates-Rector and Blanton, 2019).

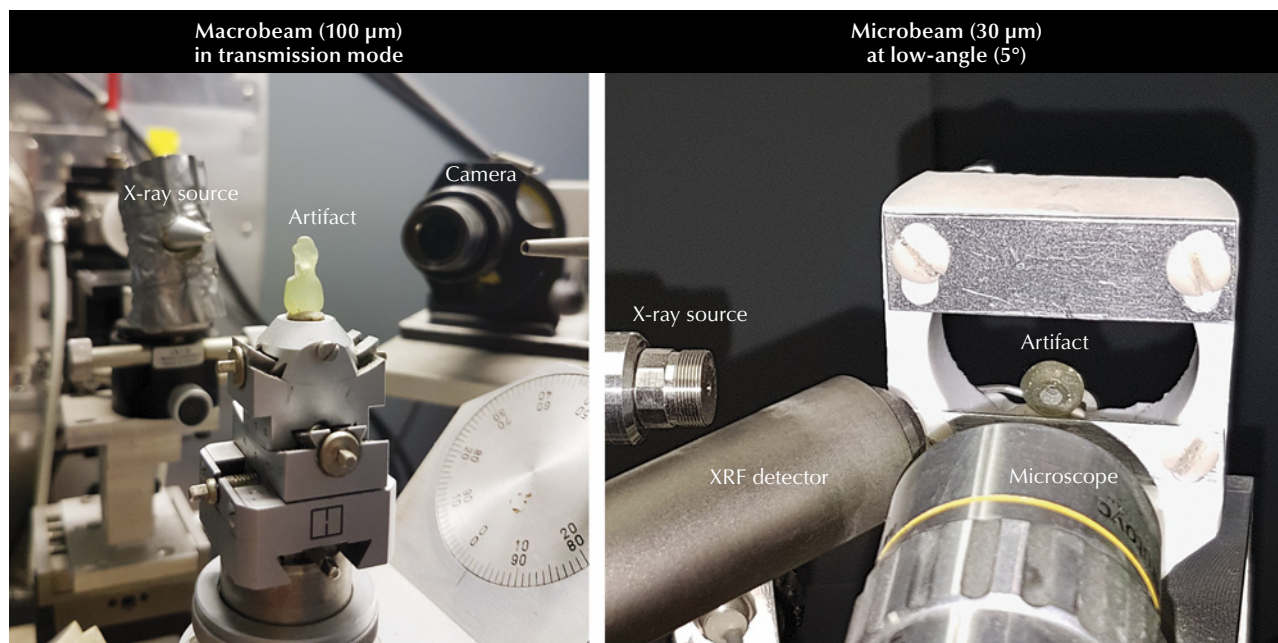


Figure 3. Photographs of macrobeam (left) and microbeam (right) X-ray diffraction setups. The X-ray photo-stimulated detector is not visible in these images. Photos by Eddy Foy.

A portable energy-dispersive X-ray fluorescence (EDXRF) spectrometer allowed qualitative and semi-quantitative characterization. These analyses were carried out using a Bruker Tracer 5i spectrometer, set at 15 kV, 100 μ A, 300 s, with a 28 micron aluminum filter to remove the L-lines from the rhodium X-ray tube. Since the artifacts did not systematically cover the whole measurement window, and their thickness was variable, the measured signal of all samples was normalized at 11 keV. Finally, to ensure that certain lines did not come from the measuring device itself, a Teflon pellet was analyzed with the same device, since this material is supposed to contain only elements that cannot be measured by X-ray fluorescence. This Teflon measurement was carried out without a filter so that the L lines of rhodium could be clearly distinguished.

For quantitative analysis, the objects were analyzed by scanning electron microscope coupled with energy-dispersive X-ray spectroscopy (SEM-EDS) in a JEOL IT500HR microscope (FEG source). The SEM images and EDS spectra were acquired without carbon coating in a low-vacuum mode (here 40 Pa). The images were acquired with a backscattered electron detector, while the EDS analysis was performed with two Oxford Ultimex 100 detectors at 20 kV for 30 s, producing spectra with 4.0–4.5 million counts. The chemical quantifications by SEM-EDS in atomic % were converted into atoms per formula unit, normalized to an anionic composition of $O_{10}(OH)_8$ so that they could easily be compared with the chemical for-

mulae known in the literature, both the theoretical formula of the mineral and those measured on natural samples (Bailey and Lister, 1989; Ruiz Cruz and de Galdeano, 2005). The results were also normalized to an anionic composition of $O_{10}(OH)_2$ for comparison with illite. To estimate the volume analyzed, Monte Carlo simulations were conducted in the Casino V2 program (Drouin et al., 2007) using the current (20 kV), matrix composition (Mg, Al, Si, O), and specific gravity (2.65) as parameters.

Two spectrometers were used to obtain the UV-Vis-NIR absorbance spectra of the archaeological objects: a Magilabs GemmoSphere and a PerkinElmer Lambda 1050 equipped with a 3D accessory and an integrating sphere. Measurements with the first instrument provided limited resolution and spectral range (approximately 1.3 nm from 365 to 1000 nm), while the second instrument allowed a resolution of 1 nm in the spectral range from 2300 to 300 nm but required a specific assembly with an accurate placement of the sample upstream of the integrating sphere.

For fluorimetry, we used a Horiba Fluorolog 3. After measuring an emission spectrum with an excitation light set at 420 nm, at a resolution of 1 nm, we obtained an excitation spectrum for the most luminescent object, also at a resolution of 1 nm. In addition, we obtained 3D luminescence spectra, which represent a series of emission spectra (along the x-axis) obtained for a regular sequence of excitation wavelengths (along the y-axis). These 3D spectra

TABLE 3. Gemological characteristics of the sudoite samples.

Inventory no.	Color	Opacity	Specific gravity	Refractive index	Long-wave UV luminescence Intensity and color
GD-01-017	Light gray	Translucent	2.625	~1.55	Weak green
GD-01-019	Medium gray-green	Translucent	2.433	1.50–1.60	Inert
GD-01-020	Light gray to dark green	Opaque	2.244	—	Weak green
GD-02-003	Medium dark grayish green	Translucent	—	—	—
GD-02-028	Light gray to dark grayish green	Translucent	2.583	—	Inert
GD-09-001	Light brown to medium dark grayish green	Opaque	2.645	~1.55	Moderate green-yellow
MA-02-027	Light to medium dark grayish brown	Translucent	—	—	—
SM-02-033	Very light gray	Translucent	—	—	—
SM-02-086	Light grayish green	Translucent	—	—	—

Some samples were not measured due to their location in the Antilles or their poor polish.

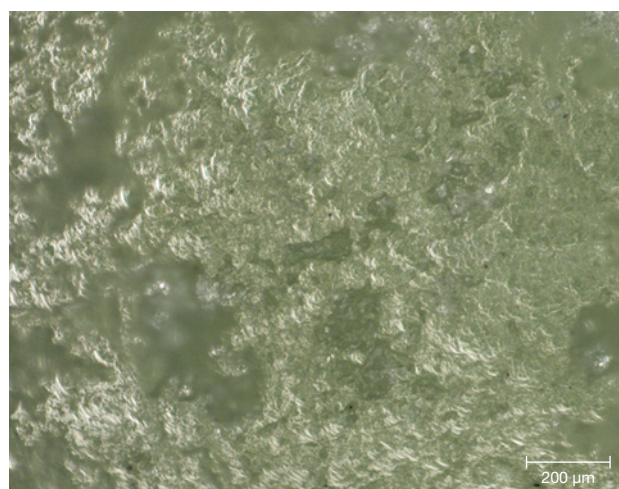
thus illustrate the variation of the emission within the range of possible excitation wavelengths.

RESULTS

Gemological Properties. Standard gemological observations and measurements were carried out (table 3). Some parameters could be measured only for objects that could be studied outside their place of conservation. The samples here show a certain diversity in terms of opacity and specific gravity. On the other hand, they are all polycrystalline and therefore always appear bright between crossed polarizers; their color is rather homogeneous. Observations revealed a laminated structure, identifiable in some curvatures of the object, where these intersect the main plane of lamination (figure 4). Despite the difficulties in determining the refractive index with a refractometer because of the shape and poor polish of the surface of these archaeological objects, three values between 1.50 and 1.60 were observed, consistent with the values given for chlorite-group minerals, which range between 1.56 and 1.68 (Albee, 1962). Albee (1962) also specifies that a relative decrease in the refractive index is expected when the filling rate

of octahedral sites decreases and the magnesium content increases relative to that of iron. In the presence of a di-trioctahedral member of the chlorite group, containing almost only magnesium, it is therefore

Figure 4. This image of the surface of artifact GD-01-017 shows the laminar texture of the material. Photograph by Alain Queffelec.



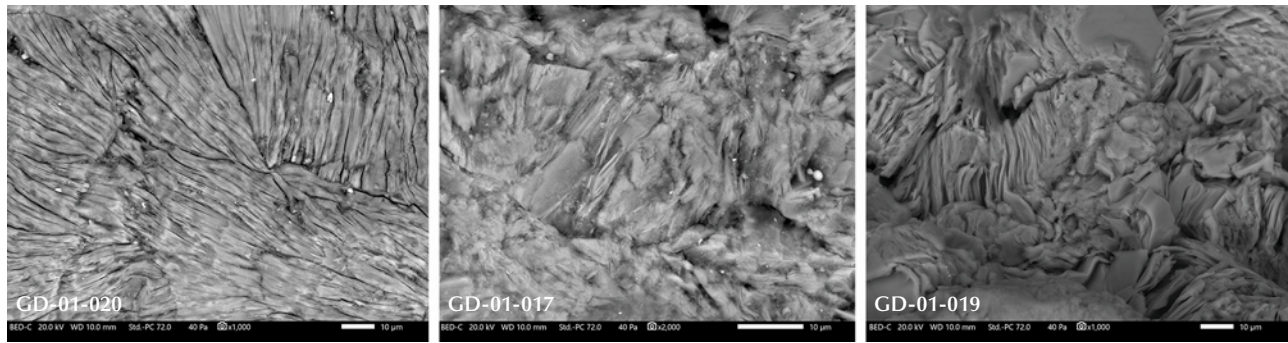


Figure 5. SEM-BSE images of the structure of sudoite, typical for a phyllosilicate (artifacts GD-01-020, GD-01-017, and GD-01-019). Images by Yannick Lefrais.

logical to observe low values in the reported range. No reactions to gemological filters (Chelsea or Han-neman) were noted, and no specific absorption was visible with a handheld spectroscope.

High-Magnification Observation. Backscattered electron (BSE) images acquired by SEM confirm the lamellar structure of the artifacts (figure 5). They also reveal alternating lighter and darker lamellae in some areas of some artifacts (figure 6). This change of grayness level indicates a slight change in chemical composition, with the lighter sheets incorporating heavier elements. Finally, the whole surface of the artifact GD-01-020 shows multidirectional

groups of sub-parallel lamellae (figure 5, left) that are not observed in the other samples, where lamellae are poorly organized at a larger scale.

X-Ray Diffraction and Phase Analysis. The diffraction patterns demonstrate the polycrystallinity of the samples and a varying degree of preferential orientation (figure 7). When compared to the PDF2-ICDD crystallographic database, X-ray diffraction clearly confirms the attribution of this material to the chlorite group, and to sudoite in particular (figure 8). The distinction between sudoite and clinocllore is not easy to make by XRD analysis alone, as noted by Bailey and Lister (1989). Three characteristics of the dif-

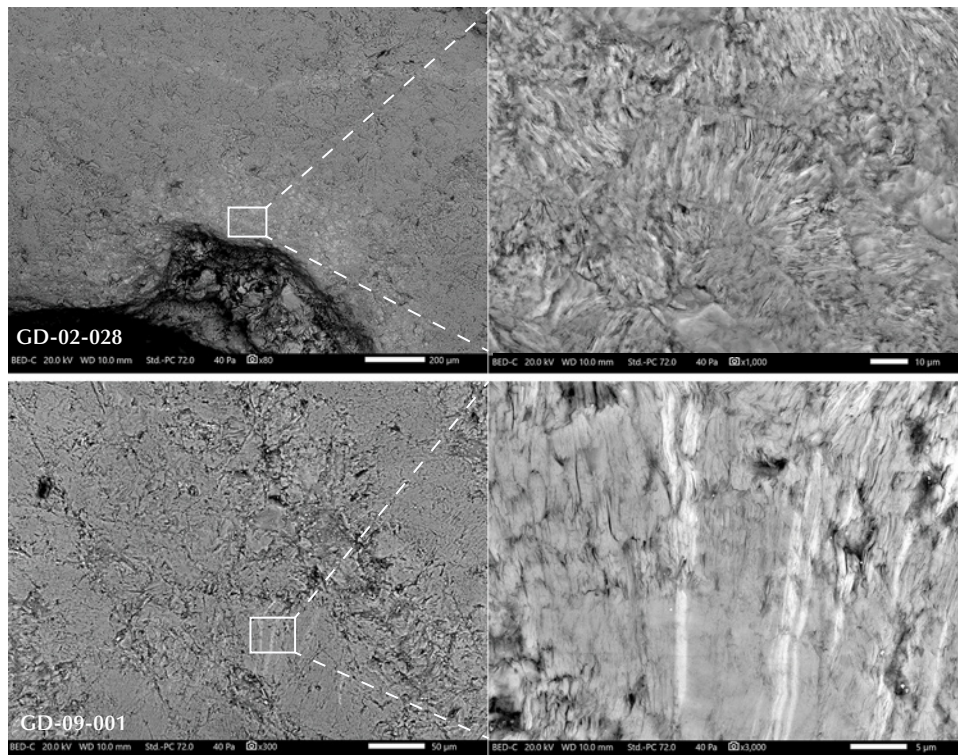


Figure 6. SEM-BSE images show lighter sheets in areas of some artifacts, revealing slight changes in the chemical composition toward heavier elements (artifacts GD-02-028 and GD-09-001). Images by Yannick Lefrais.

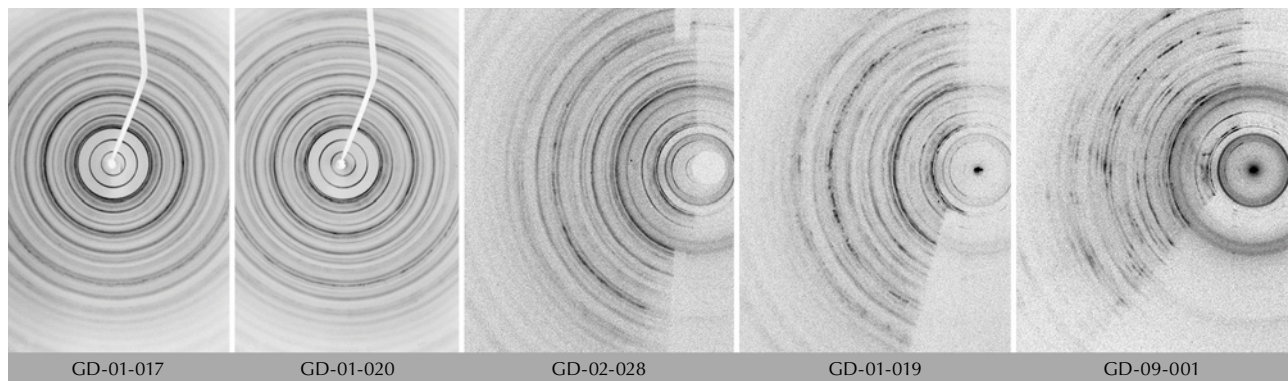


Figure 7. Diffraction patterns (from image plate) obtained in transmission (GD-01-017 and GD-01-020) and low-angle reflection mode (GD-01-019, GD-02-028, and GD-09-001). The observation of complete Debye-Scherrer rings rather than just dots demonstrates the polycrystalline character of the samples, including some preferential orientation leading to darker points.

fraction pattern are mentioned: smaller $d(060)$ values for sudoite (listed as 1.515 Å in table 4 of their work) than clinochlore (1.52–1.56 Å), a $d(001)$ value “slightly smaller” for sudoite, and a “more intense”

peak for the (003) reflection (observed near 4.70 Å) in the sudoite pattern. As for our artifacts, we were able to measure $d(060)$ values of 1.518 Å (GD-01-017), 1.509 Å (GD-01-019), 1.515 Å (GD-01-020), 1.507 Å

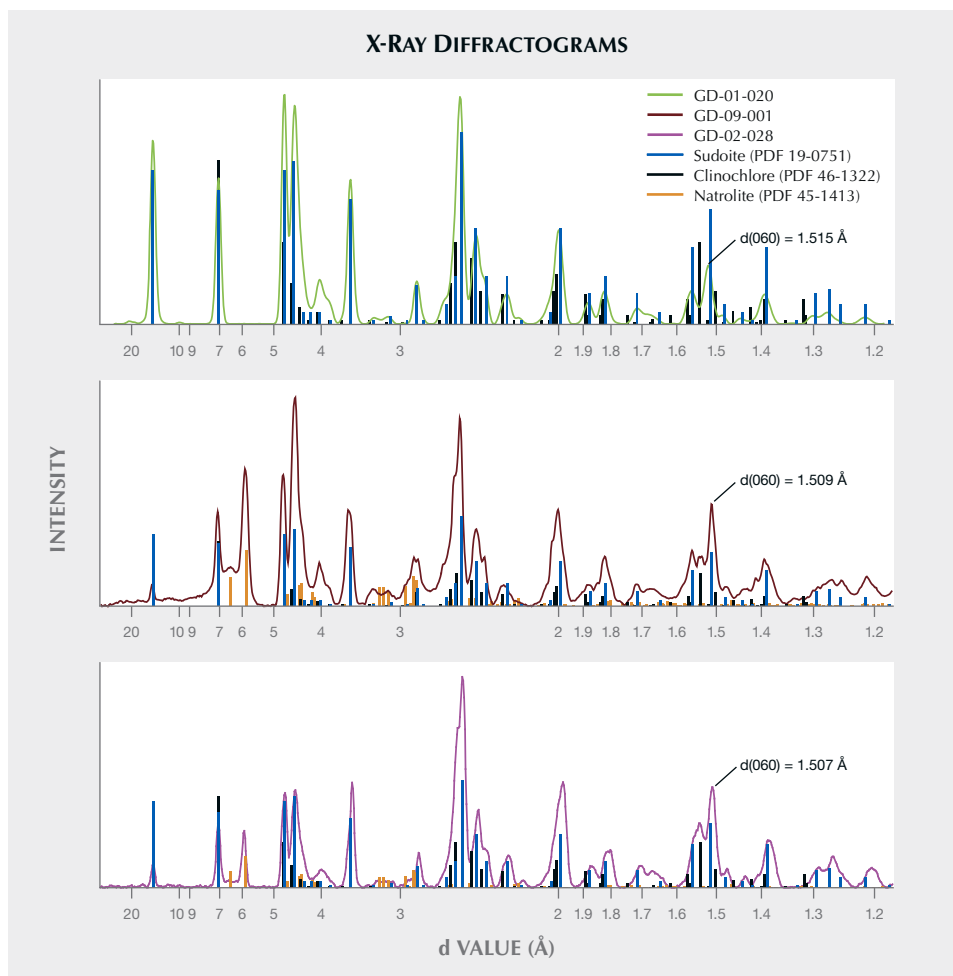


Figure 8. Diffractograms obtained on three of the five Amerindian artifacts, in transmission or low-angle mode. Sudoite diffraction pattern PDF 19-0751 fits better than clinochlore, especially for the $d(060)$. Note the presence of natrolite in different proportions. Note also that the x-axis is logarithmic.

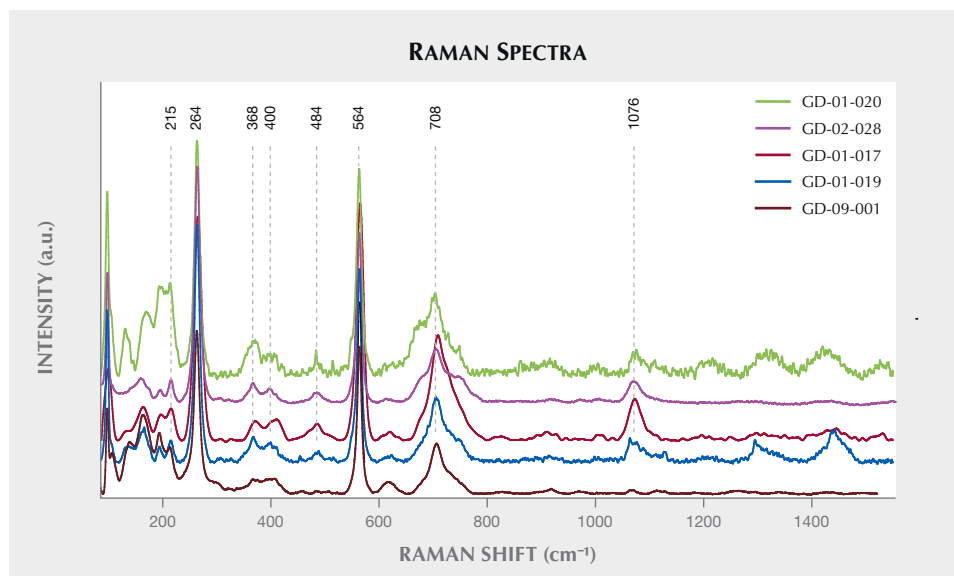


Figure 9. Raman spectra showing the consistency of the measurements from different samples. Spectra are offset vertically for clarity.

(GD-02-028), and 1.509 Å (GD-09-001). We also observed a very intense (003) reflection in most samples, but our measurements were obtained on massive samples and not powder, so the relative intensity of the peaks cannot be considered representative. Therefore, the data obtained strongly suggest identification of sudoite, and the presence of accessory clinocllore may explain some shoulders and the peak at 1.535 Å (e.g., sample GD-09-001).

This X-ray method probes a larger volume than the very small volume excited by the laser in Raman microspectroscopy. This resulted in the identification of an additional mineral for three of the samples (GD-01-019, GD-02-028, and GD-09-001), namely natrolite $\text{Na}_2(\text{Al}_2\text{Si}_3\text{O}_{10}) \cdot 2\text{H}_2\text{O}$, which is a mineral of the zeolite family (figure 8). Natrolite was not identified at the microscopic scale with Raman spectroscopy (figure 10B). The proportion of this mineral, which is highly variable, is difficult to estimate without a Rietveld refinement, which cannot be achieved with our mode of measurement.

Vibrational Spectroscopy. Raman spectroscopy, the only method applied to all the artifacts presented in this study, illustrates the homogeneity of the composition of these different lapidary objects (figure 9). These results were obtained with desktop equipment on five artifacts. The other four objects were identified as made of the same material, with analysis carried out in museums and other curatorial sites using a portable Raman spectrometer (not shown). A very good agreement can be observed between our results and the only published spectrum for the mineral sudoite (Reynard et al., 2015) (figure 10A), with a cor-

respondence of peak positions not observed with the more common mineral of the chlorite family, clinocllore (figure 10B). Sudoite is positively identified through sharp and intense bands at 264 and 564 cm^{-1} . The bands located between 3300–3600 cm^{-1} and 3600–3800 cm^{-1} originate from vibrations of the Al-OH and (Mg, Fe)-OH bonds, respectively (Reynard et al., 2015). Analyzing multiple points on the surface of the archaeological artifacts led to the recognition of rare clinocllore grains, which are probably accessory minerals (as already suggested by XRD characterization), and also of some gypsum, probably the result of pollution on the surface of the samples, which were excavated from coastal sediments.

Infrared spectroscopy (figure 11) confirmed the attribution of the material to the di-trioctahedral chlorite group based on the spectral features in the region of the hydroxyl bond vibrations: The band at 3584 cm^{-1} originates from vibrations of the (Mg, Fe)-OH bonds, while the presence of two wide bands in the 3300–3500 cm^{-1} region is interpreted as two different OH-O distances in the interlayer hydroxyl sheets and thus distinctive of the di-trioctahedral structure (Farmer, 1974; Shirozu and Ishida, 1982; Madejová et al., 2017). The characteristic splitting of the Si-O stretching band around 1000 cm^{-1} in clinocllore, which is absent from our measurements, also supports the identification as sudoite (Madejová et al., 2017). Because of the shape and fragility of the objects, some spectra were difficult to obtain, particularly for the small bead GD-01-020. Comparison with spectra from the literature shows a shift of the main bands in the 400–1200 cm^{-1} region by approximately 30 cm^{-1} . The sharp band at 830 cm^{-1} , attrib-

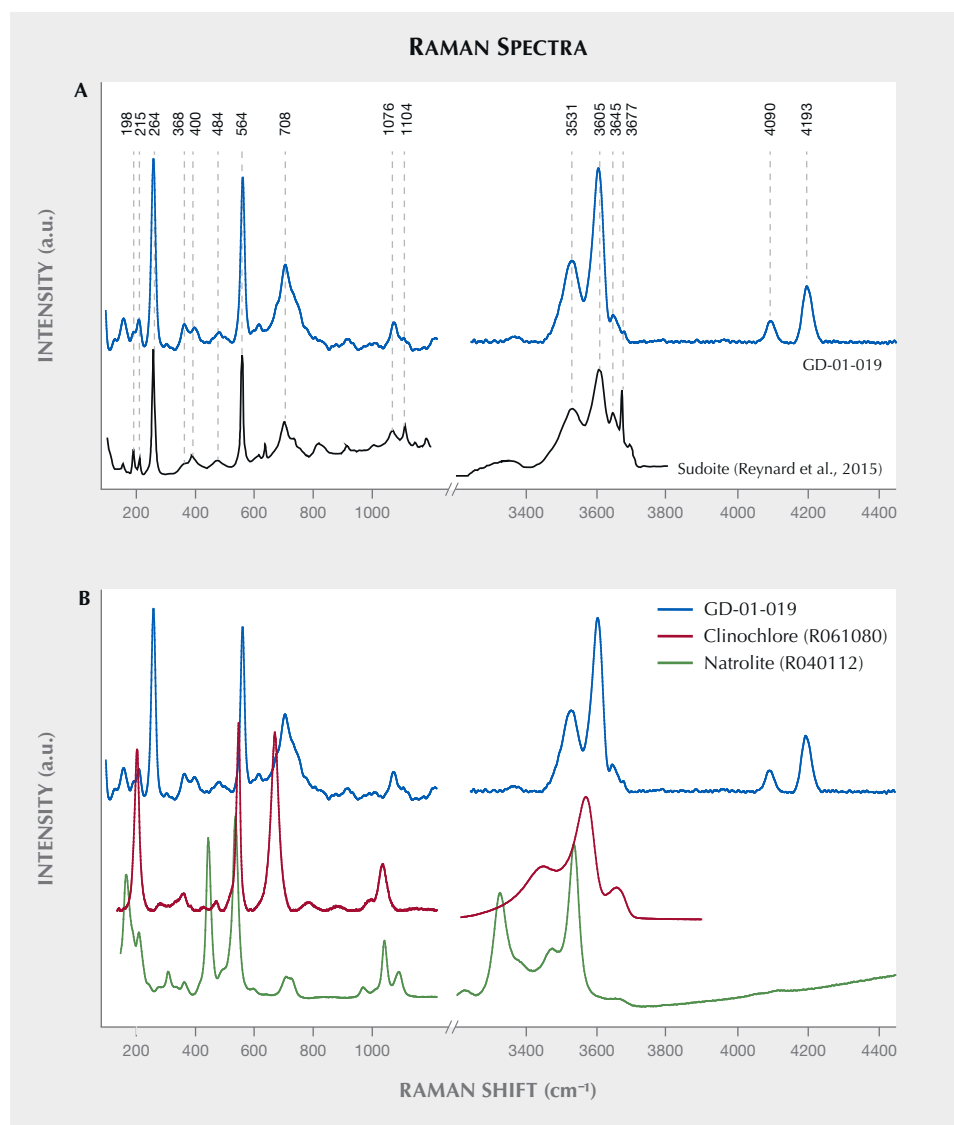


Figure 10. A: Comparison between the Raman spectra obtained on artifact GD-01-019 and the sudoite spectrum determined by Reynard et al. (2015, figure 1). B: Comparison between the Raman spectra obtained on artifact GD-01-019 and reference spectra for clinocllore and natrolite from the RRUFF database (Lafuente et al., 2016). Spectra are offset vertically for clarity.

uted to the (SiAl)OOH bond (Farmer, 1974), however, shows agreement between our experiment and the literature and therefore seems to rule out measurement artifacts. Discrepancies between the data from the literature and our measurements for the archaeological artifacts remain to be explained.

Chemical Characterization. A high degree of chemical homogeneity was observed in EDXRF analysis (figure 12). The major elements are clearly Mg, Al, and Si, consistent with the formula of sudoite, especially taking into account the low efficiency expected for light elements with this method. We also noted the presence of impurities such as P, S, Cl, K, Ca, Ti, V, Fe, and Zn, as well as very low contents of Mn and Ga. The argon (Ar) peak is an artifact related to air in the measured volume.

SEM-EDS analyses provide quantification in good agreement with the theoretical composition of sudoite (table 4) and with the published chemical compositions for different sudoite samples from around the world (table 5). Comparative chemical analysis of the light and dark laminae observed in the BSE image shows a higher potassium and/or barium content, correlated with a decrease in magnesium for the light gray sheets (table 6). The balance of charges, modified by potassium (1+) instead of magnesium (2+), is compensated by a decrease in aluminum (3+) in favor of silicon (4+). The composition of the light gray sheets could approach a mixed composition between sudoite and illite, which would be consistent with the possible presence of illite, a mineral often associated with sudoite (Billault et al., 2002; Ruiz Cruz and de Galdeano, 2005). Mixed layers of sudoite with other phyllosili-

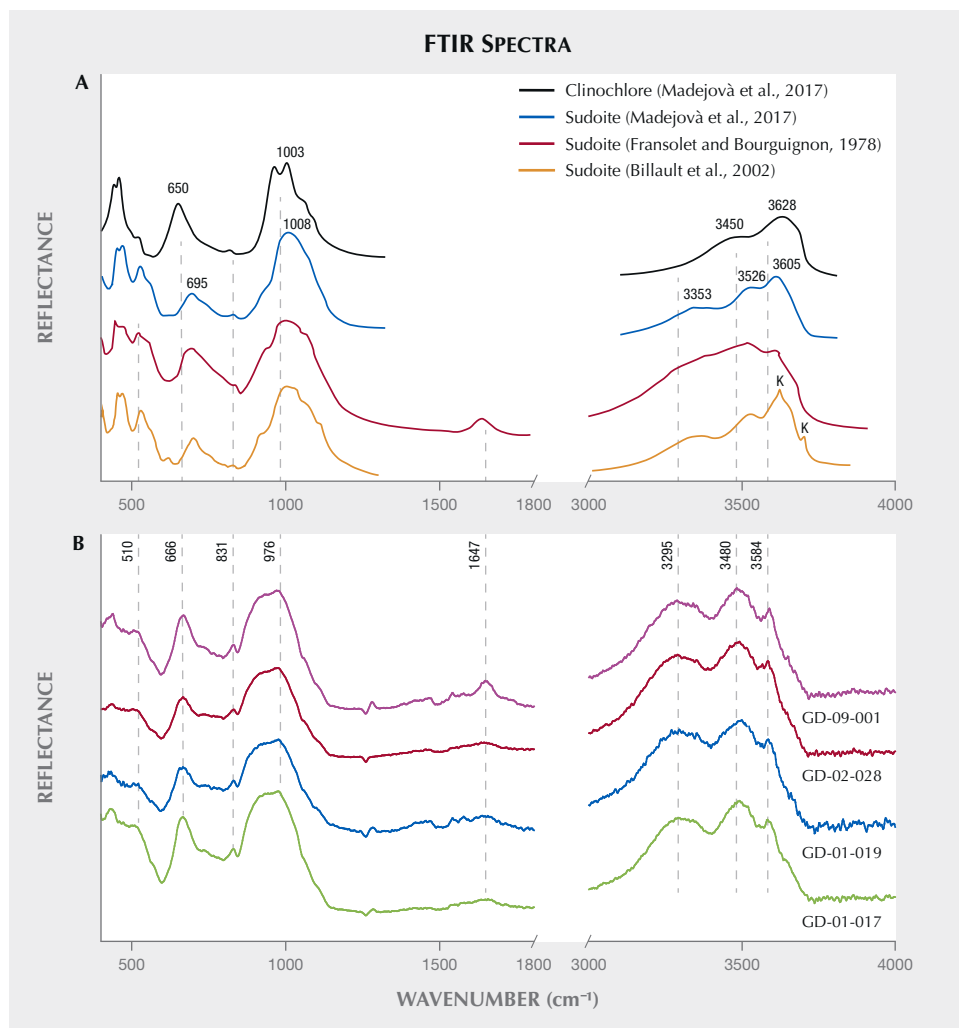


Figure 11. Clinocllore and sudoite FTIR spectra reported in the literature (A) and measured ATR-mode spectra from archaeological artifacts (B). K represents kaolinite (Billault et al., 2002). Spectra are offset vertically for clarity.

cates have been observed in Transmission electron microscope (TEM) analysis (Ruiz Cruz and de

Galdeano, 2005). However, the observation and measurement parameters used during the SEM analysis, op-

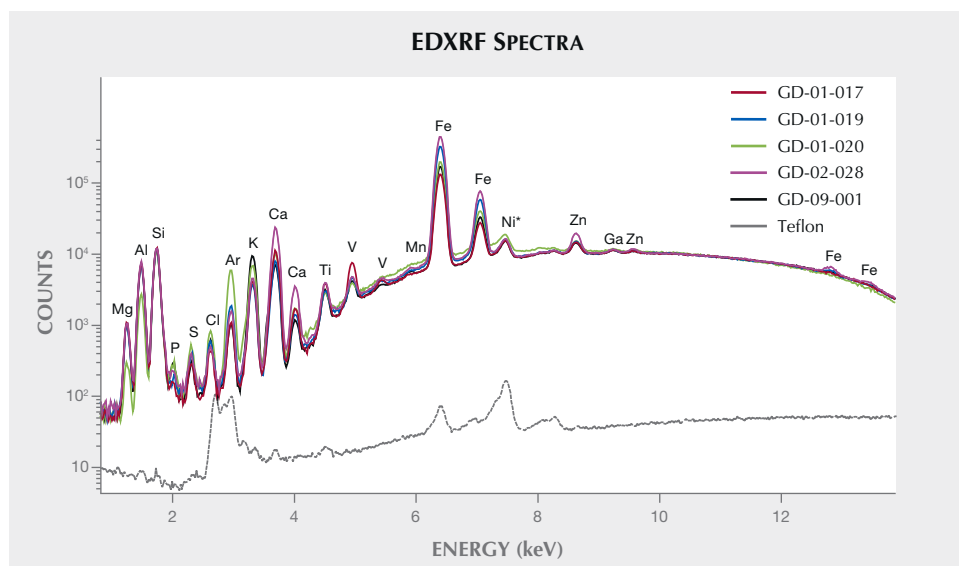


Figure 12. EDXRF spectra obtained on the five exported artifacts with identified peaks. The lower spectrum is for Teflon, measured as a blank. The Ni peak labeled with an asterisk is from the device. The intensity is displayed in logarithmic scale for better clarity of the entire signal, especially for the light elements.

TABLE 4. Chemical composition for different sites on each sudoite artifact, measured with SEM-EDS (SD standard deviation on three measurements) under low-vacuum conditions.

Measurement site	O+OH	Na	Mg	Al	Si	P	S	Cl	K	Ca	Ti	V	Mn	Fe	Sr	Ba	
GD 02-028/Site 1	Mean	18	0.04	1.88	3.78	3.04	0.01	bql	bql	0.04	0.01	bql	bdl	bdl	0.19	bdl	bdl
	SD	—	0.01	0.05	0.02	0.04	<0.01	—	—	0.01	0.01	—	—	—	0.01	—	—
GD 02-028/Site 2	Mean	18	0.04	2.47	3.42	2.55	0.01	0.01	bql	0.21	0.02	bdl	bdl	bql	0.25	0.01	0.01
	SD	—	0.01	0.16	0.04	0.05	<0.01	<0.01	—	0.07	0.01	—	—	—	0.02	0.01	0.01
GD 01-019/Site 1	Mean	18	0.02	1.68	3.44	3.63	0.01	bql	0.01	0.05	0.03	bql	bdl	bdl	0.12	bdl	bdl
	SD	—	0.01	0.07	0.10	0.15	<0.01	—	<0.01	0.02	0.01	—	—	—	<0.01	—	—
GD 01-019/Site 3	Mean	18	0.03	1.98	3.72	3.02	0.02	0.01	bql	0.02	0.02	bql	bdl	bdl	0.16	bdl	bdl
	SD	—	0.00	0.13	0.07	0.05	0.01	<0.01	0.01	0.01	0.01	—	—	—	0.01	—	—
GD 01-020/Site 1	Mean	18	0.08	1.55	3.37	3.60	0.04	0.01	0.02	0.12	0.10	0.01	bdl	bdl	0.11	bdl	bdl
	SD	—	0.02	0.13	0.18	0.21	0.01	<0.01	0.01	0.03	0.03	<0.01	—	—	<0.01	—	—
GD 01-020/Site 2	Mean	18	0.05	1.80	3.60	3.24	0.02	bql	0.01	0.12	0.04	bdl	bdl	bdl	0.12	bdl	bdl
	SD	—	0.02	0.08	0.09	0.08	0.01	—	0.01	0.03	0.01	—	—	—	0.01	—	—
GD 01-017/Site 1	Mean	18	0.02	1.97	3.82	3.07	0.01	0.01	bql	0.05	0.01	bql	bql	bdl	0.05	bdl	bdl
	SD	—	<0.01	0.04	0.02	0.03	<0.01	<0.01	—	0.02	<0.01	—	—	—	<0.01	—	—
GD 01-017/Site 2	Mean	18	0.02	1.93	3.75	3.10	0.01	0.01	0.01	0.05	0.05	bql	bql	bdl	0.06	bdl	bdl
	SD	—	<0.01	0.04	0.03	0.03	<0.01	<0.01	<0.01	0.01	0.02	—	—	—	0.01	—	—
GD 09-001/Site 1	Mean	18	0.02	1.90	3.80	3.08	0.01	0.01	0.01	0.07	0.02	bql	bdl	bdl	0.08	bdl	bdl
	SD	—	<0.01	0.02	0.01	0.01	<0.01	<0.01	<0.01	0.01	<0.01	—	—	—	<0.01	—	—
GD 09-001/Site 3	Mean	18	0.03	1.71	3.74	3.20	0.02	0.01	0.01	0.17	0.03	bql	bdl	bdl	0.08	bdl	bdl
	SD	—	0.01	0.13	0.06	0.08	0.02	—	0.01	0.08	0.02	—	—	—	0.03	—	—

Values in atoms per formula unit normalized to an anionic composition of $O_{10}(OH)_8$; bql = below quantification limit; bdl = below detection limit (<0.01 atom %).

timized for well-focused images of the structure in low-vacuum conditions, did not make it possible to measure only the very thin light gray sheets. Indeed, Monte Carlo simulations indicate that the volume analyzed would be 3–4 μm wide and 3.0–3.5 μm deep.

The natrolite phase, identified by X-ray diffraction in samples GD-09-001, GD-02-028, and GD-01-019, was not identified during the SEM analysis, based on either morphological or chemical data. A few massive grains, lacking any sheet structure, were analyzed, revealing a slightly different chemistry. They

were richer in sodium and silicon, with less magnesium and aluminum, but still far from the composition of natrolite (table 5). The analyzed volume given the parameters used (3–4 μm wide and 3.0–3.5 μm deep), being unfortunately larger than the grains themselves (1.0–1.5 μm), prevents us from being conclusive about this. Nevertheless, those grains were very few in number in the artifacts and do not seem to explain the significant diffraction peaks for this mineral phase when present. It is, however, possible that a more in-depth examination of the artifacts ex-

TABLE 5. Mean composition of the archaeological assemblage, compared with the theoretical composition of sudoite (from IMA), with the experimental composition from the literature (Bailey and Lister, 1989; Ruiz Cruz and de Galdeano, 2005), and with theoretical clinochlore and natrolite.

		O+OH	Na	Mg	Al	Si	K	Ca	Mn	Fe
Archaeological samples	Mean	18	0.03	1.90	3.65	3.15	0.08	0.03	bql	0.12
	SD	—	0.02	0.24	0.18	0.30	0.06	0.03	—	0.06
Theoretical sudoite		18		2	4	3				
Mean (Bailey and Lister, 1989)		18	0.07	1.81	3.81	3.11	0.06	0.08	0.02	0.14
SD		—	0.07	0.34	0.26	0.15	0.06	0.05	0.01	0.12
Mean (Ruiz Cruz and de Galdeano, 2005)		18	0.12	1.80	3.82	3.10	0.05	bql	bql	0.25
SD		—	0.09	0.17	0.04	0.08	0.02	—	—	0.04
Theoretical clinochlore		18		5	2	3	—	—	—	—
Theoretical natrolite		12	2		2	3	—	—	—	—

Values in atoms per formula unit normalized to an anionic composition of $O_{10}(OH)_8$. bql = below quantification limit.

hibiting natrolite by XRD could reveal the distribution and structure of this zeolite mineral.

Origin of Color and UV Luminescence. The visible absorption spectra show a continuum of absorption in the violet and the blue; a very wide, shallow transmission band in the green; and absorption rising in the orange and red that is sample-dependent but always greater than in the green (figure 13A). This ex-

plains the observed overall green color component in these objects, as described by Fransolet and Bourguignon (1978). The spectra obtained are also quite close to those of other chlorite group minerals analyzed in the literature (Bishop et al., 2008), although it is not clear whether the Fe^{2+} - Fe^{3+} charge transfer is involved with the bands delimiting the transmission window. The relatively sharp band at 375 nm (26666 cm^{-1}) could be attributed to 4E(D) spin-forbidden

TABLE 6. Composition of the lighter sheets observed on the backscattered electron image (figure 6), compared to the composition of the illite sheets analyzed by Ruiz Cruz and de Galdeano (2005).

Measurement location	Spectra	O+OH	Na	Mg	Al	Si	K	Ca	Fe	Ba	
GD-02-028/Site 2	6	12	0.04	0.50	2.67	2.37	0.55	0.03	0.06	0.04	
GD-02-028/Site 2	7	12	0.04	0.59	2.65	2.33	0.51	0.03	0.07	0.03	
GD-09-001/Site 4	42	12	0.01	0.73	2.43	2.63	0.39	0.01	0.03	bdl	
GD-09-001/Site 4	43	12	0.01	0.67	2.42	2.69	0.42	0.01	0.03	bdl	
Mean illite (Ruiz Cruz and de Galdeano, 2005)		—	12	0.26	0.13	2.65	3.27	0.65	—	0.06	—
Standard deviation		—	—	0.21	0.05	0.16	0.12	0.19	—	0.03	—

Values in atoms per formula unit normalized to an anionic composition of $O_{10}(OH)_2$. bdl = below detection limit (< 0.01 atom %).

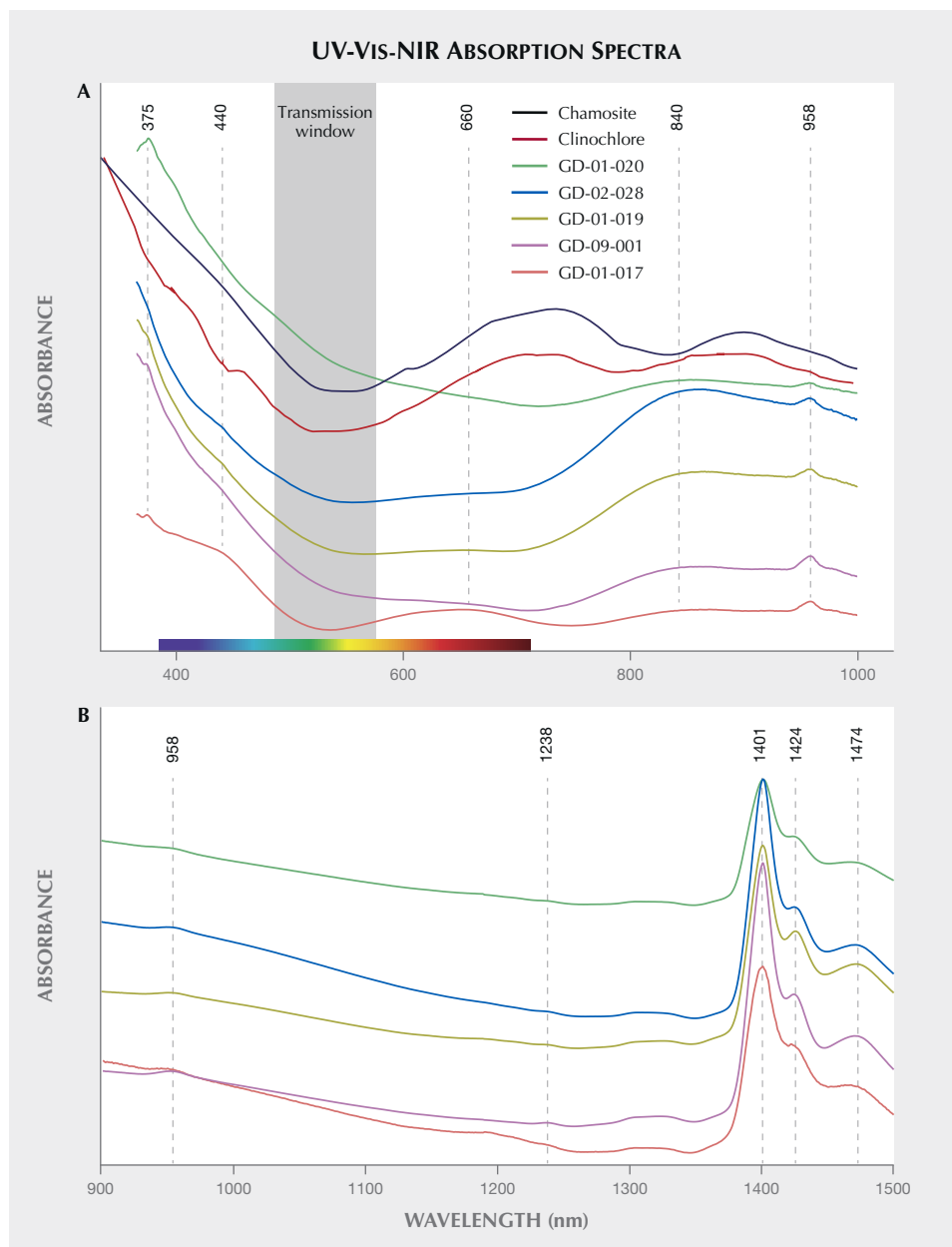


Figure 13. UV-Vis-NIR absorption spectra measured on the archaeological samples with the GemmoSphere instrument (A) and the Perkin Elmer instrument (B). The spectra for clinocllore and chamosite are from Bishop et al. (2008, figure 6). Spectra are offset vertically for clarity.

transitions of isolated Fe^{3+} (Krebs and Maisch, 1971; Palanza et al., 2010). The continuum from the UV into the visible region is thus likely related to the $\text{O}^{2-}\text{-Fe}^{3+}$ charge transfer, and it explains the brownish yellow color component in some samples. The wide bands around 440 and 660 nm vary together, and may correspond with the position of the bands of V^{3+} absorption as proposed for vanadium-doped glass by Johnston (1965, figure 1) and Wang et al. (2015). They are indeed the most important for the samples containing the most vanadium (figure 12 and table 4). While the $\text{Fe}^{2+}\text{-Fe}^{3+}$ transitions could also have been a candidate for one of these bands, the variation in

intensity of the broad absorption bands does not correlate with the concentration levels of this element, and their position is not similar to the band reported in the literature at around 710 nm (14100 cm^{-1}) for chlorite (Mattson and Rossman, 1987). However, Mattson and Rossman (1987) also indicate that the position of absorption bands due to $\text{Fe}^{2+}\text{-Fe}^{3+}$ charge transfer is highly variable. It is interesting to note that the value of 710 nm would, on the other hand, correspond very well to wide bands observed in clinocllore and chamosite, two other minerals from the chlorite group. The wide band in the near-infrared, around 830–850 nm and extending well into



Figure 14. Luminescence of the sudoite samples under short-wave (top) and long-wave (bottom) UV light. Photos by Alain Queffelec.

the visible range, could be attributed to Fe^{2+} in octahedral position (Spinolo et al., 2007), its intensity correlating with the iron content observed using EDXRF (figure 12) and SEM-EDS (table 4). Thus the transmission window is essentially due to iron: on the UV side essentially by the $\text{O}^{2-}\text{-Fe}^{3+}$ charge transfer, and on the red side by Fe^{2+} , with modulation by some V^{3+} .

Finally, water vibrations explain the 958 nm band, as well as absorptions at 1424 and 1474 nm (figure 13B), while O-H bond stretching corresponds to the 1401 nm band (Hunt, 1977; Clark et al., 1990; Clark, 1999; Bishop et al., 2008). These absorption bands could also be interpreted as the water vibrations in the natrolite structure because of their similarity with the spectra obtained by Clark et al. (1990) for this mineral. The absorptions between 1400 and 1500 cm^{-1} are actually the most intense for samples GD-01-019, GD-02-028, and GD-09-001, which are the three samples exhibiting the most intense natrolite X-ray diffraction peaks.

Figure 14 and table 3 group the ultraviolet luminescence observations. Under short-wave UV light, none of the five objects tested show significant luminescence. Under long-wave UV light, three of the five objects tested are homogeneously luminescent, with

low to moderate intensity, and show a green to green-yellow color. None show any phosphorescence.

Since the strongest long-wave UV luminescence was observed for samples GD-09-001 and GD-01-017 (figure 14), these two artifacts were also subjected to spectrofluorimetric measurements (figure 15). Note that it is indeed the two samples with the lowest iron content that show this luminescence, as is often the case due to the luminescence quenching character of iron, linked to the $\text{O}^{2-}\text{-Fe}^{3+}$ charge transfer (Fritsch and Waychunas, 1994). The emission spectrum with 420 nm excitation is very similar for the two artifacts (figure 15, A and B), suggesting a common origin. The spectrum is asymmetrical, wider on the red side, with probably several components. The maximum is located around 525 nm in the green. Yet the emission covers the entire visible spectrum, inducing a whitish color appearance. The greater sensitivity of the human eye to green wavelengths than blue wavelengths, combined with the color of the object itself that may be seen through the luminescence, results in an observed luminescence color of green-yellow. The 3D spectra obtained on the most luminescent object, GD-09-001, indicate that the luminescence reaches a maximum at 435 nm. Wavelengths lower than 420 nm could not be tested because the measured emission spectrum

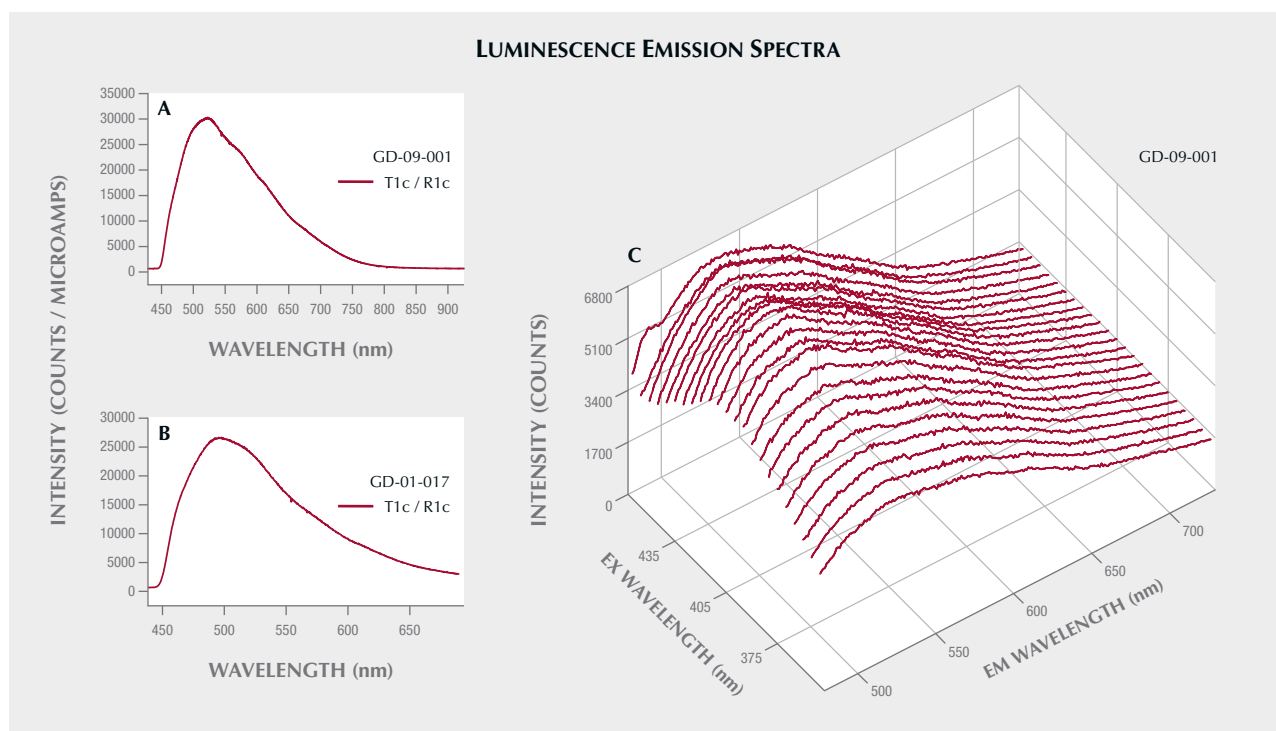


Figure 15. A and B: Luminescence emission spectra with 420 nm excitation for GD-09-001 and GD-01-017, respectively. (T1c/R1c is the corrected intensity measured by the detector normalized to the corrected intensity of the emission source.) C: 3D luminescence spectra emitted by GD-09-001 for different excitation wavelengths.

starts at that point. The same 3D spectra were obtained for GD-01-017 (not shown), and the results were similar. This excitation maximum at 435 nm is somewhat reminiscent of the absorption maximum observed around 440 nm in UV-Vis-NIR spectroscopy, potentially attributed to vanadium. It is also the samples richest in vanadium that show the strongest absorption bands at 440 and 850 nm and exhibit this luminescence, but V^{3+} is not a common emitter and there are many other possibilities, such as a color center or another trace element ion. Although there are several emissions known for chlorites, the only cause of emission explicitly identified is Cr^{3+} (Gaft et al., 2005; Czaja et al., 2014).

DISCUSSION

Importance of the Multi-Analytical Approach. The identification of sudoite large enough to be carved deserves certain analytical efforts in order to unambiguously confirm its mineralogical nature. To this end, several types of analysis (physical, chemical, and structural) have been cross-matched. A more common mineral from the chlorite group, whose similar characteristics could lead to confusion with sudoite, is clinocllore. In particular, its X-ray diffractogram is similar to that of sudoite, and it would have been

very difficult to formally exclude it, especially given the particular measurement conditions required by archaeological samples. It was possible, though, to rule out clinocllore thanks to the results of vibrational and UV-Vis spectroscopy as well as elemental analyses that confirmed a composition matching that of sudoite. Raman spectra and the sheet structure could have led to a misidentification as pyrophyllite or muscovite on the basis of some main Raman bands, but the XRD, FTIR, and chemical analyses precluded this possible confusion. Clinocllore and natrolite are present as accessory minerals in some samples. The former is identified very rarely by Raman spectroscopy, as only a few points on the surface of the artifacts show clinocllore, and in XRD. The latter is present in the XRD pattern of some artifacts.

As a material used to produce lapidary artifacts, one could also be interested in its characterization by more classic gemological methods. Unfortunately, the polycrystalline nature, limited polish, and shape and size of the objects, as well as the absence of a non-archaeological reference material, have limited the possibilities of these approaches (e.g., the rather variable specific gravity and the difficulty of measuring the refractive index). The green color could be re-

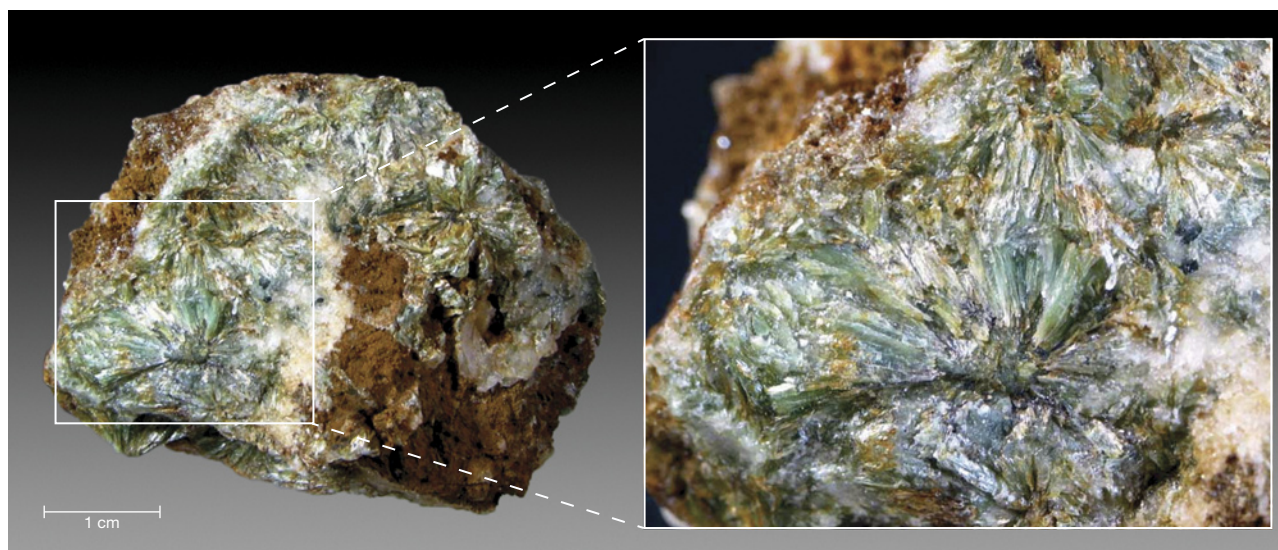


Figure 16. Photograph and microphotograph of a commercial sample of sudoite, showing the existence of centimeter-sized radial nodules. Courtesy of www.dakotamatrix.com.

lated to the sum of Fe^{3+} -, Fe^{2+} -, and V^{3+} -related absorption bands, leaving mostly a shallow transmission window in the green. The UV luminescence of the material is documented for two samples, but its cause remains unclear.

Geological Origin. Sudoite has previously been identified in various geological contexts. The main type of rock in which sudoite is found has undergone low-temperature/high-pressure metamorphism in a subduction context (Fransolet and Bourguignon, 1978; Goffé et al., 1988; Ruiz Cruz and de Galdeano, 2005). The stability field of sudoite is between 240 and 380°C, and between 4 and 8 kbar (Goffé et al., 1988). In this context, it can come from an intermediate stage of metamorphism between a dickite assemblage and a chlorite + paragonite + chloritoid assemblage, in which it is found associated with pyrophyllite, which is not the case for our samples (Ruiz Cruz and de Galdeano, 2005). It may also result from retrograde metamorphism, as proposed in Oman, with a decrease in pressure synchronous with a slight increase in temperature (Goffé et al., 1988). Sudoite can form from kaolinite in the last stages of diagenesis, above 200°C (Daniels et al., 1990), and it is also encountered in a hydrothermal context, at temperatures higher than 200°C (Beaufort et al., 2015).

Sudoite is usually found in the form of fine clay (Billault et al., 2002; Lauf, 2010). Small rosettes up to 1 mm in diameter can form (Beaufort et al., 2015), as can scaly films (Gaines et al., 1997, cited in Lauf, 2010). Only one occurrence of centimeter-sized su-

doite large enough to be carved could be found in the literature (figure 15 in Lauf, 2010), underscoring the rarity of such samples. Beaufort (2015) writes:

The only type of hydrothermal system in which sudoite has been reported in large amounts and in large volumes of altered rocks are unconformity-related uranium deposits (Percival and Kodama, 1989; Billault et al., 2002; Beaufort et al., 2005).

He more recently confirmed this to the authors: “With respect to ... sudoite occurrences in the Paleoproterozoic basins of Canada and Australia, the concept of massive can only be applied on a microscopic scale, because on a macroscopic scale this mineral is always associated with other clay minerals such as illite and kaolinite or dickite. To my knowledge, there is no gem sudoite in this type of geological context” (D. Beaufort, pers. comm., 2019). Rare larger-volume samples consist of agglomerates of radial structures, with color and transparency close to those observed in the artifacts we studied (figure 16). They strongly resemble one studied and shown in, unfortunately, a poor-quality photograph (figure 2 in Jige et al., 2003). These agglomerates are also reminiscent of the structures observed by electron microscopy on sample GD-01-020 (figure 5).

Provenance of the Antillean Archaeological Raw Material. The tectonic context of the Caribbean presents high-pressure/low-temperature (HP/LT) metamorphic rocks, especially due to the numerous subduction zones (Garcia-Casco et al., 2011; see figure 17). The suture of these subduction zones produced ophi-

olite (Garcia-Casco et al., 2006; Lewis et al., 2006), which can be the site of sudoite crystallization, as is the case in Oman (Goffé et al., 1988). Metapelites (metamorphic rocks resulting from the transformation of fine clay-rich sediments from the alteration of continental crust) subjected to a metamorphism of blueschist facies of low intensity can produce rocks containing magnesian chlorites and in particular sudoite (Goffé et al., 1988; Schreyer, 1988; Theye et al., 1992). Rocks formed under HP/LT conditions in the blueschist facies, common in the Caribbean and consistent with the presence of natrolite in some samples, would thus be an excellent candidate for the provenance of this material. It should also be noted that the morphology of the sudoite we observed under the electron microscope (figures 13 and 14) differs greatly from Canadian hydrothermal crystallizations (figure 2 in Billault et al., 2002). This criterion may also indicate that HP/LT metamorphism is more likely to be involved in the crystallization of sudoite than hydrothermal metamorphism.

The presence of sudoite in the Lesser Antilles adds to an existing set of converging clues in the mineralogy of gem materials used in Amerindian lapidary craftsmanship that indicate “long-distance” transport of the raw material. These raw materials, for which no precise source has been clearly stated, originate from rocks that do not naturally exist in the Lesser Antilles and must therefore come from the South American continent and/or the Greater Antilles (Cody, 1993; Murphy et al., 2000; Queffelec et al., 2018, 2020). Previous studies of hard rocks such

as jadeitite, used for the manufacture of a polished ax, have already highlighted such trade networks from the Greater Antilles to the Lesser Antilles (e.g., Harlow et al., 2006; Garcia-Casco et al., 2013; Schertl et al., 2019). The greenish translucent material sudoite could therefore have been part of the batch of exotic colored rocks brought to the Lesser Antilles as part of the pan-Caribbean trade network described for this period (e.g., Rodriguez, 1993; Hofman et al., 2007; Rodriguez Ramos, 2010; Laffoon et al., 2014). It should also be noted that a source of nephrite, a material frequently found in collections of ornamental objects from the same period, was recently discovered on the northern coast of Colombia (Acevedo Gómez et al., 2018), not that far from the Panamanian or Costa Rican ophiolites.

Of the nine artifacts identified as sudoite, eight are of centimeter-sized dimension, consistent with most of the other lithic beads and pendants of Amerindian cultures (e.g., Murphy et al., 2000; Queffelec et al., 2018, 2020; Falci et al., 2020). Such small pieces require only limited sizes of mineralization. Only one pendant (GD-02-003) has a size of several centimeters. Even though such large volumes of raw material may be rare, they must have been available at the outcrop itself to be exploited by the Amerindians, since it is unlikely that this kind of sheet silicate does occur in secondary deposits given its fragility. These outcrops must be of very limited dimensions, which may explain the absence of known localities so far.

All of these objects were found on three islands of the French Lesser Antilles distributed along the

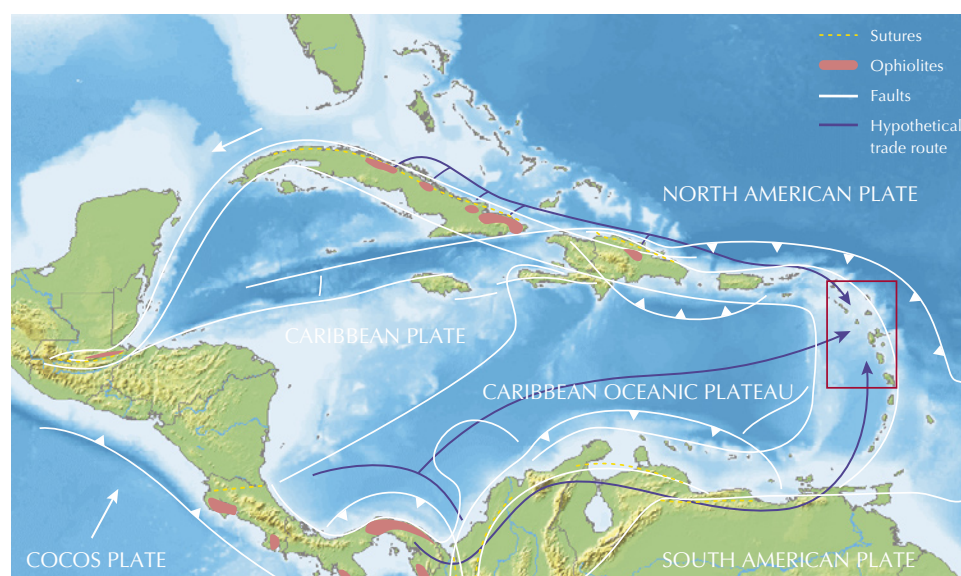


Figure 17. Plate tectonic configuration and major structural features in the Caribbean region, with the presence of ophiolites reported (after figure 1 in Garcia-Casco et al., 2006). The red rectangle on the right represents the area where the nine artifacts were recovered from archaeological excavations. Modified after Garcia-Casco et al. (2011).

Caribbean arc. Sudoite has been identified in every archaeological site that delivered dozens of lapidary artifacts known for these three islands. This underscores the possibility that this newly identified lapidary material could also be found among the archaeological collections of other islands distributed in the same cultural network, if detailed analytical studies were carried out. Identifying this material in archaeological collections will require analytical techniques such as Raman spectroscopy, which is not systematically used by archaeologists, especially in the Caribbean.

CONCLUSIONS

Sudoite was unambiguously identified using a multi-analytical strategy combining methods both structural (Raman and infrared spectroscopy, X-ray diffraction, SEM) and chemical (XRF and EDS). This magnesium-rich di-trioctahedral sheet silicate from the chlorite group is confirmed to be the raw material used by the Amerindians of the Early Ceramic period in the Lesser Antilles to create the nine personal ornaments in this study. It is also the first time this material has been identified as being used for lapidary craft from any period, and the first time it has been described in sizes suitable for carving. The origin of the color and the long-wave UV luminescence properties have also been explored by means of UV-Vis-

NIR spectroscopy and spectrofluorimetry. The greenish color is related to the presence of iron (both Fe^{2+} and Fe^{3+}), with a possible contribution from V^{3+} that would narrow the transmission window for some artifacts. The cause of the UV luminescence remains unclear.

Such a rare material is of interest for the archaeologist, since it may offer valuable information on trade networks during the period under consideration. Sudoite is one of the green rocks used in Amerindian lapidary craftsmanship in the Lesser Antilles, possibly originating from the Greater Antilles, or Central or South America. Based on metamorphic geology, it is possible to consider the origin of sudoite in the ophiolitic formations located at the sutures of the collisions between the Caribbean plate and the North American and Cocos plates. These particular zones are therefore found mainly in northern Cuba, Panama, and Costa Rica, but finding outcrops of this material will prove very difficult due to their limited size in primary deposits and their limited dispersal in secondary deposits. As it would be particularly important to specify the archaeological distribution of the sudoite raw material and its geographical origin, this calls for further detailed analytical studies of objects from the archaeological sites, both in the Antilles and on the nearby continent, and for detailed field prospecting in the areas that might have generated this material.

ABOUT THE AUTHORS

Mr. Queffelec is a PhD student and CNRS engineer in archaeometry at the UMR5199 PACEA (CNRS, University of Bordeaux, Ministère de la Culture). Mr. Bellot-Gurlet is a full professor of analytical chemistry at the UMR8233 MONARIS (Sorbonne University, CNRS). Mr. Foy is a CNRS engineer in archaeometry at the UMR3685 NIMBE (CNRS, CEA, University of Paris-Saclay). Mr. Lefrais is a CNRS engineer in archaeometry at the UMR5060 CRP2A (CNRS, Bordeaux Montaigne University). Mr. Fritsch is full professor in physics and gemologist at the UMR6502 IMN (University of Nantes, CNRS).

ACKNOWLEDGMENTS

This study was conducted through the Programme Collectif de Recherche "Parures amérindiennes en matériaux lithiques dans les Antilles Françaises: minéralogie, sources géologiques et fabrication," funded by the Guadeloupe Regional Service of Archaeology, the Guadeloupe Regional Council, and the Martinique Regional Service of Archaeology. This research was also partially supported by the LabEx LaScArBx research program (ANR-10-LABX-52). We thank the Musée Départemental Edgar Clerc, the Musée Départemental d'Archéologie et de Préhistoire de la Martinique, and François Petit for granting access to the material. We are grateful to Blanca Moquet for refractive index spot readings. We thank the three anonymous reviewers for their thorough evaluation that helped improved the quality of this article. This study received financial support from the French government in the framework of the University of Bordeaux's IdEx "Investments for the Future" program/GPR "Human Past."

REFERENCES

- Acevedo Gómez N., Scharff M.W., Garcia-Casco A., Sáenz-Samper J. (2018) Placas aladas de las sociedades Nahuange y Tairona (100–1600 DC), Sierra Nevada de Santa Marta, Colombia: materia prima y áreas de procedencia. *Latin American Antiquity*, Vol. 29, No. 4, pp. 774–792, <http://dx.doi.org/10.1017/laq.2018.51>
- Albee A.L. (1962) Relationships between the mineral association, chemical composition and physical properties of the chlorite series. *American Mineralogist*, Vol. 47, No. 7–8, pp. 851–870,

- <http://dx.doi.org/10.1346/CCMN.1989.0370301>
- Arem J.E. (1987) *Color Encyclopedia of Gemstones*, 2nd ed. Van Nostrand Reinhold, New York, 248 pp.
- Bailey S.W. (1980) Summary of recommendations of AIPEA nomenclature committee on clay minerals. *American Mineralogist*, Vol. 65, No. 1–2, pp. 1–7.
- Bailey S.W., Lister J.S. (1989) Structures, compositions, and X-ray diffraction identification of dioctahedral chlorites. *Clays and Clay Minerals*, Vol. 37, No. 3, pp. 193–202, <http://dx.doi.org/10.1346/CCMN.1989.0370301>
- Beaufort D., Rigault C., Billon S., Billault V., Inoue A., Inoue S., Patrier P. (2015) Chlorite and chloritization processes through mixed-layer mineral series in low-temperature geological systems—a review. *Clay Minerals*, Vol. 50, No. 4, pp. 497–523, <http://dx.doi.org/10.1180/claymin.2015.050.4.06>
- Bérard B. (2013) The Saladoid. In W. Keegan, C. Hofman, and R. Rodriguez Ramos, Eds., *The Oxford Handbook of Caribbean Archaeology*. Oxford University Press, pp. 184–197.
- (2019) About boxes and labels: A periodization of the Amerindian occupation of the West Indies. *Journal of Caribbean Archaeology*, Vol. 19, pp. 17.
- Billault V., Beaufort D., Patrier P., Petit S. (2002) Crystal chemistry of Fe-sudowites from uranium deposits in the Athabasca Basin (Saskatchewan, Canada). *Clays and Clay Minerals*, Vol. 50, No. 1, pp. 70–81, <http://dx.doi.org/10.1346/000986002761002847>
- Bishop J.L., Lane M.D., Dyar M.D., Brown A.J. (2008) Reflectance and emission spectroscopy study of four groups of phyllosilicates: smectites, kaolinite-serpentines, chlorites and micas. *Clay Minerals*, Vol. 43, No. 1, pp. 35–54, <http://dx.doi.org/10.1180/claymin.2008.043.1.03>
- Bonnissent D. (2008) Archéologie précolombienne de l'île de Saint-Martin, Petites Antilles (3300 BC-1600 AD). PhD thesis, Université Aix-Marseille, 261 pp.
- Brigatti M.F., Malferrari D., Laurora A., Elmi C., Mottana A. (2011) Structure and mineralogy of layer silicates: Recent perspectives and new trends. In M.F. Brigatti, and A. Mottana, Eds., *Layered Mineral Structures and Their Application in Advanced Technologies*. European Mineralogical Union Notes in Mineralogy Series, Vol. 11, pp. 1–71. Mineralogical Society of Great Britain and Ireland, London.
- Bukanov V.V. (2006) *Russian Gemstones*. Granit, Prague, 472 pp.
- Clark R.N. (1999) Spectroscopy of rocks and minerals, and principles of spectroscopy. In A.N. Rencz, Ed., *Manual of Remote Sensing for the Earth Sciences*, 3rd ed., John Wiley & Sons, Inc., New York, pp. 3–58.
- Clark R.N., King T.V., Klejwa M., Swayze G.A., Vergo N. (1990) High spectral resolution reflectance spectroscopy of minerals. *Journal of Geophysical Research: Solid Earth*, Vol. 95, No. B8, pp. 12653–12680, <http://dx.doi.org/10.1029/JB095iB08p12653>
- Cody A.K. (1993) Distribution of exotic stone artifacts through the Lesser Antilles: Their implications for prehistoric interaction and exchange. In A. Cummins and P. King, Eds., *Proceedings of the 14th International Congress for Caribbean Archaeology*, Barbados, pp. 204–226.
- Czaja M., Kadziołka-Gaweł M., Lisiecki R., Bodył-Gajowska S., Mazurak Z. (2014) Luminescence and other spectroscopic properties of purple and green Cr-clinochlore. *Physics and Chemistry of Minerals*, Vol. 41, No. 2, pp. 115–126, <http://dx.doi.org/10.1007/s00269-013-0629-x>
- Daniels E.J., Altaner S.P., Marshak S., Eggleston J.R. (1990) Hydrothermal alteration in anthracite from eastern Pennsylvania: Implications for mechanisms of anthracite formation. *Geology*, Vol. 18, No. 3, pp. 247–250, [http://dx.doi.org/10.1130/0091-7613\(1990\)018%3C0247:HAIAFE%3E2.3.CO;2](http://dx.doi.org/10.1130/0091-7613(1990)018%3C0247:HAIAFE%3E2.3.CO;2)
- Desautels P.E. (1973) *L'univers des pierres précieuses*. Arthaud, Paris, 252 pp.
- Drouin D., Couture A.R., Joly D., Tastet X., Aimez V., Gauvin R. (2007) CASINO V2.42—A fast and easy-to-use modeling tool for scanning electron microscopy and microanalysis users. *Scanning*, Vol. 29, No. 3, pp. 92–101, <http://dx.doi.org/https://doi.org/10.1002/sca.20000>
- Duda R., Relj L. (1999) *Les pierres précieuses*. Gründ, Paris, 407 pp.
- v. Engelhardt W., Müller G., Kromer H. (1962) Dioktaedrischer Chlorit (“Sudoit”) in Sedimenten des Mittleren Keupers von Plochingen (Württ.). *Naturwissenschaften*, Vol. 49, No. 9, pp. 205–206, <http://dx.doi.org/10.1007/BF00633957>
- Falci C.G., Knaf A.C.S., van Gijn A., Davies G.R., Hofman C.L. (2020) Lapidary production in the eastern Caribbean: A typotechnological and microwear study of ornaments from the site of Pearls, Grenada. *Archaeological and Anthropological Sciences*, Vol. 12, No. 2, Article no. 53, 16 pp., <http://dx.doi.org/10.1007/s12520-019-01001-4>
- Farmer V.C. (1974) The layer silicates. In V.C. Farmer, Ed., *The Infrared Spectra of Minerals*, Mineralogical Society, London, pp. 331–363.
- Fransolet A.-M., Bourguignon P. (1978) Di/trioctahedral chlorite in quartz veins from the Ardenne, Belgium. *The Canadian Mineralogist*, Vol. 16, No. 3, pp. 365–373.
- Fritsch E., Waychunas G.A. (1994) Gemstones. In M. Robbins, Ed., *Fluorescence: Gems and Minerals Under Ultraviolet Light*. Geoscience Press, Phoenix, Arizona, pp. 149–174.
- Gaft M., Reisfeld R., Panczer G. (2005) *Luminescence Spectroscopy of Minerals and Materials*. Springer-Verlag, Berlin and Heidelberg, 356 pp., <http://dx.doi.org/10.1007/b137490>
- Gaines R.V., Dana J.D., Dana E.S. (1997) *Dana's New Mineralogy: The System of Mineralogy of James Dwight Dana and Edward Salisbury Dana*. John Wiley, New York.
- García-Casco A., Torres-Roldán R.L., Iturralde-Vinent M.A., Millán G., Cambra K.N., Lázaro C., Vega A.R. (2006) High pressure metamorphism of ophiolites in Cuba. *Geologica Acta*, Vol. 4, No. 1, pp. 63–88, <http://dx.doi.org/10.1344/105.000000358>
- García-Casco A., Proenza J.A., Iturralde-Vinent M.A. (2011) Subduction zones of the Caribbean: The sedimentary, magmatic, metamorphic and ore-deposit records. *Geologica Acta*, Vol. 9, No. 3–4, pp. 217–224, <http://dx.doi.org/10.1344/105.000001745>
- García-Casco A., Knippenberg S., Ramos R.R., Harlow G.E., Hofman C., Pomo J.C., Blanco-Quintero I.F. (2013) Pre-Columbian jadeite artifacts from the Golden Rock Site, St. Eustatius, Lesser Antilles, with special reference to jadeite artifacts from Elliot's, Antigua: Implications for potential source regions and long-distance exchange networks in the Greater Caribbean. *Journal of Archaeological Science*, Vol. 40, No. 8, pp. 3153–3169, <http://dx.doi.org/10.1016/j.jas.2013.03.025>
- Gates-Rector S., Blanton T. (2019) The Powder Diffraction File: A quality materials characterization database. *Powder Diffraction*, Vol. 34, No. 4, pp. 352–360, <http://dx.doi.org/10.1017/S0885715619000812>
- Goffé B., Michard A., Kienast J.R., Le Mer O. (1988) A case of obduction-related high-pressure, low-temperature metamorphism in upper crustal nappes, Arabian continental margin, Oman: P-T paths and kinematic interpretation. *Tectonophysics*, Vol. 151, No. 1, The Ophiolites of Man, pp. 363–386, [http://dx.doi.org/10.1016/0040-1951\(88\)90253-3](http://dx.doi.org/10.1016/0040-1951(88)90253-3)
- Hammersley A.P. (2016) FIT2D: A multi-purpose data reduction, analysis and visualization program. *Journal of Applied Crystallography*, Vol. 49, No. 2, pp. 646–652, <http://dx.doi.org/10.1107/S1600576716000455>
- Harlow G.E., Murphy A.R., Hozjan D.J., de Mille C.N., Levinson A.A. (2006) Pre-Columbian jadeite axes from Antigua, West Indies: Description and possible sources. *The Canadian Mineralogist*, Vol. 44, No. 2, pp. 305–321, <http://dx.doi.org/10.2113/gscanmin.44.2.305>
- Hofman C.L., Bright A.J., Boomert A., Knippenberg S. (2007) Island rhythms: The web of social relationships and interaction networks in the Lesser Antillean Archipelago between 400 B.C. and A.D. 1492. *Latin American Antiquity*, Vol. 18, No. 3, pp. 243–268, <http://dx.doi.org/10.2307/25478180>

- Hunt G.R. (1977) Spectral signatures of particulate minerals in the visible and near infrared. *Geophysics*, Vol. 42, No. 3, pp. 501–513, <http://dx.doi.org/10.1190/1.1440721>
- Jige M., Kitagawa R., Zaykov V.V., Sinyakovskaya I. (2003) Surface microtopography of sudoite. *Clay Minerals*, Vol. 38, No. 3, pp. 375–382, <http://dx.doi.org/10.1180/0009855033830104>
- Johnston W.D. (1965) Optical spectra of the various valence states of vanadium in $\text{Na}_2\text{O}\cdot 2\text{SiO}_2$ glass. *Journal of the American Ceramic Society*, Vol. 48, No. 12, pp. 608–611, <http://dx.doi.org/10.1111/j.1151-2916.1965.tb14688.x>
- Kohyama N. (2000) In memory of Prof. Toshio Sudo. *Clay Science*, Vol. 11, No. 2, pp. 103–105, <http://dx.doi.org/10.11362/jcssj-clayscience1960.11.103>
- Krebs J.J., Maisch W.G. (1971) Exchange effects in the optical-absorption spectrum of Fe^{3+} in Al_2O_3 . *Physical Review B*, Vol. 4, No. 3, pp. 757–769, <http://dx.doi.org/10.1103/PhysRevB.4.757>
- Laffoon J.E., Ramos R.R., Baik L.C., Storde Y.N., Lopez M.R., Davies G.R., Hofman C.L. (2014) Long-distance exchange in the precolonial Circum-Caribbean: A multi-isotope study of animal tooth pendants from Puerto Rico. *Journal of Anthropological Archaeology*, Vol. 35, pp. 220–233, <http://dx.doi.org/10.1016/j.jaa.2014.06.004>
- Lafuente B., Downs R.T., Yang H., Stone N. (2016) The power of databases: The RRUFF project. In T. Armbruster and R.M. Danisi, Eds., *Highlights in Mineralogical Crystallography*, pp. 1–30. W. De Gruyter, Berlin, <http://dx.doi.org/10.1515/9783110417104-003>
- Lauf R.J. (2010) Collector's guide to the chlorite group. *Rocks & Minerals*, Vol. 85, No. 4, pp. 318–325, <http://dx.doi.org/10.1080/00357521003727272>
- Lewis J.F., Draper G., Proenza Fernández J.A., Espaillet J., Jiménez J. (2006) Ophiolite-related ultramafic rocks (serpentinites) in the Caribbean region: A review of their occurrence, composition, origin, emplacements and Ni-Laterite soil formation. *Geologica Acta*, Vol. 4, No. 1–2, pp. 237–263, <http://dx.doi.org/10.1344/105.000000368>
- Madejová J., Gates W.P., Petit S. (2017) IR spectra of clay minerals. *Developments in Clay Science*, Vol. 8, pp. 107–149, <http://dx.doi.org/10.1016/B978-0-08-100355-8.00005-9>
- Manutchehr-Danaei M. (2005) *Dictionary of Gems and Gemology*, 2nd ed. Springer, Berlin, 879 pp.
- Mattson S.M., Rossman G.R. (1987) Identifying characteristics of charge transfer transitions in minerals. *Physics and Chemistry of Minerals*, Vol. 14, No. 1, pp. 94–99, <http://dx.doi.org/10.1007/BF00311152>
- von Müller G. (1961) Vorläufige Mitteilung über ein neues dioktaedrisches Phyllosilikat der Chlorit-Gruppe. *Neues Jahrbuch für Mineralogie, Monatshefte*, Vol. 1961, pp. 112–120.
- Murphy A.R., Hozjan D.J., de Mille C.N., Levinson A.A. (2000) Pre-Columbian gems and ornamental materials from Antigua, West Indies. *G&G*, Vol. 36, No. 2, pp. 234–245, <http://dx.doi.org/10.5741/GEMS.36.3.234>
- Nägele K., Posth C., Orbegozo M.I., Armas Y.C. de, Godoy S.T.H., Herrera U.M.G., Nieves-Colón M.A., Sandoval-Velasco M., Mylopotamitaki D., Radzeviciute R., Laffoon J., Pestle W.J., Ramos-Madrigal J., Lamnidis T.C., Schaffer W.C., Carr R.S., Day J.S., Antúnez C.A., Rivero A.R., Martínez-Fuentes A.J., Crespo-Torres E., Roksandic I., Stone A.C., Lalueza-Fox C., Hoogland M., Roksandic M., Hofman C.L., Krause J., Schroeder H. (2020) Genomic insights into the early peopling of the Caribbean. *Science*, <http://dx.doi.org/10.1126/science.aba8697>
- O'Donoghue M. (2006) *Gems*, 6th ed. Elsevier, Oxford, UK, 904 pp.
- Palanza V., Galli A., Lorenzi R., Moretti F., Mozzati M.C., Paleari A., Spinolo G. (2010) Luminescence study of transition metal ions in natural magmatic and metamorphic yellow sapphires. In *IOP Conference Series: Materials Science and Engineering*, 15. IOP Publishing, <http://dx.doi.org/10.1088/1757-899X/15/1/012086>
- Queffelec A., Fouéré P., Paris C., Stouvenot C., Bellot-Gurlet L. (2018) Local production and long-distance procurement of beads and pendants with high mineralogical diversity in an early Saladoid settlement of Guadeloupe (French West Indies). *Journal of Archaeological Science: Reports*, Vol. 21, pp. 275–288, <http://dx.doi.org/10.1016/j.jasrep.2018.07.011>
- Queffelec A., Fouéré P., Bellot-Gurlet L., Bérard B. (2020) Stone ornaments from Guadeloupe and Martinique Early Ceramic period sites (200 BC – AD 400), detailed analysis and comparison with a Late Ceramic period site (AD 750 – 1000). *Journal of Caribbean Archaeology*, Vol. 20, pp. 1–44.
- Queffelec A., Fouéré P., Caverne J.-B. (2021) A database of lapidary artifacts in the Caribbean for the Ceramic Age. *Journal of Open Archaeology Data*, Vol. 9, pp. 11, <http://dx.doi.org/10.5334/joad.74>
- Reynard B., Bezacier L., Caracas R. (2015) Serpentine, talc, chlorites, and their high-pressure phase transitions: A Raman spectroscopic study. *Physics and Chemistry of Minerals*, Vol. 42, No. 8, pp. 641–649, <http://dx.doi.org/10.1007/s00269-015-0750-0>
- Rodriguez M. (1993) Early trade networks in the Caribbean. In A. Cummins and P. King, Eds., *Proceedings of the 14th International Congress for Caribbean Archaeology*. International Association for Caribbean Archaeology, Barbados, pp. 306–314.
- Rodriguez Ramos R. (2010) What is the Caribbean? An archaeological perspective. *Journal of Caribbean Archaeology*, Vol. 3, pp. 19–51.
- Rouse I. (1992) *The Tainos: Rise and Decline of the People Who Greeted Columbus*. Yale University Press, New Haven, Connecticut.
- Ruiz Cruz M.D., de Galdeano C.S. (2005) Compositional and structural variation of sudoite from the Betic Cordillera (Spain): A TEM/AEM study. *Clays and Clay Minerals*, Vol. 53, No. 6, pp. 639–652, <http://dx.doi.org/10.1346/CCMN.2005.0530610>
- Schertl H.-P., Maresch W.V., Knippenberg S., Hertwig A., Belando A.L., Ramos R.R., Speich L., Hofman C.L. (2019) Petrography, mineralogy and geochemistry of jadeite-rich artefacts from the Playa Grande excavation site, northern Hispaniola: Evaluation of local provenance from the Río San Juan Complex. *Geological Society, London, Special Publications*, Vol. 474, No. 1, pp. 231–253, <http://dx.doi.org/10.1144/SP474.3>
- Schreyer W. (1988) Experimental studies on metamorphism of crustal rocks under mantle pressures. *Mineralogical Magazine*, Vol. 52, No. 364, pp. 1–26, <http://dx.doi.org/10.1180/minmag.1988.052.364.01>
- Shirozu H., Ishida K. (1982) Infrared study of some 7 Å layer silicates by deuteration. *Mineralogical Journal*, Vol. 11, No. 4, pp. 161–171, <http://dx.doi.org/10.2465/minerj.11.161>
- Spinolo G., Fontana I., Galli A. (2007) Optical absorption spectra of Fe^{2+} and Fe^{3+} in beryl crystals. *Physica status solidi (b)*, Vol. 244, No. 12, pp. 4660–4668, <http://dx.doi.org/10.1002/pssb.200790018>
- Theye T., Seidel E., Vidal O. (1992) Carpholite, sudoite, and chloritoid in low-grade high-pressure metapelites from Crete and the Peloponnese, Greece. *European Journal of Mineralogy*, Vol. 4, No. 3, pp. 487–508, <http://dx.doi.org/10.1127/ejm/4/3/0487>
- Wang A., Freeman J.J., Jolliff B.L. (2015) Understanding the Raman spectral features of phyllosilicates. *Journal of Raman Spectroscopy*, Vol. 46, No. 10, pp. 829–845, <http://dx.doi.org/10.1002/jrs.4680>
- Wilson S.M. (2007) *Archaeology of the Caribbean*. Cambridge University Press, New York, 205 pp.

THE BRILLIANCE YOU EXPECT FROM THE BRAND YOU TRUST

LABORATORY-GROWN DIAMOND REPORT
February 16, 2021
GIA Report Number: 6213478953
Identification: Laboratory-Grown
Shape and Cutting Style: Square Modified Brilliant
Measurements: 5.58 x 5.46 x 3.98 mm

LABORATORY-GROWN DIAMOND SPECIFICATIONS*
Carat Weight: 1.50 carat
Color: D
Clarity: SI1
Cut: Excellent

ADDITIONAL INFORMATION
Polish: Excellent
Symmetry: Excellent
Fluorescence: Medium Blue
Inscriptions: GIA 6213478953, LABORATORY-GROWN
Comments: *SAMPLE *SAMPLE *SAMPLE *SAMPLE
This is a man-made diamond produced by HPHT (High Pressure High Temperature) growth process and has evidence of post-growth treatments to change the color.

PROPORTIONS
slightly thick - thick
74%
73.0%
none
Profile to actual proportions

CLARITY CHARACTERISTICS
KEY TO SYMBOLS
Crystal, Cloud, Feather, Natural
Red symbols denote internal characteristics (inclusions). Green or black symbols denote external characteristics (blemishes). Diagram is an approximate representation of the diamond, and symbols show actual type, position, and approximate size of clarity characteristics. All clarity characteristics may not be shown. Details of these are not shown.

GIA COLOR SCALE
D E F G H I J K L M N O P Q R S T U V W X Y Z
Colorless Very Light Light

GIA CUT SCALE
EXCELLENT VERY GOOD GOOD FAIR POOR

GIA CLARITY SCALE
FLAWLESS (FL) VERY VERY Slightly Included (VVS1, VVS2) Very Slightly Included (VSI1, VSI2) Slightly Included (SI1, SI2) Moderately Included (I1, I2) Included (I3)

LABORATORY-GROWN DIAMOND SPECIFICATION*
Shape and Cutting Style: Square Modified Brilliant
Measurements: 5.58 x 5.46 x 3.98 mm
Carat Weight: 1.50 carat
Color: D
Clarity: SI1

PROPORTIONS
Depth: 73.0%
Table: 74%
Girdle: Slightly Thick to Thick
Culet: None

*This GIA Laboratory-Grown Diamond Report describes color and clarity specifications on the same scale as the GIA Diamond Grading Report for natural diamonds. The specifications do not correlate to nature's continuum of rarity. To learn more about laboratory-grown diamonds, including how GIA differentiates them from natural diamonds, scan the QR code or visit diamond.gia.edu/ENR1603.

This report is not a guarantee or valuation. For additional information and important limitations and disclosures, please see GIA references or call 1-800-421-7283 or visit gia.edu. ©2021 Gemological Institute of America, Inc.

Get brilliant about your laboratory-grown diamonds with
GIA's new digital LGDR report, now with full color and clarity specifications.

LGDR by  **GIA**[®]

LEARN MORE
GIA.edu/aboutlgdr



PURPLE GEM SPINEL FROM VIETNAM AND AFGHANISTAN: COMPARISON OF TRACE ELEMENT CHEMISTRY, CAUSE OF COLOR, AND INCLUSIONS

Philippe M. Belley and Aaron C. Palke

This study compares two purple gem spinel samples with regard to trace element chemistry and visible light absorption spectra, and presents the first reported example of a spinel with a saturated purple color caused predominantly by chromium and cobalt. Sample VN, from a placer deposit in the Luc Yen district of Vietnam, exhibited strong saturation, orange-red fluorescence in UV, and magnesite and graphite inclusions. Sample AF was from Badakhshan, Afghanistan, with light to medium saturation and containing phlogopite, amphibole, and probable fluid inclusions. UV-Vis-NIR spectra are compared along with trace element chemistry. Sample VN is colored primarily by cobalt (17.9 ppma) and chromium (593 ppma), with minor color contribution from Fe (2437 ppma), and contains significantly more cobalt than typical Cr-enriched red, pink, and purple gem spinels (<6 ppma Co). The dominant contributions of chromophores Cr^{3+} and Co^{2+} to the color of sample VN are responsible for its higher color saturation than that of sample AF, which is colored dominantly by Fe^{2+} and Fe^{3+} (3089 ppma total Fe) and contains negligible concentrations of other chromophores (<10 ppma V^{3+} , Cr^{3+} , and Co^{2+}). In the Vietnamese purple spinel, the relatively low Fe concentration is likely crucial in creating the attractive saturated color. This sample is enriched in Co, Ni, Cr, V, Zn, and Ga. In contrast, the purple spinel from Afghanistan is relatively impoverished in all trace elements except Fe and Mn. Sample VN represents an approximate intermediate between natural gem spinel populations colored dominantly by Cr^{3+} vs. dominantly by Co^{2+} . Cr^{3+} -, (Fe^{2+} , Fe^{3+})-, and Co^{2+} -dominant (in terms of color) gem spinels are easily differentiated by chemical composition using a discrimination plot of Co/Cr vs. Co/Fe, but this is not valid for spinel dominantly colored by V^{3+} or containing significant concentrations of Fe.

Gem-quality spinel occurs in a variety of colors as a result of a diverse array of possible chromophores and chromophore combinations (Schmetzer et al., 1989; Andreozzi et al., 2019): combinations of Fe^{2+} and Fe^{3+} (light blue/violet to green to black with increasing Fe concentration; Hålenius et al., 2002); Co^{2+} (blue; Shigley and Stockton, 1984; D'Ippolito et al., 2015); Cr^{3+} (red); and V^{3+} (orange; Andreozzi et al., 2019). Vivid spinels colored by cobalt (blue) and chromium (red) are particularly sought after in the gem trade. Purple spinel (figure 1) is generally colored by Fe or by a combination of Cr, V, and

subordinate Fe (Andreozzi et al., 2019). The current study compares the chemical composition and color of two purple spinel samples, from Vietnam and Afghanistan (figure 2), to each other and in the

In Brief

- A purple sample from the Luc Yen district of Vietnam is colored primarily by Co^{2+} and Cr^{3+} , with only minor contribution of Fe^{2+} and Fe^{3+} to visible light absorption.
- In contrast, a purple spinel from Badakhshan, Afghanistan, is colored exclusively by Fe^{2+} and Fe^{3+} , containing negligible concentrations of other chromophores.
- Purple coloration of spinel caused by a combination of Co^{2+} and Cr^{3+} is more saturated than that caused by $\text{Fe}^{2+}/\text{Fe}^{3+}$.

See end of article for About the Authors and Acknowledgments.

GEMS & GEMOLOGY, Vol. 57, No. 3, pp. 228–238,

<http://dx.doi.org/10.5741/GEMS.57.3.228>

© 2021 Gemological Institute of America



Figure 1. The vivid colors seen in fine gem-quality spinel are derived from the mixing between multiple different chromophores in a range of ratios and concentrations, as in this fine 13.52 ct violetish purple spinel. Courtesy of the Dr. Edward J. Gübelin Collection. Photo by Robert Weldon/GIA.



Figure 2. Map of Asia showing the geographic origin of the two spinel samples: Badakhshan Province in Afghanistan and the Luc Yen district of Vietnam.

broader context of all gem spinel. One is a saturated purple sample from a placer deposit near Khao Ka in the Luc Yen district of Vietnam (figure 3). The second

sample is a purple spinel with light to medium saturation, mined from a marble-hosted deposit in Badakhshan, Afghanistan (figure 4).

Figure 3. This placer deposit, the source of sample VN, is situated in rice paddies at Khao Ka in the Luc Yen district of Vietnam. Photo courtesy of Geir Gussiås (Balder Gems), 2017.





Figure 4. The purple spinel deposit in Badakhshan, Afghanistan. Photo courtesy of Ikram Muhammad and ANAAR Gems, 2017.

MATERIALS AND METHODS

Materials. The Vietnamese spinel (sample VN, figure 5) was acquired from Geir Atle Gussiås and Mai Tran of Balder Gems. They purchased it from miners onsite at the Khao Ka alluvial deposit, northeast of Nà

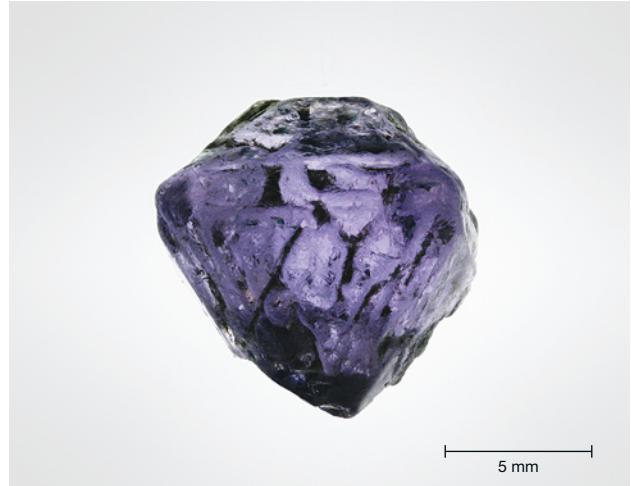
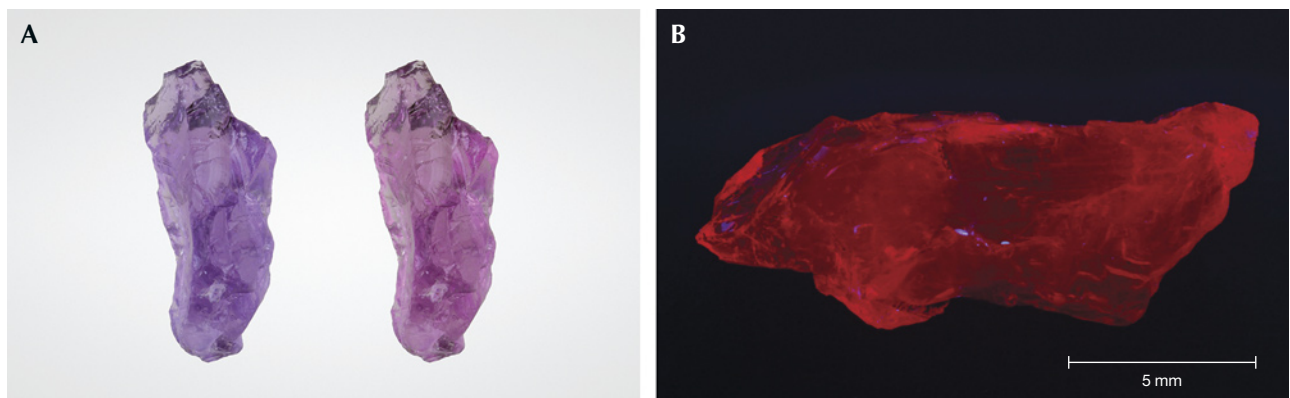


Figure 6. Spinel sample AF from Badakhshan, Afghanistan. Photo by Aaron Palke.

Hà, An Phú, in the Luc Yen district (approx. 21°58'54.37" N, 104°50'44.77" E; see also Chauviré et al., 2015). Mr. Gussiås suspected that the spinel sample was enriched in both cobalt and chromium due to its unusual color; he has reported a similarly saturated purple stone, faceted and just under 2 ct from the same placer locality. The Luc Yen region is underlain by supracrustal metamorphic rocks including significant quantities of marble, the typical source rock for gem spinel (Chauviré et al., 2015 and references therein). The purple spinel (sample AF, figure 6) from a metacarbonate outcrop in the Badakhshan Province of Afghanistan (the "Parawara mine" in Boehm, 2017) was mined in 2017 and donated by gem and mineral dealer Ikram Muhammad. Samples VN

Figure 5. Spinel sample VN from the Luc Yen district, Vietnam (12.5 × 5.0 mm). A: In daylight (left) and incandescent (right) illumination. B: In long-wave UV (365 nm). Photos by Aaron Palke.



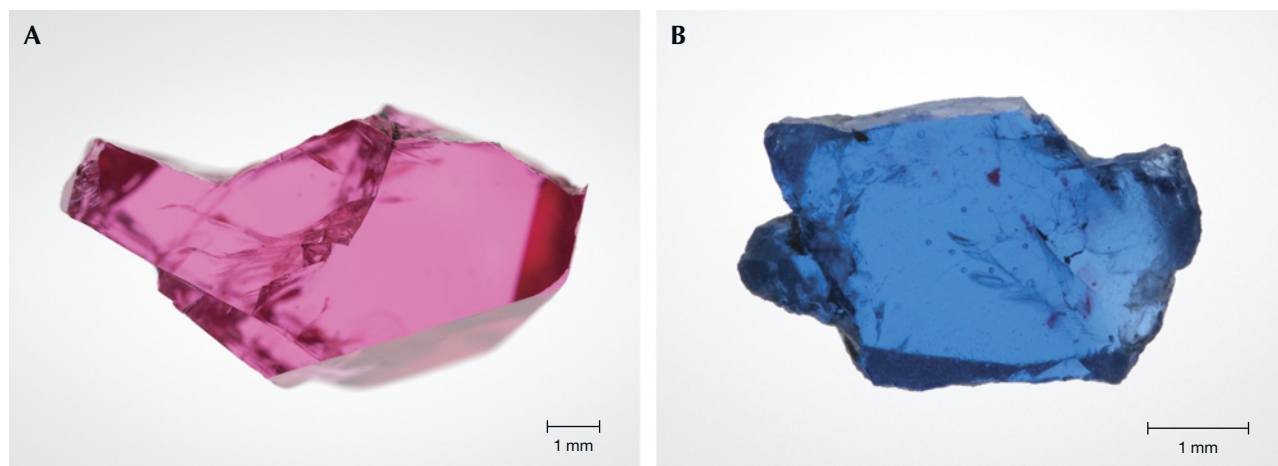


Figure 7. GIA reference samples GIA-Cr (A, 2.641 mm thick) and GIA-Co (B, 1.053 mm thick). Photos by Aaron Palke.

and AF were flat-polished for UV-Vis spectrometry at GIA's Carlsbad laboratory, with thicknesses of 2.155 mm and 4.486 mm, respectively.

Two spinel samples from the GIA collection provided reference UV-Vis spectra of Co^{2+} -dominant, and Cr^{3+} -dominant spinel color end members for use in assessing the color contribution of these chromophores in sample VN. The spinel dominantly colored by Cr^{3+} is vivid pink (GIA sample 100305165116, 2.641 mm thick, named "GIA-Cr"; figure 7A) and the spinel dominantly colored by Co^{2+} is vivid blue (GIA sample 100305162587, 1.053 mm thick, named "GIA-Co"; figure 7B).

Methods. Electron Probe Microanalysis (EPMA). For EPMA analysis, the samples were mounted in epoxy pucks and polished. Chemical compositions were obtained with a JEOL JXA-8230 electron microprobe (University of Ottawa) in wavelength-dispersion (WD) mode. The operating voltage was 20 kV, with 20 nA beam current and 5 μm beam diameter. Counts were collected for 20 seconds for each element. The following standards were used (all $K\alpha$): hematite (Fe), chromite (Cr, Co, Al, Mg), rutile (Ti), tephroite (Mn), pentlandite (Ni), vanadinite (V), and gahnite (Zn). Matrix correction calculations were performed using the Armstrong/Love-Scott $\varphi(\rho Z)$ method (Armstrong, 1988). Limits of detection were 0.01 wt.% (MgO , Al_2O_3), 0.02 wt.% (V_2O_3), and 0.03 wt.% (Cr_2O_3 , FeO, CoO, NiO, MnO).

Trace Element Analysis. Laser ablation–inductively coupled plasma–mass spectrometry (LA-ICP-MS) analyses of samples VN and AF were performed using a 193 nm ArF excimer laser ablation system (ASI Aus-

tralia RESOLUTION M-50-LR) connected to an Agilent 7700x quadrupole ICP-MS at the Pacific Centre for Isotopic and Geochemical Research at the University of British Columbia in Vancouver, Canada. Measurements were performed for 40 s at a laser repetition rate of 5 Hz, 20 ns pulse width, using a spot size of 89 μm . On-sample fluence was 3 J/cm^2 . Ablation was carried out under a helium atmosphere. A mixture of He (from the sample cell) and Ar served as carrier gas and was admixed with N_2 for signal enhancement. The mass spectrometer was tuned for sensitivity, $\text{ThO}/\text{Th} < 0.2\%$ and a mass bias with $238/232 \approx 101\%$. Spots were pre-ablated to remove surface contamination, followed by 40 s of ablation and a 30 s washout time. The following masses were collected: ^7Li , ^9Be , ^{11}B , ^{49}Ti , ^{51}V , ^{53}Cr , ^{55}Mn , ^{56}Fe , ^{59}Co , ^{60}Ni , ^{67}Zn , and ^{69}Ga . Measurements on the following elements were collected but not detected in the spinel samples: Sc, Cu, Sr, Y, Zr, Hf, Ta, and rare earth elements. Calibration was carried out by standard-sample bracketing using the silicate glass SRM NIST 610 as the external standard and ^{25}Mg as the internal standard using values from EPMA (table 1). USGS basalt glass reference material BCR-2G (Rocholl, 2007) was cross-checked for quality control and was within the range consistent with values in the GeoReM database (Jochum et al., 2005). The coefficient of variation for individual trace element measurements in BCR-2G is $\leq 6\%$, with the exception of Be (~11%) and B (~38%). Measured B concentrations varied unpredictably despite drift correction, and thus the data was rejected. Data reduction was performed using the Iolite v.3.0 software (Paton et al., 2011).

LA-ICP-MS trace element data was collected for samples GIA-Cr and GIA-Co at GIA using a Thermo

TABLE 1. EPMA analyses of chemical composition in purple spinel samples.

Sample no.	VN		AF	
Color	Purple		Purple	
Origin	Khao Ka, Vietnam		Badakhshan, Afghanistan	
No. of spots	4		3	
	Weight %	SD	Weight %	SD
MgO	26.17	0.10	26.69	0.09
Al ₂ O ₃	70.85	0.25	71.50	0.14
TiO ₂	0.01	0.01	0.01	0.01
V ₂ O ₃	0.03	0.01	<0.02	
Cr ₂ O ₃	0.22	0.02	<0.03	
MnO	<0.03		<0.03	
FeO	0.86	0.02	1.08	0.01
CoO	<0.03		<0.03	
NiO	<0.03		<0.03	
ZnO	1.44	0.05	<0.03	
Total	99.58		99.28	
Normalized to 32 oxygens				
Mg	7.504		7.620	
Al	16.062		16.137	
Ti	0.001		0.001	
V	0.005		—	
Cr	0.033		—	
Mn	—		—	
Fe	0.138		0.173	
Co	—		—	
Ni	—		—	
Zn	0.205		—	
Σ _{cations}	23.948		23.931	

SD = standard deviation

Limits of detection (wt.%): 0.01 (MgO, Al₂O₃), 0.02 (V₂O₃), and 0.03 (Cr₂O₃, FeO, CoO, NiO, MnO)

iCap-Q ICP-MS coupled to an Elemental Scientific Lasers NWR213 nm laser ablation system with a frequency-quintupled Nd:YAG laser (213 nm wavelength with 4 ns pulse width). Ablation was carried out with 55 μm spot sizes with fluence around 8±1 J/cm² and a 15 Hz repetition rate. NIST 610 and 612 glasses were used as external standards with ²⁴Mg set as the internal standard with a value assigned at 17.08 wt.%. Masses analyzed include ⁷Li, ⁹Be, ⁴⁷Ti, ⁵¹V, ⁵²Cr, ⁵⁵Mn, ⁵⁶Fe, ⁵⁹Co, ⁶⁰Ni, ⁶⁶Zn, and ⁶⁹Ga. The trace element compositions of GIA reference samples are reported in table 2.

Parts per million by weight (ppmw) values were converted to parts per million atoms (ppma) using the following formula:

$$[\text{ppma}] = [\text{ppmw}] \times (\text{mol. wt. of spinel}) / (7 \times \text{atomic wt. of element})$$

where 7 is the total number of atoms in one formula unit of spinel.

Spectrophotometry. Ultraviolet/visible/near-infrared (UV-Vis-NIR) absorption spectra were measured using a custom-built setup equipped with an Ocean Optics HR4000 CCD spectrometer and an Avantes light source incorporating both halogen and deuterium light sources. Light was transmitted to the sample placed at the entrance to an integrating sphere and then to the detector using fiber-optic cables. Data was collected with one accumulation using an integration time of 10 s at wavelength interval of 0.76 nm and spectral resolution of 0.90 nm from 300 to 800 nm.

Reference Spectra and Absorption Peak Assignment.

The UV-Vis spectrum for purple spinel sample VN was compared to two reference spectra: a Cr-dominant spinel spectrum (vivid pink, GIA-Cr) and a Co-dominant spinel spectrum (vivid blue, GIA-Co). The spectra were selected for their highly dominant absorption signature by the chromophore of interest with negligible absorption by other chromophores. The spectra contain very small Fe²⁺ absorption peaks that were imperceptible when the spectra were scaled down for data processing.

The reference chromophore absorption peaks (wavelength in nm) are averages for Mg-Al spinel samples reported by Andreozzi et al. (2019) and D'Ipp-

TABLE 2. LA-ICP-MS analyses of trace element concentrations in samples used for Cr and Co reference spectra.

Sample	GIA-Cr			GIA-Co			Detection limit
Color	Vivid pink			Vivid blue			
No. of spots	6			3			
	Avg.	Avg.	SD	Avg.	Avg.	SD	
	ppmw	ppma	ppma	ppmw	ppma	ppma	ppmw
Li	11.0	32.1	1.5	112	330	62	0.08
Be	2.27	5.1	0.5	2.98	6.75	3.22	0.58
Ti	97.5	41.4	3.1	72.8	31.1	1.4	0.4
V	176	70.2	5.4	131	52.6	1.1	0.08
Cr	3640	1423	80	197	77.3	7.6	0.9
Mn	8.7	3.2	0.3	137	50.8	1.2	0.2
Fe	127	46.1	3.1	7030	2570	70	5
Co	bdl	bdl		569	197	6	0.02
Ni	bdl	bdl		1115	388	52	0.04
Zn	358	111	9	819	256	30	0.3
Ga	35.4	10.3	0.8	152	44.7	5.3	0.04

SD = standard deviation

bdl = below detection limits

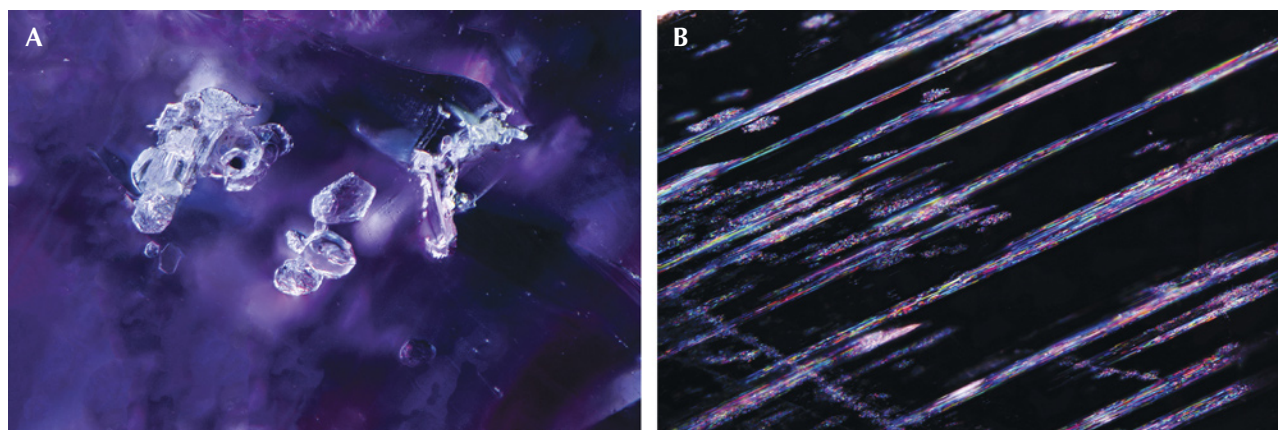


Figure 8. Inclusion scenes in spinel sample VN. A: Magnesite crystals that occasionally coexist in composite inclusions along with graphite (field of view 1.26 mm). B: Needle-like inclusions (field of view 3.57 mm). Photomicrographs by Aaron Palke.

polito et al. (2015; cobalt only): ($^M\text{Cr}^{3+}$) 349.4365, 387.3352, 420.9564, 531.5635, 570.5204; ($^M\text{V}^{3+}$) 394.2329, 541.0837; ($^M\text{Fe}^{3+}$) 458.5660, 476.2484; ($^T\text{Fe}^{2+}$) 374.2733, 386.7225, 406.9652, 554.5731, 587.8204, 798.6127; ($^T\text{Mn}^{2+}$) 428.2166; ($^T\text{Co}^{2+}$) 552.6287, 588.0105, 630.7159.

Raman Spectroscopy Analysis. Raman spectra of inclusions in the spinels were collected with a Renishaw inVia Raman microscope system. The Raman spectra of the inclusions were excited by a Stellar-REN Modu Ar-ion laser producing highly polarized light at 514 nm and collected at a nominal resolution of 3 cm^{-1} in the $2000\text{--}200\text{ cm}^{-1}$ range. Each spectrum was accumulated three times with a collection time of 10 s at $20\times$ or $50\times$ magnification. In many cases the confocal capabilities of the Raman system allowed inclusions beneath the surface to be analyzed.

RESULTS

Sample Descriptions. Samples VN and AF are transparent with few inclusions. Sample VN, 3 mm in thickness (later polished to 2.155 mm), had a medium tone, strong saturation, purple hue, weak to moderate orange-red fluorescence under long-wave (365 nm) ultraviolet radiation, and a very slight color change between daylight (standard 6500 K fluorescent bulb) and incandescent illumination (standard halogen incandescent bulb at $\sim 2700\text{ K}$); see figure 5, A and B. Sample AF, 5 mm in thickness (later polished to 4.486 mm), had a medium tone, moderate saturation, and purple hue (figure 6) and was nonfluorescent when exposed to long- and short-wave UV.

Inclusions. The purple spinel from Vietnam contained several distinct mineral inclusions. Raman spectroscopy allowed the identification of several black platelets as graphite and several colorless minerals as magnesite, which are also known to occur in red gem spinel from Vietnam (Malsy et al., 2012). Occasionally, composite inclusions of graphite and magnesite were seen (figure 8A). Additional inclusions in sample VN were observed but could not be positively identified with Raman, such as platelet-like colorless crystals (potentially phlogopite crystals) and needle-like inclusions that resembled rutile inclusions (figure 8B) seen in other gem minerals. Among the inclusions seen in the Afghan spinel were fields of negative crystals (presumably hosting fluid inclusions), tiny black dust-like particles, and colorless mineral inclusions. Some of these inclusions were identified by Raman spectroscopy as phlogopite. The elongate inclusion in figure 9 was identified by Raman spectroscopy as an amphibole-group mineral, but the peaks overlapped with the background spinel signal, precluding conclusive amphibole species identification.

Chemical Composition. Spinel compositions were measured using EPMA and LA-ICP-MS, where the EPMA data (table 1) is used to provide major and minor element composition, including Mg for use as an internal standard for LA-ICP-MS.

The purple spinel from Vietnam (sample VN) contained significant concentrations of multiple chromophores (table 3): 593 ppma Cr, 17.9 ppma Co, 84.8 ppma V, and 2437 ppma Fe. The purple spinel from Afghanistan (sample AF) was very poor by comparison in most chromophore elements—namely Ni, Zn,

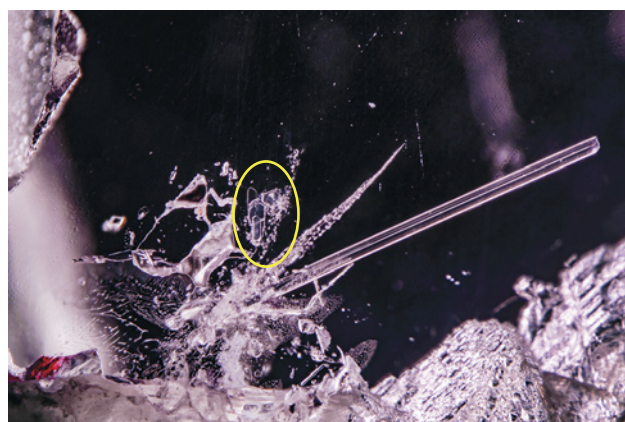


Figure 9. Pseudo-hexagonal platelets of phlogopite (circled in yellow) and secondary fluid inclusions, together with a prismatic amphibole, in spinel sample AF. Photomicrograph by Aaron Palke; field of view 4.79 mm.

and Ga—but contained more Fe (3089 ppma) and Mn (56.8 ppma).

Absorption Spectra. In the absorption spectrum of sample VN, two transmission windows occurred between ~430 and 510 nm (blue-green range of visible spectrum), and above 650 nm (red range of the visible spectrum). The absorption was characterized by two broad peaks centered at approximately 390 and 545 nm, in addition to a characteristic cobalt peak at ~630 nm (figure 10). The absorption spectrum profile for the purple spinel from Afghanistan was flatter than for the Vietnamese sample, with peaks at 558 nm (broad), 383 nm, 370 nm, two small peaks at 455 and 475 nm in the trough between the former, and a significant and rapid increase in absorption at wavelengths below 360 nm (figure 10). The absorption bands are consistent with those of iron (D’Ippolito et al., 2015).

DISCUSSION

Color. Sample VN had characteristic absorption maxima attributed to Cr³⁺ at ~530 and ~390 nm; Co²⁺ at ~620 nm (the reference absorption is 630 nm, from D’Ippolito et al., 2015); and ¹Fe²⁺ (shoulder at ~370 nm; figure 10; Andreozzi et al., 2019). To better illustrate the color contribution of cobalt and other chromophores in this Vietnamese purple spinel, reference spectra of spinels colored by Co²⁺ and Cr³⁺ were used to perform scaled subtractions from the VN spectrum (reference peaks for Co²⁺ at ~620 nm and Cr³⁺ at ~389 nm; similar to the method of Palke and Sun, 2018). The reference spectra (GIA-Co and GIA-Cr) showed imperceptible color contributions by other

chromophores when scaled down for the subtraction, and therefore they did not noticeably reduce peaks from other chromophores in the resulting difference. The resulting subtracted spectra (figure 11) clearly demonstrated that sample VN was dominantly colored by both Co²⁺ and Cr³⁺, while the color contribution by ¹Fe²⁺ (e.g., the peak at 374 nm) was present but negligible. Color contribution by V³⁺ is possible and difficult to quantify due to peak overlaps with Cr³⁺, but when present it is relatively minor (see for example, absorption spectra of Cr-V-bearing spinels in Malsy and Klemm, 2010). A notable feature of the VN absorption spectrum is a relatively prominent “shoulder” at ~620 nm, which demonstrates a noteworthy effect of Co²⁺ on the color of this purple spinel even without data processing. Sample VN is the first described example of natural purple spinel in which both Cr³⁺ and Co²⁺ are the prominent contributors to the coloration and are roughly equally weighted (e.g., similar absorption peak heights above background for each chromophore, resulting in a distinctly purple hue), as opposed to Cr³⁺-(Fe²⁺, Fe³⁺)-dominant or Fe (Fe²⁺, Fe³⁺) alone (e.g., Schmetzer et al., 1989; Malsy and Klemm, 2010). Kuksa et al. (2019) presented compositional data and a photograph of a Vietnamese spinel described as “bluish” (within the reference sample known as sample 5), which ap-

TABLE 3. LA-ICP-MS analyses of trace element concentrations in purple spinel samples.

Sample Color	VN			AF			Detection limit
	Purple			Purple			
No. of spots	4			3			
	Avg. ppmw	Avg. ppma	SD ppma	Avg. ppmw	Avg. ppma	SD ppma	ppmw
Li	23	69	1	13	39	2	0.5
Be	10	23	2	2	5	1	0.9
Ti	31.6	13.6	1.9	37.3	15.9	2.1	5.8
V	210	84.8	3.5	22.9	9.2	0.7	0.3
Cr	1499	593	39	6.3	2.5	0.5	5.4*
Mn	89.9	33.7	0.6	152.8	56.8	0.7	4.8
Fe	6617	2437	24	8447	3089	10	5.2
Co	51.4	17.9	0.3	5.6	1.9	0.1	0.2
Ni	35.6	12.5	0.7	13.3	4.6	0.3	1.6
Zn	10510	3310	110	214	67	5	7.3
Ga	302	89	1	97	28	1	0.3

SD = standard deviation

Sc <1.5 ppmw, Cu <0.7 ppmw

*Cr detection limit for sample AF = 4.3 ppmw

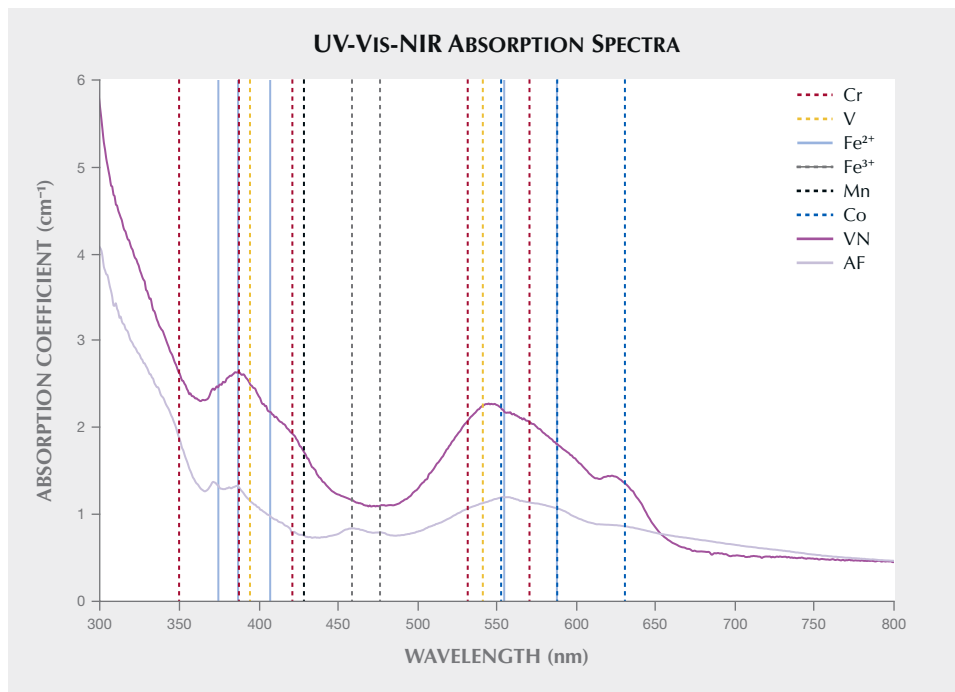


Figure 10. UV-Vis-NIR absorption spectra of spinel samples VN (purple) and AF (light purple). Chromophore absorption bands after D'Ippolito et al., 2015 (Co²⁺) and Andreozzi et al., 2019 (other elements).

peared vivid blue with a slight purplish hue in the figure. This sample appeared dominantly colored by cobalt with subordinate chromium, and its chemical composition is discussed further below.

Purple spinel sample VN has a higher color saturation than purple sample AF (colored by ^TFe²⁺

with minor ^MFe³⁺), which is shown by the greater peak-trough difference in absorption spectrum (figure 10). This is evidently due to the greater visible light absorption by Cr³⁺ and particularly Co²⁺ per unit of concentration compared to the predominant iron chromophore, Fe²⁺ (e.g., ~20× molar absorptiv-

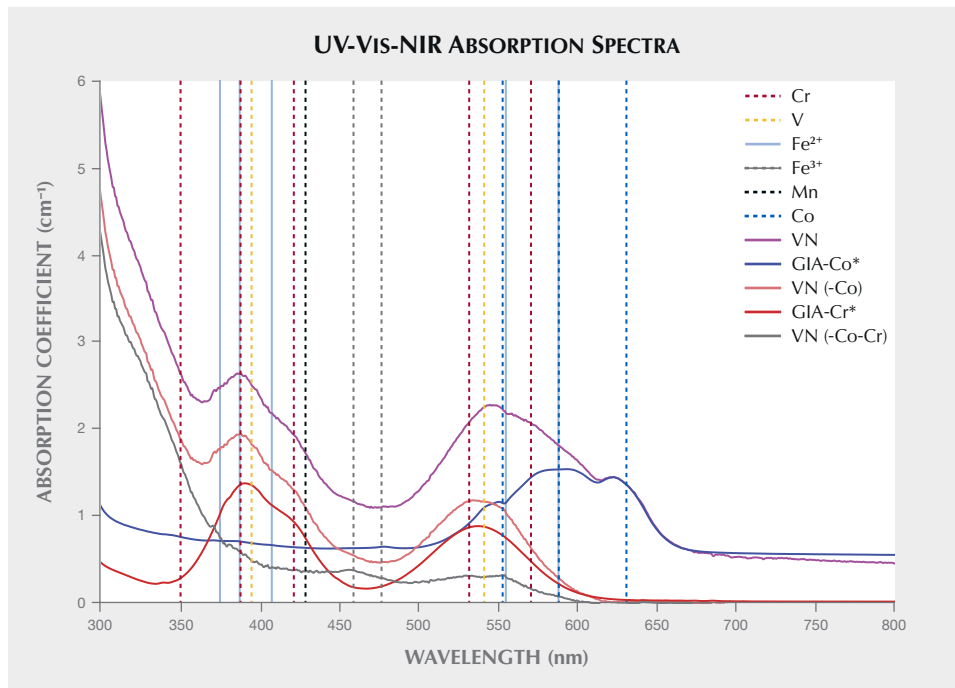


Figure 11. UV-Vis-NIR absorption spectra for VN (purple), VN with scaled subtraction of a reference spectrum of Co-bearing vivid blue spinel (pink), and scaled subtraction of both Co-rich and Cr-rich spinel reference spectra (gray). The Co-dominant (GIA-Co, scale factor 0.095, blue) and Cr-dominant (GIA-Cr, scale factor 0.082, red) spectra are included for comparison. Chromophore absorption bands after D'Ippolito et al., 2015 (Co) and Andreozzi et al., 2019 (other elements).

ity of Co^{2+} relative to Fe^{2+} , Chauviré et al., 2015), but could also be accentuated by VN's red fluorescence. Therefore, the combination of elevated cobalt (17.9 ppma) and chromium (593 ppma) concentrations as the dominant chromophores result in an attractive purple color that is more saturated, with stronger red and blue hues, than spinel colored primarily by Fe^{2+} . Sample 3 from Kuksa et al. (2019), a brownish purplish red spinel from Vietnam, also serves as an interesting comparison to purple sample VN. Sample 3 contained a similar concentration of Cr, slightly over half the Co concentration, and four times the Fe concentration. Unlike sample VN, which is purple primarily due to Cr and Co, Kuksa et al.'s sample 3 was brownish purplish red, likely representative of a color defined primarily by Cr and Fe. Kuksa et al. (2019), did not measure light absorption, so the causes of color have not been quantified.

Spinel sample VN represents the "missing link" in Schmetzer et al.'s (1989) spinel color/chromophore diagram, being roughly intermediate between the red (Cr^{3+}) and blue (Co^{2+}) end members.

Chromophore Trace Elements in Gem Spinel.

Cobalt-enriched spinel, generally vivid blue in color, typically contains low Cr concentrations (<60 ppma; Hanser, 2013; Chauviré et al., 2015; Kuksa et al., 2019), with two outliers known from Vietnam. One Cr-rich outlier (1111 ppma Cr and 1236 ppma Co; Chauviré et al., 2015) reported from Vietnam is vivid blue in color with no visible reddish or purplish hues, indicating that cobalt has a much higher molar absorptivity than chromium, similar to cobalt's higher molar absorptivity relative to iron (Chauviré et al., 2015). The other outlier, sample 5 of Kuksa et al. (2019), has a vivid slightly purplish blue color. Purple spinel sample VN appears to be approximately compositionally intermediate between Cr-dominant pink/red spinels and Co-dominant blue spinels, whereas sample 5 is intermediate between sample VN and Co-dominant blue spinels, as shown in a plot comparing the relative concentrations of Co to Cr, and Co to Fe (figure 12).

Most Cr-enriched spinels (red, pink, magenta, and orange gem spinels) are very poor in cobalt (Co <6 ppma; Malsy and Klemm, 2010), and thus their color is largely determined by Cr^{3+} , V^{3+} , and Fe (Fe^{2+} , Fe^{3+}) concentrations (Schmetzer et al., 1989; Androzzzi et al., 2019). Among spinel trace element compositions recorded in the scientific literature, only Kuksa et al.'s (2019) sample 3 has a cobalt-to-chromium ratio

similar to that of sample VN. However, their sample 3 is poorer in cobalt overall (10.6 ppma) and four times richer in iron than VN. Thus, sample VN is primarily an intermediate between a Cr-dominant red spinel and a Co-dominant blue spinel, while sample 3 is intermediate between spinels having Cr^{3+} and Fe (Fe^{2+} , Fe^{3+}) as the dominant chromophores, respectively. This also correlates with their relative positions in a chemistry-based discrimination plot (figure 12). Unlike Kuksa et al.'s sample 3, VN has a sufficiently high Co^{2+} concentration and low Fe (Fe^{2+} , Fe^{3+}) concentration so as to be colored strongly saturated purple with an absorption spectrum showing clear characteristic absorption maxima from both Cr^{3+} and Co^{2+} .

While sample VN plots intermediate to Cr-dominant and Co-dominant spinels in a plot of Co/Cr vs. Co/Fe (figure 12), sample AF plots in the iron-dominant portion (Cr-poor, high Co/Cr, low Co/Fe). Overall, gem spinels appear to be easily differentiated according to dominant chromophores using a chemical discrimination plot of Co/Cr vs. Co/Fe, although this plot will not work well for spinel in which V^{3+} is the dominant chromophore, or for spinel based on $\text{Fe}^{2+}/\text{Fe}^{3+}$ relative abundance or with elevated Fe concentrations (e.g., green and black Fe-rich spinels; Hålenius et al., 2002).

CONCLUSIONS

The purple spinel sample from the Khao Ka placer deposit in the Luc Yen district of Vietnam (sample VN) was colored primarily by cobalt (17.9 ppma) and chromium (593 ppma), with minor iron (2437 ppma) and possibly vanadium (84.8 ppma). It contained significantly more cobalt than typical chromium-enriched gem spinels (<6 ppma Co). The similarly important contributions of cobalt and chromium to visible light absorption, the first such natural example to be reported, resulted in a purple of higher saturation than in the purple spinel sample from Afghanistan, which only had an iron chromophore (3089 ppma Fe; <10 ppma V, Cr, and Co). In the Vietnamese purple spinel, a relatively low iron concentration was also essential in creating an attractive saturated color, as shown by a comparison with a similar but more iron-rich spinel from the same region.

The purple spinel from Vietnam was enriched in chromium, cobalt, vanadium, gallium, and zinc relative to the sample from Afghanistan, which was poor in all chromophore elements with the exception of being slightly richer in iron and manganese.

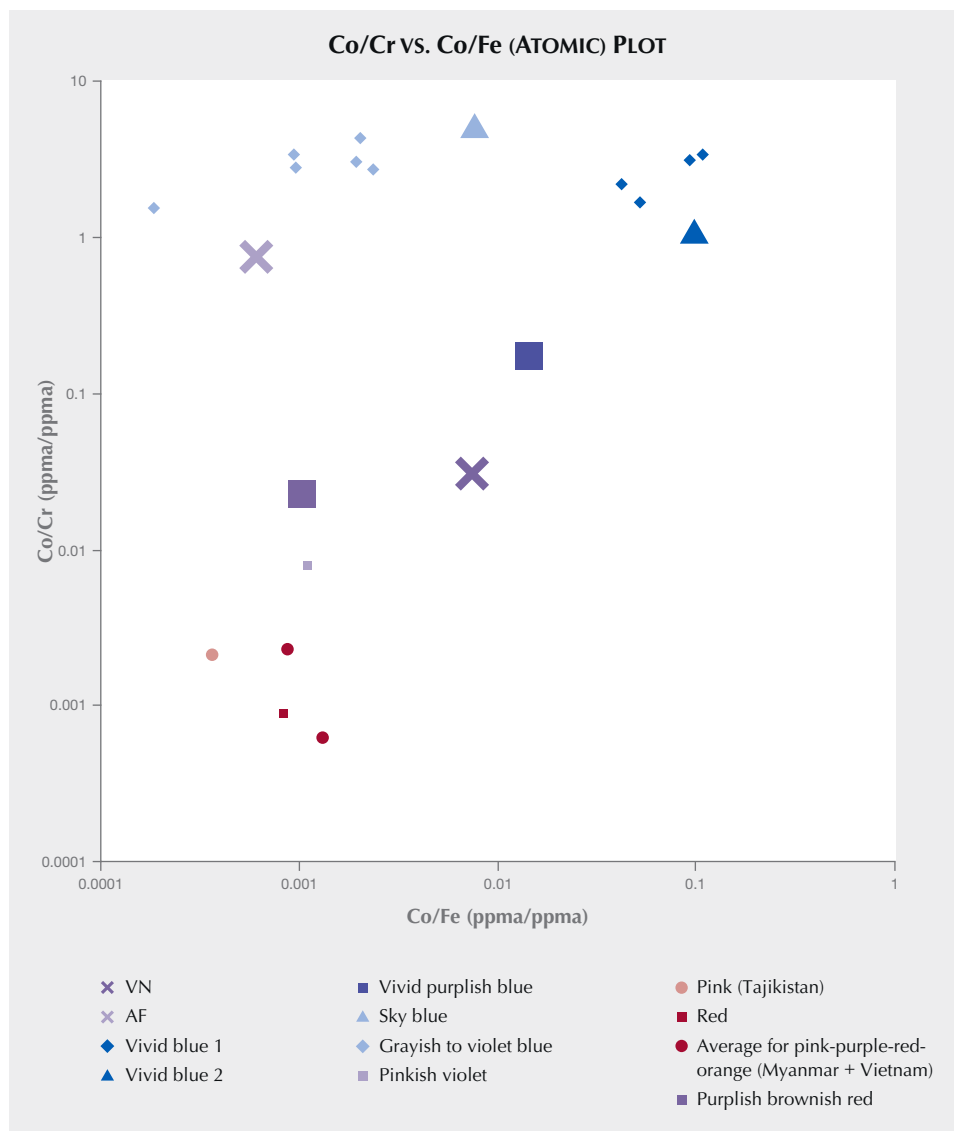


Figure 12. Co/Cr vs. Co/Fe (atomic) plot discriminating between spinel of different dominant chromophores, categorized by color category. Data sources: Vivid blue 1: Kuksa et al., 2019; Chauviré et al., 2015 (SATBLU); Hanser, 2013. Vivid blue 2: Sample GIA-Co (present study). Vivid purplish blue: Kuksa et al., 2019 (sample no. 5). Sky blue: Chauviré et al., 2015. Grayish to violet blue: Chauviré et al., 2015 (GREBLU); Hanser 2013; D'Ippolito et al., 2015 (Nat. 2). Pinkish violet: Kuksa et al., 2019 (sample no. 1). Pink (Tajikistan) and average for pink, purple, red, and orange spinel from Myanmar and Vietnam: Malsy and Klemm, 2010. Red: Kuksa et al., 2019. Purplish brownish red: Kuksa et al., 2019 (sample no. 3). Sample GIA-Cr is excluded from the plot due to being an extreme outlier with $Co/Cr < 4.85 \times 10^{-6}$.

The Vietnamese purple spinel represents an approximate intermediate between natural spinel populations colored dominantly by chromium and those colored dominantly by cobalt. A vivid purplish blue spinel from Vietnam reported by previous authors represents an intermediate more strongly weighted

toward cobalt. Gem spinels of different colors are easily differentiated by chemical composition using a discrimination plot of Co/Cr vs. Co/Fe, but this is valid for spinel not dominantly colored by V^{3+} or containing elevated concentrations of Fe (e.g., green and black Fe-rich spinel).

ABOUT THE AUTHORS

Dr. Belley is an assistant professor in the Department of Earth Sciences at Memorial University of Newfoundland in St. John's, Canada. Dr. Palke is senior manager of research at GIA in Carlsbad, California.

ACKNOWLEDGMENTS

Helpful comments from the peer reviewers improved the quality of the manuscript. We thank the Gübelin Gem Lab (Lucerne, Switzerland) for assistance and use of facilities for preliminary spectroscopic analyses. We are grateful to Marg Amini (University of British Columbia) for support with LA-ICP-MS, Ikram Muhammad for donating the spinel from Afghanistan, and Geir Gussiås for providing samples, information, and photographs.

REFERENCES

- Andreozzi G.B., D'Ippolito V., Skogby H., Hälenius U., Bosi F. (2019) Color mechanisms in spinel: a multi-analytical investigation of natural crystals with a wide range of coloration. *Physics and Chemistry of Minerals*, Vol. 46, No. 4, pp. 343–360, <http://dx.doi.org/10.1007/s00269-018-1007-5>
- Armstrong J.T. (1988) Quantitative analysis of silicate and oxide minerals: Comparison of Monte-Carlo, ZAF, and Phi-Rho-Z procedures. In D.E. Newbury, *Microbeam Analysis*, pp. 239–246.
- Bellefleur P.M., Groat L.A. (2019) Metacarbonate-hosted spinel on Baffin Island, Nunavut, Canada: Insights into the origin of gem spinel and cobalt-blue spinel. *Canadian Mineralogist*, Vol. 57, pp. 147–200.
- Boehm E. (2017) Gem Notes: Purple spinel from Badakhshan, Afghanistan. *Journal of Gemmology*, Vol. 35, No. 8, pp. 694–696.
- Chauviré B., Rondeau B., Fritsch E., Ressigeac P., Devidal J.-L. (2015) Blue spinel from the Luc Yen district of Vietnam. *G&G*, Vol. 51, No. 1, pp. 2–17, <http://dx.doi.org/10.5741/GEMS.51.1.2>
- D'Ippolito V., Andreozzi G.B., Hälenius U., Skogby H., Hametner K., Günther D. (2015) Color mechanisms in spinel: cobalt and iron interplay for the blue color. *Physics and Chemistry of Minerals*, Vol. 42, No. 6, pp. 431–439, <http://dx.doi.org/10.1007/s00269-015-0734-0>
- Hälenius U., Skogby H., Andreozzi G.B. (2002) Influence of cation distribution on the optical absorption spectra of Fe³⁺-bearing spinel s.s.–hercynite crystals: Evidence for electron transitions in ^{VI}Fe²⁺–^{VI}Fe³⁺ clusters. *Physics and Chemistry of Minerals*, Vol. 29, pp. 319–330, <http://dx.doi.org/10.1007/s00269-002-0240-z>
- Hanser C.S. (2013) Blue Co-spinel from Luc Yen, Vietnam: a spectroscopic study. Bachelor's thesis, University of Freiberg, Germany, 50 pp.
- Jochum K.P., Nohl U., Herwig K., Lammel E., Stoll B., Hofmann A.W. (2005) GeoReM: a new geochemical database for reference materials and isotopic standards. *Geostandards and Geoanalytical Research*, Vol. 29, No. 3, pp. 333–338, <http://dx.doi.org/10.1111/j.1751-908X.2005.tb00904.x>
- Kuksa K.A., Sokolov P.B., Marakhovskaya O.Y., Gussis G.A. (2019) Mineralogy, geochemistry and genesis of the Luc Yen noble spinel deposit, Vietnam. *Mineralogy*, Vol. 5, pp. 56–69, <http://dx.doi.org/10.35597/2313-545X-2019-5-3-56-69> [in Russian].
- Malsy A., Klemm L. (2010) Distinction of gem spinels from the Himalayan Mountain Belt. *Chimia*, Vol. 64, No. 10, pp. 741–746, <http://dx.doi.org/10.2533/chimia.2010.741>
- Malsy A.K., Karamelas S., Schwarz D., Klemm L., Armbruster T., Tuan D.A. (2012) Orange-red to orange-pink gem spinels from a new deposit at Lang Chap (Tan Huong-Truc Lau), Vietnam. *Journal of Gemmology*, Vol. 33, No. 1, pp. 19–27.
- Palke A.C., Sun Z. (2018) What is cobalt spinel? Unraveling the causes of color in blue spinels. *G&G*, Vol. 54, No. 3, p. 262.
- Paton C., Hellstrom J., Paul B., Woodhead J., Hergt J. (2011) Iolite: freeware for the visualization and processing of mass spectrometric data. *Journal of Analytical Atomic Spectrometry*, Vol. 26, No. 12, pp. 2508–2518, <http://dx.doi.org/10.1039/c1ja10172b>
- Rocholl A. (2007) Major and trace element composition and homogeneity of microbeam reference material: basalt glass USGS BCR-2G. *Geostandards and Geoanalytical Research*, Vol. 22, No. 1, pp. 33–45, <http://dx.doi.org/10.1111/j.1751-908X.1998.tb00543.x>
- Schmetzer K., Haxel C., Amthauer G. (1989) Colour of natural spinels, gahnospinel and gahnites. *Neues Jahrbuch für Mineralogie, Abhandlungen*, Vol. 160, pp. 159–180.
- Shigley J.E., Stockton C.M. (1984) 'Cobalt-blue' gem spinels. *G&G*, Vol. 20, No. 1, pp. 34–41, <http://dx.doi.org/10.5741/GEMS.20.1.34>



CONGRATULATIONS

This year, readers from all over the world participated in the 2021 *Gems & Gemology* Challenge. Entries arrived from around the world as readers tested their gemological knowledge by answering questions listed in the Spring 2021 issue. Those who earned a score of 75% or better received a GIA Certificate of Completion recognizing their achievement. Participants who scored a 96% or higher are listed below.

G&G Challenge Winners

Russia

Sergey Ivasenko

Ukraine

Nataliya Vovk

United Kingdom

Bingham Hendersen

Ana Lucia Tres

United States

Kenneth Fogelberg

Heather Gallacher

Jessica Kramer

Jana Miyahira-Smith

Tim Richardson

Shelly Verwymeren

Ryan Waddell

Answers

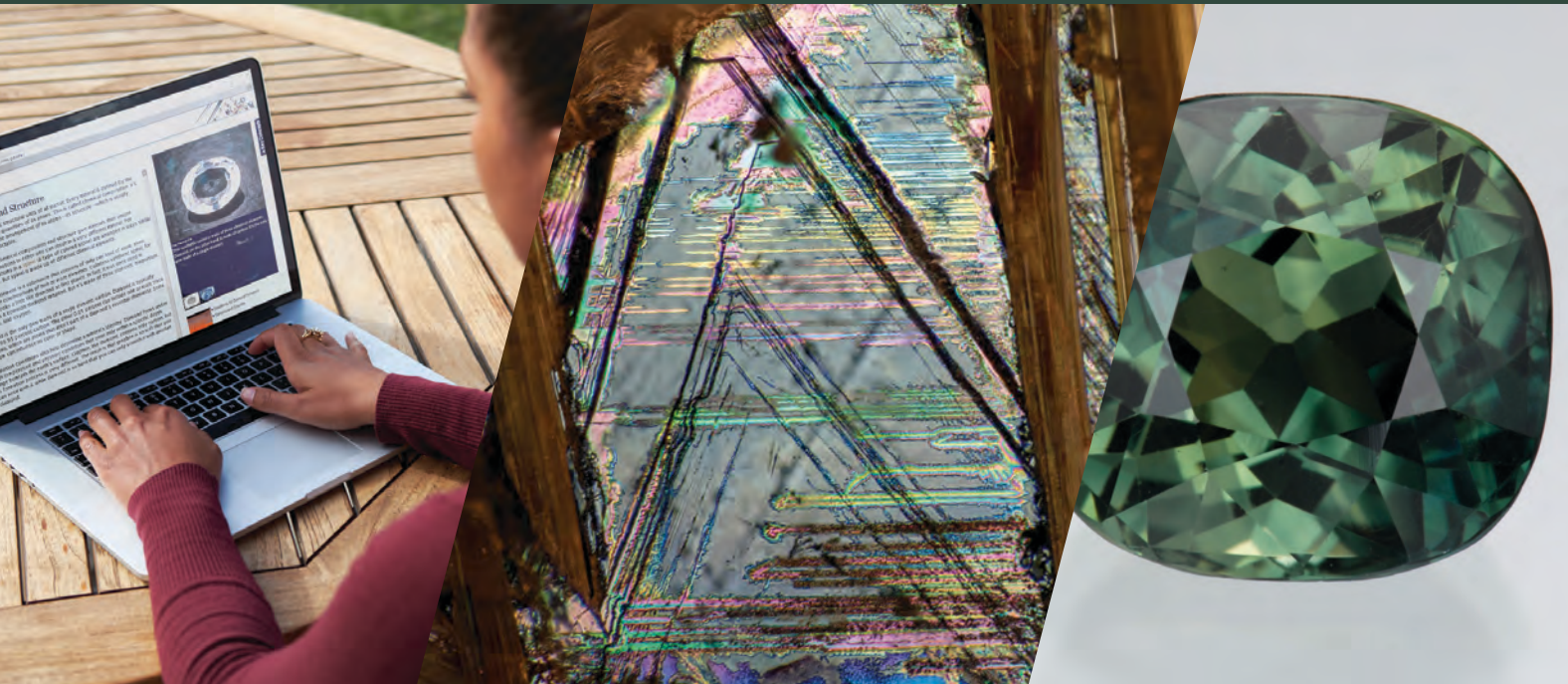
See pages 50–51 of the Spring 2021 issue for the questions.

1 (a), 2 (b), 3 (b), 4 (c), 5 (b), 6 (c), 7 (d), 8 (d), 9 (c), 10 (c), 11 (b), 12 (d), 13 (b),

14 (a), 15 (b), 16 (b), 17 (c), 18 (a), 19 (c), 20 (b), 21 (b), 22 (b), 23 (a), 24 (a), 25 (d)

CONTINUING EDUCATION

2022 Schedule
Coming Soon



Seminars Open to All

- Online & In-Person Seminars
- Developed for Gem and Jewelry Professionals
- GIA Alumni Receive a 10% Discount



GIA ALUMNI
ASSOCIATION™

GIA.edu/ContEd-Seminars

PERSIAN TURQUOISE: THE ANCIENT TREASURE OF NEYSHABUR

Bahareh Shirdam, Andy H. Shen, Mingxing Yang, Zahra Mokhtari, and Hamed Fazliani



Figure 1. This gold ring with a phoenix motif features a Neyshabur turquoise (13 × 17 mm), with a 0.02 ct ruby on each side and diamond accents. Courtesy of Taktala Jewelry, Tehran.

Turquoise is an opaque, blue to green gem material that has been worn, used, and appreciated by different civilizations for thousands of years. Originally called *piruzeh* in Persian, the gem has spiritual value in Persian culture is such that its name carries the meanings of victory, triumph, and prosperity. In Per-

sian literature, turquoise has been celebrated by poets, and various legends and beliefs are associated with it (Vinogradov et al., 1966).

Archeological discoveries from the Deh Luran Plain in western Iran indicate that turquoise was first utilized around 7000 BCE (Hole et al., 1969). The quantity of turquoise artifacts discovered in burial sites suggests the importance of this mineral in this ancient civilization's traditions. While the estimated age of these artifacts is valid, no scientific study has linked them to any specific deposit.

See end of article for About the Authors and Acknowledgments.

GEMS & GEMOLOGY, Vol. 57, No. 3, pp. 240–257,

<http://dx.doi.org/10.5741/GEMS.57.3.240>

© 2021 Gemological Institute of America

TABLE 1. Deh Luran Plain zones with evidence of turquoise ornaments.

Period	Chronology	Zone	Province
Neolithic	7000 BCE	Ali Kosh	Ilam
	6500 BCE	Mohamad-Djaffar	Ilam

The Neyshabur (Latinized as Nishapour) deposit is known for yielding turquoise with unique color and quality. This production has historically been known as “Persian turquoise” (figure 1), yet Iran’s turquoise deposits were never limited to Neyshabur. Other important mines include the Baghu deposit in southern Semnan Province and the Shahr-i Babak deposit in western Kerman Province, the latter of which was mentioned in Marco Polo’s *Book of the Wonders of the World* between 1390 and 1430 (Weisgerber, 2004).

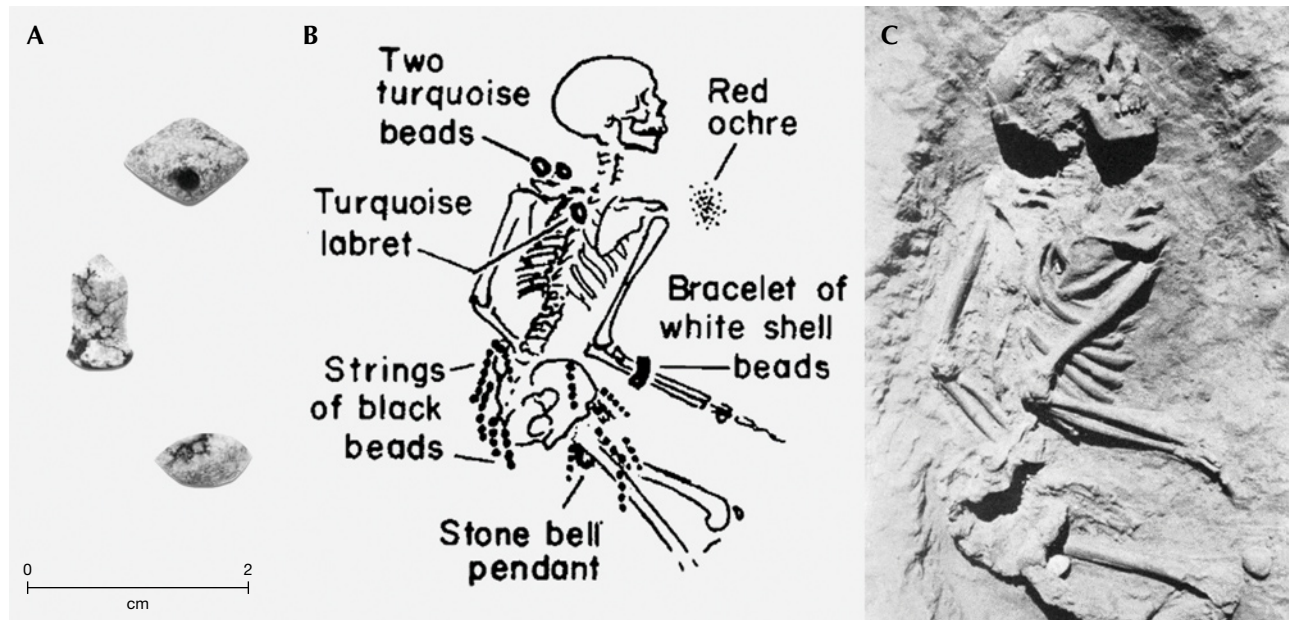
Located in the Razavi Khorasan Province of northeastern Iran, 53 km from the city of Neyshabur, the Neyshabur mine has produced the majority of Iranian turquoise for more than a millennium. Yet in recent decades there have been claims that the mine is on the verge of closure, that its turquoise quality has diminished, or that it is running out of material. Such claims often carry enormous weight with con-

sumers. After visiting the Neyshabur turquoise mine in 2020, a report was conducted on the current state of the mine. This article seeks to uncover the facts and offer objective insight on the current state of the Neyshabur turquoise mine.

According to Hole et al. (1969), the earliest Persian turquoise artifacts were discovered in the Deh Luran Plain in western Iran. Radiocarbon dating suggests that turquoise beads found in burial sites from the Ali Kosh and Mohamad-Djaffar zones date back to 7000 BCE and 6500 BCE, respectively (table 1).

These turquoise ornaments came in various forms such as beads, pendants, and piercings. The most interesting group of turquoise beads was associated with one of the burials from the Mohamad-Djaffar zone, where two beads and a piercing referred to as a labret were found (figure 2). The highly polished beads were found near the neck, and the labret lay near the breastbone.

Figure 2. A: Turquoise ornaments associated with a burial in the Mohamad-Djaffar zone. On the top and bottom are beads, possibly from a pendant, while the middle ornament is a piercing referred to as a labret. B: The position of the turquoise artifacts in the burial. C: An actual photo of the burial. These images from Hole et al. (1969) are used with permission of the University of Michigan Museum of Anthropological Archaeology.



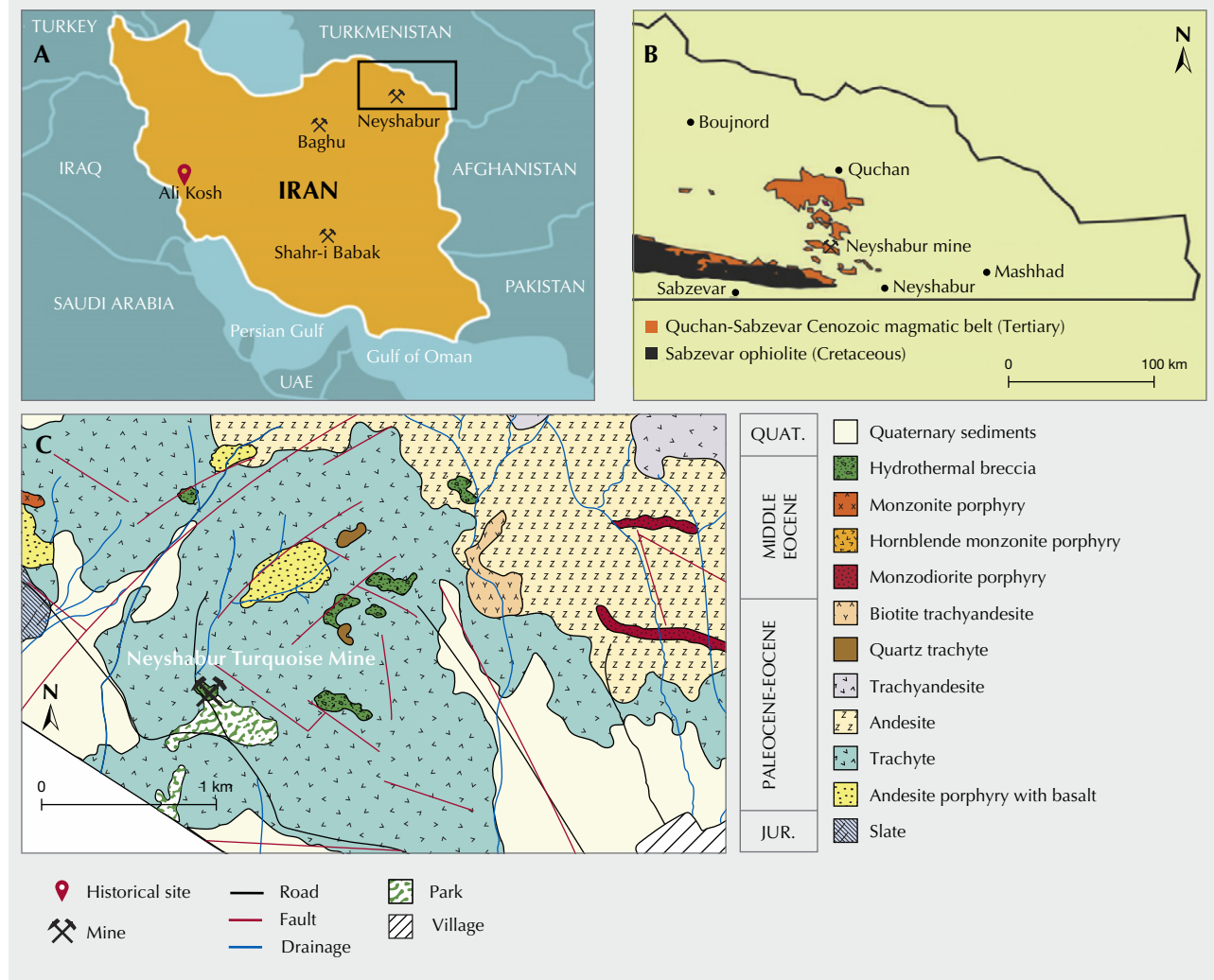


Figure 3. A: Locations of Iran's main turquoise mines. B: The Quchan-Sabzevar magmatic belt (Eshbak et al., 2019). C: Geological map of the Neyshabur mine, 1:10000 scale (Ghiasvand et al., 2017).

It should be noted that turquoise has not been known to occur in the Mohamad-Djaffar zone, which is part of the Ali Kosh historical site (figure 3A). The closest possible source is at least 900 km away.

LOCAL GEOLOGY

The Neyshabur turquoise mine is located at the far east end of the Quchan-Sabzevar magmatic arc (figure 3B). This arc in northeastern Iran indicates a complex tectonic-magmatic evolution and is characterized by extensive magmatic activity with a range of geochemical signatures. Magmatic activities started there during the Cretaceous, peaking during the Eocene (40 Ma) and then continuing into the Plio-

Pleistocene (2 Ma). The volcanic and plutonic rocks of the arc can be divided into three groups (Spies et al., 1984), including Eocene intermediate igneous rocks, Oligocene acidic igneous rocks, and Miocene-Pleistocene alkaline basalts.

Major rock units of the Neyshabur mine are divided into three groups: volcanic, subvolcanic intrusions, and hydrothermal breccia (Ghiasvand et al., 2017). Although the volcanic rocks of trachyte and andesite are most widespread in the area (figures 3C and 4), subvolcanic intrusions such as monzosyenite and monzodiorite have outcrops inside the mine. Primary minerals of volcanic and subvolcanic units include pyrite, magnetite, specularite, chalcocopyrite,



Figure 4. A volcanic mass outcrop in the eastern part of Raish Mountain. The village of Ma'adan is visible in the center. Photo by B. Shirdam.

and bornite. Secondary minerals are turquoise, chalcocite, hematite, covellite, and goethite.

THE NEYSHABUR TURQUOISE MINE

Previously owned by various organizations, the Neyshabur turquoise mine became a cooperative in 2003. It is currently owned by shareholders who are all residents of Olia and Sofla, the two parts of Ma'adan village (figure 4). Some of these shareholders work in the mine, while the rest manage businesses related to cutting or selling.

The mine is located at Raish Mountain, where turquoise has been recovered for millennia. Traditionally, wherever a turquoise vein was exposed on

the mountain surface and its value was recognized, the vein would be followed down into the ground by either strip mining or digging short tunnels.

Another technique, deep-vein mining, was the most difficult and dangerous in centuries past. Whereas once only gold and silver were considered valuable enough to justify digging underground in other parts of the world, turquoise carried such importance in Persian culture that some deep shafts in the mountain date back many centuries. After a suitable site was found, tunnels were excavated in the rock to remove the vein. Narrow vertical shafts were driven through the rock, widening out to horizontal galleries where the ore was found. Sometimes hori-

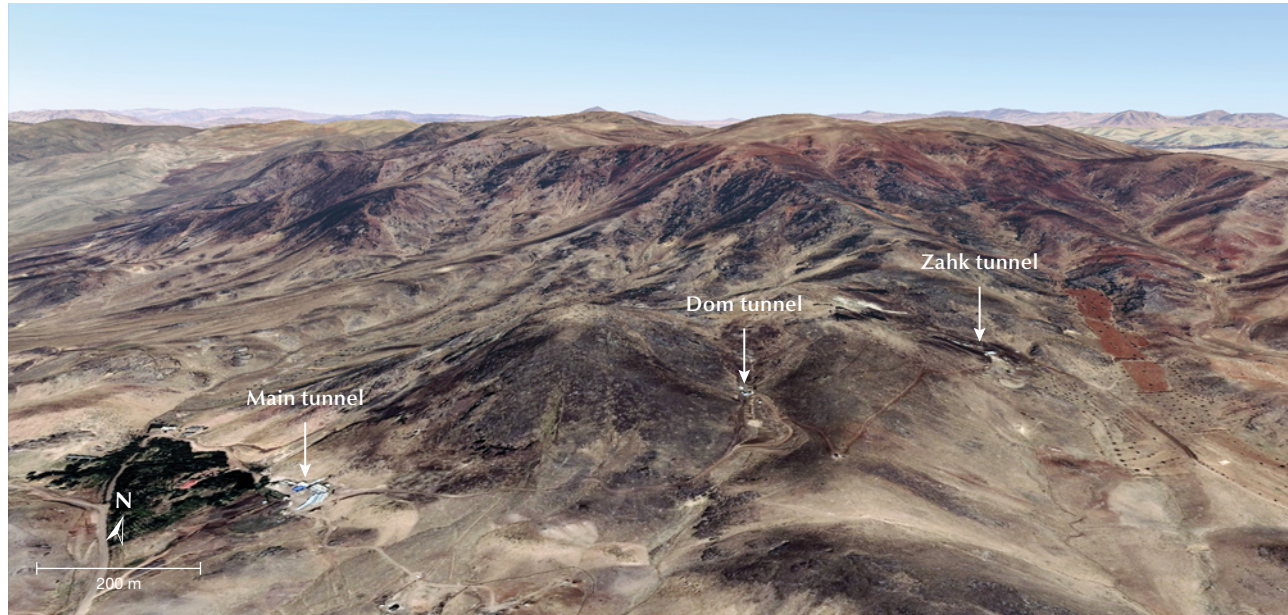


Figure 5. 3D image of Raish Mountain and the Neyshabur mine's three principal tunnels. The compass arrow points north. From Google Earth.

zontal adits¹ from a hillside were driven as well. Working below ground, the miners had to deal with the need for lighting and the dangers of poor ventilation. Some of these old mining operations are still standing, while others have collapsed.

Today the Neyshabur turquoise mine consists of three active tunnels, shown in figure 5: Main², Dom, and Zahk. Each will be discussed separately.

Main Tunnel. The Main tunnel consists of four major active tunnels: Chah Abdar³, Ardalani, Sabz⁴, and Rokub. Starting from the Main tunnel (main drift⁵) (figure 6), the first crosscut leads to the mine's shaft and the downward path to Chah Abdar (figure 7). The shaft, a vertical passageway for ventilation and material transport, is equipped with a hoist and extends 80 m underground. At regular intervals along the shaft, horizontal openings are driven toward turquoise layers that lie 11 levels⁶ below the main drift. Chah Abdar is on the lowest level of the mine, reaching groundwater that leaks into the tunnel. The manway path for accessing Chah Abdar is constructed of downward stairs (figure 8), ramps, and winzes⁷.

The first and second access tunnels are called Ardalani and Sabz, respectively (figure 6). They have active stopes⁸ and raises⁹ ascending to nine active floors, 30 m above the main drift. The raises are excavated in the form of an inclined path or manway ladders (figure 9). The Main tunnel, more than 2 km

in length, is not only used as a transport drift but also has stopes on its path. The Rokub tunnel is actually part of the Main tunnel. It begins around 700 m from the tunnel's entrance and covers such a large area that it has been divided into Rokub I and Rokub II (figure 7).

One characteristic of the Neyshabur mine is the height variation of its tunnels. This is most obvious in the Main tunnel, which begins at 1.5 m high and gradually increases to 3 m or higher, where old stopes were excavated.

The rock units exposed in the Main tunnel can be divided into volcanic units, hypabyssal intrusive rocks, and hydrothermal breccia (Ghiasvand et al., 2017). Volcanic rocks, including trachyandesite and

¹Horizontal passages driven from the surface into the side of mountain.

²The tunnel's original Persian name, "Asli," literally translates to "Main."

³Persian for "water well."

⁴Persian for "green."

⁵All horizontal or subhorizontal openings made in a mine are generically known as "drift."

⁶Horizontal openings on a working horizon in a mine.

⁷Vertical connections between different levels driven from an upper level downward.

⁸Openings made in the process of extracting ore and minerals.

⁹Vertical connections between different levels driven from a lower level upward.

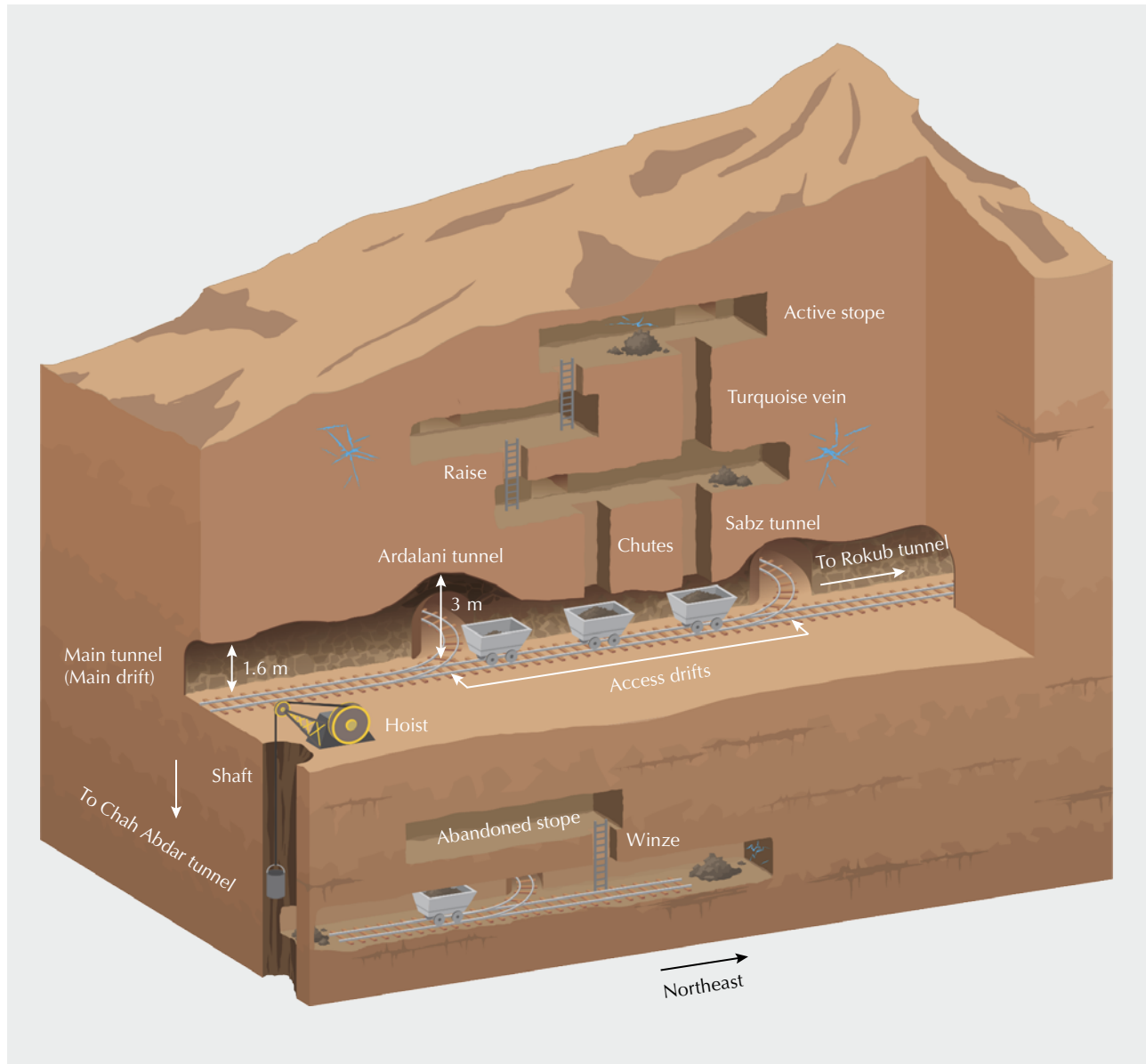


Figure 6. Schematic view showing part of the Neyshabur underground turquoise mine.

andesite, occupy a large part of the Main tunnel. The texture of these bedrocks is porphyritic and their matrix is mainly fine-grained. Subvolcanic intrusive rocks with a combination of quartz monzosyenite porphyry and monzodiorite porphyry are exposed in the Sabz tunnel. The texture of these rocks is porphyritic with a medium-grained matrix.

A hydrothermal breccia unit is observed in the beginning of the Main tunnel and in the downward path to Chah Abdar (figure 6). The existence of different geological units, host rocks, and elemental

anomalies causes variation in turquoise color and quality. For example, veins from the Sabz tunnel's stope have a significant greenish color (figure 10), while turquoise from Ardalani's upper level exhibit a blue color (figure 11).

Dom Tunnel. This name is short for the Persian *dovom*, meaning it is the second tunnel. As shown in figure 12, Dom is located 70 m above the main tunnel. There are nine levels above and three levels below the Dom tunnel's entrance level.

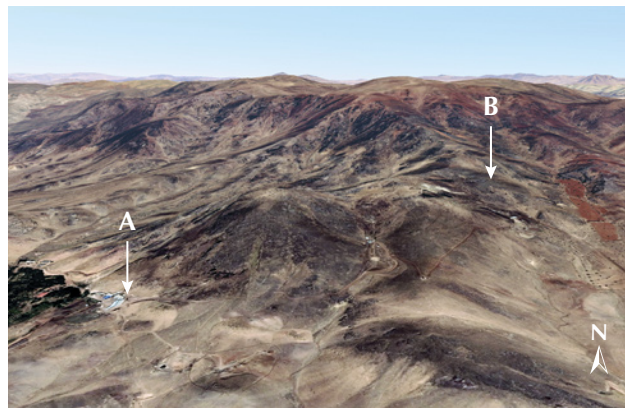
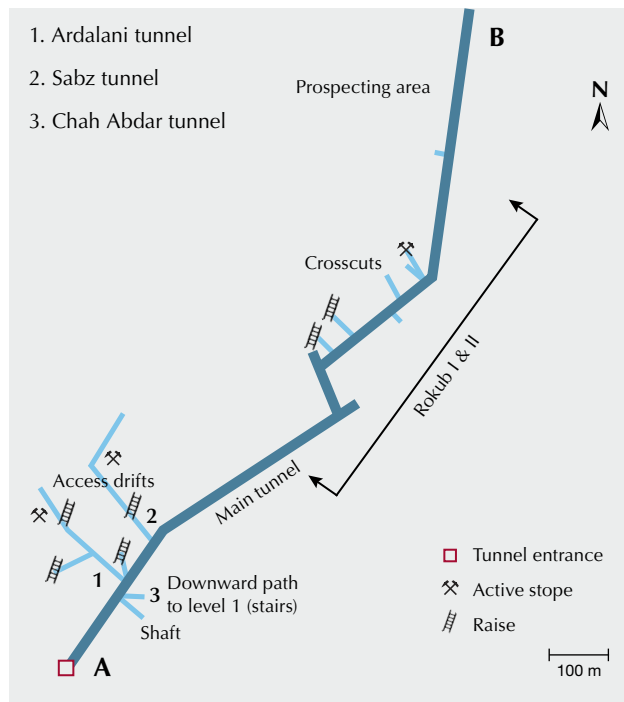


Figure 7. In this map of the Main tunnel, A is the entrance and B is the end of the tunnel. The compass arrow points north.

The same geological units of the Main tunnel are observed in this one, though volcanic rocks and specifically andesite are more widespread. Subvolcanic intrusive rocks are highly altered in this tunnel.

Thick veins of turquoise (figure 13) were observed in the stopes, but most significant was the array of differently colored turquoise observed together (figure 14) in the upper floors of the tunnel. Signs of older mining activities were observed in many places, where the roof was unusually high and later backfill of the stope had caused a slightly steep slope (figure 15).



Figure 8. The winze path down to the Chah Abdar tunnel. Photo by B. Shirdam.



Figure 9. A raise in the form of an inclined path up to the higher levels. Photo by B. Shirdam.

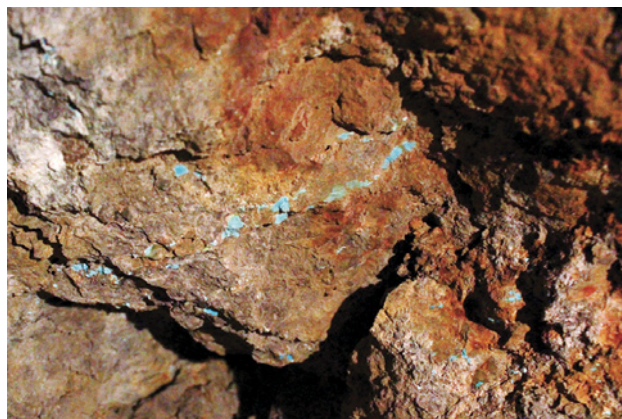


Figure 10. A turquoise vein from the Sabz tunnel's stope. Photo by B. Shirdam.

While smaller than the Main and Zahk tunnels, Dom is the most difficult to navigate. Even though we

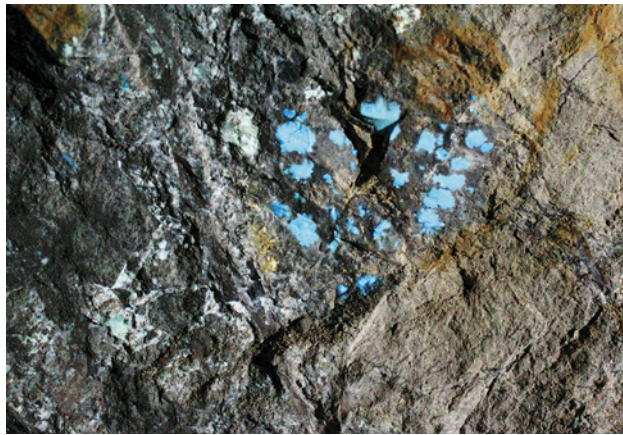


Figure 11. Turquoise from the third level above the Ardalani tunnel. Photo by B. Shirdam.

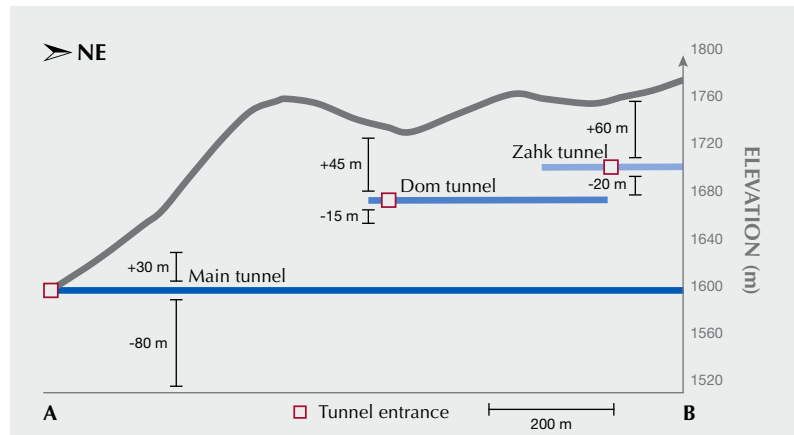


Figure 12. Cross section of Raish Mountain and the positions of the three main tunnels.



Figure 13. Thick vein of turquoise from the Dom tunnel. Photo by B. Shirdam.

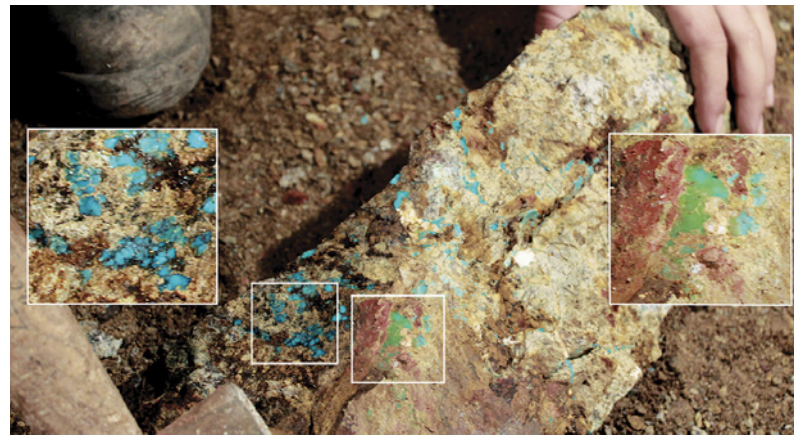


Figure 14. An array of blue to green turquoise colors. Photo by B. Shirdam.



Figure 15. An old stope that has been back-filled to create a path for miners. Photo by R. Shirdam.



Figure 16. The winze to the lower Zahk tunnel. Photo by B. Shirdam.

were instructed many times before entering the mine to follow the lights to reach active stopes, Dom's maze-like path sometimes caused serious confusion.

Zahk Tunnel. Located in the northeastern part of the mine, the Zahk tunnel's entrance is nearly 100 m above the Main tunnel (figure 12). While Zahk appears smaller at the entrance than the Main and Dom tunnels, it has so many levels that it is divided into upper Zahk and lower Zahk. As the name indicates,

Figure 17. Turquoise from the upper Zahk tunnel. Photo by B. Shirdam.

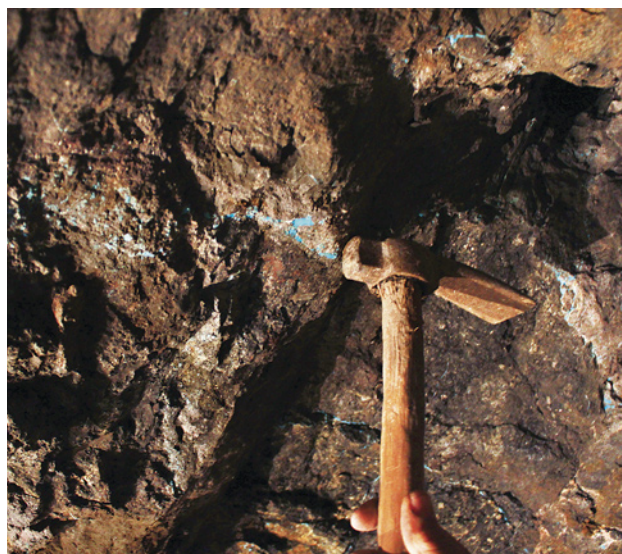


Figure 18. A turquoise vein from the lower Zahk tunnel. Photo by B. Shirdam.

upper Zahk is applied to the 15 levels above the entrance that have been excavated up in the mountain for more than 60 m. Lower Zahk (figure 16) consists of four levels below the tunnel's entrance, with a depth of 20 m (again, see figure 12). Since lower Zahk is just above the Dom tunnel, its tailings are dumped down into the eastern wing of the Dom tunnel and then transported out of the mine.

The upper levels of upper Zahk have the thickest turquoise veins of the entire mine (figure 17). Fine turquoise veins in the Neyshabur mine are usually around 1 to 2 cm thick but sometimes reach 4 cm thick in upper Zahk. Among the three tunnels, Zahk is currently twice as productive as the others. Visiting the stopes of lower Zahk, we observed that the vein color tended more toward blue (figure 18), while upper Zahk contained both blue and greenish blue turquoise (again, see figure 17).

Volcanic rocks were again the primary bedrocks of the tunnel. Signs of silicic and argillic alterations were noticeable.

The Neyshabur mine is essentially a work in progress, involving not only turquoise extraction but also its exploration. As observed in figure 7, the prospecting areas have been highlighted after geological and geochemical studies, and these are expected to expand the mine. Another tunnel not explained in this article, called "Khoraj," is an exploration tunnel that is expected to be joined to the mine network in the future (figure 19).

Mining. Due to the irregular distribution of turquoise veins, stope and pillar (figure 20B) is the main mining



Figure 19. The Khoraj exploration tunnel is located in the south of the mine, and it is expected to join the mine's network below the Main tunnel. Photo by R. Farkhari.

system applied in the Neyshabur mine. This is considered a variant of the room-and-pillar system shown in figure 20A, with a notable difference in the

location and order of pillars. Wherever turquoise veins are observed, a stope is excavated, leaving the mine's untouched material working as pillars. When the stope's roof contains numerous turquoise veins, Neyshabur's stope-and-pillar system changes to cut and fill, in which the stope's floor is filled with a layer of mine waste material.

Stoping, the process required for extracting turquoise veins, is conducted by drilling and blasting. Every working day, after the miners have left, the drilling crew enters the tunnels, drilling blast holes inside the walls (figure 21). To minimize damage to turquoise veins, the number of blast holes is limited and their distance from the veins is controlled. As this is a primary deposit with hard host rocks, pneumatic drilling is carried out using compressed air to drive a rotating percussion drill bit. The compressed air generated is distributed across the mine via an extensive piping network (figure 22).

After the drilling crew leaves the tunnels, the blasting crew begins their work, inserting predetermined amounts of explosives into the drill holes. After the mine's complete evacuation, the blasting is carried out and the mine is left to ventilate blast fumes until the next morning. The next day, any wall or stope where work is to be performed is examined for cracks or other signs of stress or weakness.

Ventilation. Ventilation in the mine is mostly natural. As a result of centuries of traditional mining, many deep shafts and openings connect the mountain's surface to the tunnels. The depth of these old shafts reaches to more than 80 m in some places. Due to the temperature difference between the

Figure 20. Comparison of the more orderly room-and-pillar mining system (A) and the irregular distribution of the stope-and-pillar system used at Neyshabur (B).

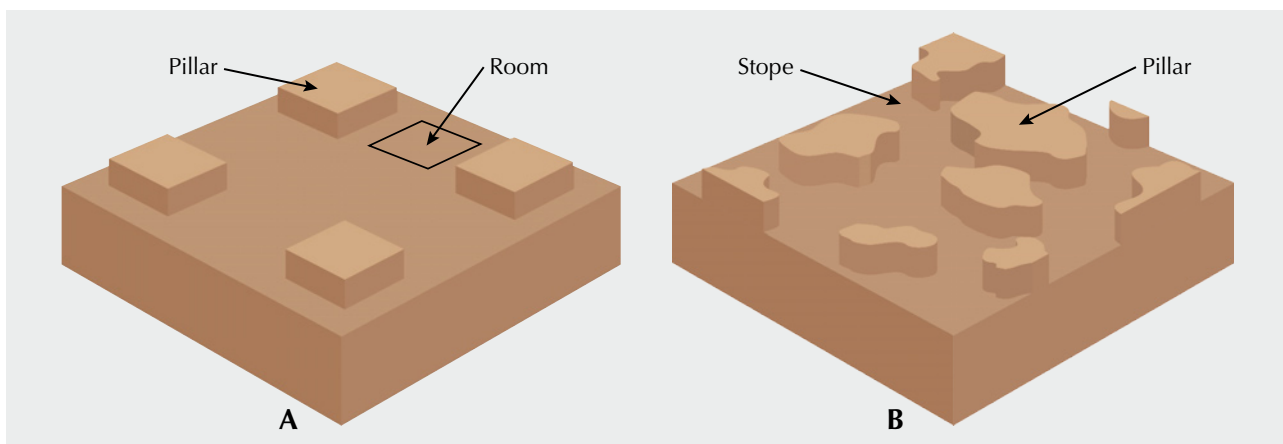




Figure 21. A drilling crew prepares to dig a blast hole. Photo by M. Bakhshandeh Zahmati.

mountain's surface and the mine, air flows through and creates natural ventilation. In the wintertime, it is colder outside the mine than inside. Warm air is lighter than cold, so the warm air rises through the shafts, drawing in fresh, cold air. In the summertime,

the cool air in the mine settles, drawing in warm air through openings.

After blasting, when the ventilation is not completed by the next morning, portable ventilators are sometimes used to speed up the process.

Figure 22. Compressed air tubes in the tunnels. Photo by R. Azizi.





Figure 23. In the stopes, the supervisor watches from above as the miners sort turquoise. Photos by B. Shirdam.

Working Area. The miners work in groups, each of which is responsible for a stope. These groups usually have three to five people (figure 23), plus a supervisor who oversees them as they sort, classify, and cob the extracted turquoise *in situ*. The turquoise is sorted and classified based on its color, quality, vein thickness, shape, and toughness and then placed in bags to be transported to the mine's storeroom.

Although waste rocks are removed through shafts and by wagons (figure 24), the turquoise bags are carried out by miners themselves to avoid any unnecessary damage. All tunnels and their access drifts have rail tracks. Once the wagons are filled with waste rocks, they are hauled out by locomotive and sent to a dump.

Figure 24. At the Dom tunnel's entrance, the wagons are returned to the mine after emptying the waste. Photo by B. Shirdam.

TURQUOISE PRODUCTION

Among Iran's three main turquoise deposits, only the Neyshabur mine is dedicated to turquoise pro-





Figure 25. The four major quality levels of rough turquoise production from Neyshabur: turquoise nuggets (A), turquoise with the host rock attached (B), chalky turquoise (C), and turquoise chips (D). Photos by B. Shirdam.

duction. Baghu turquoise is from the Kuh Zar mine, a gold and copper deposit, and Shahr-I Babak turquoise comes from the Meiduk mine, a porphyry copper deposit. The mining strategies at Kuh Zar and Meiduk are focused on the extraction of gold and copper, respectively, rather than turquoise. Despite the fine color of Baghu turquoise, the Kuh Zar mine currently reports no official production of turquoise. On the other hand, the Meiduk open-pit mine is working with the Shahr-I Babak turquoise cooperative to manage the turquoise extracted in the process of copper mining. Open-pit mining has caused an unstable turquoise yield. When there is a turquoise vein on one of the horizontal levels known as benches, the mine can produce an average of three tons per month, but otherwise there could be no production for months. More information on the Kuh Zar and Meiduk mines will be published in subsequent reports.

With more than 200 workers, an average production of four tons of rough turquoise per month, and an annual production of 40 to 42 tons, Neyshabur is

Iran's largest turquoise mine. Although the Main tunnel is the largest, as shown in table 2, more than 70% of the mine's turquoise comes from the Zahk tunnel.

Mine to Market. Turquoise Quality. Rough turquoise from Neyshabur is classified into four categories based on color, porosity, shape, and size.

Type I: Turquoise nuggets and slabs. Nuggets and slabs are the result of cavities and veins filled by turquoise. These are quite compact, usually flawless, and have been separated from the host rock during extraction (figure 25A). Nuggets and slabs display even color and can produce high-end finished turquoise.

Color is divided into three grades according to saturation. The first grade offers the most vivid colors. A second grade, called "half color"¹⁰ among locals, shows a less saturated blue and green compared to

¹⁰"Nim rang" in Persian.

the first grade, while the third grade has a pale to white hue. It should be noted that the classification of turquoise color is a subjective matter and varies depending on trade, culture, fashion trends, supply, and personal opinion (Lowry and Lowry, 2010). These three color grades for type I turquoise apply for all rough turquoise categories.

Type II: Turquoise with the host rock attached. Turquoise veins, slabs, and nuggets that are sold with the host rock attached fall into this category (figure 25B). If the vein or seam is thick and carries an even and vivid color, it would easily rival the first grade of turquoise. A spiderweb pattern is the result of cutting this type of turquoise.

Type III: Chalky turquoise. This comes in light to pale blue, green, and white colors and in various sizes (figure 25C). The material is porous and requires treatment. Depending on porosity and color, chalky turquoise undergoes a different process for stabilizing and color enhancement.

Type IV: Turquoise chips. After sorting and packing the rough turquoise in bags, some small pieces are left that have been broken, either during extraction or transport (figure 25D). These pieces that vary in color and quality are sold as chips and often used for turquoise inlay (e.g., figure 29).

It is important to mention that the Neyshabur mine does not apply any treatment and only sells the stones in their natural form. All treatments are applied in lapidary and turquoise inlay workshops.

Auctions. Whenever a certain amount of turquoise has been accumulated, the Neyshabur cooperative sends out a call for sale and holds an auction in the mine's yard (figure 26). Bags of turquoise are brought out, and a base price is offered based on the general



Figure 26. A turquoise auction taking place in the mine's yard. Photo courtesy of the Neyshabur turquoise mine cooperative.

TABLE 2. Rough turquoise production of the Neyshabur mine in 2020.

Tunnel	Production (kg)
Main	5,103
Dom	6,884
Zahk	30,315
Total	42,302

quality of the raw material. Finally, the auction begins, and each bag is sold to the highest bidder. The cooperative's auctions are limited, usually holding three to four sessions per year.

The main purchasers of turquoise at these auctions are lapidaries, jewelry companies, and gemstone traders from Mashhad, Neyshabur, and Esfahan. Local lapidary workshops from Ma'adan village have access to a set share of rough turquoise annually that can be purchased at a lower price without participating in auctions.

Turquoise Lapidary and Products. Although the art of cutting and polishing turquoise has a long history in Iran (Vidale and Lazzari, 2016; Hole et al., 1969),



Figure 27. Slabbing rough turquoise in a lapidary workshop in Mashhad. Photo by M. Bakhshandeh.

the lapidary industry has grown in recent decades. More than 300 lapidary workshops have been established in Ma'adan village and the city of Neyshabur.

Mashhad, Tehran, Esfahan, and Neyshabur are the main centers for Iranian turquoise cutting, and they also have an active export market due to tourism and international flights. Most of the foreign clients are from Singapore, Kuwait, the United Arab Emirates, and Spain (Ahmadi et al., 2018). Yet it is important to mention that Iranian turquoise does not occupy a large portion of the global market.

About 60% of the yield from Neyshabur requires treatment. Unless the slabs and veins are very thin, the first color grade of turquoise from categories I and II does not require any treatment and lends itself to cutting and polishing without enhancement (figure 27). The second color grade may require treatment, depending on the cutter's judgment. Chalky turquoise, on the other hand, will break unless it is stabilized. While the idea of wearing untreated turquoise may sound appealing, exposure to chemicals, oils, perfume, sweat, and even sunlight and heat can cause its color to change. As traders in Iran put it, the turquoise will "die."

Since turquoise is an opaque gemstone, the cutting styles are limited. While faceting is an option,

cabochon cutting has always been standard, even in recent jewelry designs (figure 28).



Figure 28. Neyshabur turquoise (12 × 18 mm) with a spiderweb pattern and framed with diamond accents, set in gold. Courtesy of Taktala Jewelry, Tehran.



Figure 29. Turquoise inlay on copper handcrafts housed in the Aghajani Gallery, Tehran. Photo by B. Shirdam.

The mine also yields turquoise chips that are widely used in Iran for inlay. This handicraft, which originated in the city of Mashhad, is done by placing the chips in a mosaic pattern on the surface of plates, dishes, ornaments, decorative objects, and wall art (figure 29).

CONCLUSIONS

The site visit conducted in 2020 (figure 30) suggests that with three tunnels extracting an average of 40 tons per year, the mine is in fact quite active and still expanding. While turquoise evaluation is based on quality rather than geographic origin, the vivid colors and



Figure 30. Author B. Shirdam (in the background) with miners in the Sabz tunnel. Photo by R. Shirdam.



Figure 31. This Persian turquoise necklace designed by Suzanne Belperron, also shown on the cover of this issue, contains graduated beads measuring 6.3–14.68 mm and a diamond clasp. Photo by Robert Weldon/GIA; courtesy of Sima G. Ltd., New York.

untreated nature of cut turquoise from the Neyshabur mine have been often found alluring (figure 31).

Despite the Neyshabur mine's productivity and tradition, this turquoise has yet to find its place in the global market. It has been plagued by claims that the mine is closing. Also, the generic term "Persian turquoise" has been hindered by inconsistent quality and pricing standards, causing some customers to question the product. Although most turquoise in the global market is either stabilized or treated, Iranian traders insist on focusing on untreated turquoise.

While the untreated version of the gemstone may be important to some customers, its high price, limited quantity, and sensitivity to chemicals are a drawback for others. In recent years many private companies in Iran have focused on treatment, improving the quality of second and third color grade material to produce commercial-quality turquoise for trading in the domestic and global market.

With a cohesive marketing and pricing strategy, turquoise from Neyshabur and other Iranian mines could once again compete in the global market.

ABOUT THE AUTHORS

Ms. Shirdam is a PhD candidate, Dr. Shen (corresponding author) is a distinguished professor, and Dr. Yang is a professor, at the Gemmological Institute, China University of Geosciences in Wuhan. Dr. Mokhtari is a professor of geology at the University of Neyshabur in Neyshabur, Iran. Dr. Fazliani is managing director of the Neyshabur turquoise mine cooperative.

ACKNOWLEDGMENTS

The authors sincerely thank the Neyshabur turquoise mine cooperative and all the hardworking miners and experts, especially Mr. Reza Farkhari, the mine's technical manager, for their kind help and support during several visits.

REFERENCES

- Ahmadi R., Karimi A., Hajipour A. (2018) Investigation of the status of turquoise mineral industry in Iran and its global export. *Eghtesad Asia*, No. 561, pp. 9–11 (in Persian).
- Bazin D., Hübner H. (1969) Copper deposits in Iran. Geological Survey of Iran, Tehran.
- Eshbak P., Malekzadeh Shafaroudi A., Karimpour M.H. (2019) Petrography, geochemistry, U-Pb dating, Sr-Nd isotopes, and petrogenesis of Jalambadan igneous rocks, NW Sabzevar. *Geosciences*, Vol. 28, No. 112, pp. 167–180.
- Ghiasvand A., Karimpour M.H., Malekzadeh Shafaroudi A., Hidarshan Shahri M.R. (2017) Age and origin of subvolcanic rocks from NE Iran: Link between magmatic “flare-up” and mineralization. *Chemie der Erde*, Vol. 78, No. 2, pp. 254–267, <http://dx.doi.org/10.1016/j.chemer.2017.12.002>
- Hole F., Flannery K.V., Neely J.A. (1969) *Prehistory and Human Ecology of the Deh Luran Plain: An Early Village Sequence from Khuzistan, Iran*. University of Michigan Press. <http://dx.doi.org/10.3998/mpub.11395036>
- Lowry J.D., Lowry J.P. (2010) *Turquoise: The World Story of a Fascinating Gemstone*. Gibbs Smith, Layton, Utah.
- Spies O., Lensch G., Mihm A. (1984) Geochemistry of the post-ophiolitic tertiary volcanics between Sabzevar and Quchan/NE Iran geodynamic project (geotraverse) in Iran. Geological Survey of Iran, Report 51, pp. 248–264.
- Vidale M., Lazzari A. (2016) *Lapis Lazuli Bead Making at Shahr-i Sokhta: Interpreting Craft Production in an Urban Community of the 3rd Millennium BC*, Serie Orientale Roma, Vol. 6, Antilia.
- Vinogradov A.V., Lopatin S.V., Mamedov E.D. (1966) The turquoise of the Kyzyl-Kum. *Soviet Anthropology and Archeology*, Vol. 4, No. 4, pp. 11–28, <http://dx.doi.org/10.2753/AAE1061-1959040411>
- Weisgerber G. (2004) The turquoise mines at Nishapur. In T. Stollner, R. Slotta, and A. Vatandoust, Eds., *Persian Antiques Splendor (Mining Crafts and Archaeology in Ancient Iran)*. Deutsches Bergbau-Museum Bochum, Bochum, Germany, pp. 502–509.

For online access to all issues of GEMS & GEMOLOGY from 1934 to the present, visit:

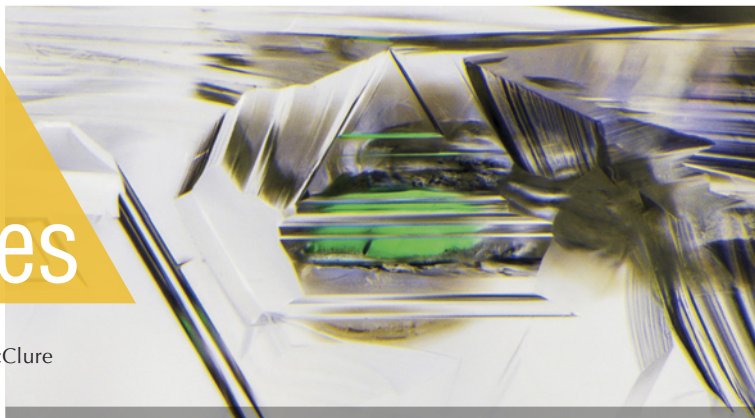
gia.edu/gems-gemology



Lab Notes

Editors

Thomas M. Moses | Shane F. McClure



HPHT-Processed DIAMOND with Counterfeit GIA Inscription

In June 2021, GIA's Antwerp lab received a diamond treated by high pressure and high temperature (HPHT) that was falsely inscribed with a GIA report number referencing an untreated diamond originally graded by GIA in 2010. The diamond was submitted for Update service, in which a stone is matched to its previous report and regraded based on its current condition. Careful comparison of the diamond with its accompanying report number showed that the weight and grading parameters were very similar, but certain differences readily led to the conclusion that this was not the same stone.

The HPHT-processed diamond was a round brilliant weighing 1.497 ct and measuring 7.30–7.34 × 4.50 mm (figure 1), while the original diamond weighed slightly more (1.502 ct) and measured 7.29–7.34 × 4.56 mm. They had the same clarity (IF) and fluorescence (none) but different color grades (D for the original diamond, E for the HPHT-processed diamond).

Additional conclusive differences were detected when the newly submitted stone was further analyzed with advanced spectroscopic techniques. Whereas the diamond from 2010 was type Ia, the submission from 2021 tested as type IIa. Photolumines-



Figure 1. Face-up view of the 1.497 ct, E-color HPHT-processed diamond submitted in 2021 for update service.

cence (PL) spectroscopy using various laser excitation wavelengths confirmed a natural origin, but with color enhancement by HPHT treatment.

In addition to a clearly fraudulent inscription (not pictured), microscopic

examination of the girdle revealed remnants of an original GIA inscription (figure 2). Based on this information, we found that this HPHT-processed stone had already been submitted to GIA in 2013 but was repolished afterward in an attempt to obscure the original inscription. Our records showed that in 2013, the diamond was also inscribed with “BELLATAIRE” (indicating HPHT treatment), but this information had been removed from the girdle and the remnants were even less visible than the original GIA inscription.

examination of the girdle revealed remnants of an original GIA inscription (figure 2). Based on this information, we found that this HPHT-processed stone had already been submitted to GIA in 2013 but was repolished afterward in an attempt to obscure the original inscription. Our records showed that in 2013, the diamond was also inscribed with “BELLATAIRE” (indicating HPHT treatment), but this information had been removed from the girdle and the remnants were even less visible than the original GIA inscription.

In addition to issuing a new report for this HPHT-treated diamond, GIA made the fraudulent inscription unreadable, according to standard procedure, and the stone was inscribed with “TREATED COLOR” (figure 3).

The Antwerp lab had recently reported a similar case of fraud, but that concerned a laboratory-grown diamond with a counterfeit inscription referencing a natural diamond (Sum-

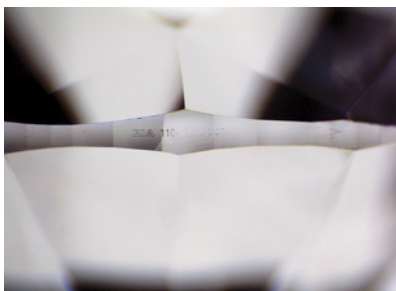


Figure 2. Remnants of the original GIA report number could still be detected on the girdle of the diamond (in addition to the fraudulent inscription, which is not pictured).

Figure 3. “TREATED COLOR” was inscribed on the girdle after spectroscopic analysis confirmed that the color of the stone was enhanced by HPHT treatment.



Editors' note: All items were written by staff members of GIA laboratories.

GEMS & GEMOLOGY, Vol. 57, No. 3, pp. 258–267.

© 2021 Gemological Institute of America

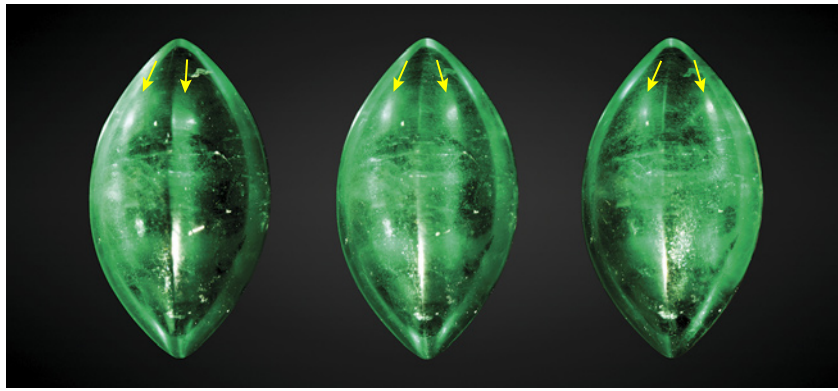


Figure 4. In this 1.93 ct double cat's-eye emerald, the chatoyant bands indicated by yellow arrows are observed from different angles of lighting.

mer 2021 Lab Notes, pp. 150–152). Both types of fraud are common in the marketplace and show the importance of careful verification of not only a diamond's growth method (natural versus laboratory-grown) but also its color origin.

Ellen Barrie, Sander Teuthof, and Sally Eaton-Magaña

EMERALD

A Unique Double Cat's-Eye Emerald

Chatoyancy is generally produced by light reflection from numerous parallel needle-like inclusions or fibrous structures when a stone is skillfully fashioned as a cabochon. Stones such as emerald, chrysoberyl, and scapolite

are known for the cat's-eye effect (see Summer 2015 Gems News International, pp. 200–201). Recently GIA's Tokyo laboratory examined a unique green marquise double-cabochon stone, weighing 1.93 ct and measuring 11.88 × 6.68 × 4.79 mm, that offered a particularly interesting example of chatoyancy (figure 4).

This stone had a spot refractive index of 1.58 and a specific gravity of 2.74, and standard gemological properties indicated that it was emerald. The stone characteristically had a ridgeline and a high-dome structure (figure 5) containing numerous reflective oriented needles and tubes (figure 6) parallel to the width and perpendicular to the length of the stone. It was noteworthy that the light reflection

Figure 5. Emerald cabochon fashioned with a high-dome structure and ridgeline. The width of the stone is 6.68 mm.

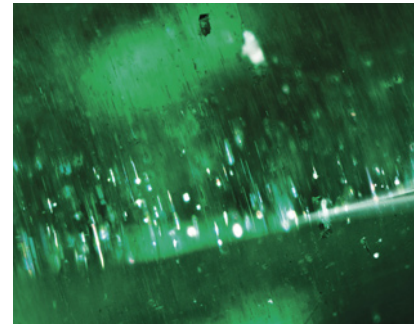
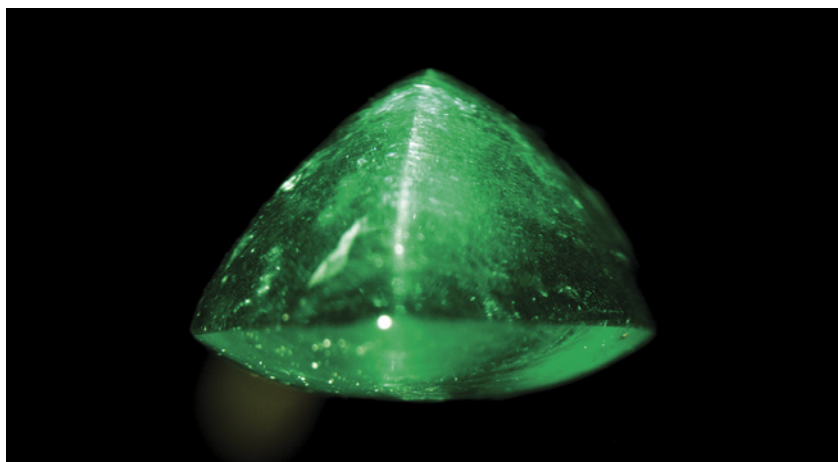


Figure 6. Numerous parallel needles and tubes causing chatoyancy. Field of view 1.75 mm.

from the inclusions created two distinct chatoyant bands along the length of the ridgeline (figure 4) under overhead light. These chatoyant bands were observed from different angles of lighting, as shown in figure 4. This double cat's-eye effect might result from a combination of face angles, inclusions, and the high-dome cabochon structure and ridgeline. Such an unusual cutting style could be responsible for creating this double cat's-eye (figure 7). The principle of double cat's-eye seen in this emerald is different from those of the dual-color double star effect rarely seen in ruby, sapphire, and quartz (e.g., K.

Figure 7. The double cat's-eye seen in the emerald results from the light reflection from oriented inclusions and the cutting style, as shown in this diagram.

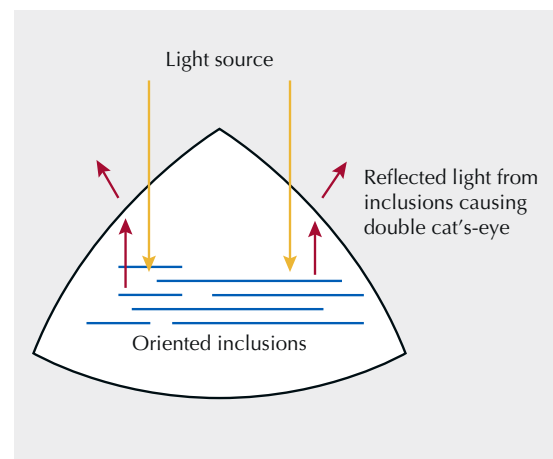




Figure 8. Eleven semitranslucent to opaque green and brown fossilized shells. Most of these specimens show clear shell outlines with green emerald grains.

Schmetzer et al., "Dual-color double stars in ruby, sapphire, and quartz: Cause and historical account," Summer 2015 *G&G*, pp. 112–143). This is a unique example of an unusual optical effect due to the cutting style and inclusion scene.

Makoto Miura

Fossilized Shell Consisting of Emerald

Fossilized shells can be replaced by various types of gemstones, such as quartz and chalcedony (Spring 2014 *Gem News International*, p. 77), opal (A. Cody and D. Cody, *The Opal Story: A Guidebook*, Melbourne, 2008), and demantoid garnet (Winter 2013 *Gem News International*, pp. 257–258). In rare cases, emerald may also participate in the petrification of the shell and form pseudomorphs.

Recently, the Hong Kong laboratory received 11 fossilized shells composed primarily of emerald, measuring $13.00 \times 8.20 \times 6.16$ mm to $24.54 \times 16.72 \times 12.57$ mm and weighing 3.22 to 20.63 ct (figure 8). Most of them preserved the distinctive gastropod shell outlines, with different degrees of weathering. Under magnification, numerous small

light green to green anhedral emerald crystals contained very fine fluid inclusions associated with well-formed brassy pyrite grains (figure 9), which is one of the most common mineral in-

Figure 9. Well-formed pyrite is a common accessory mineral associated with Colombian emerald. Field of view 14 mm.



clusions in Colombian emeralds (S. Saeseaw et al., "Geographic origin determination of emerald," Winter 2019 *G&G*, pp. 614–646). An X-ray radiograph further revealed the spiral skeleton of the shell and scattered pyrite crystals (figure 10). The polycrystalline emerald was deposited evenly throughout the specimens, indicating complete replacement.

Fossilized gastropods were reported from the Matecaña tunnel of the Gachala emerald mine in Colombia (P. Vuillet et al., "Les émeraudes de Gachalá, Colombie," *Le Regne Minéral*, No. 46, July/August 2002, pp. 5–18). Gachala is not a principal emerald mining district but can produce high-quality material. (D. Fortaleche et al., "The Colombian emerald industry: Winds of change," Fall 2017 *G&G*, pp. 332–358). It is located on the Lower Cretaceous fossiliferous sedimentary rocks of the Eastern Cordillera Basin (B. Horton et al., "Construction of the Eastern Cordillera of Colombia: Insights from the sedimentary record," in J. Gómez and D. Mateus-Zabala, Eds., *The Geology of Colombia*, Chap-

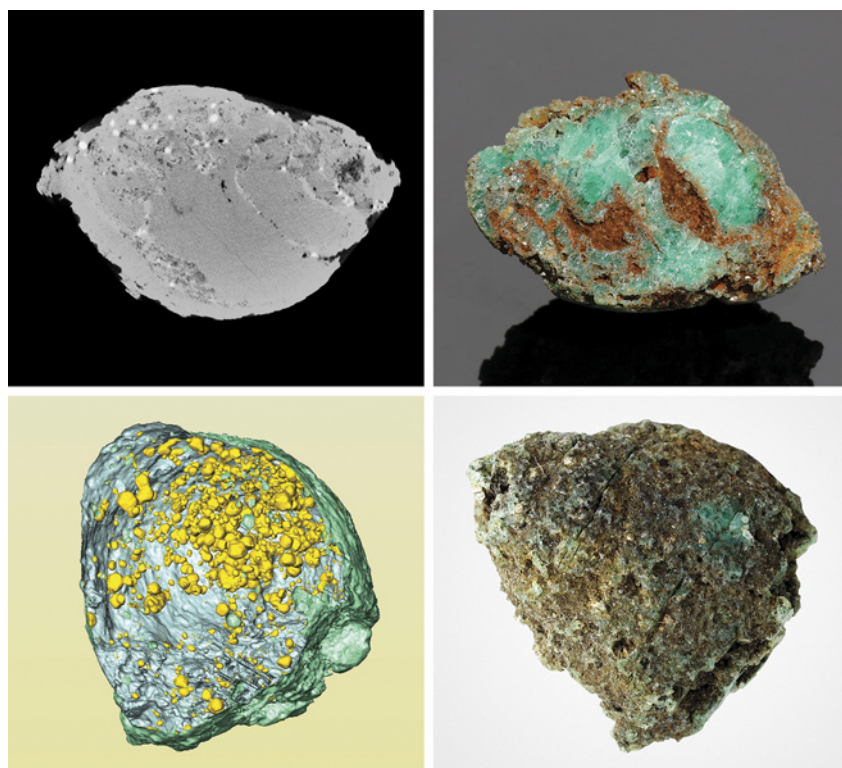


Figure 10. Clear shell structure and internal banding are shown in the X-ray radiograph (top left) of a fossilized shell measuring $22.06 \times 14.85 \times 10.32$ mm and weighing 14.89 ct (top right). Scattered pyrite crystals (yellow in the colorized image on the bottom left) are deposited in a fossilized shell measuring $13.91 \times 11.89 \times 9.32$ mm and weighing 5.07 ct (bottom right).

ter 3, Vol. 3, 2020, Servicio Geológico Colombiano, Publicaciones Geológicas Especiales 37, pp. 67–88), where pyrite and emerald crystallized during the circulation of hydrothermal mineralizing fluids in black shales (G. Giuliani and L. Groat, “Geology of corundum and emerald gem deposits,” Winter 2019 *G&G*, pp. 464–489) and subsequently precipitated to form the fossilized shells.

Ching Yin Sin and Xiaodan Jia

GLASS Imitation of Star Sapphire

The market for sapphire simulants and synthetics is plentiful, as sapphire is likely the most popular of all colored stones. The high cost of natural, gem-quality sapphire means it is not obtainable for much of the world’s population. This has opened the doors of creativity to produce blue stones with high luster resembling the natu-

ral material. Recently, the author obtained a parcel of blue cabochons with an unusual star pattern resembling star sapphire (figure 11). After a series of tests were performed, the material was identified as manufactured glass.

Gemological investigation revealed an average specific gravity of 2.46 and a refractive index of 1.40. The cabochons were inert to long-wave ultraviolet radiation but exhibited strong chalky blue fluorescence under short-wave ultraviolet radiation. Observation under a microscope revealed gas bubbles shallow to the surface within the blue regions of the stones and small conchoidal fractures along the girdles. One cabochon was cut in half vertically for further scientific investigation (figure 12). This cross section uncovered a large core of white glass raised to the surface of the dome in a star pattern. Flow lines were also visible within the white glass core. Finally, a thin layer of blue

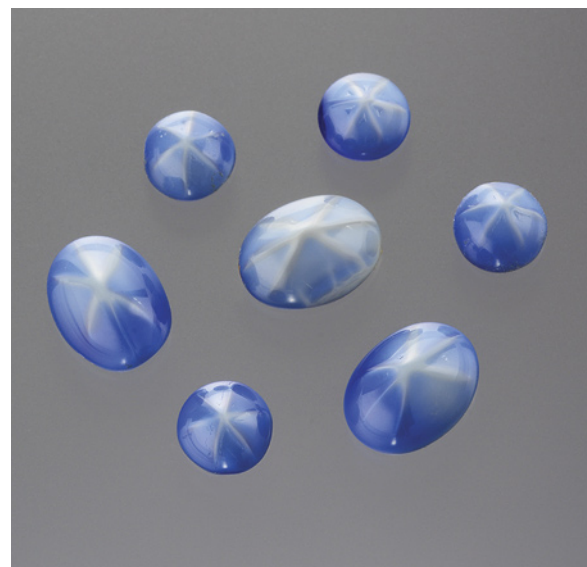


Figure 11. Glass cabochons with weights ranging from 0.47 to 1.29 ct were obtained by the author. The stones displayed white six-ray stars across their domes, resembling star sapphire.

glass around the perimeter of the cabochon was seen in the cross section, creating the bodycolor of the stone (again, see figure 12).

Asterism is an optical phenomenon that can be defined as a star-shaped concentration of reflected or refracted light from inclusions within a gemstone cut en cabochon. Genuine asterism is also mobile if the stone and/or light source is moved. These

Figure 12. A vertical cross section of the glass cabochon showcases the internal structure and diagnostic flow lines imitating star sapphire.

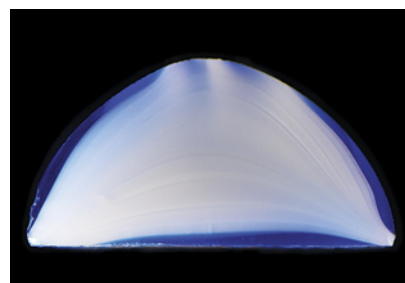




Figure 13. These 10 CVD-grown diamonds submitted to the New York laboratory were fairly large (2.24 ct to 5.90 ct) with high color grades (D to F) and excellent clarity (VVS₂ to VS₁).

glass imitation star sapphires, however, do not exhibit genuine asterism, as their stars were simply molded into shape and are fixed in place.

Glass imitations span the gamut of gemstones. Faceted transparent colorless glass is one of the oldest and simplest diamond simulants. Glass beads coated with pearlescent paint are a common pearl imitation, and colored glass of various opacities is capable of imitating almost any colored gemstone. Recent *G&G* articles on colored stone imitations include “Artificial glass imitating a Paraíba tourmaline” (Winter 2020 Lab Notes, pp. 518–520), “Greenish blue glass imitating gem silica” (Summer 2020 Gem News International, pp. 314–315), and “Glass bangles” imitating jadeite and nephrite (Spring 2019 Lab Notes, pp. 93–94).

Britni LeCroy

LABORATORY-GROWN DIAMONDS New CVD Material Submitted for Analysis

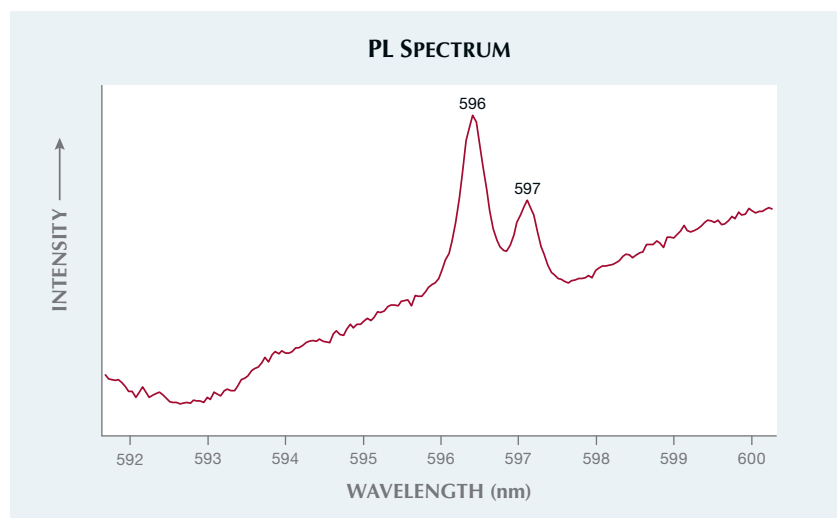
Since the introduction of its new digital Laboratory-Grown Diamond service, GIA has recently seen a vast increase in the number of diamonds grown by chemical vapor deposition (CVD). These are often large and of exceptional clarity. The New York laboratory recently examined a batch of 10

large, high-quality CVD-grown diamonds from a single client, Shanghai Zhengshi Technology. The diamonds ranged from 2.24 ct to 5.90 ct and came in a variety of fancy shapes, as well as the standard round brilliant cut. All of them had high color grades, ranging from D to F, and excellent clarity, with grades between VVS₂ and VS₁ (figure 13).

The diamonds were all identified as type IIa using Fourier-transform infrared (FTIR) spectroscopy, with the 3123 cm⁻¹ peak that is attributed to

most as-grown CVD synthetics and the 3017 cm⁻¹ peak that can be found in treated CVD synthetics both notably absent from their spectra. PL spectroscopy using a 514 nm laser revealed SiV (737 nm), NV⁻ (637 nm), and NV⁰ (575 nm) centers in all of the diamonds. Also observed was the 596/597 nm doublet, a feature commonly seen in as-grown CVD diamond indicating no treatment was applied (figure 14) (S. Otake, “Melee diamonds: Metal defects and treated color,” Fall 2018 *G&G*, p. 304).

Figure 14. PL spectrum showing the 596/597 nm doublet observed in an as-grown CVD diamond.



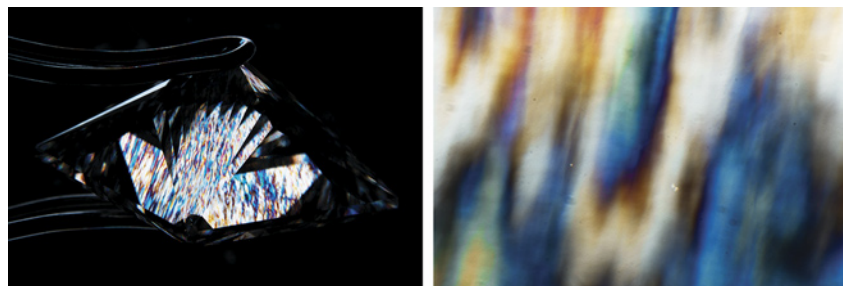


Figure 15. Each CVD-grown diamond showed a strong birefringence pattern displaying many interference colors. The pattern is not disrupted by the presence of pinpoint inclusions in the diamonds. Field of view 19.27 mm (left) and 1.26 mm (right).

The diamonds showed strong birefringence when viewed under cross-polarized light, exhibiting both low and high interference colors (figure 15). DiamondView imaging revealed mostly blue, purple, or pink fluorescence, with blue-violet dislocations that were clearly observed in all of the diamonds tested. More notable was the absence of the striations commonly seen in CVD diamonds, which indicate start-stop growth and changing growth conditions (figure 16). The absence of striations implies that these diamonds might have been grown in one continuous step—the fact that the dislocations appear to be homogenous and uninterrupted supports this theory.

This group of lab-grown diamonds possessed high clarity and high color for as-grown material, demonstrating the potential for large lab-grown diamonds to make large inroads in the

gem diamond market. With continuing improvements to growth technology, lab-grown diamond identification faces many challenges. While large batches of CVD synthetics from different manufacturers have been documented by GIA in the past (e.g., W. Wang et al., “CVD synthetic diamonds from Gemesis Corp.,” Summer 2012 *G&G*, pp. 80–97), this set offers insight into potential new CVD growth conditions for CVD synthetic diamonds.

Elina Myagkaya and Paul Johnson

Laboratory-Grown Diamond with Internal Laser Markings

With the recent influx of laboratory-grown diamonds into the market and to aid consumer awareness of diamond origin, manufacturers are often marking their laboratory-created dia-

Figure 16. DiamondView imaging revealed homogenous, unbroken dislocations without the distinct banding that is common in CVD-grown diamonds.

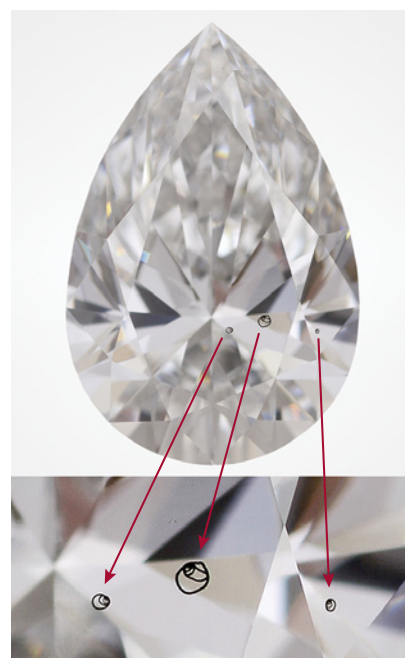
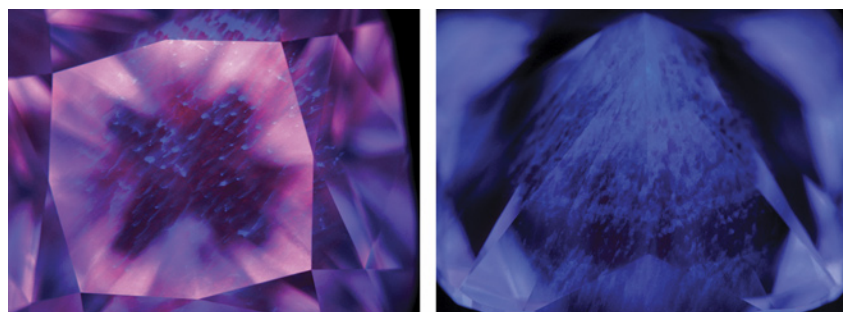


Figure 17. The 2.44 ct pear-cut CVD-grown diamond with internal spiral markings.

monds using internal inscriptions. The New York laboratory recently examined a 2.44 ct pear-shaped CVD (chemical vapor deposition) grown diamond with unusual internal spiral markings (figure 17).

The three spiral markings were black and all in the same plane (i.e., at the same depth). The line thickness of these markings was about 40 microns (figure 18), whereas laser inscriptions are generally less than 20 microns. It was suspected that these markings were created by accidental laser dam-

Figure 18. Micro image of the largest spiral marking; the line thickness is 40 microns.





Figure 19. These four non-nacreous pink and light pink pearls submitted for identification weighed (left to right) 1.30, 2.88, 4.41, and 5.88 ct.

age rather than laser inscription. Raman mapping of the surface above the markings revealed a much broader diamond Raman peak compared to the rest of the crystal. This is the result of laser damage to the crystal lattice. Further Raman mapping using confocal settings identified a graphite peak at about 1620 cm^{-1} . This offered proof that a laser, graphitizing the diamond, had created the markings.

The “inclusions” likely resulted from the laser marking the surface; this is done to provide a template to guide the polisher in producing the final shape. The intent would have been to score the surface; however, the laser appeared to have been inadvertently focused below the surface, resulting in the unusual internal markings.

As the markings are internal and graphitized, they are considered clarity features. The clarity grade was determined to be SI₁, followed by a report comment stating, “Clarity grade is based on manufacturing remnants that are not shown.”

Paul Johnson, Stephanie Persaud, and Cori Bulgrin

Dyed Non-Nacreous PEARLS

Recently, 90 items purported to be pearls were submitted to GIA's Bangkok laboratory for identification. While the majority were confirmed to be natural pearls, four samples warranted further study. Each of these four samples exhibited a non-nacreous surface, and on first impression they appeared to be conch pearls owing to their pink and light pink coloration. Their measurements ranged from $6.53 \times 5.11 \times 4.92$ mm to $10.64 \times 10.46 \times 7.28$ mm, and they weighed 1.30, 2.88, 4.41, and 5.88 ct, respectively (figure 19).

Observation through a $10\times$ loupe and a microscope revealed that the samples were non-nacreous pearls. However, it was also readily apparent that the colors had been modified and were not natural. The 1.30 ct pearl exhibited the flame-like structure routinely observed in pearls such as conch, but the obvious red dye visible over the entire surface made it difficult to determine whether the flame structure was really present (figure 20A). The 2.88 ct pearl displayed a subtle flame structure, and some pink

dye was visible on the surface and within many surface blemishes (figure 20B). Some surface areas of the 4.41 ct pearl showed the original bodycolor (figure 20C), but much of the surface showed the same dye features seen in the previous two pearls. Finally, the 5.88 ct pearl exhibited a nice flame pattern throughout, with some surface areas on the base and circumference modified by working (*The Pearl Book*, CIBJO Pearl Commission, 2020; N. Nilpetploy et al., “A study on improving the surface appearance of low-quality *Pinctada maxima* bead cultured pearls,” *GIA Research News*, March 24, 2021).

The color origin of this pearl was a little more challenging to identify because most areas were a lighter color, and as a result, the color modification evidence was harder to see with the unaided eye. However, magnification revealed pink dye concentrations within cracks on the base and in some surface-reaching structural features (figure 20D). Real-time micro-radiography (RTX) revealed a variety of structures within the pearls. The organic-rich and void features ob-

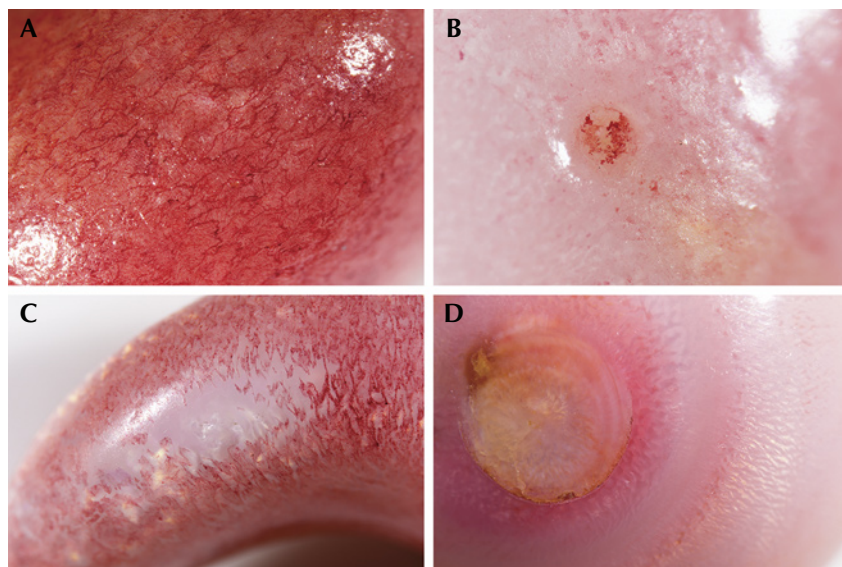


Figure 20. A: Red dye visible within surface-reaching features of the 1.30 ct pearl; field of view 3.60 mm. B: Red dye concentrated in and around surface-reaching features of the 2.88 ct pearl; field of view 2.88 mm. C: An underlying white area where the red dye did not cause discoloration of the 4.41 ct pearl. Flame structure is evident in the white area; field of view 7.20 mm. D: Clear flame structure with areas of pink dye concentrated in the surface features of the 5.88 ct pearl; field of view 7.20 mm.

served could be interpreted as characteristic of some non-bead cultured pearls. While they may be considered suspect, similar features have been observed in natural non-nacreous pearls (E. Fritsch and E.B. Misiorowski, "The history and gemology of Queen conch 'pearls'," Winter 1987 *G&G*, pp. 208–221; S. Singbamroong et al., "Observations on natural non-nacreous pearls reportedly from *Tridacna* (clam) species," 34th International Gemmological Conference, Vilnius, Lithuania, 2015; Summer 2018 Lab Notes, pp. 211–212). To date, there have been no reports of any *commercially produced* non-nacreous cultured pearls in the market. Thus, based on surface observations and their internal structures, they were identified as treated-color natural non-nacreous pearls.

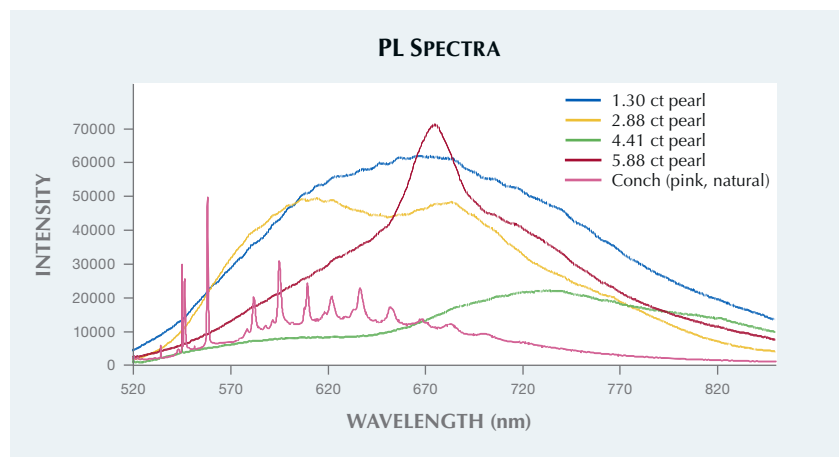
Further examination under long-wave ultraviolet radiation showed a weak to moderate red reaction over the colored areas, while the white area on the 4.41 ct pearl and the

lighter-colored areas on the 5.88 ct pearl exhibited bluish reactions of moderate to strong intensity. Ultraviolet-visible (UV-Vis) reflectance spectra revealed absorption features

expected for pink pearls in the visible range, but the absorption patterns differed from those typical of naturally colored conch pearls. Raman spectra collected using a 514 nm laser revealed peaks (doublet) related to the vibration modes of aragonite at 702 and 705 cm^{-1} . All of the pearls showed additional weak peaks at 485, 640, and 827 cm^{-1} and less-defined features between 1000 and 1700 cm^{-1} . However, none were associated with the polyenic peaks observed in most naturally colored non-nacreous pearls (Summer 2017 Lab Notes, pp. 230–231; Summer 2018 Lab Notes, pp. 211–212). The photoluminescence spectra also differed from those expected for naturally colored pink conch pearls and lacked the obvious polyenic peaks routinely observed in such pearls (figure 21).

Surface observation using the loupe and microscope combined with the results obtained from advanced analyses on the colored surface areas led us to conclude that the colors of the four pearls had been modified. While this is not so surprising when it comes to nacreous pearls, it is, from the author's experience, more unusual to encounter color-modified natural non-nacreous pearls. Since these sam-

Figure 21. Photoluminescence spectra of the four pearls together with the spectrum of a pink conch pearl from GIA's reference database. The spectra of the treated pearls differ from that of the conch pearl, which shows a series of very clear polyenic peaks. These peaks are characteristic of many naturally colored porcelainous pearls.



ples appeared visually similar to conch pearls, we can speculate that the original white or lightly colored pearls were dyed pink to imitate those produced by the Queen conch mollusk (*Lobatus gigas*, formerly known as *Strombus gigas*). This would make sense based on consumer demand in the market. However, the exact reason for treating these particular samples is unknown.

Areeya Manustrong

ZIRCON with Unusual Color-Change Behavior

The Carlsbad laboratory recently had the chance to examine a 4.60 ct cushion-cut zircon with truly unusual color behavior. Standard gemological testing confirmed that the stone's properties were consistent with zircon: an over-the-limit RI, an SG of 4.72, weak yellow fluorescence in short-wave UV and no fluorescence in long-wave UV, and a typical uranium-related pattern in the spectroscope with a prominent sharp peak at 653 nm. The zircon's color was green using a standard white light fluorescent illuminant with a color temperature of 5500 K (figure 22). The stone's color was also checked using a standard incandescent illuminant, but there was no discernible difference from the cool fluorescent illuminant (table 1). However, the color of the zircon was markedly different using white light LEDs with variable color temperature from 2700 K (warm) to 6500 K (cool), where the color went from grayish purple in cool LED light to green in warm LED light (figure 23). Notably, the color observed in the cool LED light was quite similar to the color seen when the stone was taken outside and observed in diffused daylight.

The discrepancy between the colors seen using the cool fluorescent illuminant (green) and either daylight or the cool LED illuminant (grayish purple) can be understood by studying the absorption spectrum of the zircon compared to the emission spectrum of the cool fluorescent bulb (figure 24).

TABLE 1. Color behavior of the color-change zircon under different illuminants.

Illuminant	Observed color
Incandescent (2700 K)	Green
Daylight (overcast afternoon, Carlsbad, Calif.)	Grayish purple
Cool fluorescent (6500 K)	Green
Warm LED (2700 K)	Green
Cool LED (6500 K)	Grayish purple

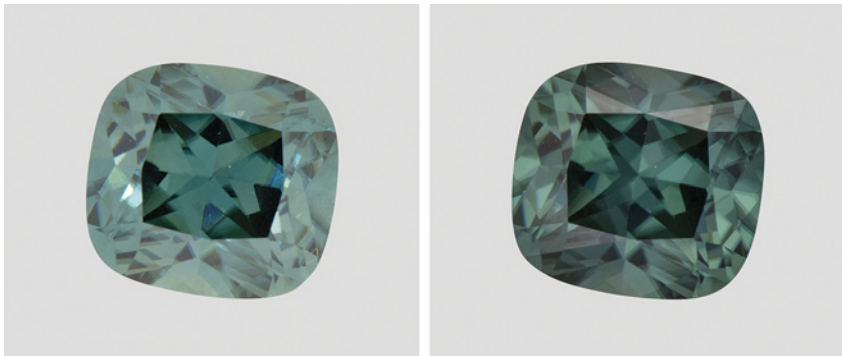
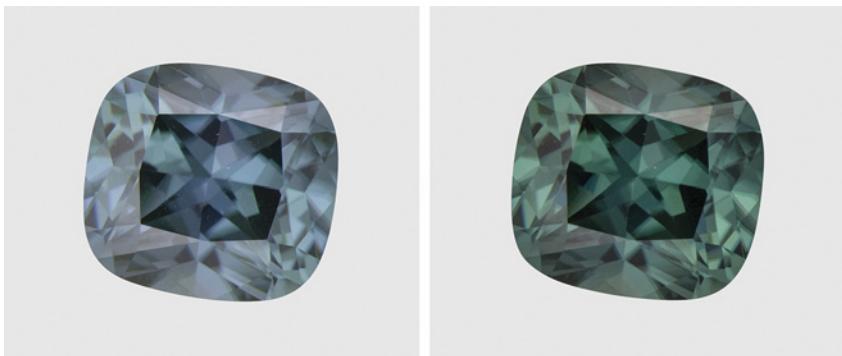


Figure 22. The color of the 4.60 ct zircon is shown in standard cool fluorescent illumination (left) and in warm (2700 K) LED illumination (right). There was little difference in bodycolor when viewed under the two light sources.

The perception of cool white light output from the fluorescent bulb is achieved with two relatively sharp emission bands at about 435 nm and 545 nm, which is in contrast to the

much smoother broad-band emission pattern of true daylight. One of the sharp emission bands in the fluorescent illuminant overlaps significantly with sharp absorption bands in the

Figure 23. The color of the 4.60 ct zircon is shown in LED illumination with cool white light at 6500 K (left) and in warm white light at 2700 K (right).



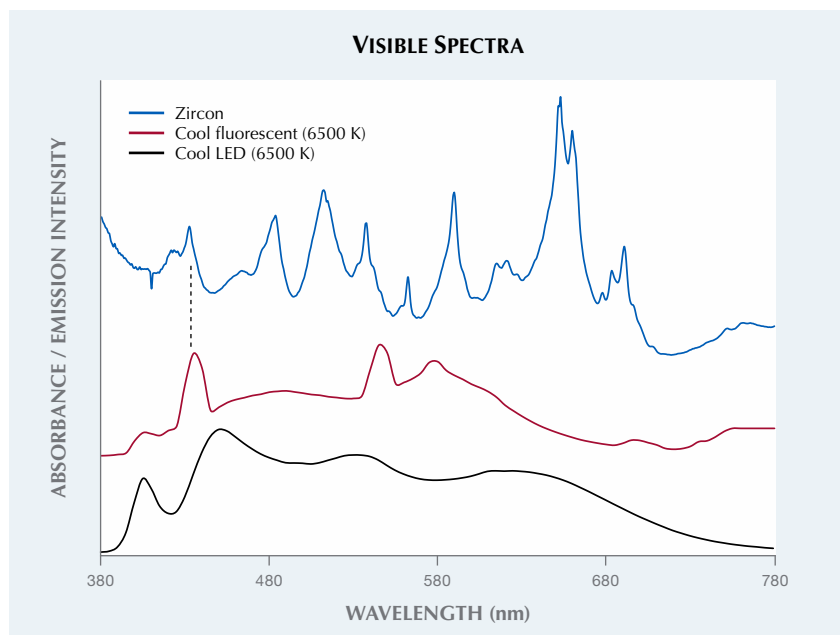


Figure 24. The visible absorption spectrum of the color-change zircon (top) compared to the emission spectrum of a standard cool (6500 K) fluorescent illuminant showing the overlap of sharp emission bands from the fluorescent light and sharp absorption bands in the absorption spectrum (dashed line). Also shown is the emission spectrum of the cool (6500 K) LED used in the lab for color grading at GIA.

zircon at 424 and 433 nm. The fact that a significant portion of the blue emission from the fluorescent bulb is

selectively absorbed by the zircon skews its color away from the blue color that ought to be observed in true

daylight. This blue can also be observed using cool LEDs, which tend to have smoother broad emission patterns more closely resembling black-body radiation patterns of true daylight and incandescent light. This unusual color-change behavior is only expected in gems with sharp absorption bands, likely related to either rare earth or actinide elements. Of particular note, these color-change zircons are occasionally recovered from the gem mining areas around Mogok, Myanmar. For these gems, LEDs should provide a more reliable color grading illumination environment than fluorescent light sources.

Aaron Palke

PHOTO CREDITS

Ellen Barrie—1, 2, 3; Makoto Miura—4, 5, 6; Johnny Leung—8, 9, 10; Cheryl Wing Wai Au—10 (top); Ching Yin Sin—9, 10 (bottom); Emiko Yazawa—10 (bottom); Jessa Rizzo—11; Nathan Renfro—12; Sood Oil (Judy) Chia—13; A'Dhi Lall—15; Elina Myagkaya—15, 16; Jian Xin Liao—17; Paul Johnson—18; Lhapsin Nillapat—19; Kwanreun Lawanwong—20; Robert Weldon—22, 23



G&G

Micro-World

Editor

Nathan Renfro

Contributing Editors

Elise A. Skalwold and John I. Koivula

Apatite in Blue Sapphire

One of the beauties of working with gemstones is that each time you peer into a stone, you get a glimpse of the universe held within. When we first examined the scene from figure 1 in a star sapphire, we were delighted with the view. A feature that immediately stands out is the triangular crystal, which displays terraced growth features and iridescence on the surface when illuminated with a fiber-optic light. Analysis with micro Raman revealed that this crystal is apatite.

What makes the scene even more stunning is the way the crystal seems to float over a cloud of rutile silk. This same silk is what creates asterism in the stone.

While in this case the apatite crystal resides in a sapphire from Sri Lanka, apatite has also been reported in

corundum from a variety of sources, including Afghanistan, Cambodia, Madagascar, Myanmar, Nigeria, Pakistan, Tanzania, Thailand, the United States, and Vietnam.

Apatite can be found not only in ruby and sapphire from different origins, but also in many other types of gems. In our laboratory, we have encountered apatite inclusions in emerald, spinel, and garnet.

Apatite is a relatively common mineral, so it is not surprising to find it so often as an inclusion. Although it may occur frequently, in this instance it is anything but mundane.

*E. Billie Hughes
Lotus Gemology, Bangkok*

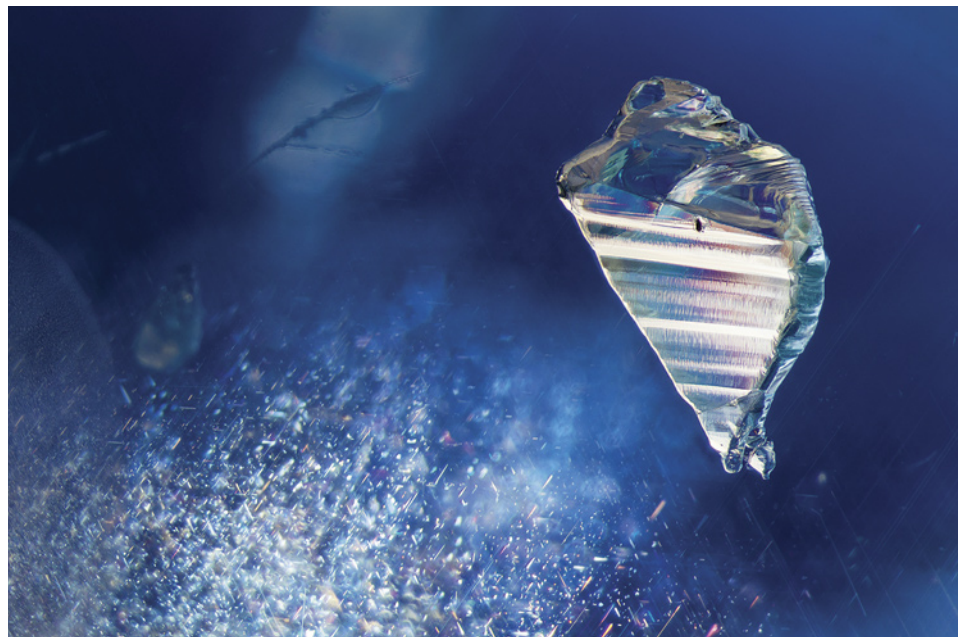


Figure 1. An apatite crystal is suspended over a cloud of rutile silk in this untreated star sapphire. Photomicrograph by E. Billie Hughes; field of view 6 mm.



Figure 2. This natural 2.01 ct Fancy Light brownish greenish yellow diamond octahedron was faceted to highlight an octahedral-shaped cloud inclusion. Photo by Nathan Renfro.

Faceted Octahedral Diamond with Octahedral-Shaped Inclusion

Recently, the authors examined a 2.01 ct faceted diamond octahedron (6.28 × 5.98 × 7.14 mm) with a Fancy Light brownish greenish yellow color grade that showed a distinctive internal appearance (figure 2). Microscopic examination revealed an octahedral-shaped inclusion scene composed of minute inclusions and clouds. The faceting arrangement of the diamond was likely meant to highlight the octahedron. Viewed from one perspective, the hexagonal facet shows the internal octahedron in such a way that the inclusion scene resembles a six-pointed star (e.g., figure 3; see the video at <https://www.gia.edu/gems-gemology/fall-2021-microworld-diamond-octahedral-inclusion>). Similar octahedral-shaped inclusions have been encountered before in natural diamonds (Winter 2015 Lab Notes, pp. 428–429; Spring 2011 Lab Notes, pp. 50–52).

Oftentimes, such symmetrical clouds are dark-colored or gray (W. Wang and W. Mayerson, “Symmetrical clouds in diamond—The hydrogen connection,” *Journal of Gemology*, Vol. 28, No. 3, 2002, pp. 143–152). These can also

About the banner: This sunstone from Tanzania contains numerous platelets of hematite that are responsible for the aventurescence in this phenomenal gem. Photomicrograph by Nathan Renfro; field of view approximately 5 mm.

GEMS & GEMOLOGY, VOL. 57, No. 3, pp. 268–275.

© 2021 Gemological Institute of America

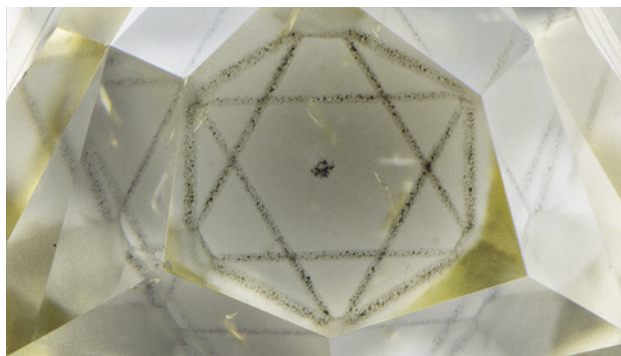
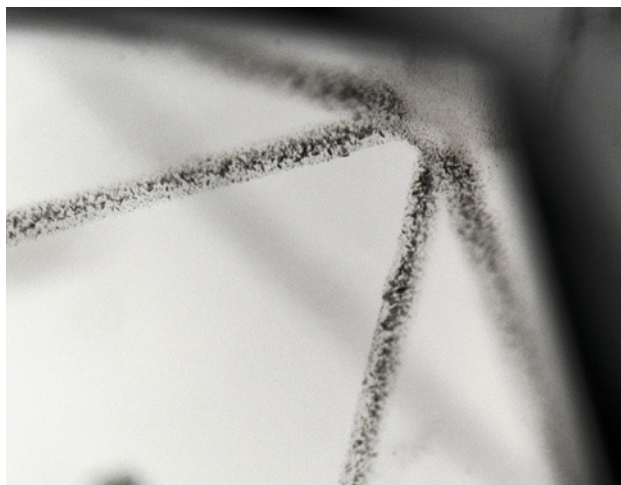


Figure 3. The faceting pattern for this diamond includes four hexagonal facets that provide a window of the octahedral-shaped inclusion. From this viewing angle, the octahedron resembles a six-pointed star. Photomicrograph by Nathan Renfro; field of view 4.69 mm.

contain evidence of hydrogen, nickel-related defects, or graphite (S. Eaton-Magaña et al., “Inclusion and point defect characteristics of Marange,” *Diamond and Related Materials*, Vol. 71, 2016, pp. 20–29). At higher magnification, the individual inclusions that combine to create the cloud can be seen (figure 4).

The cloud inclusion resulted in an SI₁ clarity grade. The diamond exhibited no fluorescence to long-wave UV and blue N3-related fluorescence within the diamond when ex-

Figure 4. This detail of one of the octahedron’s vertices indicates that the cloud comprises small inclusions. The portion of the octahedral cloud closest to the vertex within this image has a depth of approximately 1.8 mm below the hexagonal-shaped facet. Photomicrograph by Sally Eaton-Magaña; field of view 1.50 mm.



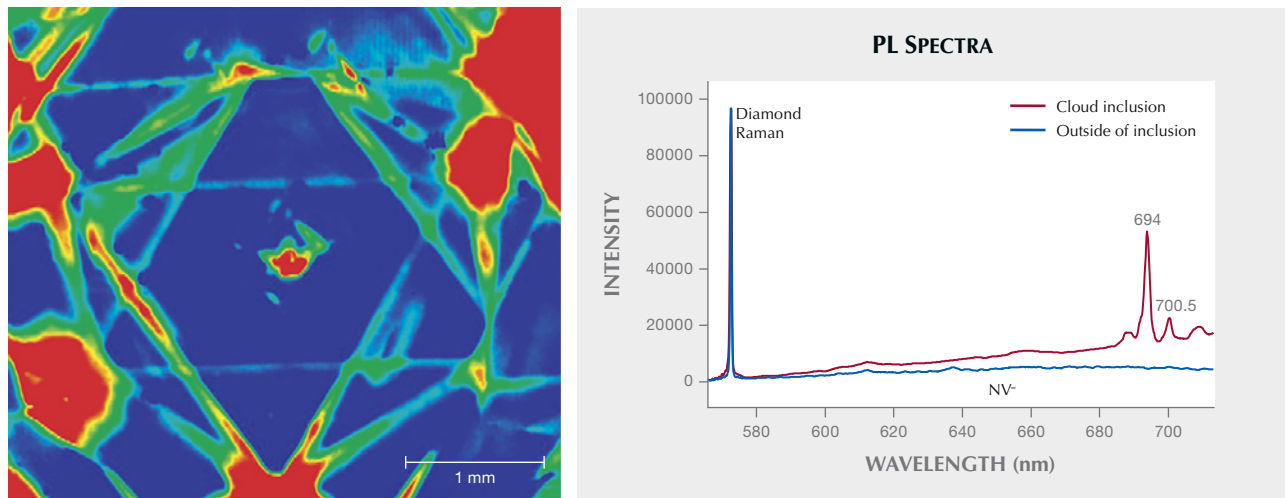


Figure 5. Left: This false-color PL map was compiled from thousands of spectra (each pixel is 15 microns in size) and plots the intensity of a peak centered at 694 nm (associated with nickel and often seen in hydrogen clouds). The detection of this peak corresponds well with the hydrogen cloud. The data were collected with 532 nm excitation at liquid nitrogen temperature, and the peak intensity is normalized by ratioing to the diamond Raman peak. Right: These two spectra were collected from a “red” and “blue” portion of the PL map. The diamond Raman areas are scaled equally. The cloud inclusions indicated elevated concentrations of peaks that include those at 694 and 700.5 nm; outside of the inclusion, there are increased concentrations of NV⁻ at 637 nm.

posed to the deep UV within the DiamondView. The cloud inclusion itself showed no distinctive fluorescence compared to the rest of the diamond. The IR absorption spectrum indicated the presence of strong nitrogen aggregates and a strong hydrogen peak at 3107 cm⁻¹ associated with the N₃VH defect. The visible/near-infrared absorption spectrum contained typical cape features and a hydrogen-related band at 835 nm. The hydrogen features detected in the IR and Vis-NIR absorption spectra correspond with the presence of the octahedral cloud inclusion.

Spectroscopically, the most interesting results came from photoluminescence (PL) mapping of the octahedral-shaped cloud inclusion. This was performed at liquid nitrogen temperature using 532 and 455 nm excitations. Using 532 nm excitation, we saw elevated concentrations of peaks at 694 and 700.5 nm within the cloud inclusion (figure 5). The elevated concentrations of these peaks are consistent with previously characterized hydrogen clouds (e.g., Fall 2020 Lab Notes, pp. 416–419). The 694 and 700.5 nm peaks are ascribed to nickel and are often seen in hydrogen-rich diamonds (K. Iakubovskii and G.J. Adriaenssens, “Optical characterization of natural Argyle diamonds,” *Diamond and Related Materials*, Vol. 11, No. 1, 2002, pp. 125–131). In the 455 nm PL mapping, a nickel-nitrogen-related defect at 496.7 nm called the S3 center (T. Hainschwang et al., “The Rhodesian Star: An exceptional asteriated diamond,” *Journal of Gemmology*, Vol. 34, No. 4, 2014, pp. 306–315) was also detected within the cloud. Outside of the inclusion, we detected higher concentrations of the NV⁻ defect (principal emission at 637 nm).

While the faceting pattern dramatically highlights the octahedral-shaped inclusion to resemble a six-pointed star,

the cloud is not confined to a narrow focal plane as it might appear in figures 2 and 3. Instead, the cloud spans throughout much of the volume of the faceted stone. Creative faceting by the polisher provides a unique perspective on the cloud inclusion that makes this unusual diamond even more memorable.

Sally Eaton-Magaña and Nathan Renfro
GIA, Carlsbad
Alpesh Vavadiya
GIA, Mumbai

Hematite “Rose” Inclusion in Aquamarine

Recently, a 23.67 ct pear cabochon aquamarine with light greenish blue color and poor clarity was sent to the Taiwan Union Lab of Gem Research (TULAB) for identification. Microscopic observation of this aquamarine from the basal direction showed a number of negative crystals and black to brown hematite, confirmed by Raman spectroscopy. Hematite inclusions in gems usually appear in shapes such as flaky, striped, dendritic, or filamentous. Yet the hematite inclusions in this aquamarine seem to resemble a rose blossom composed of mathematical fractals (figure 6). It is worth mentioning that the rose form of hematite is common in hand specimens but rarely seen as inclusions. Photomicrography with brightfield illumination reveals this unique inclusion that shares a dash of science and romance.

Shu-Hong Lin
Institute of Earth Sciences,
National Taiwan Ocean University
Taiwan Union Lab of Gem Research, Taipei

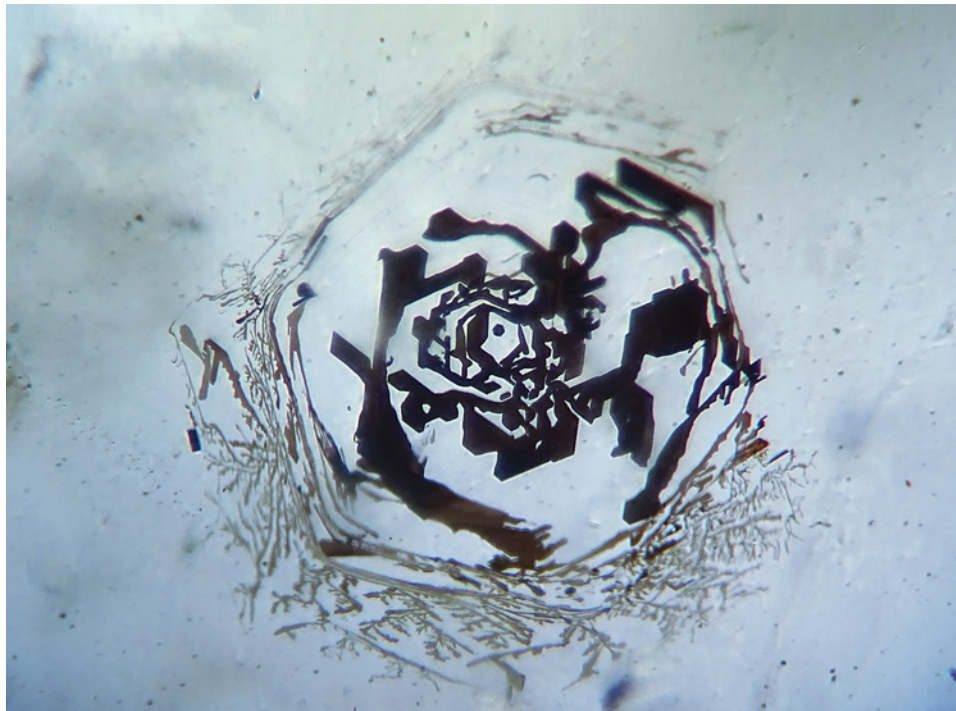
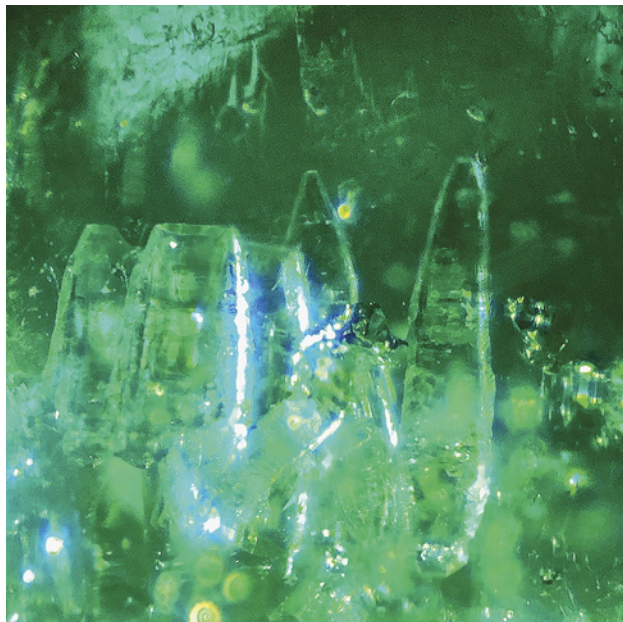


Figure 6. The aquamarine cabochon showed a fractal-like hematite inclusion with the beautiful outline of a rose. Photomicrograph by Shu-Hong Lin; field of view 0.64 mm.

Parasite Crystals in a Colombian Emerald

The author recently examined a 1.21 ct transparent faceted emerald. Gemological observation and chemical and spectroscopic analysis indicated that this natural emerald orig-

Figure 7. Parasite crystals in an emerald from Colombia, shown under oblique fiber-optic illumination. Photomicrograph by Kyaw Thu; field of view 0.125 mm.



inated from Colombia. Moreover, microscopic examination with a combination of oblique fiber-optic and darkfield illumination presented the classic jigsaw pattern with a three-phase inclusion; this type of primary fluid inclusion is relatively common in Colombian emeralds. Interestingly, oblique fiber-optic illumination detected some colorless transparent crystal inclusions surrounded by fluid, as seen in figure 7.

Raman microspectrometry analysis of the well-formed prismatic crystals indicated that the unusual fluorocarbonate minerals were parasite. These very rare parasite mineral inclusions have been found only in emeralds from the Muzo mine (Winter 1982 Lab Notes, p. 230; E.J. Gübelin and J.I. Koivula, *Photoatlas of Inclusions in Gemstones*, Vols. 1–3).

Kyaw Thu
S Gemmological Institute
Yangon, Myanmar

Iridescent Botryoidal Growth in Untreated Akoya Pearl

Cultured akoya pearls (*Pinctada fucata*) are typically admired for their high luster and desirable overtone. Nearly all pearls from this species undergo color treatment before entering the market. One untreated akoya pearl examined by the author exhibited an iridescent and botryoidal sub-surface appearance when viewed with a fiber-optic light under microscopic magnification (figure 8). This was in sharp contrast to the pearl's appearance without magnification, which showed a light gray bodycolor and smooth surface.

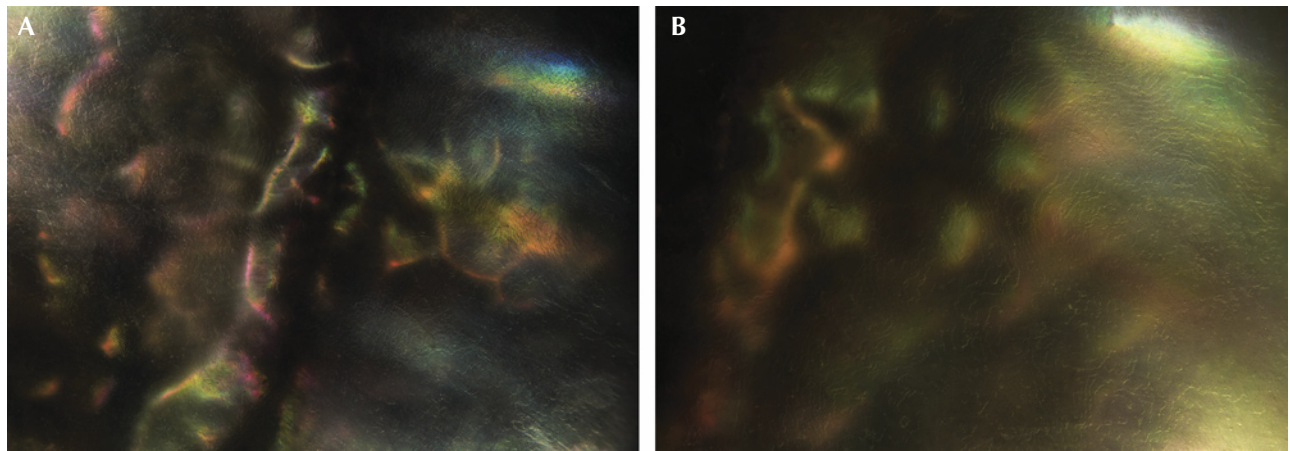


Figure 8. Iridescent and botryoidal subsurface growth seen in a pair of untreated akoya pearls. Note the nacre lines visible at the surface (top right of image B), giving context to the unusual growth and phenomenon below the surface. Photomicrographs by Britni LeCroy; field of view 3.57 (A) and 2.34 mm (B).

The light gray bodycolor of the pearl was caused by large voids or gaps surrounding its bead nucleus, which could be seen using real-time X-ray microradiography (RTX). Akoya pearls possess very thin nacre platelets that are transparent to translucent when viewed under strong lighting, allowing the viewer to see into the deeper layers of the pearl. The strong iridescence was caused by light interference within alternating layers of aragonite and conchiolin—the two substances that create nacreous pearls and that also have different refractive indices. Specifically, this iridescence is caused when incoming overhead light is reflected from the surfaces between the successive aragonite and conchiolin layers. When the reflected light rays from a bottom layer of nacre interfere with the incoming light, iridescence is created. In pearls, this feature is known

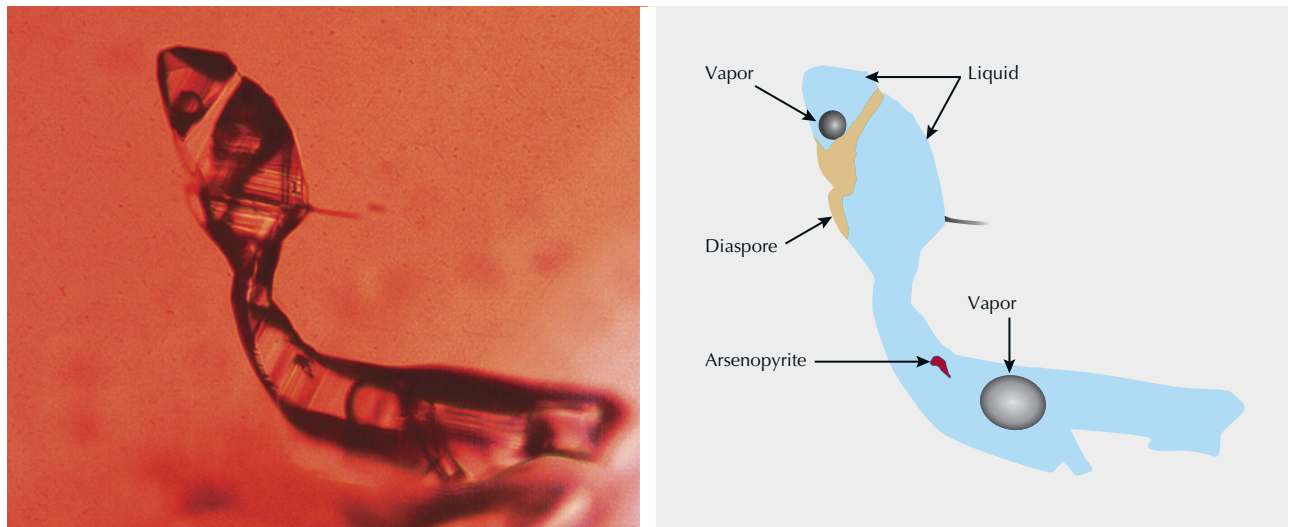
as orient (E. Fritsch and G.R. Rossman, “An updated on color in gems. Part 3: Colors caused by band gaps and physical phenomena,” Summer 1988 *G&G*, pp. 81–102). The underlying botryoidal structure combined with the iridescence from the overlying nacre was responsible for the unusual pattern or orient seen in this akoya pearl. This is the first time the author has encountered such a phenomenon in a pearl.

Britni LeCroy
GIA, Carlsbad

Fascinating Fluid Inclusions in Chinese Ruby

Gem rubies from the Yuanjiang deposit in Yunnan Province, China, host mineral inclusion assemblages com-

Figure 9. Fluid inclusion mimicking a snake in Yuanjiang ruby from China (left). The diagram on the right shows the details of this “snake.” Photomicrograph by Wenqing Huang; field of view 0.26 mm.



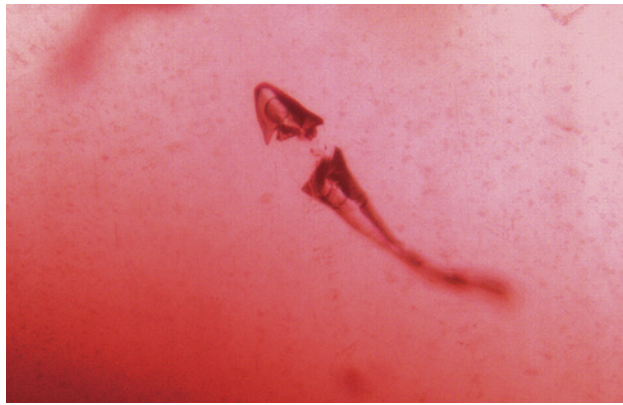


Figure 10. This Yuanjiang ruby from China contains an interesting fish-like fluid inclusion. Photomicrograph by Wenqing Huang; field of view 0.17 mm.

parable with those in rubies from other marble-hosted deposits (W.Q. Huang et al., "Trace element geochemistry and mineral inclusions constraints on the petrogenesis of a marble-hosted ruby deposit in Yunnan Province, China," *Canadian Mineralogist*, Vol. 59, No. 2, 2021, pp. 381–408). Moreover, the fluid inclusion scenes in rubies from all of these deposits are also similar (G. Giuliani et al., "Fluid inclusions in ruby from Asian marble deposits: Genetic implications," *European Journal of Mineralogy*, Vol. 27, No. 3, 2015, pp. 393–404).

Two rubies from the Yuanjiang deposit showed several interesting fluid inclusions. The most impressive one strongly resembles a snake raising its head (figure 9). The other mimics a fish (figure 10). As shown in figures 9 and 10, the whole fluid cavity was split into two parts, both of which show a bubble. Raman spectroscopy analysis identified the transparent tabular crystals in the snake as diaspore (figure 9). The "snake" also hosted a solid inclusion of arsenopyrite (FeAsS); the needle on its head could not be characterized by Raman spectroscopy due to its fineness. The fluid composition was dominated by CO₂ with minor components such as H₂S, COS, and CH₄, as revealed by Raman spectra and microthermometry. How these special inclusions formed has been speculated elsewhere (W.Q. Huang, "Fluid inclusion and titanite U–Pb age constraints on the Yuanjiang ruby mineralization in the Ailao Shan–Red River metamorphic belt, southwest China," *Canadian Mineralogist*, 2021, accepted). This morphology-forming process has been explained by two mechanisms that evolved step by step. The first is morphological ripening that resulted in negative shapes of fluid inclusions; the second consists of subsequent reactions between the trapped H₂O and the host corundum during the cooling of the inclusion, generating a diaspore that segregated the fluid completely.

Inclusions (mostly mineral inclusions) in gemstones that mimic scenery and landscapes are fascinating and relatively common. One novelty inclusion, an interesting "fried egg" of epigenetic residue trapped in a fissure, was

recently found in rock crystal quartz (Fall 2020 *G&G Micro-World*, pp. 430–431). However, such novelty inclusions, especially fluid inclusions mimicking animals, are exceptionally rare.

Wenqing Huang (67019822@qq.com)
National Center of Supervision and Inspection on
Quality of Gold and Silver Products
Nanjing Institute of Product Quality Inspection
Nanjing, China

Tourmaline in Paraíba Tourmaline

The authors examined the 3.21 ct Paraíba tourmaline shown in figure 11. The stone was moderately included with fine thread-like trichite fluid inclusions, growth tubes, and many fractures. Growth tubes are often open on one or both ends and may contain epigenetic minerals encapsulated within such as limonite, cookeite, hematite, prosopite, and tourmaline (E.J. Gübelin and J.I. Koivula, *Photoatlas of Inclusions in Gemstones*, Vol. 2, pp. 763, 764, and 780–781). In this tourmaline, we observed a long prismatic crystal that had a morphology consistent with tourmaline, which was confirmed using Raman spectroscopy. This offered an interesting example of a gem tourmaline that contained a tourmaline inclusion.

Sudarat Saeseaw and Suwasan Wongchacree
GIA, Bangkok

Willemite in Topaz

The authors recently had the opportunity to examine a 28.61 ct transparent freeform custom-cut study block of colorless topaz (figure 12) from Jos in Plateau State, Nigeria, that hosted a very large forest green inclusion of chlorite with an intricate stepped surface structure. Magnification showed that the chlorite inclusion was partially rimmed by

Figure 11. A tourmaline inclusion in Brazilian Paraíba tourmaline. Photomicrograph by Suwasan Wongchacree; field of view 4.8 mm.



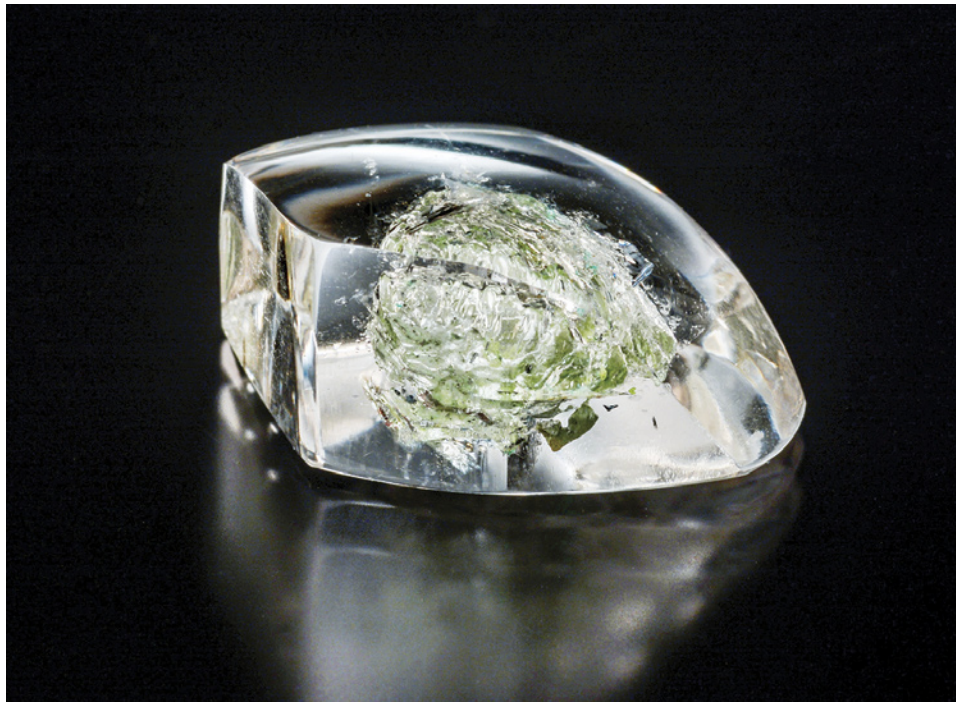


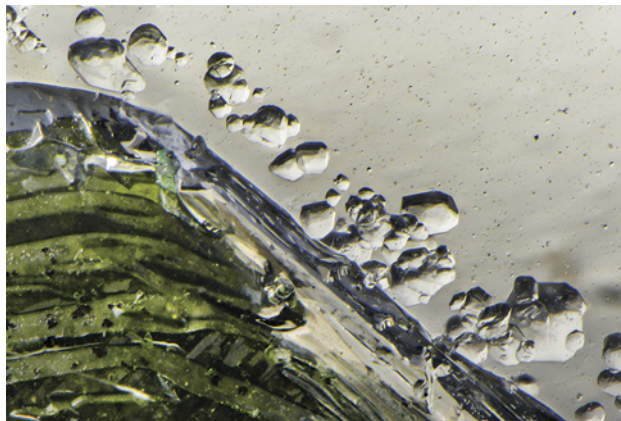
Figure 12. This 21.36 × 14.94 × 9.44 mm custom-cut study block of topaz from Jos, Nigeria, is host to several interesting inclusions. Photo by Diego Sanchez.

transparent near-colorless crystals (figure 13) identified by laser Raman microspectrometry as willemite (Zn_2SiO_4), a trigonal zinc silicate.

The willemite crystals in this topaz fluoresced bright yellow-green to short-wave ultraviolet radiation, giving the chlorite a partial fluorescent halo. This is the only known example of the mineral willemite as inclusions in topaz from any locality.

In addition to the willemite, bright bluish green patches of color on the chlorite might be the microcline feldspar amazonite, but Raman analysis could not identify them.

Figure 13. Transparent colorless willemite crystals appear to be tumbling down the slope of a large chlorite inclusion in a Nigerian topaz. Photomicrograph by Nathan Renfro; field of view 4.02 mm.



There were also some tiny rounded opaque inclusions with metallic luster that resembled metal sulfides. Bright red epigenetic hematite was found in one surface-reaching cleavage crack, and a few tiny transparent brownish yellow high-relief crystals of sphalerite were also present with the willemite.

John I. Koivula and Nathan Renfro
GIA, Carlsbad

Quarterly Crystal: Fibers and Rods in Euclase

From time to time in the laboratory, we run into problems that we just cannot resolve. Just such a situation was recently encountered when we examined a very unusual 10.82 ct transparent euhedral crystal of orange-pink euclase measuring 14.71 mm wide, pictured in figure 14. We knew from experience that the natural surface striations on this transparent crystal would make conclusive identification of the inclusions difficult at best. The euclase crystal, recently recovered during limited mining in Livramento de Nossa Senhora in Bahia, Brazil, was acquired from Luciana Barbosa of the Gemological Center in Asheville, North Carolina. The cause of the unusual padparadscha-like orange-pink color of this euclase production was determined to result from impurities of Mn^{3+} (L. Gilles-Guéry et al., "Mn³⁺ and the pink color of gem-quality euclase from northeast Brazil," accepted by *American Mineralogist*, 2021).

On examination with a gemological microscope, we observed fine branching fibers and rods of white to red-brown color suspended in the euclase (figure 15). The red-brown color of some of the inclusions suggested epigenetic alteration at some point. As shown in the photomicrograph



Figure 14. The orange-pink color of this 10.82 ct Brazilian euclase is reminiscent of padparadscha sapphire. Photo by Diego Sanchez.

in figure 16, we observed a tiny hollow cylindrical void containing a dark brown fluid and a mobile gas bubble. The color of the fluid made it difficult to clearly see the gas bubble, unless it was moving.

As we suspected, laser Raman microspectrometry could not pin down the identification of the inclusions. Raman testing only showed the peaks for the euclase host. We also tried energy-dispersive X-ray fluorescence (EDXRF) to pick up any hints of unusual chemistry, but again useful information eluded us. After several tries at both Raman

and EDXRF, we finally realized that destructive analysis would be needed for a clear identification of the inclusions. Since this well-formed euclase crystal has a very rare and unusual color, we decided not to use destructive analysis. We would keep the euclase intact, to be enjoyed as a gem mineral specimen.

*John I. Koivula and Nathan Renfro
Ian Nicastro
San Diego, California*

Figure 15. Attempts to identify these acicular inclusions discovered in the 14.71 mm euclase crystal proved unsuccessful. Photomicrograph by Nathan Renfro; field of view 2.56 mm.

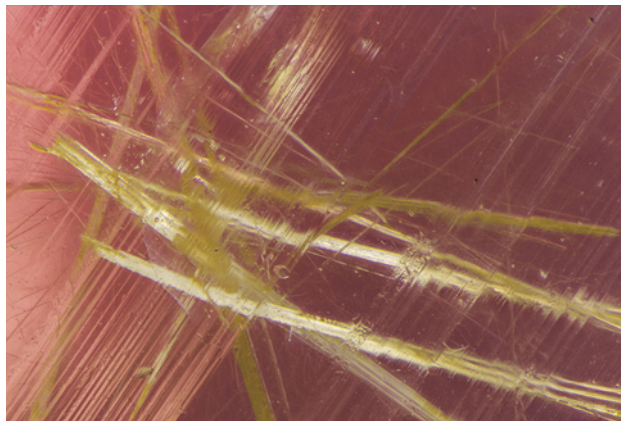
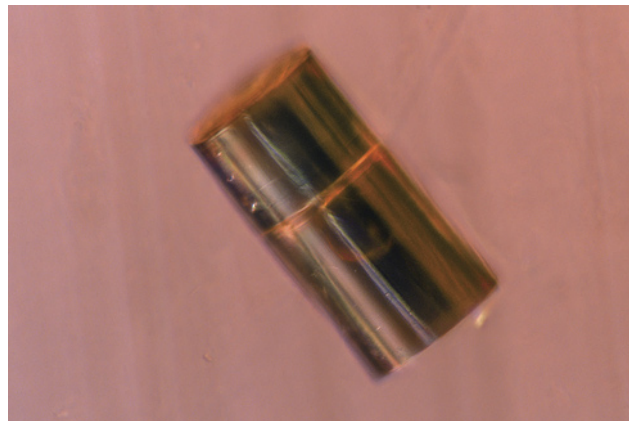


Figure 16. With a dark brown fluid and a moving bubble, this tiny cylindrical void was a surprising discovery. Photomicrograph by Nathan Renfro; field of view 0.288 mm.





Gem News International

Contributing Editors

Emmanuel Fritsch, *University of Nantes, CNRS, Team 6502, Institut des Matériaux Jean Rouxel (IMN), Nantes, France* (fritsch@cnsr-immn.fr)

Gagan Choudhary, *Gem Testing Laboratory, Jaipur, India* (gagan@gjepcindia.com)

Christopher M. Breeding, *GIA, Carlsbad* (christopher.breeding@gia.edu)

COLORED STONES AND ORGANIC MATERIALS

Fura Gems' inaugural ruby sale. Fura Gems hosted its first sales event for rough Mozambican rubies in August and September 2021. The international gem mining and marketing company has assets in Colombia (emerald), Australia (sapphire), and Mozambique (ruby). After previous sales events for Colombian emeralds in the first months of 2021, the firm now offered its rubies to the trade for the first time.

Mozambican rubies have been available in the trade since 2009, and the region quickly became one of the most important sources for the red variety of corundum. Fura is only the third company to bring rubies to the trade in a formalized tender. During the first years after the deposit's discovery in 2009, gems were recovered by artisanal miners and traded locally.

In 2014, the first large-scale sale of Mozambican rubies by an organized mining group took place. During that tender, Gemfields offered nearly two million carats of rough ruby, and they have hosted 14 auctions since then. Mustang Resources hosted a rough ruby tender in 2017, which was not well received by the trade. Fura took over existing ruby mining permits and equipment in Mozambique from various companies, including Mustang Resources, acquiring the largest ruby mining license in the country.

Invited buyers were able to view Fura's rubies in Jaipur and Bangkok, locations that host the largest colored stone manufacturing industries in the world. Each company was able to view the stones over two days in a secured space. Precautions against COVID-19 included a limited number of attendees per day, which caused the entire event to last

more than 24 days across the two locations. This allowed all potential buyers ample time to inspect the rough rubies.

The rough gems were offered in pre-graded schedules, based on size and color. The grading system was designed with the gem cutting process in mind, especially aiming for the most commonly used calibrated sizes. Stones with similar hues are put in the same category, creating separate classes for stones with purer red color vs. those with a stronger orangy/purplish tint. Stones with lower saturation are separated from those with stronger saturation. Specific grades are designed to highlight those with lighter colors that would result in fancy sapphires such as pink and reddish orange.

All stones were offered as found in the mine and untreated. A significant percentage of Mozambican rubies can benefit from heat treatment to lighten the color, but this decision was left to the final buyer. While heat treating rubies might improve their appearance, it can also lower the value in the current market. This is especially true for larger stones.

Figure 1. Small lots made up of stones weighing more than 1 g often showed more color variety within a single grade. Photo by Wim Vertriest, courtesy of Fura Gems.



Editors' note: Interested contributors should send information and illustrations to Stuart Overlin at soverlin@gia.edu or GIA, The Robert Mouawad Campus, 5345 Armada Drive, Carlsbad, CA 92008.

GEMS & GEMOLOGY, VOL. 57, NO. 3, pp. 276–290.

© 2021 Gemological Institute of America



Figure 2. The majority of the stones offered were on the smaller side (below 0.5 g). These lots were highly desired by manufacturers for their intense colors and bulky appearance, which will result in smaller finished stones with a saturated body-color. Photo by Wim Vertriest; courtesy of Fura Gems.

The material showed a wide range of red tints, including strong orangy and purplish colors, but most goods still fell within the color range of ruby. Some stones had lighter saturation that could result in fancy sapphires, especially pinkish materials. This is in line with the regular production from Montepuez, Mozambique, that we have seen over the last decade. Rubies with a dark tone, sometimes referred to as “closed color,” were rare at this tender. All the material showed some fluorescence under long-wave UV, a feature that is absent in certain types of classic Mozambican ruby.

Over 63 kg of rough ruby was offered (figures 1 and 2). The vast majority of the rough weighed under 0.5 g, but with a bulky shape that would result in a good yield. A few hundred stones weighed more than 0.5 g, and some exceptional pieces exceeded 2 g.

The rough rubies had the typical rounded crystal appearance of gems found in secondary deposits, as was confirmed by Fura, which mines the material from gravels that contain a higher concentration of rubies. This is in contrast with primary deposits, where gems are extracted directly from the host rock.

Evaluating rough rubies is a challenging affair. Before assigning a value to a parcel, buyers had to account for each stone’s final shape and cutting style, weight, and potential improvement through treatment. They submitted closed bids via an online platform before the closing date. On closing day, Fura reviewed all the offers and, once accepted, notified the successful buyers.

The company reported that 35 of the 47 lots sold, including all high- to medium-grade lots. They also announced that the price per carat for goods in the calibrated sizes exceeded expectations. According to several ruby dealers, this category is in highest demand and the material was most attractive.

This auction comes at a time when the industry is struggling for rough stones, as many of the regular supply chains have been disrupted by the COVID-19 pandemic. The manufacturers have a clear hunger for rough rubies, though they also have limited financial reserves. Nevertheless, the addition of Fura as a Mozambican rough ruby supplier, along with Gemfields and the artisanal mining community, makes for an exciting change in the gem scene.

Wim Vertriest and Pitchaya Lopiti
GIA, Bangkok

Mabe cultivation in Mayotte. The Laboratoire Français de Gemmologie (LFG) received some mabe samples (figure 3) from Antoine Ganne of the Mayotte-based company Nuru Kombe for gemological characterization. According to the company, these samples were cultivated in *Pteria penguin* bivalves in a lagoon off the coast of Mayotte. This French territory is situated in the Indian Ocean between northwestern Madagascar and northeastern Mozambique, with one main island and several islets.

Mabe is the Japanese term designating an assembled cultured blister, traditionally from *Pteria penguin* but nowadays from other mollusks as well (CIBJO Pearl Commission, *The Pearl Book*, CIBJO, Milan, 2020, 79 pp.). Mabe is made of purpose-grown cultured blisters that have been cut from their shell. The original bead upon which they grew is removed, and the cavity is filled with various synthetic materials. It is then backed by a layer of shell, with the assemblage held together by an adhesive.

The studied samples ranged from light brown to brown (some of a “golden” color) with pronounced secondary colors such as blue, green, and red (again, see figure 3). Under the microscope, all samples presented the characteristic nacreous structures associated with overlapping layers of

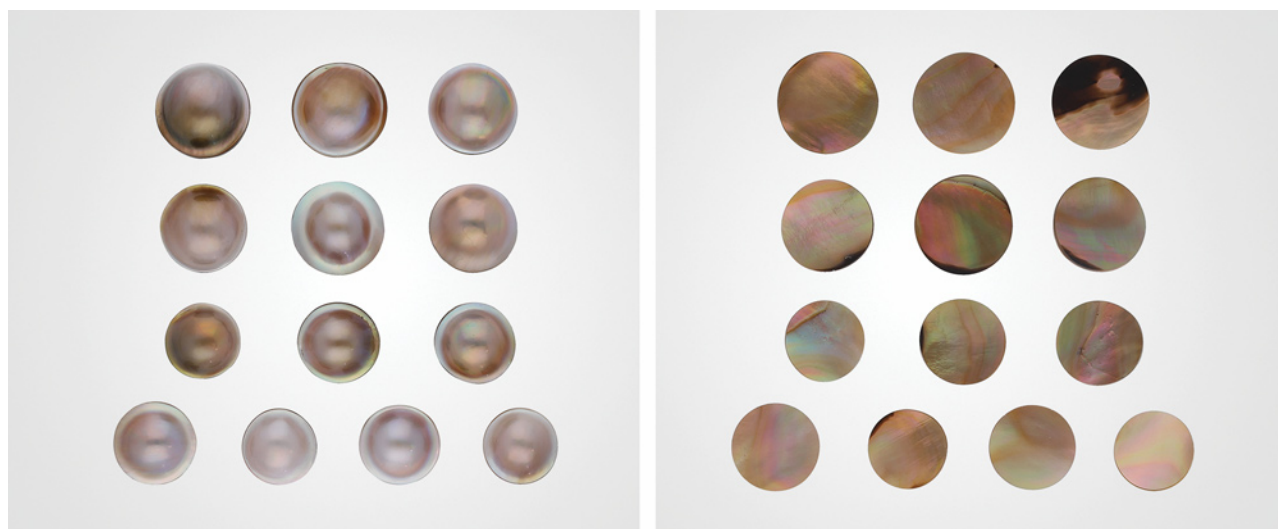


Figure 3. These assembled cultured blisters (*mabe*) showing a curved top (left) and flat bottom (right) were cultivated in Mayotte. The largest is 21 mm in diameter. Photos by LFG.

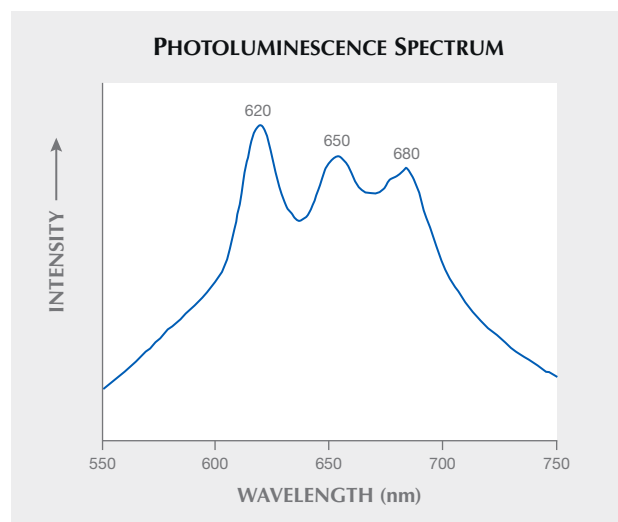
aragonite. The curved and flat sides looked very similar, suggesting they originated from the same mollusk species. The samples reacted purple to red under a long-wave UV lamp and remained inert under short-wave UV lamp excitation. Those with a more pronounced brown color exhibited a stronger intense luminescence. A similar luminescence reaction was observed in cultured pearls from *Pteria sterna* from Mexico (L. Kiefert et al., "Cultured pearls from the Gulf of California, Mexico," *Spring 2004 GeG*, pp. 26–38). This response is due to a type of porphyrin (a tetrapyrrole with a cyclic structure) that also plays an important role in the samples' coloration.

Raman analysis using a 514 nm laser revealed bands associated with aragonite along with a series of bands from 800 to 1600 cm^{-1} characteristic of porphyrins (S. Karampelas et al., "Raman spectroscopy of natural and cultured pearls and pearl producing mollusc shells," *Journal of Raman Spectroscopy*, Vol. 51, No. 9, 2020, pp. 1813–1821). Photoluminescence spectra obtained using a Raman spectrometer and the same laser excitation presented bands in the orange and red part of the electromagnetic spectrum at about 620, 650, and 680 nm (figure 4). The relative intensity of these bands can vary. Luminescence spectra using a xenon lamp with 365 nm excitation presented similar bands with additional bands at about 435, 465, and 525 nm. The latter bands are possibly linked to the nacre of the samples, while the triplet of bands at 620, 650, and 680 nm has been attributed to a uroporphyrin (Y. Iwahashi and S. Akamatsu, "Porphyrin pigment in black-lip pearls and its application to pearl identification," *Fisheries Science*, Vol. 60, No. 1, 1994, pp. 69–71).

The UV-Vis reflectance spectra of the samples featured a series of bands with various relative intensities at about 380, 400, 460, and 495 nm, along with a band at about 280 nm (figure 5). The latter band is linked to organic matter and the nacreous part of the samples, and the series is possibly linked to porphyrins (Kiefert et al., 2009).

All samples were inert under X-ray and EDXRF analysis, with an Mn content below the detection limit and Sr contents ranging from 3180 to 5280 ppm, indicating saltwater origin. X-ray microradiographs (figure 6) showed lighter tones at the rim, indicating a higher-density material such as calcium carbonate (usually aragonite) in the case of natural and cultured pearls, while the darker tones in the core indicated lower-density material such as organic matter and resin (S. Karampelas et al., "Real-time microradiography of pearls: A comparison between detectors," Winter 2017

Figure 4. Photoluminescence spectrum of a brown *mabe* sample from Mayotte using a Raman spectrometer under 514 nm laser excitation. Three bands appearing at the orange and red parts of the electromagnetic spectrum at about 620, 650, and 680 nm are linked with uroporphyrin.



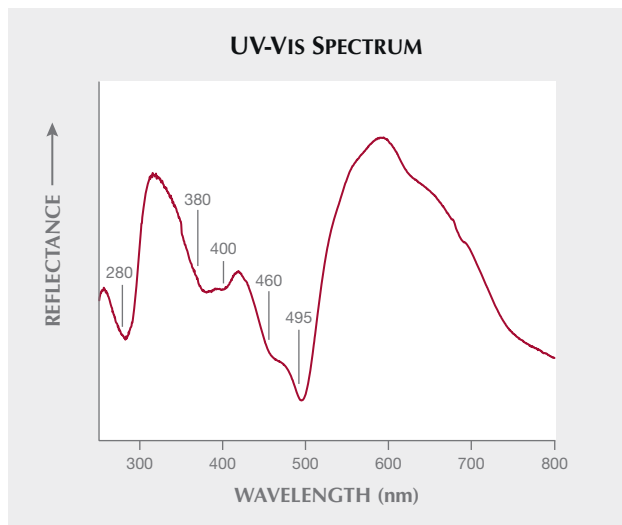


Figure 5. The UV-Vis spectrum of a brown mabe sample from Mayotte displays bands at about 380, 400, 460, and 495 nm that are linked to porphyrin, along with a band at about 280 nm that is linked to nacre and organic matter.

G&G, pp. 452–456). The samples, which could be called “mabe” or “assembled cultured blister” according to the current CIBJO standards, had a nacre thickness from 0.4 to 1 mm (again, see figure 6).

Mabe from Mayotte has only appeared recently in the market. The exact supply is still unknown, and other similar products are cultivated in other parts of the world, including Southeast Asia, Australia, and some Pacific island nations (P.C. Southgate and J.S. Lucas, *The Pearl Oyster*, 2008, Elsevier, Amsterdam). Nevertheless, this material could help develop the economy of Mayotte, where all the operations take place and jewelry pieces with a French touch are locally made.

Sophie Leblan, Ugo Hennebois, Aurélien Delaunay, Bérengère Meslin Sainte Beuve, Annabelle Herreweghe, and Stefanos Karampelas (s.karampelas@lfg.paris) LFG, Paris

Maxence Vigier and Emmanuel Fritsch University of Nantes, CNRS-IMN, France

SYNTHETICS AND SIMULANTS

Honey brown and light yellow hydrogrossular: An uncommon jade imitation. Hydrogrossular or hydrogarnet is a translucent to opaque, water-bearing calcium aluminum silicate garnet that commonly shows microcrystalline texture. It has a range of colors: brown, colorless, green, gray, pink, and yellow. The most popular is the shade of green known in the trade as “Transvaal jade” or “African jade.” Recently, the GIT-Gem Testing Laboratory (GIT-GTL) received two samples of hydrogrossular garnet for identification: the light yellow carved pendant (~70 ct, 36 × 21 mm) and the honey

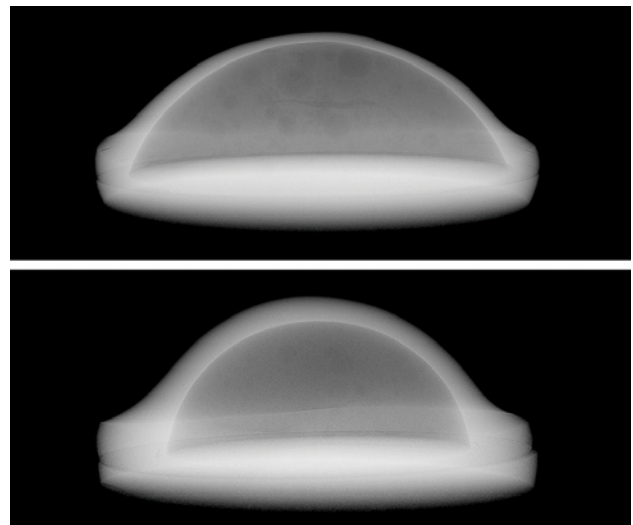


Figure 6. X-ray microradiographs of two mabe from Mayotte show a lighter rim due to higher-density material (calcium carbonate), while the darker tones at the core represent a lower-density material such as resin. The top sample (21 mm in diameter) has a nacre thickness of 0.4 mm. The bottom sample (13 mm in diameter) has a nacre thickness of 1 mm. Images by S. Leblan, LFG.

brown oval cabochon (8 ct, 15 × 12 mm) shown in figure 7. These are not typical colors used for jade imitations.

Standard gemological testing of the honey brown cabochon showed a specific gravity of ~3.66 and a refractive index of ~1.71, while those of the light yellow piece were

Figure 7. This light yellow carving (36 × 21 mm) and honey brown cabochon (15 × 12 mm) were identified as hydrogrossular. Photo by C. Kamemakanon; courtesy of Pachara Chonlakit.



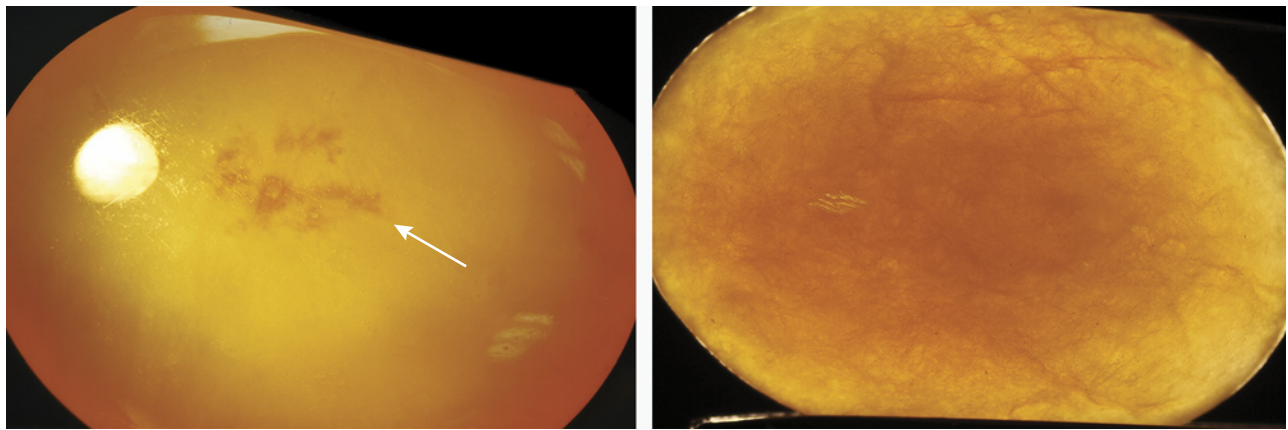


Figure 8. The microscopic observation of the honey brown hydrogrossular sample (left) revealed a fine-grained aggregate structure and color patches (white arrow), as compared with the coarse-grained aggregate structure of the brown jadeite sample (right). Oblique fiber-optic light. Photomicrographs by S. Promwongnan; field of view ~14 mm.

undeterminable due to the nature of the mounting and carving. Nonetheless, both stones exhibited weak red fluorescence to long-wave UV and were inert to short-wave UV radiation, and displayed massive fine-grained aggregate structures with a translucent glassy appearance (figure 8, left), which was quite different from the coarse-grained aggregate structure of jadeite (figure 8, right).

The identity was also confirmed by advanced testing. The Raman spectra of both samples showed dominant peaks at 374, 415, 548, 825, and 879 cm^{-1} and other smaller peaks at 246, 278, 508, 627, and 1005 cm^{-1} (figure 9) that matched perfectly with the spectrum of grossularite in the RRUFF reference database (R040065). Semi-quantitative chemical analyses of both stones revealed

enriched contents of silica, calcium, and aluminum, which are closely consistent with grossularite, a calcium-aluminum garnet.

The infrared spectrum of the honey brown cabochon sample, measured in reflection mode between 580–1400 cm^{-1} , showed characteristic reflectance peaks at 616, 843, 866, and 954 cm^{-1} that are similar to the spectra of the hydrogrossular reference sample (figure 10) as well as green hydrogrossular (see Fall 2015 GNI, pp. 342–343). Note that the reflectance spectrum should be almost identical to the transmission spectrum of the sample, and the same features should be observed in both cases.

The infrared spectra of both samples, measured in transmission mode between 1000 and 5000 cm^{-1} and dis-

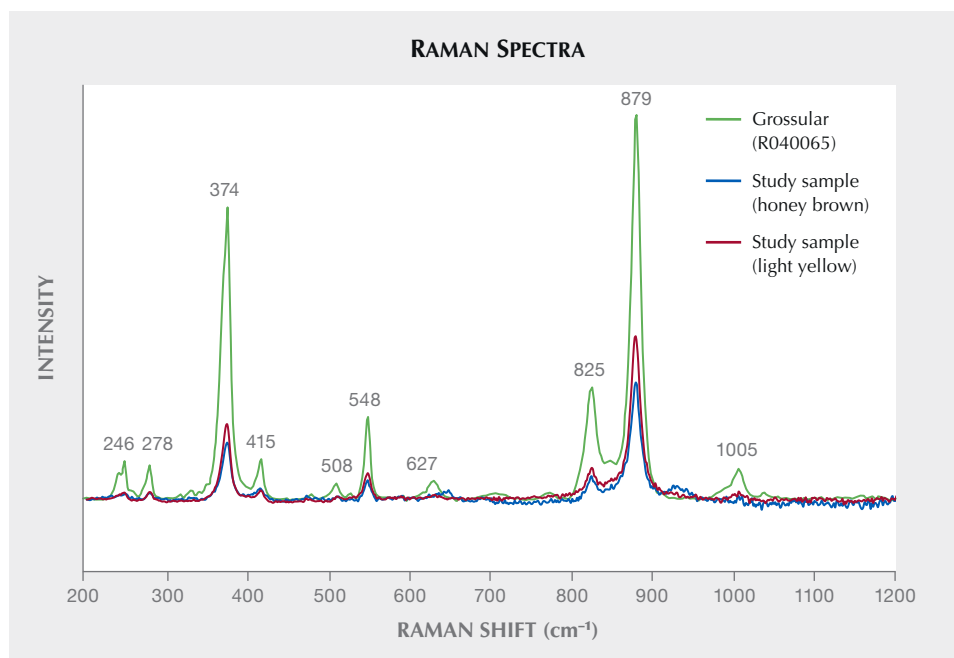


Figure 9. Raman spectra of the honey brown and light yellow samples (blue and red lines, respectively) as compared to the reference spectrum of grossularite from the RRUFF database (green).

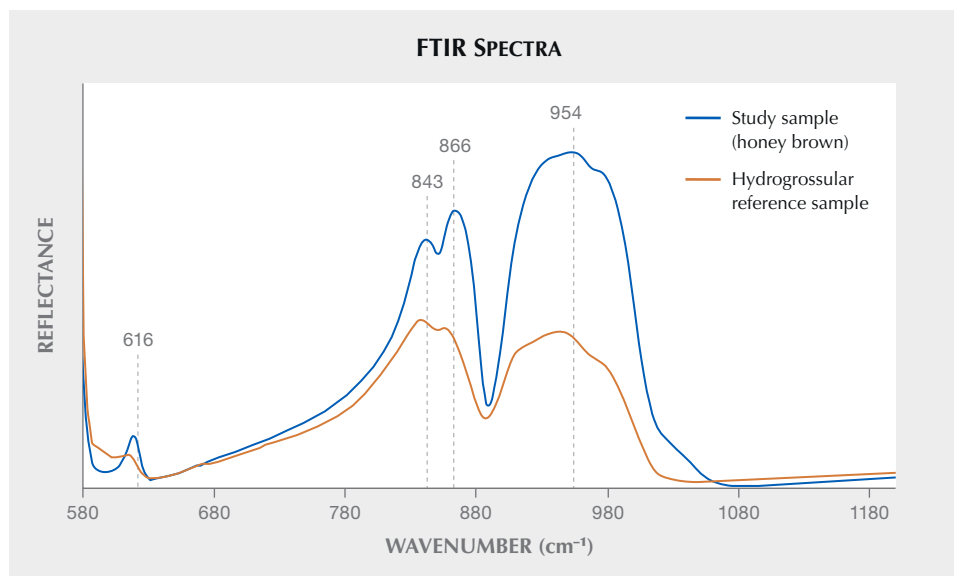


Figure 10. The infrared spectrum in reflection mode of the honey brown sample (blue line) exhibits characteristic reflectance peaks of hydrogrossular garnet at 616, 843, 866, and 954 cm^{-1} , as compared with the spectrum of the hydrogrossular reference sample (purple line). The spectrum of the light yellow sample was not measured due to the nature of the carving.

played in % transmittance, showed very strong broad absorption bands between $\sim 3000\text{--}4000\text{ cm}^{-1}$ that are somewhat similar to the spectrum of our hydrogrossular reference sample (figure 11), and coincide with water-related absorption bands of hydrogrossular ($>5\text{ wt.}\% \text{ H}_2\text{O}$) centered at 3598 and 3662 cm^{-1} (see G.R. Rossman and R.D. Aines, "The hydrous components in garnets: Grossular-hydrogrossular," *American Mineralogist*, Vol. 76, No. 7-8, 1991, pp. 1153–1164). In comparison, our grossular (tsavorite and hessonite) samples reveal much narrower absorption bands between 3500–3700 cm^{-1} (figure 11). Thus, the presence of very strong broad (water-related) absorption bands has confirmed that both stones submitted for investigation were indeed hydrogrossular.

In summary, the gemological properties, Raman spectra, and chemical compositions of the light yellow and honey brown samples are consistent with those of grossular garnet. However, the infrared spectra showing characteristic transmission peaks of hydrogrossular at 616, 843, 866, and 954 cm^{-1} and very strong occurrence of structural water (i.e., significant OH replacing Si in tetrahedral sites) have confirmed that these two stones are indeed hydrogrossular rather than grossular garnet. It is worth noting that one of the materials commonly used to imitate jade is fine-grained aggregate hydrogrossular garnet, not single-crystal garnet.

Supparat Promwongnan (psupparat@git.or.th),
Budsabakorn Srisataporn, and Jirapit Jakkawanvibul
Gem and Jewelry Institute of Thailand (GIT), Bangkok

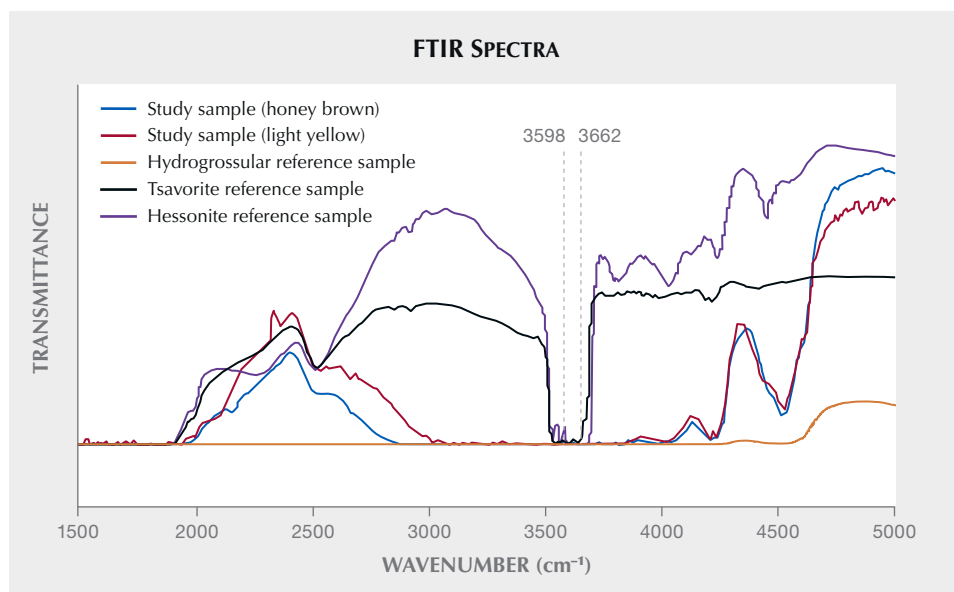


Figure 11. Infrared spectra by transmission mode of the honey brown and light yellow samples (blue and red lines, respectively) show very strong broad (water-related) absorption bands between $\sim 3000\text{--}4000\text{ cm}^{-1}$ as compared with the spectra of a hydrogrossular reference sample (purple line) and grossular (tsavorite and hessonite) samples (green and black lines, respectively). The vertical dashed lines at 3598 and 3662 cm^{-1} mark water-related absorption bands of hydrogrossular ($>5\text{ wt.}\% \text{ H}_2\text{O}$) based on Rossman and Aines (1991).

Pink aventurine quartz with alurgite inclusions. “Strawberry quartz” is not a strictly defined term in gemology but generally recognized in the market as single-crystal quartz with numerous striped or flaky hematite inclusions, which cause a pink to red overall appearance (D.I. Belakovskiy, “New acquisitions of the Fersman Mineralogical Museum, Russian Academy of Sciences (1997–2001),” *New Data on Minerals*, Vol. 38, 2003, pp. 101–112). Strawberry quartzes, due to limited mine production and rough sizes, are usually cut into beads, cabochons, or faceted stones or used for small carvings, all very popular products in the Taiwanese market.

Recently, a bangle was submitted for identification service to the Taiwan Union Lab of Gem Research (TULAB) as strawberry quartz (figure 12). The bangle had a brownish pink color in appearance and had a number of orangy pink to orangy red flaky crystals visible under the microscope. It had a refractive index of 1.54 and a specific gravity of 2.60. The material was found to be crystal aggregates through a polariscope and showed aventurescence under penlight.

In order to identify this material and its inclusions, the bangle was analyzed with micro-Raman spectrometry and the RRUFF database. It was found that the material was actually polycrystalline quartz and the red flaky inclusions were muscovite ($\text{KAl}_2(\text{Si}_3\text{Al})\text{O}_{10}(\text{OH},\text{F})_2$) (figure 13). SEM-EDS analysis of the inclusions exposed to the surface further verified them as iron-bearing muscovite; however, EDXRF analysis revealed trace amounts of manganese in addition to iron. In other words, this bangle should be defined as brownish pink aventurine quartz with pink to red muscovite inclusions. In comparison to those strawberry quartz



Figure 12. This bangle was submitted as “strawberry quartz” to TULAB. Photo by Shu-Hong Lin.

with hematite inclusions, the red muscovite showed slight differences under the microscope. Hematite inclusions in strawberry quartz are usually striped, hexagonal, or irregular flaky crystals with medium to very dark red color under the microscope (figure 14, left); however, the red muscovite inclusions in the sample were mostly rounded flaky crystals with medium light to medium orangy red color (figure 14, right).

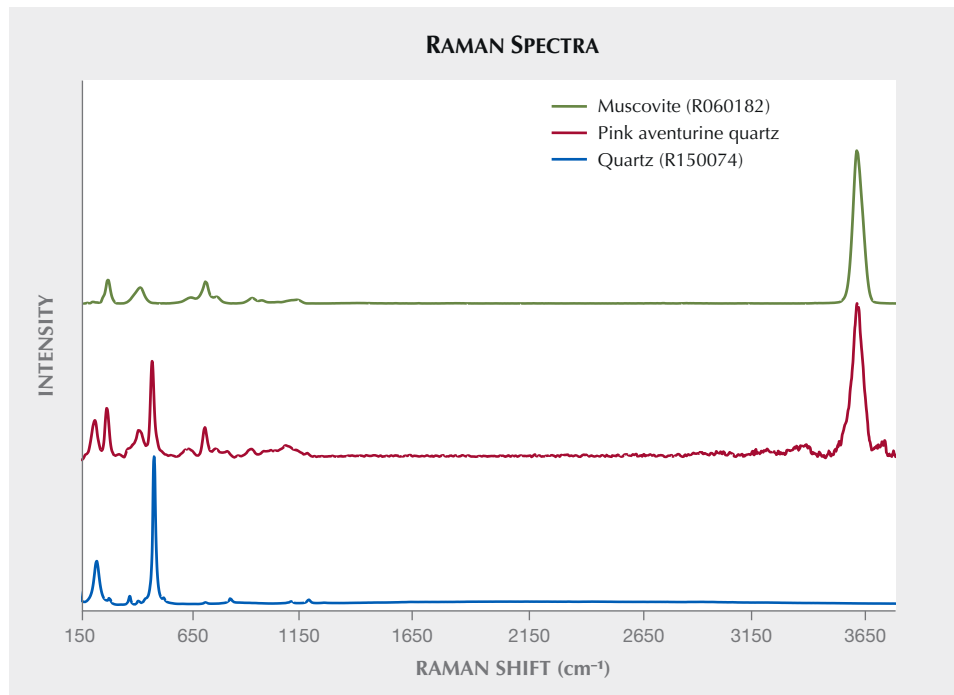


Figure 13. Raman spectra comparisons between the red inclusions and those of quartz and muscovite from the RRUFF database identified the bangle as aventurine quartz with orangy red muscovite inclusions. The stacked spectra are baseline-corrected and normalized.

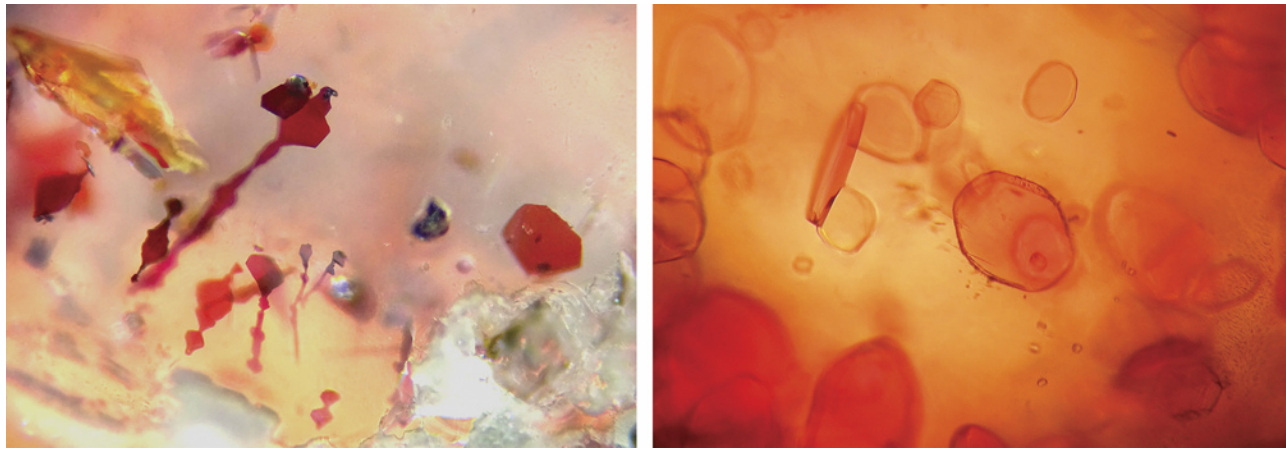


Figure 14. Microscopic images of the red striped and irregular flaky hematite in strawberry quartz (left) and the orangy red muscovite (alurgite) inclusions in the pink aventurine quartz sample (right). Photomicrograph by Shu-Hong Lin; field of view 1.26 mm.

Moreover, the visible light absorption spectra of the bangle were analyzed and compared to those of mica on the Mineral Spectroscopy Server of Caltech. The pink aventurine quartz presented absorption peaks at 445, 454, 515, and 548 nm (figure 15), consistent with the spectrum of alurgite (GRR727, Mineral Spectroscopy Server of Caltech), which is a reddish purple variety of muscovite.

Since “strawberry quartz” is not a strictly defined marketing name, consumers should notice that there are actually different types of quartz with various inclusions sold with the same trade name. As an atypical strawberry quartz material, pink aventurine quartz with alurgite can be distinguished with hematite-included strawberry quartz

through the methods of polariscope, microscope, and micro-Raman spectroscopy.

Shu-Hong Lin

Institute of Earth Sciences,

National Taiwan Ocean University

Taiwan Union Lab of Gem Research, Taipei, Taiwan

Yu-Ho Li

Institute of Earth Sciences,

National Taiwan Ocean University

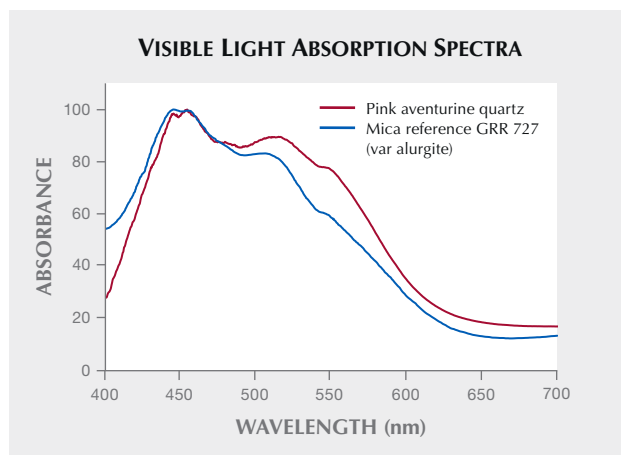
Huei-Fen Chen

Institute of Earth Sciences,

National Taiwan Ocean University

Center of Excellence for Oceans, National Taiwan Ocean University, Keelung, Taiwan

Figure 15. The visible light absorption spectrum of the pink aventurine quartz was compared to the reference spectrum of mica (Mineral Spectroscopy Server of Caltech); results revealed that the visible light absorption spectra were consistent with that of alurgite. The overlapped spectra are normalized.



TREATMENTS

FTIR observation on sapphires treated with heat and pressure. Characteristics of sapphires heated with pressure have been discussed in several gemological publications in the past few years (e.g., M.S. Krzemnicki et al., “Sapphires heated with pressure – A research update,” *InColor*, Vol. 42, 2019, pp. 86–90). As previously reported, heat with pressure treatment is commonly applied to Sri Lankan sapphires, in either untreated geuda or conventionally heated blue sapphires, to enhance the blue color. The material has been treated at high temperature (approximately 1200–1800°C) with an application of pressure at nearly 1 kbar, using the facilities at HB Laboratory Co., Ltd. (H. Choi et al., “Sri Lankan sapphire enhanced by heat with pressure,” *The Journal of the Gemmological Association of Hong Kong*, Vol. 39, 2018, pp. 16–25).

Fourier-transform infrared (FTIR) spectroscopy is considered a useful tool in revealing heat treatment of corundum (e.g., C.P. Smith, “A contribution to understanding the infrared spectra of rubies from Mong Hsu, Myanmar,” *Journal*

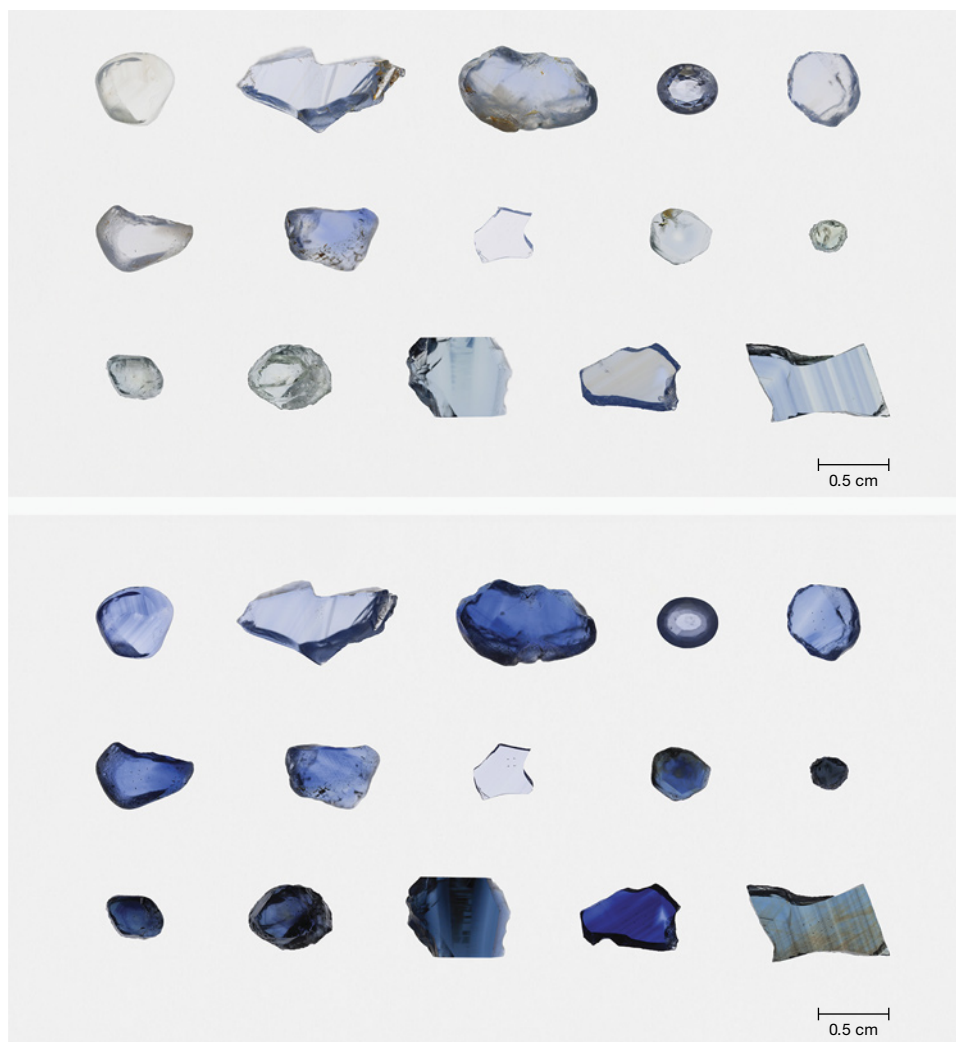


Figure 16. Color-calibrated photos of blue sapphires from different origins in the study before (top) and after (bottom) heat with pressure treatment. Photos by Sasithorn Engniwat.

of *Gemmology*, Vol. 24, 1995, pp. 321–335). Previous studies reported a great variability of FTIR spectra for sapphires heated with pressure, and FTIR spectra of this treated material generally showed a unique pattern of hydroxyl-related broad bands in the 2800–3500 cm^{-1} range, with the prominent position at around 3050 cm^{-1} (e.g., Krzemnicki et al., 2019). The origin of the resulting distinct IR broad bands has not been clearly determined. As discussed in Krzemnicki et al. (2019), broad bands centered at around 3050 cm^{-1} in sapphires heated with pressure share similar IR features observed in some acceptor-dominated corundum—heated or unheated natural materials, as well as laboratory-grown samples. (Acceptors refer to ions with the charge of -1 relative to the lattice, such as Mg^{2+} in corundum; see E.V. Dubinsky et al., “A quantitative description of the cause of color in corundum,” Spring 2020 *G&G*, pp. 2–28.)

According to a previous study (M.D.T. Phan, “Internal characteristics, chemical compounds and spectroscopy of sapphire as single crystals,” PhD dissertation, University of Johannes Gutenberg Mainz, 2015, <https://dnb.info/1075170532/34>), iron (Fe^{3+}) content in corundum

can affect the position of the 3310 cm^{-1} IR peak. In sapphires heated with pressure, the starting material is generally limited to Sri Lankan stones. Since blue sapphires from Sri Lanka typically contain relatively low Fe concentrations (A.C. Palke et al., “Geographic origin determination of blue sapphires,” Winter 2019 *G&G*, pp. 536–579), the starting materials used in the study were expanded to various deposits, including Myanmar, Madagascar, Sri Lanka, Montana, Australia, Nigeria, Cambodia, and Thailand, to cover a wide range of Fe contents presented in natural corundum (figure 16). The 36 untreated and 8 conventionally heated blue sapphires were treated using heat with pressure under the conditions reported in Choi et al. (2018). Their FTIR spectra and chemical analysis using laser ablation–inductively coupled plasma–mass spectrometry (LA-ICP-MS) were measured in the same analysis area to observe whether there was any change in FTIR spectra for different amounts of Fe. After heat with pressure treatment, the vast majority of treated sapphires in this study (>90%) showed essentially the same hydroxyl-related IR broad bands in the 2800–3500 cm^{-1} range with different prominent band posi-

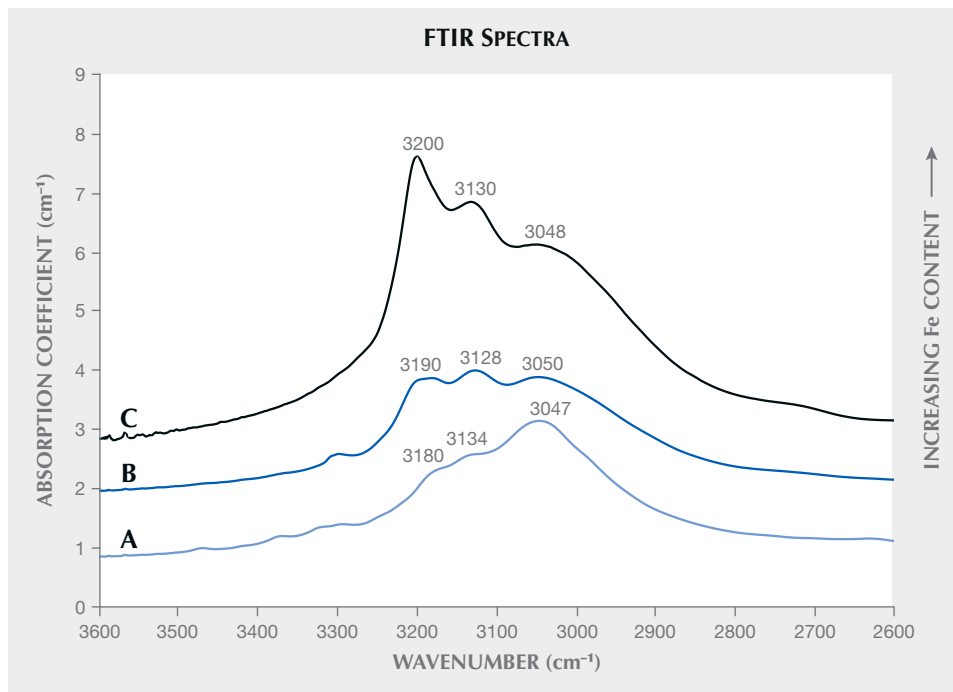


Figure 17. Comparison of representative non-polarized FTIR spectra from sapphires heated with pressure at different Fe concentrations: (A) 275 ± 25 ppma Fe, (B) 927 ± 48 ppma Fe, and (C) 2280 ± 163 ppma Fe. Spectra are offset vertically for clarity.

tions at around 3050, 3130, or 3200 cm^{-1} (figure 17). The IR broad band centered at around 3050 cm^{-1} with related bands at ~ 3130 and ~ 3200 cm^{-1} (figure 17A) can be observed in sapphires heated with pressure that contained Fe <700 ppma (figure 18, circle), whereas IR broad bands with comparable band intensities at around 3050, 3130, and 3200 cm^{-1} (figure 17B) can be found in treated sapphires with 550–1350 ppma Fe (figure 18, triangle).

At relatively high Fe concentrations (>900 ppma) (figure 18, square), the FTIR spectra of sapphires heated with pressure displayed IR broad bands with a prominent band position at around 3200 cm^{-1} (figure 17C). In the overlapped Fe range of the samples (500–700 ppma Fe and 900–1350 ppma Fe), different IR patterns could be obtained, possibly due to heterogeneity of the samples and different characteristics of analytical techniques—bulk analysis for FTIR and spot analysis for LA-ICP-MS.

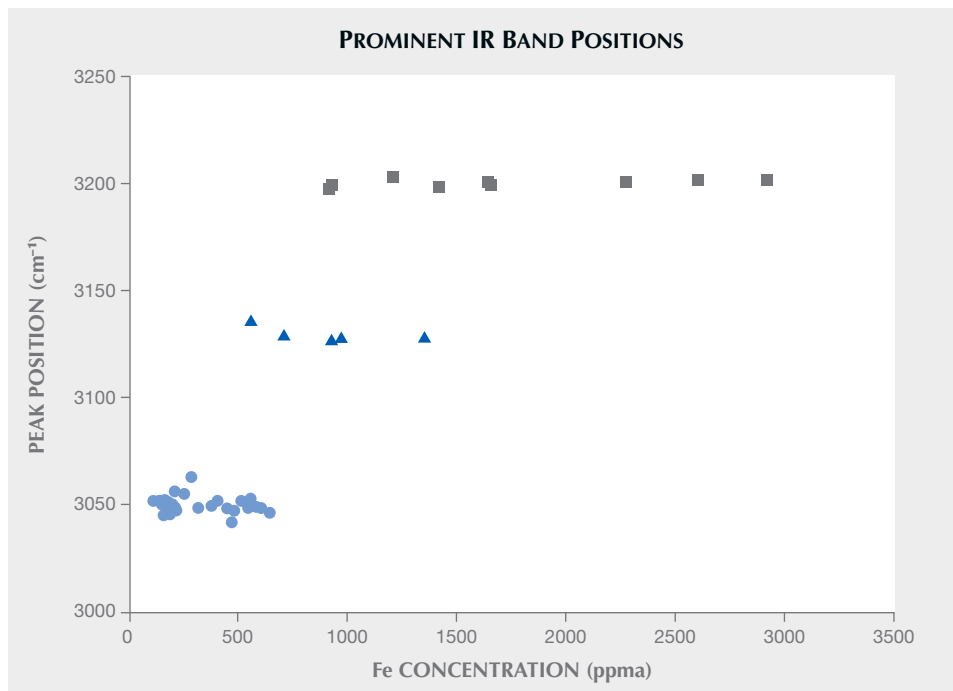


Figure 18. The relationship between which band of multiple IR absorption bands is prominent for sapphires heated with pressure and Fe concentrations analyzed by LA-ICP-MS of the treated materials. The circle (●), triangle (▲), and square (■) symbols correspond to FTIR patterns A, B, and C, respectively, from figure 17.

This study shows other possible FTIR spectra patterns that might be observed in sapphires heated with pressure, as well as prominent IR bands of the treated material that can shift position with different Fe concentrations.

Wasura Soonthorntantikul and Sudarat Saeseaw
GIA, Bangkok

Aaron Palke and Shane McClure
GIA, Carlsbad

Heat treatment effects on the behavior of the 3161 cm^{-1} feature in low-iron metamorphic yellow sapphire. Heating is the most common treatment to improve the color and/or clarity of corundum. Untreated natural yellow sapphires from metamorphic deposits often have low color saturation; therefore, heat treatment is typically performed to intensify the yellow coloration. However, the chemical composition of the stones, the heating temperatures employed, the duration of the treatment process, as well as the composition of the furnace atmosphere—reducing or oxidizing—are also important factors that influence the color alteration (K. Nassau, "Heat treating ruby and sapphire: Technical aspects," Fall 1981 *G&G*, pp. 121–131; J.L. Emmett et al., "Treatments," in R.W. Hughes, Ed., *Ruby & Sapphire: A Gemologist's Guide*, 2017, pp. 197–247).

The identification of heat treatment in a yellow sapphire is challenging for gemologists. Apart from visible inclusion changes, Fourier-transform infrared (FTIR) absorption spectra are one of the few remaining clues to identify the treatment of low iron content metamorphic yellow sapphires. These sapphires as formed are acceptor dominated when $[\text{Mg}^{2+}] > [\text{Ti}^{4+}] + [\text{Si}^{4+}]$ with the charge compensation being accomplished totally or partially by hydrogen (H^+) (E.V. Dubinsky et al., "A quantitative description of the causes of color in corundum," Spring 2020 *G&G*, pp. 2–28). In corundum, H^+ forms a bond with oxygen creating OH^- . It is the OH^- that is responsible for the broad peak at 3161 cm^{-1} (and the series of peaks at 3161, 3242, and 3355 cm^{-1}) when associated with Mg^{2+} (C.P. Smith et al., "Infrared spectra of gem corundum," Fall 2006 *G&G*, pp. 92–93). However, the origin of the 3161 cm^{-1} peak is not well understood. The article by N. Fukatsu et al. ("Incorporation of hydrogen into magnesium-doped α -alumina," *Solid State Ionics*, Vol. 162, 2003, pp. 147–159) showed that when OH^- is incorporated into Mg^{2+} -doped synthetic sapphire, the 3161 cm^{-1} peak was not present but a broad band appeared in the 3000 cm^{-1} region. If the hydrogen is eliminated either in nature or in the laboratory, the trapped hole (h^*) forms to provide charge compensation. The trapped hole pairs with Fe^{3+} , creating a trapped-hole- Fe^{3+} ($\text{h}^*\text{-Fe}^{3+}$) pair, which is a very strong yellow chromophore in corundum. In this report, the authors aim to study the effects of heat treatment in changing the 3161 cm^{-1} feature and creating the yellow coloration.

Twelve yellow sapphires reportedly from Sri Lanka and Madagascar that initially displayed a weak to strong 3161

cm^{-1} peak or a 3161 cm^{-1} series in FTIR were selected for heat treatment in an oxidizing atmosphere (air) at 500°, 700°, 900°, and 1050°C for a fixed duration of six hours at each temperature. For a final step, some stones were heated at 1550°C in pure oxygen to assure the complete elimination of hydrogen. The samples were fabricated as optical wafers with at least two polished surfaces perpendicular and/or parallel to the c-axis. The samples possess a sufficiently large and clean area to get high-quality FTIR spectra. After each heat treatment step, FTIR spectra were collected at the same position for each sample by fixing it in an identical position in the sample holder.

Heat treatment can cause the H^+ to move to different sites by diffusion or at sufficiently high temperatures to diffuse completely out of the sample. The diffusion coefficient of hydrogen in corundum is exponentially dependent on temperature. After heat treatments at 500°C and 700°C, the intensities of 3161 cm^{-1} peaks and the color appearance of the stones were essentially unaltered. Thus, there is little outward diffusion for a sample of this size. However, heating at 900°C and above for six hours in air will begin to diffuse the hydrogen out of the lattice. As the hydrogen begins to diffuse out, trapped holes form and pair with Fe^{3+} to maintain charge compensation, increasing the yellow coloration.

At the same time, the amplitude of the 3161 cm^{-1} feature will decrease proportionally. The test at 1550°C for six hours was conducted in pure oxygen to eliminate any possibility of the water vapor in air contributing hydrogen. With this last step, the outward diffusion of all the hydrogen in the stone was complete, eliminating OH^- peaks in FTIR spectra and maximizing the yellow trapped-hole coloration.

Figure 19 shows these heating processes as applied to stones from Sri Lanka with a strong 3161 cm^{-1} feature and to some of the stones from Madagascar with a weak 3161 cm^{-1} feature. As expected, both types exhibited a similar diffusion reduction in the initial hydrogen content with temperature and time. The coloration of some of the Madagascar stones was zoned, with areas colored by the $\text{h}^*\text{-Fe}^{3+}$ pair, by $\text{h}^*\text{-Fe}^{3+}$ plus Fe^{3+} , and some by Fe^{3+} only, depending on the distributions of Fe^{3+} and $\text{h}^*\text{-Fe}^{3+}$ in the stone. Usually, the zones in which $\text{h}^*\text{-Fe}^{3+}$ is dominant will increase yellow coloration with high-temperature heat treatment by removing the hydrogen, whereas the areas with Fe^{3+} alone are rarely strongly zoned.

Interestingly, a characteristic peak at 3161 cm^{-1} in certain Sri Lankan samples could be occasionally transformed to the broadband series in 3000 cm^{-1} region with a broad band at 2625 cm^{-1} when heated at 900°C and above in air, as presented in figure 20. Previously, the 3000 cm^{-1} broad band series has been reported as indicative of heat treatment observed in Punsiri-type heated blue sapphires (G. DuToit et al., "Beryllium treated blue sapphires: Continuing market observations and update including the emergence of larger size stones," *GIA Research News*, 2009, <https://www.gia.edu/gia-news-research-nr62609>) and could be observed in unheated high-Fe yellow sapphires from

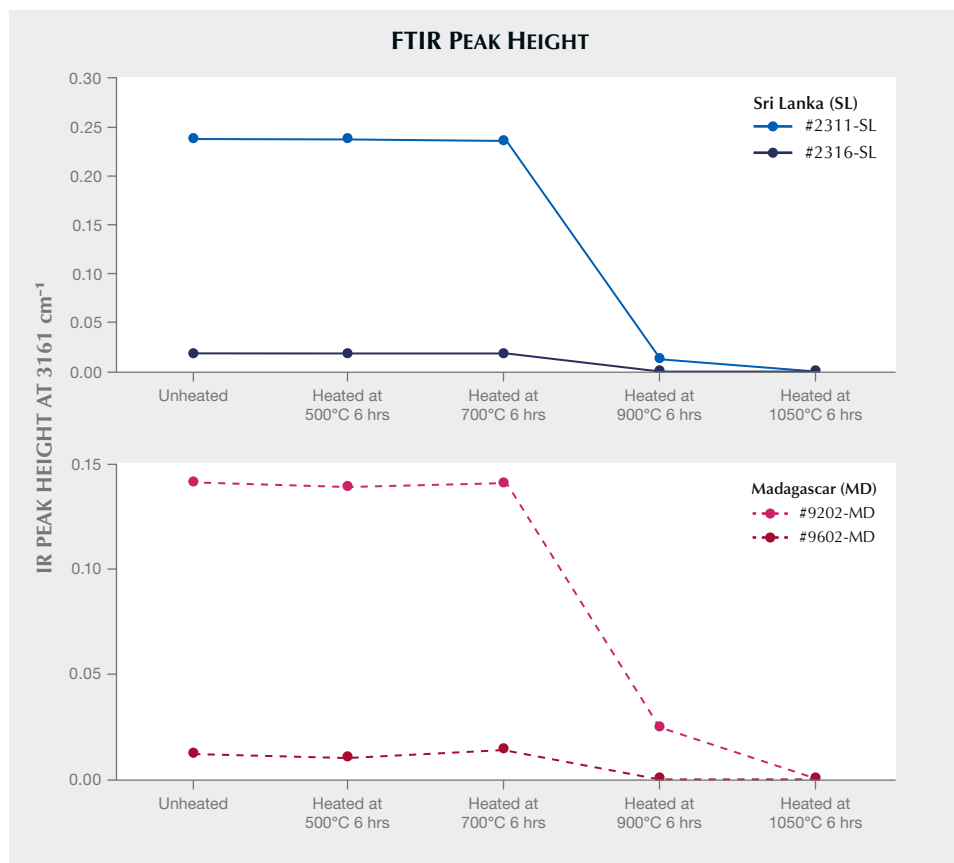


Figure 19. Plot of FTIR peak height at 3161 cm⁻¹ of representative yellow sapphires from Sri Lanka (above) and Madagascar (bottom), before and after heating at different temperatures between 500° and 1050°C for six hours.

basalt-hosted deposits, such as Thailand and Australia (Fall 2016 GNI, pp. 325–327). However, the 3000 cm⁻¹ broad band series could also be found in heat-treated Sri Lanka yellow sapphires, as seen from this study.

In summary, heat treatment was carried out in an oxidizing atmosphere to increase the trapped-hole color centers and deepen the yellow coloration. Sri Lankan samples colored mainly by the h⁺-Fe³⁺ pair can produce stronger yellow

coloration by heat treatment, but only at high temperatures (900°C and above). The heating temperature at 900°C starts to change the 3161 cm⁻¹ peak/series in FTIR and the color appearance in metamorphic yellow sapphires. It may well be that heating for a much longer time at 900°C would more completely diffuse out the hydrogen. The amplitude of the 3161 cm⁻¹ peak is insignificantly altered when heated at low temperature (below 700°C) but

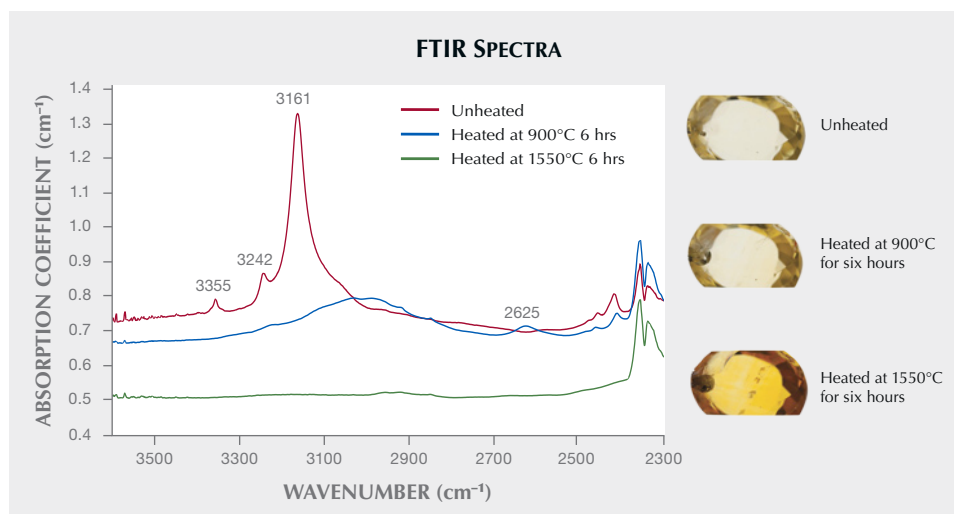


Figure 20. Sri Lankan sample no. 2801 showing a 3161 cm⁻¹ series (red) in FTIR with initially light yellow color, then altered to 3000 cm⁻¹ broad band series (blue) with a bit stronger yellow zone after heating at 900°C for six hours. Finally, the broad bands disappeared (green) and a much stronger yellow coloration was generated at 1550°C, thickness 3.748 mm, 190 ± 41 ppm Fe.

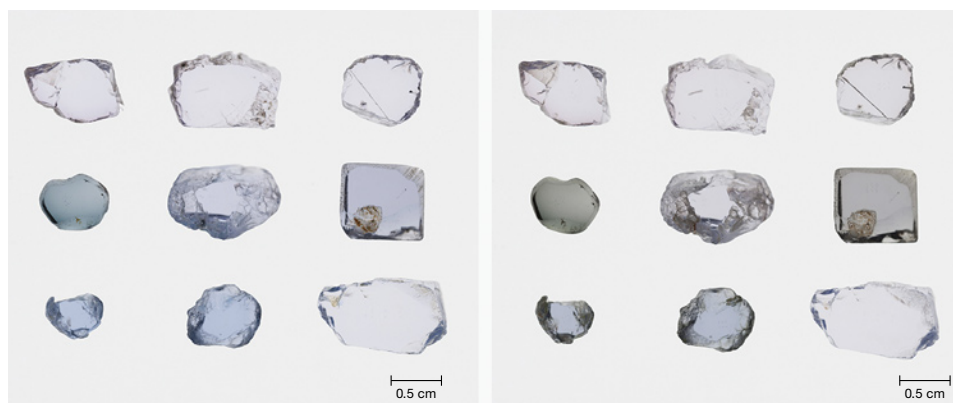


Figure 21. Color-calibrated photos of blue to violet spinels before heating (left) and after heating at 1000°C for four hours (right). There are three groups of spinel samples in this study: violet (top row), iron-dominated blue (middle row), and cobalt-dominated blue (bottom row). Photos by Sasithorn Engniwat.

can be greatly reduced when heated at 900°C and above, and sometimes converted to the 3000 cm^{-1} broadband series, and then it disappears at much higher heating temperature. Although the 3000 cm^{-1} broadband series might not be indicative of heat treatment in basalt-related yellow sapphires, it is able to indicate heat treatment in Sri Lankan yellow sapphires. Careful consideration should be exercised when using FTIR to identify heat treatment in corundum.

Ungkhana Atikarnsakul
GIA, Bangkok

John L. Emmett
Crystal Chemistry
Brush Prairie, Washington

Spectroscopic characteristics of low-temperature heated blue to violet spinel. Although spinel is rarely treated, there have been some heated spinels available in the trade. The effect of heat treatment on pink to red spinel has been previously reported [e.g., S. Saeseaw et al., "Distinguishing heated spinels from unheated natural spinels and from synthetic spinels," 2009, *GIA Research News*, <https://www.gia.edu/gia-news-research-NR32209A>; A. Peretti et al., "Heat-treatment of spinel," in *World of Magnificent Spinel: Provenance and Identification*, GRS Gem-research Swisslab, 2015, pp. 269–278]. Chromium-bearing spinel with pink to red color generally becomes darker after heat treatment, and the clarity of spinel containing particulate clouds can be significantly enhanced by heating between approximately 950° and 1150°C (S. Saeseaw et al., 2009).

In addition to the most popular pink to red spinel, another important and desirable variety is blue spinel, especially with a vibrant cobalt blue color. The dominant chromophores in blue to violet spinel includes Fe^{2+} and Fe^{3+} at both tetrahedrally (T) and octahedrally (M) coordinated sites of spinel structure as well as Co^{2+} at the T site (G.B. Andreozzi et al., "Color mechanism in spinel: A multi-analytical investigation of natural crystals with a wide range of coloration," *Physics and Chemistry of Minerals*, Vol. 46, 2019, pp. 343–360; V. D'Ippolito et al., "Color mechanism in spinel: Cobalt and iron interplay for the blue color,"

Physics and Chemistry of Minerals, Vol. 42, 2015, pp. 431–439). Previous works have revealed the application of cobalt diffusion treatment to enhance blue color in spinel (e.g., S. Saeseaw et al. "GIA lab reports on a new cobalt diffusion treatment of natural spinel," *GIA Research News*, 2015, <https://www.gia.edu/gia-news-research/cobalt-diffusion-natural-spinel-report>). A study on the heat treatment of blue spinel without external chemical diffusion is lacking in the literature, to our knowledge.

To understand the change of chromophores in blue to violet spinel caused by heat treatment, this preliminary study involved exploratory heat treatment of samples from various localities: Madagascar, Myanmar, Tanzania, and Vietnam. The samples were separated into three groups: violet, iron-dominated blue, and cobalt-dominated blue spinel (figure 21, left). UV-Vis-NIR spectrum of representatives in each group show relatively similar absorption spectra (figure 22), consisting of a strong UV-edge absorption at approximately below 330 nm; multiple absorption bands between 350 and 1100 nm of Fe^{2+} , Fe^{3+} at T and M sites; and multiple bands between 500 and 670 nm of Co^{2+} at the T site (Andreozzi et al., 2019; D'Ippolito et al., 2015). With a very similar absorption pattern between violet and blue iron-dominated spinels, the difference in color appearance is associated with different intensity of absorption bands which is more intense in iron-dominated blue spinel due to higher Fe concentrations (Andreozzi et al., 2019). The spinel samples were heated at 600°, 700°, 800°, 900°, and 1000°C in air and held for four hours at each heating temperature. Progressively heating from 600° to 1000°C showed that violet color changed little in this temperature range, whereas blue spinel became more grayish after heating at approximately 800°–900°C (figure 21, right). Heat treatment could affect the color appearance of iron-dominated blue spinel colored much more than cobalt-dominated blue spinel. After heat treatment (figure 23), the spectra displayed generally broader absorption bands, with less prominent bands below 650 nm and more prominent bands at around 920 nm. The broadening of the chromium emission peak in photoluminescence spectroscopy (PL) is an effective criterion for detecting heat treatment in spinel [e.g., Saeseaw et al., 2009; Peretti

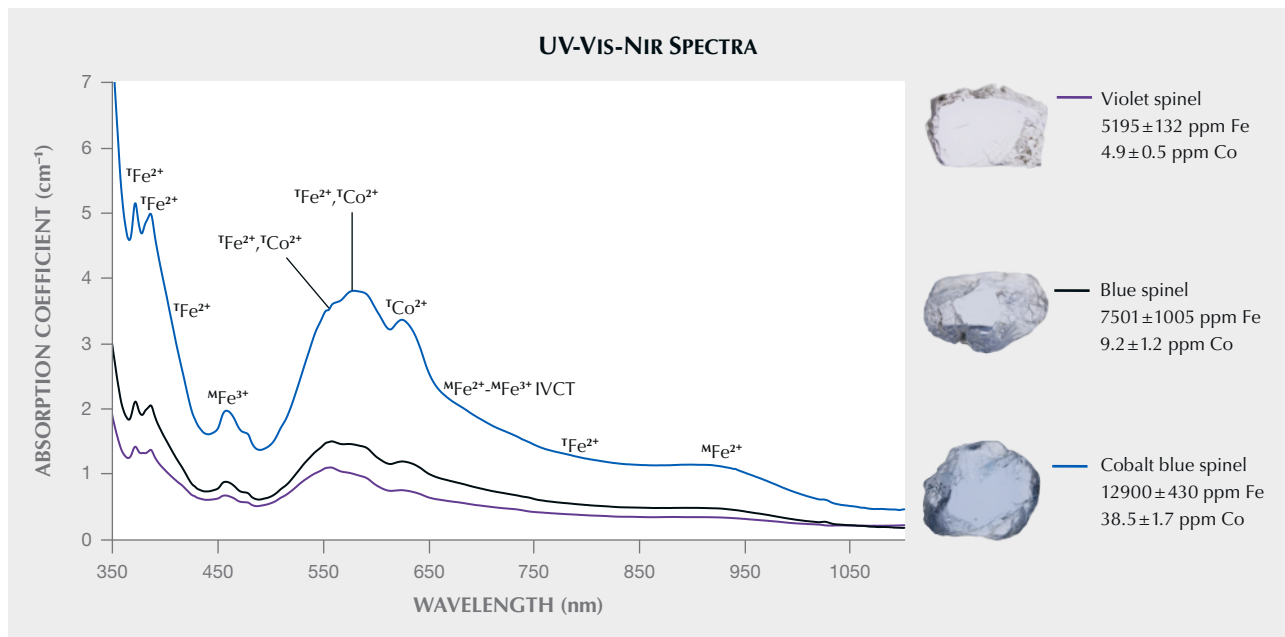


Figure 22. Representative UV-Vis-NIR spectra of unheated spinels for the three color groups. They have relatively similar absorption spectra with different intensities and some band positions, depending on Fe and Co contents. A series of Fe absorption bands in the spectrum consists of Fe²⁺ at T site (^TFe²⁺) bands at approximately 371, 385, 400, 558, 580, and 780 nm; Fe²⁺ at M site (^MFe²⁺) band at around 920 nm; Fe³⁺ at M site (^MFe³⁺) band at 457 nm; ^MFe²⁺-^MFe³⁺ intervalence charge transfer (IVCT) band at about 655 nm; and Co²⁺ at T site (^TCo²⁺) bands at approximately 558, 580, and 625 nm (Andreozzi et al., 2019; D'Ippolito et al., 2015). Fe and Co concentrations reported in the figure were analyzed by LA-ICP-MS.

et al., 2015). PL spectra of the treated samples in this study were also analyzed and showed that the Cr emission peak of the material broadened after heating at 800°–900°C. The change in color and spectroscopic data after heat treatment resulted from a direct spinel transforming to a partially inverse spinel (R. Widmer et al., "Effects of heat treatment on red gemstone spinel: Single-crystal X-ray, Raman, and photoluminescence study,"

Physics and Chemistry of Minerals, Vol. 42, 2015, pp. 251–260) as well as the changes of valence and site distribution of Fe chromophores in the spinel structure. The less desirable blue color of the treated spinel in this preliminary study, regardless of any improvement in clarity, suggests that the heat treatment of the blue to violet spinels was likely unintentional. In addition, as demand for gray colored spinels has increased in the trade over

Figure 23. UV-Vis-NIR spectra comparisons of cobalt blue (top), blue and violet spinels (bottom) in figure 22, before heating (solid line) and after heating at 1000°C for four hours (dashed line). Broader absorption bands, with less prominent bands below 650 nm and more prominent bands at around 920 nm, were observed.

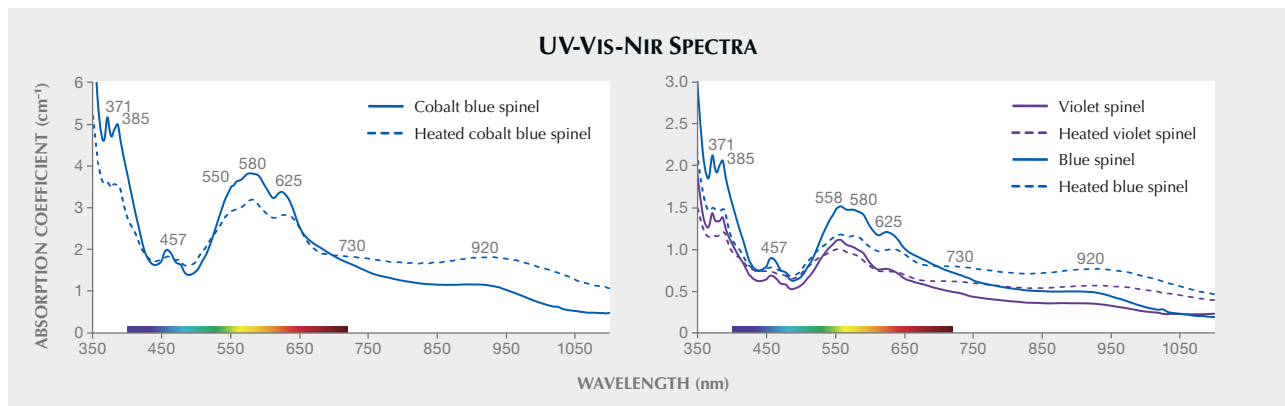




Figure 24. The GIA Library & Museum Facebook page stimulates spirited discussion among gemologists, bibliophiles, and gem enthusiasts. Photo composite by Robert Weldon/GIA.

the past few years (Spring 2019 GNI, p.130), some concerns about heat treatment in gray spinels should be raised.

Wasura Soonthorntantikul and
Vararut Weeramongkhonlert
GIA, Bangkok
Aaron C. Palke
GIA, Carlsbad

ANNOUNCEMENTS

GIA Library and Museum Facebook group. Dedicated to the beauty and fascination of gemological books and mineral exhibits, the Richard T. Liddicoat Gemological Library & Information Center and the GIA Museum launched a Facebook group on August 2, 2021.

The group has attracted over 600 bibliophiles, museum curators, gemological enthusiasts, students, researchers, and experts worldwide. It aims to provide greater digital access to our library and museum and stimulate enthusiastic discussion of the many themes covered in our collection of books, periodicals, and exhibits (figure 24). These subjects include gemology, geology, mineralogy, jewelry manufacturing, design, jewelry history, localities, and the gem industry.

Features include library-curated video segments and book reviews, commentary on rare bookplates or covers, and short interviews with notable library patrons. The Facebook group also highlights specific rare books from the library's digital collection on the Internet Archive (<https://archive.org/details/gialibrary>). A growing proportion of the library's notable rare books and manuscripts are digitized and offered to the public—free of charge. Over 700 books have been digitized, and the project is ongoing. The museum provides unique glimpses and the stories behind some of the amazing gems and minerals from GIA's collection.

To become a member of this group, please visit <https://www.facebook.com/groups/gialibraryandmuseum>

James Shigley receives Robert M. Shipley Award. Dr. James E. Shigley (figure 25), GIA's distinguished research fellow, has received the American Gem Society's Robert M. Shipley Award for his significant contribution to the science of gemology. The prestigious award was announced at the AGS Conclave in Dallas on September 13. Dr. Shigley was unable to attend the ceremony but was honored at GIA's Carlsbad campus by president Susan Jacques, research colleagues, and family, where he was presented with a plaque and pin acknowledging his decades of commitment to gem research.

During his almost 40-year career with the Institute, Shigley has authored or coauthored more than 85 *Gems & Gemology* articles, edited the *G&G In Review* book series, and been the face of GIA's research mission, lecturing extensively on gems and gem identification. He is also the recipient of the 2017 AGS Lifetime Achievement Award.

Figure 25. Dr. James Shigley is the 2021 recipient of the American Gem Society's Shipley Award. Photo by Kevin Schumacher.

